Modelling and Simulation of Intermediate Temperature Solid Oxide Fuel Cells and their Integration in Hybrid Gas Turbine Plants

A Thesis Submitted By

Osarobo Omorogieva Ighodaro

For the Degree of Doctor of Philosophy

School of Chemical Engineering and Advanced Materials

Newcastle University

June 2016

ABSTRACT

Solid oxide fuel cells (SOFCs) are gaining prominence as power sources amongst other types of fuel cells due to their high electric energy efficiencies, their ability to integrate with other energy cycles in a hybrid system, fuel choice flexibility and low pollutant emissions. Operation of an SOFC involves complex coupling of the electrochemical reactions, chemical reactions and transport phenomena simultaneously in the cell's main components consisting of gas channels, porous electrodes and the dense ceramic electrolyte. Consequently, mathematical modelling of these processes becomes an essential research tool aiming to provide detailed insight, while reducing cost, time and the effort associated with experimentation. The main aim of this thesis is to develop mathematical models in the cell and at system level to better understand the complex operation of SOFCs and its associated cycle under practical conditions with the aim of enhancing the power output and efficiency of the cell.

At the cell level, a two dimensional along the channel micro-scale isothermal model of a SOFC is developed and validated against experimental data and other simulated result from literature. The steady state behaviour of the cell was determined by numerical solution of the combined transport, continuity and kinetic equations. The model is capable of predicting the cell performance including polarisation behaviour and power output. The model is used to study the effect of the support structure, geometric parameters and the effect of operating conditions on cell performance. Several parametric studies, such as the effect of operating conditions and geometric parameters on cell performance with a view to optimising the cell.

Also, at the cell level, a two dimensional along the channel model was developed which integrates a heat transfer model and direct internal reforming kinetics into the earlier developed isothermal model. This non-isothermal model was also validated against experimental data. The developed model not only predicts the performance of the SOFC at different design and operating conditions, it also provides an insight on the different phenomena and the distributions of current density, temperature and gas pressures within the cell. Microstructural parametric studies of the reaction layer were also carried out.

At the system level, the SOFC was integrated in a hybrid gas turbine plant. The integrated cycle was modelled using energy and exergy thermodynamic analysis. The analysis was done using the non-isothermal models developed for SOFC at the cell level and through the development of thermodynamic models for the other components such as the compressors, turbines, mixers, recuperators and combustors in the hybrid system. Performance comparison of two different hybrid configurations was carried out. Electrical efficiency, fuel utilisation efficiency, and exergy destruction were used in assessing the system performance.

The results from the developed models shows that the anode supported SOFCs gives the best cell performance amongst other support structures when operated at intermediate temperatures and that the cathode ohmic overpotential is the single largest contributor to the cell potential loss. Also, the inclusion of the heat transfer model and internal reforming kinetics significantly improves the cell predictions. The study on the effect of integrating the SOFC in a hybrid system showed an overall improvement with respect to electrical efficiency

Table of Content

List of Figures

List of Tables

Nomenclature

c_i	Concentration of species i, $mol\ m^{-3}$
$c_{p,i}$	Specific heat capacity at constant pressure $J\ mol^{-1}\ K^{-1}$
d_p	Diameter of conducting particle m
d_{pore}	Pore diameter, m
D_{ij}	Diffusion coefficient, $m^2\ s^{-1}$
$D_{kn,ij}$	Knudsen diffusion coefficient, $m^2\ s^{-1}$
E^{ocv}	Open circuit voltage, V
E	Cell Voltage, V
ex	Exergy
ϵ	Effectiveness
F	Faraday's constant, $96487\ C\ mol^{-1}$
ΔG	Molar Gibbs free energy change, $J\ mol^{-1}$
h	Heat transfer coefficient, $W\ m^{-2}\ K^{-1}$
h_i	Specific molar enthalpy of species i, $J\ mol^{-1}$
i	Current density, $A\ cm^{-2}$
i_v	Volumetric current density, $A\ cm^{-2}$
i_0	Exchange current density, $A\ cm^{-2}$
$\vec{I}$	Identity matrix
j_i	Mass diffusive flux vector
k_f	Thermal conductivity of fluid mixture, $W\ m^{-1}\ K^{-1}$
k_s	Thermal conductivity of component, $W\ m^{-1}\ K^{-1}$
k_{sf}	Forward reaction rate for water-shift gas reaction, $mol\ m^{-3}\ Pa^{-2}s^{-1}$
k_{rf}	Forward reaction rate for methane reforming, $mol\ m^{-3}\ Pa^{-2}s^{-1}$
k_{sb}	Backward reaction rate for water-shift gas, $mol\ m^{-3}\ Pa^{-2}s^{-1}$
k_{rb}	Backward reaction rate for methane reforming, $mol\ m^{-3}\ Pa^{-2}s^{-1}$
k_{sq}	Equilibrium constant for the water-shift gas reaction
k_{rq}	Equilibrium constant for the methane reforming reaction
l	Layer thickness
M_i	Molecular weight of species i , $kg\ \mathrm{k}mol^{-1}$
$\dot{n}$	Molar flow rate of species i, $mol\ s^{-1}$
$\dot{n}_{el}$	Number of electrons transferred
n_{io}	Number fraction of ionic conducting particles
n_{el}	Number fraction of electronic conducting particles

N_t	Number density of all the particles
N_u	Nusselt number
p	Pressure, Pa
p_{io}	Percolation probability of ion-conducting particles
p_{el}	Percolation probability of electronic conducting particles
p_i	Partial pressure of species i, Pa
q	Heat flux, $W\ m^2$
Q	Heat supplied, W
R	Universal gas constant, $8.3143\ J\ mol^{-1}\ K^{-1}$
r_i	Source term of species i
T	Temperature, K
u	Velocity flux, m^2/s
w_i	Mass fraction of species, i
W_t	Work done, kW
x_i	Mole fraction of species i
z	Average coordinating number
z_{io}	Coordinating number of ionic conducting particles
z_{el}	Coordinating number of electronic conducting particles.

Greek Symbol

α	Charge transfer reaction
ε	Porosity
τ	Tortuosity
σ_i	Ionic conductivity, $S\ m^{-1}$
σ_s	Electronic conductivity, $S\ m^{-1}$
μ	Dynamic viscosity of component, $kg\ m^{-1}\ s^{-1}$
ρ	Density, $kg\ m^{-3}$
v_i	Stoichiometric coefficient of species i
λ	Excess air coefficient
ŋ	Efficiency
η	Overpotential, V
$\emptyset$	Potential, V
θ	Contact angle between electronic and ionic particles
φ	Volume fraction of electronic conducting particles

Subscripts

a	Anode
act	Activation

c	Cathode
f	Fuel
rl	Reaction layer
bl	Backing layer
ref	Reference state
r	Reaction
g	Gas
ph	Physical
ch	Chemical
eq	Equilibrium

Superscripts

eff	effectiveness
b	Flow layers

Abbreviations

0D	Zero dimensional
1D	One dimensional
2D	Two dimensional
3D	Three dimensional
AC	Air compressor
ACH	Anode channel
ADL	Anode diffusion layer
AFC	Alkaline fuel cells
AI	Anode side interconnects
BS	Booster
B-V	Butler Volmer
C	Combustor
CCH	Cathode channel
CER	Cathode exhaust recycle
CFD	Computational fluid dynamics
CRL	Cathode reaction layer
DIR	Direct internal reforming
DMFC	Direct methanol fuel cell
FC	Fuel compressor
FEM	Finite element method
FVM	Finite volume method

GT	Gas turbine
HRSG	Heat recovery steam generator
HT	High temperature
IIR	Indirect internal reforming
IT	Intermediate temperature
LHV	Lower heating value
LT	Low temperature
LTE	Local temperature equilibrium
LTNE	Local temperature non equilibrium
M	Mixer
MCFC	Molten carbonate fuel cell
OX	Oxidation
PEMFC	Proton exchange membrane fuel cell
PR	Pre reformer
R	Recuperator
RD	Reduction
RHE	Recuperator heat exchanger
S	Separator
SOFC	Solid oxide fuel cell
TPB	Triple phase boundary

Acknowledgement

I would like to express my special appreciation and thanks to my supervisor Professor Keith Scott, you have been a tremendous mentor for me. I would like to thank you for encouraging my research and for allowing me to grow as a research scientist. Your advice on the research has been priceless. To my viva examiners, Professor Rui Chen and Professor Allen Wright, I also want to thank you for letting my defence to be quite enjoyable and for your brilliant comments and suggestions. I would especially like to thank my friends and colleagues in the Fuel cell group who are always there to support and provide advice.

A special thanks to my family, words cannot express how grateful I am to my mother, who has always wanted one of her children to be a doctor (wish fulfilled), your constant prayers, encouragement and support has seen me through, my seven siblings and my beautiful nieces and nephews, (nothing beats family), thank you so much for your support and sacrifices. Special thanks also to my mother in-law for your prayers and support.

The aware of this degree has come at some personal cost, having lost my dearest uncle Tony Okodugha and my pseudo Granma Cecilia Obuseli during the period. Both of you had been sources of inspiration and encouragement to me. It still hurts when I think that I left for the PhD with your encouragement and love and I return to meet you no more. Rest in Peace.

I will like to thank all my friends who supported me in writing especially Jennifer Nwosu who had the extra burden of proof reading my thesis, to all the others especially Henry Egware and Benjamin Aburime, I say a big thank you for helping me strive towards my goal.

To my professional mentor, Professor Salami, I might never have dreamt of a PhD in Newcastle if not for you, thank you sir.

At the very end, I express my profound appreciation to my lovely wife who spent many sleepless nights with me and always my support in difficult moments, and to my sons Maximilian and Alexander (the two addition PhDs I obtained during the PhD) you have made my life complete, for that I am eternally grateful.

CHAPTER1 : Introduction

1.1 Hydrogen, the fuel for our future

The increasing concern and public awareness for a cleaner environment and the need for sustainable, efficient and clean energy production has caused renewed interest in alternative energy sources. Global energy consumption between 1970 and 2010 and projections to 2030 is presented in Figure (1-1). Within these years energy demand is seen to double and it is expected to keep rising. The heavy reliance on fossil fuel[1] as the major energy source is becoming a major global concern as it is known to have significant negative impact on the environment. A key product of the combustion of fossil fuel is carbon dioxide which strongly absorbs infrared radiation.

The rapid pace of industrialization in the last decade has caused an increase in CO_2 content in the atmosphere, a phenomena which is strongly linked to global warming[2]. In addition, the world's fossil fuel reserves are limited and fast dwindling due to the rapid pace of exploitation, enhanced life style and increasing world population, besides they are confined to a few regions in the world, a situation that could create some form of energy crisis in the event of civil and political conflicts in these regions. One solution to this impending energy crisis is to use of more renewable sources and technologies[3].

According to the 2013 report from the International energy agency on the World's energy outlook[4], power generation from renewables is projected to increase by over 7000TWh from 2011 to 2035, accounting for about half of the increase in power generation.

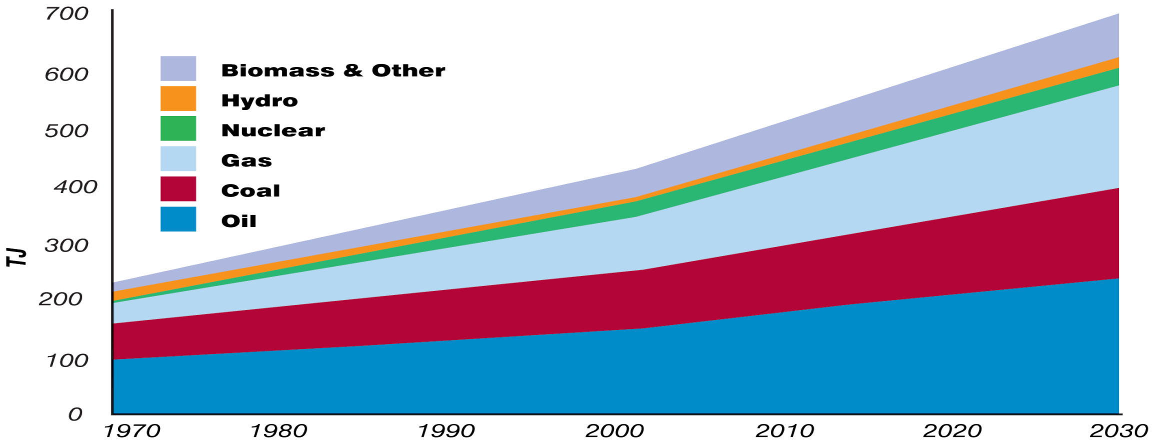

Figure 1-1: World energy consumption projections from 1970 to 2000[5]

Quite a number of alternative energy technologies are been researched and developed. Sunlight, wide, tides, waves and geothermal heat are familiar images of such technologies; while been potential sources of electrical energy, issues relating to stability (cloudless days, windless days or low tides) and portability greatly limits their usage.

Among the alternative fuel sources, hydrogen, as an energy carrier is receiving considerable attention since it is abundantly available making up about 75% of all matter in the universe. It can be obtained from several sources such as renewable (hydroelectric, wind, ocean thermal, geothermal, biomass, solar thermal), nuclear (fission and fusion reactors) and fossil (coal, petroleum, natural gas, shale gas)[6], thus increasing global energy supply security. It is also known to be emission free (when used in a fuel cell) which reduces environment degradation activities. Unfortunately, hydrogen unlike oil or coal is not found in its natural state; it has to be produced from other energy source before it is used as a clean energy source. This attribute of hydrogen is illustrated in Figure (1-2) showing how hydrogen is produced from a variety of sources using different techniques and its various end user applications. As seen in the figure, hydrogen can be obtained from the various techniques such as:

- *Electrolysis:* this involves the splitting of water into its constituent hydrogen and oxygen using electricity from renewable sources
- *Conversion of biomass:* this is carried out either by electrochemical or biochemical conversion of biomass into intermediate products from which hydrogen is produced either by reformation or fermentation processes, these conversion processes include:

  -*gasification:* involves subjecting the biomass to high temperatures and pressures so as to reduce the organic materials to hydrogen and carbon dioxide/monoxide.

  -*pyrolysis:* involves the conversion of biomass into bio-oil by thermal decomposition, after which *catalytic steam reforming* is carried out on it (liquid or vapour gases), producing hydrogen.

  -*fermentation*: involves the use of anaerobic microorganisms such as bacteria or yeast to produce hydrogen directly

- *Solar conversion:* involves using solar conversion techniques to produce hydrogen though either of the following: -
  -*thermolysis*: entails using the heat obtained from concentrated heat source to drive electrochemical reactions that produces hydrogen or to drive electrolysis reaction at high temperature to decompose water. -
  -*photolysis*: entails using solar photons to produce hydrogen directly through biological or electrochemical systems.

These characteristic of hydrogen contributes significantly to energy security, besides; hydrogen combustion is known to have the potential for higher energy production than any other type of fuel.

The annual production of H_2 is estimated to be about 0.1Gton, of which 98% comes from reforming of fossil fuel[7]. The portion of hydrogen produced through renewable sources has increased in recent years and it is projected to increase more significantly in future years. Renewable energy contribution in primary energy sources is projected to rise from 13% in 2011 to 18% in 2035[4]. Countries like Norway and Denmark are known to be in the forefront of this; since 2003, Norway has had a hydrogen highway between Oslo and Stavanger, of which part of the hydrogen used is obtained from renewable energy sources mainly through electrolysis from hydropower and solar[8], while Denmark continues to expand their combined heat and power (CHP) facility opened in 2007, using hydrogen produced through electrolysis from excess wind power and this has so far saved 14% of fossil fuel usage[9].

The major barriers to using hydrogen as an fuel carrier, are that hydrogen is only as clean as the method of production and the lack of cost effective, efficient and safe methods of storage and transportation for its various mobile and stationary applications[7].

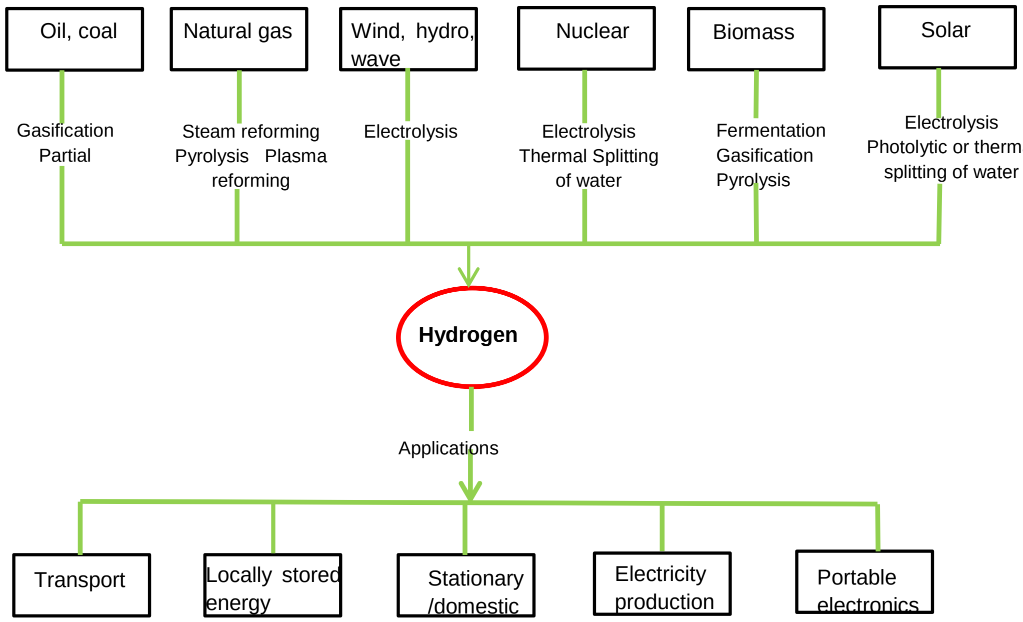

Figure 1-2: Linkage between hydrogen production methods and its end user applications [10]

Researchers strongly believe that the relationship between hydrogen and electricity is an attractive route to achieving sustainable energy supply, and that fuel cells are strongly considered as replacements to conventional heat as the primary way to produce electricity from the chemical energy stored in fossil fuels[11].

1.2 Fuel cells

Fuel cells (FC) are energy conversion devices that produce electrical energy directly from the chemical energy stored in the fuel through electrochemical reaction processes. Water and heat are the usual by-products from the process. Conventional engines typically generate electrical energy from fuels in a series of energy conversion steps which usually includes:

1. The burning of the fuel; a process which converts its chemical energy into heat
2. The heat is then used to generated steam (steam turbines) or to increase the energy of the combusted gases (gas turbines)
3. The steam or the products of combustion are now used in turning the turbine blades in a process that converts the stored heat into mechanical energy
4. Lastly, mechanical energy is used to power a generator which generates electrical power.

A fuel cell side-steps these processes, rather it generates electrical power in one single step[12] without including any moving parts and fewer sources of energy loss. Its characteristics of high energy efficiency, near zero emissions, noiseless operation, flexible sizing, fuel flexibility (for some of the cell type) and mechanical simplicity makes it an attractive option for electrical energy generation. A typical unit fuel cell is made of three main components as shown in Figure 1-3a: anode (fuel electrode), cathode (air electrode) and electrolyte. The reactant gases are continuously supplied to the fuel and air electrodes; ions produced as a result of the electrochemical reactions migrate from one of the electrodes through the electrolyte to the other electrode. As a result of the reactions taking place, electrons are generated, these electrons flow through an external circuit producing electric current. Unit cells are usually arranged together in series in a process called ‘stacking’ in other to achieve higher power capacities as depicted in Figure 1-3b

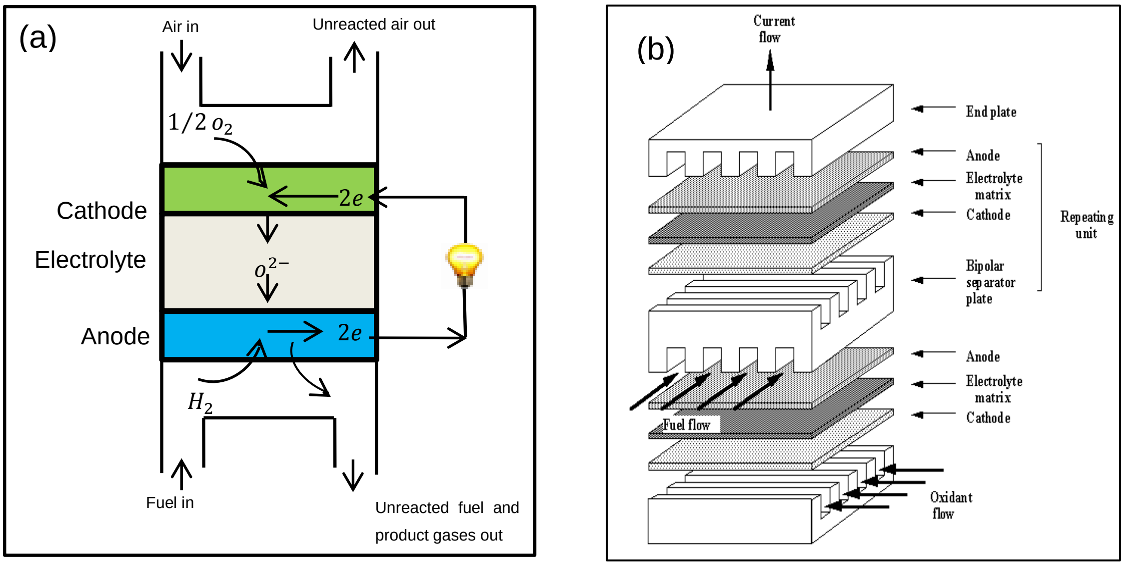

Figure 1-3: Schematic showing the operations of a fuel cell (a) Unit fuel cell (b) Fuel cell stack

Fuel cells developmental origin attributed to Sir William Groove, who in the early 1900’s built a cell consisting of platinum strips as electrodes and sulphuric acid as electrolyte[13], electricity was produced when hydrogen and oxygen were combed unto the electrodes. Since then huge developments have been made in fuel cell systems development especially by the U.S space agency, when as early as the

1960s, they had begun to use fuel cells to provide electricity, guidance and communication for their space missions. The technology became a major research interest in the 1990s after been forgotten for terrestrial applications in bid to provide clean energy[11].

1.2.1 Types of fuel cells

There are a range of different fuel cell types, each with its own unique material properties and operations. They are suited to different applications and can be categorised according to the nature of the electrolyte and fuel used. Figure 1-4 represents the mechanism by which the different types of fuel cell operate.

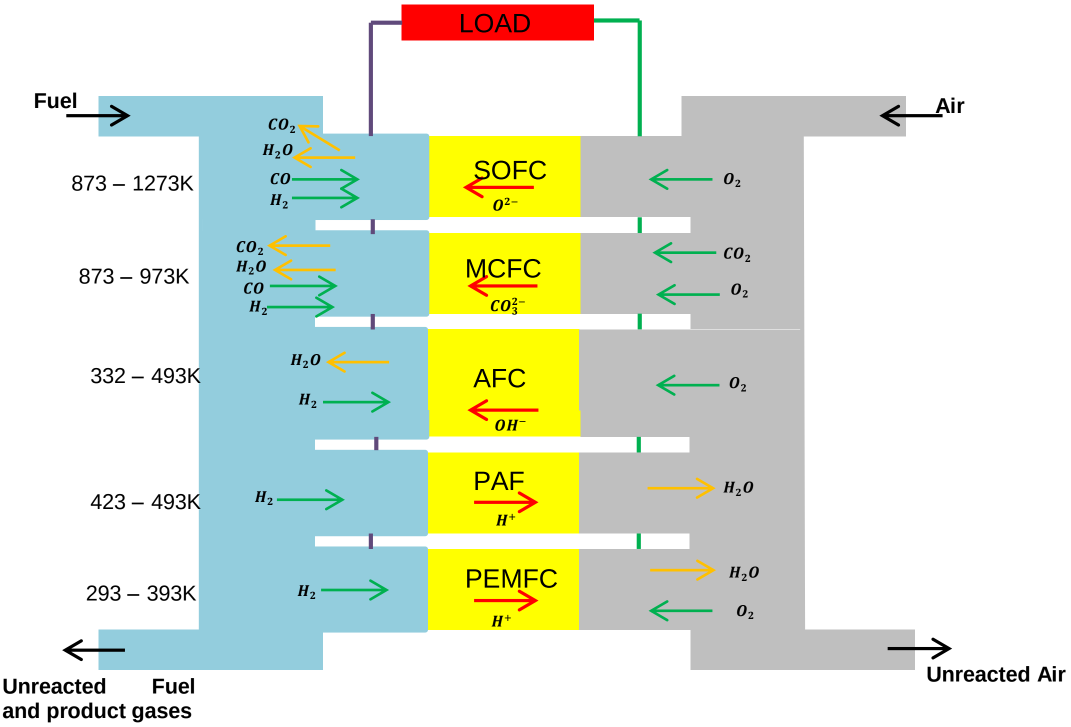

Figure 1-4: Different fuel cell types and their operation

The top two in the diagram operate at high temperatures (usually between 873K – 1273K), whilst the last four are low and medium temperature fuel cells. They differ from each other in many other aspects such as operating conditions, type of ion conducted across the electrolyte, constitutive materials and performance characteristics. Common types of fuel cells are briefly discussed below [12, 14, 15]:

Solid oxide fuel cell

Solid oxide fuel cell (SOFC) operate at high temperatures ranging from 873K to 1273K, it employs an all solid oxide ions (O^{2-}) conducting electrolyte which conducts the ions from the cathode to the anode, its origins is attributed to Nernst, who in 1899 was the first to describe zirconia (ZrO_2) as an oxide ion conductor. However it was much later that some Swiss scientists actually developed the solid oxide technology by experimentally studying the electrolyte properties of different materials[16]. SOFCs has good fuel flexibility as it allows a wide range of hydrocarbon fuels such as methane, biomass, and ethanol to be used directly in the cell or indirectly by reforming. A further advantage of the SOFC is its ability to be integrated in hybrid systems thereby improving the overall work output and efficiency. Its major downside is the high cost of ceramic materials and the problems associated with carbon deposition when fuels containing carbon is used. In a H_2 fed SOFC, the following electrochemical reactions occur:

$$Anode\ reaction\ layer: \quad H_2 + O^{2-} \rightarrow H_2O_{(g)} + 2e^- \tag{1-1}$$

$$Cathode\ reaction\ layer: \quad \frac{1}{2}O_2 + 2e^- \rightarrow O^{2-} \tag{1-2}$$

$$\boldsymbol{Overall}: \quad H_2 + \frac{1}{2}O_2 \rightarrow H_2O \tag{1-3}$$

If CO is also oxidized in the reaction layers, the additional electrochemical reactions which occur are:

$$Anode\ reaction\ layer: \quad CO + O^{2-} \rightarrow CO_2 + 2e^- \tag{1-4}$$

$$Cathode\ reaction\ layer: \quad \frac{1}{2}O_2 + 2e^- \rightarrow O^{2-} \tag{1-5}$$

$$\boldsymbol{Overall}: \quad CO + \frac{1}{2}O_2 \rightarrow CO_2 \tag{1-6}$$

Alkaline fuel cell

The alkaline fuel cell (AFC) operates at temperature ranging from 323K to 493K. It uses an alkaline salt solution as its electrolyte of which potassium hydroxide is the most common due to its low cost, high solubility and not been excessively corrosive. Hydroxide ions (OH^-) are conducted through electrolyte from the cathode to the anode. Its invention is attributed to Sir William Grove as far back as the early 1990's. It was later developed as a viable power unit by Thomas Francis Bacon in the 1930's.

The oxidizing reaction at the anode is given by

$$2H_2 + 4OH^- \rightarrow 4H_2O + 4e^- \tag{1-7}$$

The electrons from this reaction pass through an external circuit to the cathode, where it reduces oxygen to produce hydroxide ions (OH^-).

$$O_2 + 4e^- + 2H_2O \rightarrow 4OH^- \tag{1-8}$$

AFC are quite popular, they were used for powering military space vehicles (Apollo). Its main advantages are its low system costs (inexpensive electrode materials compared to other fuel cells) and lower cathode activation losses which allow having operating voltages as high as 0.875V. Its downside is the possibility of CO_2 poisoning as alkaline solutions do not reject carbon dioxide so the fuel could become poisoned through the conversion of KOH to potassium carbonate (K_2CO_3). Following this, AFC typically operates on pure oxygen which increases cost because generating and storing pure oxygen is quite expensive. These disadvantages have led to a decline in interest in AFC.

Proton exchange membrane fuel cell

The polymer electrolyte membrane fuel cell (PEMFC) uses a proton conducting membrane as electrolyte. The membrane conducts protons (H^+) from the anode to the cathode at low temperatures ranging between 333K and 373K.

The reactions occurring at the anode and cathode are given respectively as:

$$H_2 \rightarrow 2H^+ + 2e^- \quad (1\text{-}9)$$

$$\frac{1}{2}O_2 + 2H^+ + 2e^- \rightarrow H_2O \quad (1\text{-}10)$$

PEMFC's are major candidates for potable power applications as well as for small scale distributed stationary power generation. Their main advantages includes fast start up time due to its low temperatures, compactness due to its thin membrane ($<50\mu m$) structure and elimination of corrosion issues since it is only water that is present in the cell. Its disadvantages include high cost of operation and its water management problems since its water content is directly dependent on the proton conductivity. However, care must be taken to minimise the amount of water to prevent electrode flooding since it blocks the pores thus limiting diffusion. On the other hand there should be sufficient water to avoid membrane dehydration. A balance is therefore needed between the production of water and its evaporation.

Phosphoric acid fuel cell

The phosphorous fuel cell (PAFC) uses concentrated phosphoric acid as its electrolyte which conducts hydrogen ions (H^+) from the anode to the cathode. It operates at temperatures ranging between 423K and 493K; it was the first fuel cell to be produced commercially and enjoys widespread usage.

The cell reactions are expressed as:

$$Anode\ reaction: \qquad 2H_2 \rightarrow 4H^+ + 4e^- \quad (1\text{-}11)$$

$$Cathode\ reaction: \qquad O_2\,(g) + 4H^+ + 4e^- \rightarrow 2H_2O \quad (1\text{-}12)$$

Due to its operating temperature, the water produced in the form of steam can be used for combined heating and power; this significantly increases its efficiency. Unlike PEMFC, PAFC is CO_2 tolerant; it could also tolerate small concentrations of CO thus broadening its choice of fuel, although it is intolerant to sulphides. At low temperatures phosphoric acids have poor ionic conductivity, this increases the severity of CO poisoning of the anode platinum catalyst. PAFC are also known to have low power densities.

Molten carbonate fuel cell

Molten carbonate fuel cells (MCFC) operate between 873K and 973K, its electrolyte is composed of alkali carbonates such as (Li, Na, K). It conducts carbonate ions CO_3^{2-} from the cathode to the anode. Due to its operating temperatures, cheap metals can be used as catalyst in the cell, this greatly reduces overall cost. High energy efficiency is another advantage of MCFC as its efficiency alone is about 60% and increases to about 85% when used in a hybrid system. Unlike PEMFC and PAFC, they wouldn't require any external reforming to convert hydrocarbon fuels to hydrogen, rather due to its high temperature operation, the fuels are converted inside the MCFC in the process of internal reforming; another cost saving characteristic. They are not prone to poisoning by CO_2 and CO; on the contrary these carbon oxides can be used as fuel thus increasing its fuel flexibility option to include fuels like coal. Its primary disadvantage is durability, its high operating temperature and the carbonate based electrolyte tend to accelerate component breakdown and corrosion; thereby decreasing cell life.

Direct methanol fuel cell

The direct methanol fuel cell (DMFC) also uses a polymeric membrane (proton conducting) as electrolyte (similar to that of the PEMFC) which drives hydrogen ions (H^+) from the anode to the cathode. It has the advantage of been able to use methanol directly as fuel without first reforming. The cell operates at temperatures ranging between 293K and 363K.

The electrochemical reactions occurring in the cell are expressed as:

$$Anode\ reaction: \quad CH_3OH + H_2O \rightarrow 6H^+ + CO_2 + 6e^- \tag{1-13}$$

$$Cathode\ reaction: \quad {}^{3}/_{2}\, O_2 + 6H^+ + 6e^- \rightarrow 3H_2O \tag{1-14}$$

Its major advantage is the high energy density of methanol which is greater than that of highly compressed hydrogen. The use of methanol as fuel reduces cost since it is less expensive compared to other fuels and capable of internal reforming, also methanol is readily available and quick to refill. A major drawback of DMFC is the problems associated with fuel crossover; a phenomenon by which methanol diffuses through the membrane from the anode to the cathode without reacting, this decreases the efficiency significantly since the crossed over methanol (unreacted) reacts with air on the cathode side resulting in a loss of cell voltage, hence cell performance. Some other disadvantages are its toxicity and flammability, its oxidation reaction kinetics is also very slow.

A comparative summary of the different fuel cell types discussed above is presented in Table 1.1

Table 1-1: Fuel cell type and their characteristics [14, 15, 17]

	SOFC	**AFC**	**PEMFC**	**PAFC**	**MCFC**	**DMFC**
Mobile ions	O^{2-}	OH^-	H^+	H^+	CO_2^{3-}	H^+
Operating temperature	500-1000ºC.	50-220ºC.	60-100ºC.	150-220ºC.	600-700ºC.	20-90ºC.
Producing water at	Anode	Anode	Cathode	Cathode	Anode	Cathode
Fuel	Methane Hydrogen	Hydrogen	Hydrogen	Hydrogen	Methane Hydrogen	Methanol
Electrolyte	Ceramic membrane	Alkaline-potassium hydroxide	Polymer membrane	Phosphoric acid	Molten carbonate	Polymer Membrane
Interconnector	Stainless steel or nickel or ceramic	Metal	Carbon or Metal	Graphite	Nickel or stainless steel	Carbon or Metal
Electrodes	Perovskite and perovskite/metal cement	Transition metals	Carbon	Carbon	Nickel and nickel oxide	carbon
Catalyst	Nickel	Platinum	Platinum	Platinum	Nickel	Platinum
Efficiency [%]	>60 (hybrid)	40 -50	40-60	40-50	>60 (hybrid)	40-60
Reformer type	Internal	External	External	External	Internal	External
Typical applications and power output	Stationary 5-200kW APUs ~5kW	Spacecraft 1-15kW, Vehicles 20kW	Vehicle 100kW stationary 1-10kw	Stationary 200kW- MW	Stationary 200kW-MW	portable electronic systems
H_2	Fuel	Fuel	Fuel	Fuel	Fuel	Fuel
CO	Fuel	Poison	Poison	Poison	Fuel	Poison
CH_4	Fuel	Neutral	Neutral	Neutral	Fuel	Neutral
CO_2 and H_2O	Neutral	Poison	Neutral	Neutral	Neutral	Neutral
Limitations	Slow start-up, durability, expensive	Wettability, corrosion	Wettability, expensive	Large, heavy, expensive	Durability, corrosion	Low efficiency, expensive

1.3 Solid Oxide Fuel Cells

Solid oxide fuel cells (SOFCs) have recently gaining prominence amongst the other fuel cell types stemming from the following features [18, 19]:

- *Choice of fuel:* good fuel choice flexibility; SOFCs can use a wide range of fuels such as hydrogen, methanol, diesel fuel or carbon based fuels e.g. natural gas
- *Efficiency:* SOFCs have potentials for high electrical energy efficiencies which increases significantly when it is integrated into a hybrid system [20]
- *Constant power production:* it has the ability to continuously generate power unlike diesel engines and generators
- *High reactive activity:* Electrochemical reactions in SOFCs proceed quickly due to its high operating temperature; this improves the electrode kinetics reactions (due to the large exchange currents) and reduces activation losses.
- *Energy security:* Reduces oil consumption and cuts oil imports, in addition, due to its high operating temperature, SOFCs exhausts heat at significantly high temperatures, this can then be used for other forms of power generation and CHP.
- *Application:* SOFCs are suited for a range of applications such as stationary power production, decentralised generating units, vehicular transportation and military applications.
- *Cell management:* Since SOFCs are solid ceramic cells, a number of the issues such as catalyst wetting, electrode flooding, electrolyte migration encountered with other fuel cells are not encountered

As discussed above, SOFCs derive most of its advantages from its high operating temperature, however, due to its high operating temperature, there are challenges associated with the development and commercialisation of SOFCs. These challenges include slow start up times as a result of large thermal gradients that exist in SOFCs, increased material and manufacturing cost due to the choice of expensive alloys such as doped lanthanum chromite ($LaCrO_3$), ceramics and gas seals that are used in the cell, issues of durability associated with thermo-mechanical stability and chemical stability due to high temperature operation, oxidizing and reducing atmospheres in the cell.

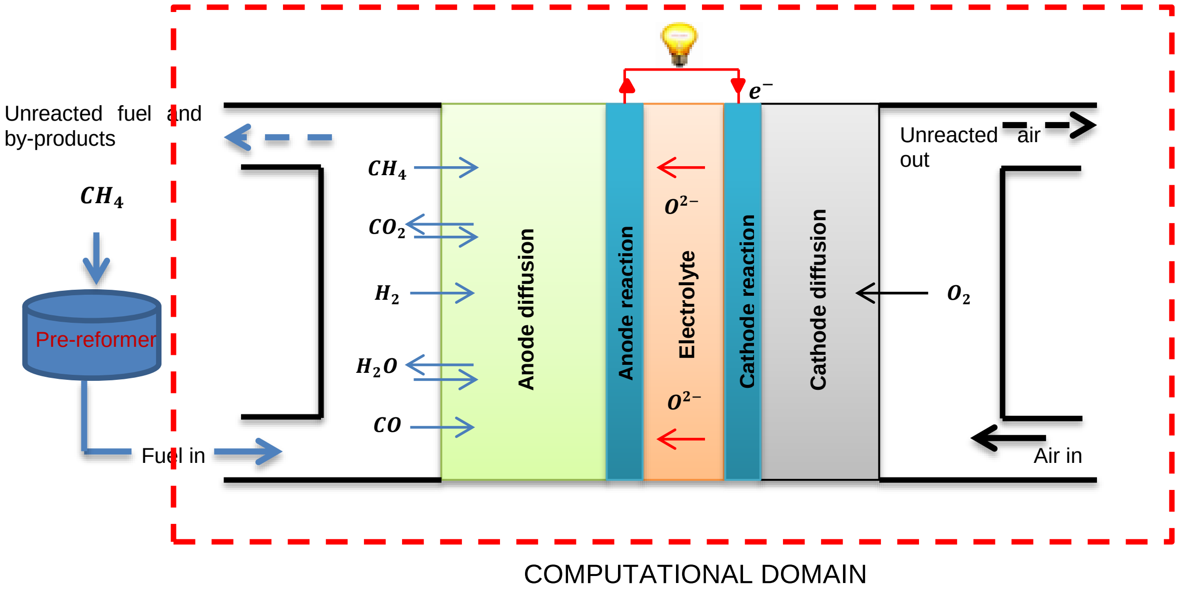

Figure 1-5: Basic operating principle of a SOFC

SOFCs are made of two porous electrodes on either side of an electrolyte made up a solid oxide material. Oxide ions migrate from the cathode through the electrolyte to the anode. The basic operating principle of a SOFC is presented in Figure (1-5) where the fuels (CH_4, H_2, H_2O, CO and CO_2) flows across the fuel channel, it then gets diffused through the anode to the reaction sites, also the oxidant (usually air) is fed into the air channel and diffuses to the reaction site where oxygen is reduced. The resulting oxygen anion O^{2-} migrates through the electrolyte matrix to the anode where it reacts with the Hydrogen releasing electrons to produce electricity through an external circuit. H_2O is produced from the reaction, it flows out through the pores on the anode.

1.3.1 SOFC components

A SOFC is a complete solid device made up of a ceramic material electrolyte placed between two porous cermet electrodes (anode and cathode) and interconnects on either side that electrically connects both electrodes. For the SOFC to operate successfully, the selection of materials for the individual components has to be properly done, the thermal expansion of the components should be within a range of each other to prevent mechanical failure. Other desired characteristics which the material components of SOFCs should have includes good chemical stability, high electrical conductivity (electrodes and interconnects), high ionic conductivity (electrolyte) and an overall low cost of production. The material choice is usually a compromise between the above characteristics. Detailed characteristics of each of the major cell components are discussed [18, 21-23]

Electrolyte

The electrolyte is an impervious solid made of ceramic; it is sandwiched between the anode and cathode. The desired properties of electrolytes used in SOFC are mainly dictated by its high operating temperatures. A good SOFC electrolyte should have high ionic conductivities; necessary for the migration of oxygen ions through it, however, its electronic conductivity should be low as this inhibits the passage of electrons through it. Its thermal expansion should be a good match with that of other cell components and it should be chemically stable when in contact with oxidising and reducing environments.

Although electrolytes can be used as structural support in which case a thickness of $\sim 150\mu m$ are used, more research attention is on anode supported cells. In such cell configuration, the electrolyte layer is expected to be very thin typically within the range from $10 - 20\mu m$. At these thickness, there will be a significant reduction in losses due to ohmic resistance [24, 25], thereby improving the cell performance.

Yttria stabilized zirconia (YSZ) is well known and used as a SOFC electrolyte. It exhibits most of the characteristics of a good SOFC electrolyte at temperatures above 700ºC.

Other alternative materials that are have been investigated include Scandia stabilized zirconia (SSZ); they are known to have very high ionic conductivities however, it is more suitable for electrolyte supported cells and for operating temperatures below 550°C[26], its major drawback is performance degradation with time and high cost; samarium doped ceria (SDC) and gadolinium doped ceria (GDC) are both known to have good ionic conductivity however, they have been found to exhibit significant electronic conductivities in reducing atmospheres [27]. Perovskites based on $LaGaO_3$, such as Sr and Mg doped (LSMG) exhibits high ionic conductivity and low electronic conductivities, however, LSMG's are quite expensive and durability problems have been reported with electrode materials[28]

Anodes

The anode is a porous structure which experiences highly oxidising environments. A good anode material should have high electronic conductivities, necessary for the effective transportation of electrons to the interconnect. It should also have good catalysing properties needed for the oxidation reactions taking place on it. Stability in oxidizing environments and sufficiently porous for the effective transportation of reactant gases and products are also key characteristics a good anode material should have. Its thermal expansion coefficient should match those of the other components and it should have minimum or no reactivity with the electrolytes and interconnect, both of which are in contact with it.

Most anodes are porous cermet, the microstructural characteristics of these cermet (particle size, porosity, contact angle between particles, active triple phase boundary (TPB)) are very important in determining the cell performance and ensuring stability of the anode[27].

The current state of the art for anode materials is a composite of nickel and yttria stabilized zirconia Ni/8YSZ (i.e. Ni with 8% mole of YSZ)[29]. Ni/YSZ has good electronic conductivity and adequate ionic conductivity, stable under reducing conditions, has high activity for electrochemical and reforming reactions. Also the mechanical rigidity allows the anode to be the support structure for the cell.

Alternative materials such as Ceria based anodes, e.g. yttria or Samaria stabilised ceria (YSC, SSC) and perovskite anodes are also been considered as replacements of Ni/YSZ [30, 31]

Cathode

The cathode is a porous material which experiences reducing environment. A good cathode material should have high electronic conductivity, should be stable in reducing environments and be sufficiently porous to allow the transport of oxygen to the reaction sites. Its thermal expansion also has to be a good match with other cell components and like the anode, it should exhibit little or no reactivity with either the electrolyte nor the interconnect.

Typical material for the cathode consists of perovskite materials such as strontium stabilised lanthanum manganite (LSM) with the general formula: $La_{1-x}Sr_xMnO_3$, they are known to be good catalyst for the dissociation of the oxygen molecule, although during early development, noble expensive metals were considered. LSM is known to have high activity for oxygen reduction, good matching thermal expansion coefficient with YSZ and also to be stable in high temperatures. Further enhancement in the cathode performance can be achieved through the use of composite materials such as YSZ/LSM composites[32]

Interconnect

The interconnect (also known as bipolar plate) serves as a physical barrier separating the fuel of one individual cell from the air of the neighbouring one, it also conducts electrical current between each layer of the cell stack and helps in distributing the reactant gases evenly across the face of the electrodes[24, 32]. Therefore, a good interconnect should have high electronic conductivity and low contact resistance with electrodes. It should be stable in both oxidising and reducing environments and its thermal expansion should match those of other cell components. Furthermore, the interconnect should be impermeable to the reactant gases and generally exhibit good mechanical strengths.

Metals can be used as interconnects at intermediate temperature operation; these are relatively inexpensive compared to ceramic interconnectors at high temperature operation. Stainless steel is an attractive option because its thermal expansion matches that of zirconia based electrolyte material[33] however corrosion can be a major challenge, chromium based alloys can then be used to combat the corrosion phenomena.

1.3.2 Classifications of SOFCs

SOFCs can broadly be classified according to their operating temperatures, geometric designs, transported ion, nature of its support and fuel reforming method in Table 1.2

Table 1-2: Classification of solid oxide fuel cells

CLASSIFICATION CRITERIA	TYPES
Temperature Levels	Low temperature SOFC (LT-SOFC) [773K -873K] Intermediate temperature SOFC (IT-SOFC) [873K -1073K] High temperature SOFC (HT-SOFC) [1073K – 1273K]
Cell geometric designs	Planar SOFC Tubular SOFC Monolithic SOFC Integrated Planer SOFC
Transported ion	Oxide ion (O^{2-}) Protonic ion (H^{+})
Type of Support	Self-supporting (Anode-supported, cathode supported, electrolyte supported) External-supporting (Interconnector supported, Metal substrate supported)
Fuel reforming type	External reforming SOFC Direct internal reforming SOFC (DIR-SOFC) Indirect internal reforming SOFC (IRR-SOFC)

Classification according to operating temperature

Based on their inlet operating temperature, SOFCs may be classified into three sub groups:

- Low temperature (LT-SOFC 773 – 873K),
- Intermediate temperature (IT-SOFC 873 – 1073K)
- High temperature (HT- SOFC >1073K).

The source of the main challenge to the commercialisation of SOFC technology is its operating temperature, this has led to growing interests in studying SOFC operations at lower temperatures(773K - 1073K)[34]. Major technological motivation for lowering the operating temperature are reduced corrosion rate of metallic components (severe corrosion of metals is known to occur at high temperatures), improved durability (sintering and inter-diffusion of species between components increases at higher temperatures). Also, a range of materials can now be used that allow for cheaper fabrication, sealing techniques become less difficult, rapid start up and shut down time, less complications with regards to mechanical and chemical compatibility of components, reduced degradation rates, radiation losses becomes less severe making heat management of the cell easier[32, 35]. However, the advantages high temperature operations has over lower temperatures includes; higher electrode kinetics which reduces the sluggishness of the reactions, reduced resistivity of the cell components which decreases the ohmic polarisation and increased system efficiency when combined with hybrid systems due to better thermal integration.

Classification according to cell geometric designs

Based on the geometric designs, SOFCs may be classified according to its geometric configuration, the most common of these geometries [14, 22, 36] are discussed briefly below:

a) Flat Planar SOFCs consists of flat layers of electrodes, electrolytes and current collectors placed on top of each other as shown in Figure 1-6a. The configuration is simple and cheap to construct. Its power density and stack performance are quite high as its design allows the building of SOFC stacks just by piling SOFC cells on top of each other. Its main disadvantages are problems associated with gas sealing as the edge of the components are susceptible to leaking, it also tends to get very brittle when it undergoes thermal and mechanical stresses.

b) Monolithic SOFC consists of thin laminates of air electrode/electrolyte/fuel electrode and interconnectors that are formed and co-sintered together as shown in Figure 1-6b, this results in high volumetric power densities and eliminates the need for gas seals however, the stacks are formed by co-sintering which is a rather difficult process considering the different microstructural characteristics of the different components in the cell.

c) Tubular SOFC design is the most advanced SOFC design in terms of development. The cell components are made into thin strips in cylindrical tubes shapes shown in Figure 1-6c, with air flowing on the inside of the tubes while fuel flows on the outside. Tubular configuration overcomes most of the drawbacks associated with the other configurations such as gas sealing (tubular design requires sealing only at one end). Also its geometry helps in reducing the mechanical stresses. However, this geometry has high manufacturing costs and much lower power densities compared to the planar design due to the longer path for the electrical power production.

d) Integrated planar SOFC is a mixture of the tubular and planar geometries as it seeks to retain the specific advantages of the tubular and planar configuration arrangement, taking advantage of the low cost of manufacturing and short current path of the planar geometry and incorporating the thermal compliance property from the tubular as shown in Figure 1-6d.

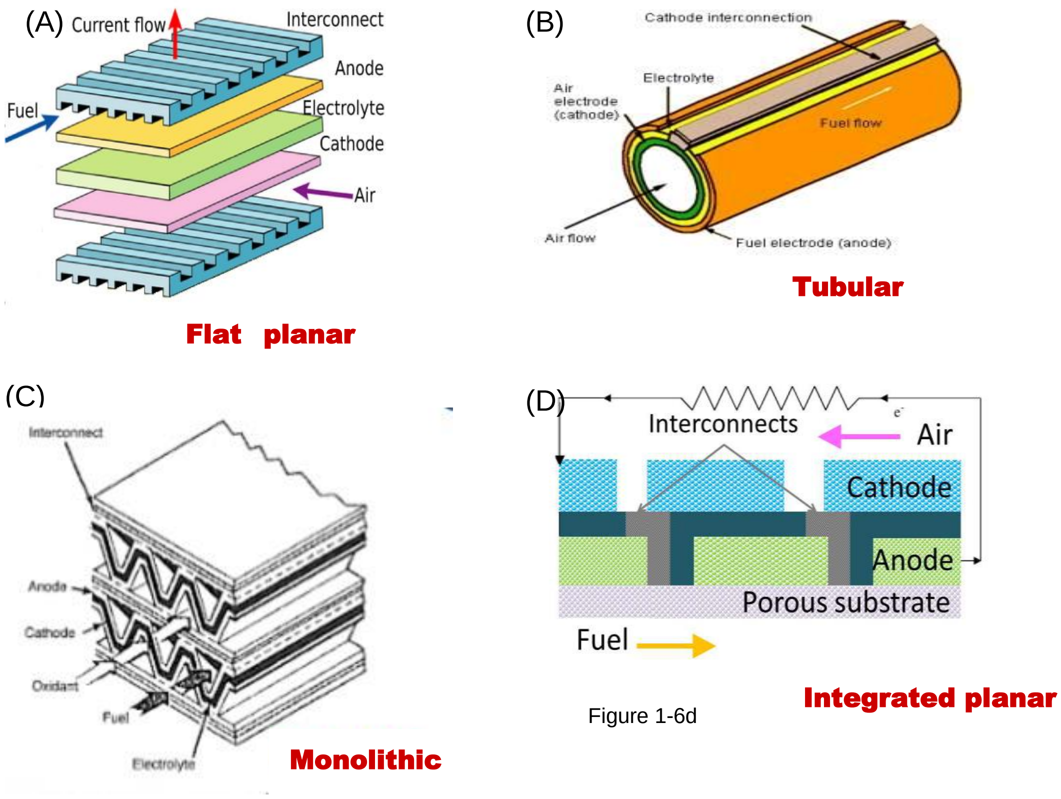

Flat planar

Tubular

Monolithic

Integrated planar

Figure 1-6: SOFC geometric designs (a) Flat planar (b) Tubular (c) Monolithic (d) Integrated planar

Classification according to type of support layer

Based on the layer that mechanically supports the cell, SOFCs can be classified into: self-supported and externally-supported. In the self-supported system, the cell component (the anode, cathode or electrolyte) with the thickest layer serves as the mechanical support for the whole cell. On the other hand in the externally-supported structure, the entire cell (made up of thin layered components) is configured on the external support which could be either the interconnector or on a porous substrate. The different cell support configurations are shown in Figure 1-7

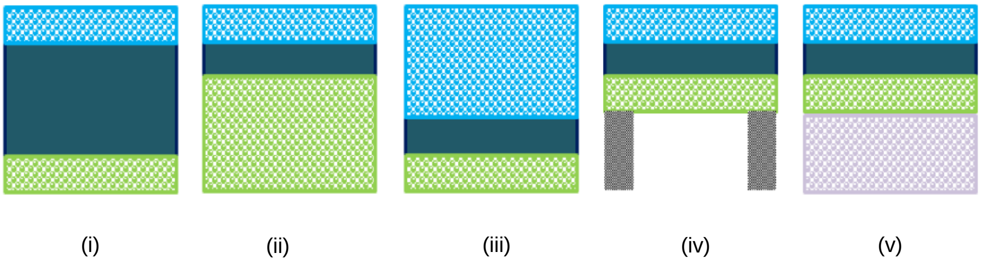

Figure 1-7: SOFC support layers (i) Electrolyte support (ii) Anode support (iii) Cathode support (iv) Interconnect support (v) metal substrate support.
(The electrolyte, anode, cathode, interconnect and metal are colored as dark-green, light green, light blue, grey and light purple respectively)

Classification based on fuel reforming type

SOFCs can either use hydrogen (H_2) or carbon monoxide (CO) or a mixture of them for its electrochemical reaction, any other hydrocarbon (fuel) that can be used in SOFC would first be reformed into H_2 and/or CO. The reforming action could be done outside the cell in a process called external reforming or inside the cell in internal reforming. The internal reforming process could occurs simultaneously with the electrochemical reactions on the anode side, this method is called direct internal reforming (DIR-SOFC), When the reforming takes place in a separate reformer distinct from the cell components but still in close thermal contact with the anode, the reforming process is then known as indirect internal reforming (IIR-SOFC). The DIR-SOFC has a much higher rate of heat transfer than the IIR-SOFC, translating to a higher SOFC work output and efficiency. The IIR-SOFC provides the advantage of eliminating the need for a separate reformer and also reducing the problems associated with carbon deposition on the anode. However, its main drawback is the uneven temperature distribution between the cell and the reformer due to the mismatch between the endothermic reforming reactions and the exothermic electrochemical reactions, this could create local temperature hotspots leading to thermal stresses and consequently mechanical failure.[37]

1.3.3 SOFC fuels

The electrochemical reactions in SOFCs occur in the reaction layers of the electrodes; these reaction layers are thin layers that are distinct from the diffusion layers. Their thickness is usually between 10-20µm[35]. The reaction layers are a mixture of ion-conducting particles and electron-conducting particles. The gases are transported through the pores to and from the electrolyte boundary. This region is also referred to as triple phase boundary (TPB).

A major advantage of SOFC is its ability to operate with a wide variety of hydrocarbon fuels. Short chain hydrocarbons like methane and higher hydrocarbons can be reformed to H_2, CO, H_2O and CO_2 by the steam reforming reaction shown in Equation (1.15). In a reforming reaction process, CO can either act directly as a fuel in the electrochemical reaction given in Equation (1.6) or indirectly through the water-shift gas reaction by converting to H_2 and CO_2 by adding steam as shown in Equation (1.16):

$$Steam\ reforming\ reaction: \quad C_nH_m + nH_2O \leftrightarrow nCO + \left(n + \frac{m}{2}\right) H_2 \tag{1-15}$$

$$Water - shift\ gas\ reaction: \quad CO + H_2O \leftrightarrow CO_2 + H_2 \tag{1-16}$$

1.4 Thesis objective and structure

The overall aim of this thesis is to develop a comprehensive computational SOFC model which is then integrated into a hybrid gas turbine plant. The SOFC model will be capable of analysing and predicting the operational behaviour of a planar type SOFC at intermediate temperatures while the hybrid system aims at evaluating the plants energy efficiencies and exergy production in steady state conditions.

The research study is comprised of the following targets:

i. To develop a general SOFC model which can easily be applied to different situations
ii. To develop a two-dimensional (2D) hydrogen fed isothermal model to analyse the transport properties through the electrodes and flow channels
iii. To prove the validity of the model by comparison of the numerical results with experimental data taken from literature
iv. To develop a 2D hydrogen fed non-isothermal model to analyse the temperature distribution within the cell
v. To develop a 2D multicomponent fed non-isothermal model to study the effects of the chemical reactions occurring in the electrodes
vi. To study the versatility of the physical domain of the developed models by simulating electrode-supported SOFC designs
vii. To provide numerical results simulating the performance of the SOFC and examine the effect of the key operating and design parameters on the characteristics and performance of the cell with a bid to optimising the cell performance
viii. To develop a thermodynamic numerical model of a SOFC-GT hybrid plant. This will be used to study the effect of integrating SOFCs in hybrid systems by carrying out energy and exergy studies
ix. To develop unique flow configurations for the air re-heating system of the hybrid plant.

Recent models in literature treats the electrodes as two distinct layers: diffusion and reaction layers. The reaction layers are very thin layers modelled only as the reaction sites where the electrochemical reactions occur, this simplifies the model as insights into the physical and chemical phenomena occurring in this region are not considered. Also, a good number of the models in open literature that used the micro-modelling approach developed models that were only valid for binary mixtures and neglected the independence of micro-structural parameters; as such they neglected a key characteristic of SOFCs which is its fuel choice flexibility and over simplified the predictive features of the microstructural properties in the model. Furthermore, SOFC hybrid modelling is still quite novel, with authors focusing more on energy studies. Therefore, this present research develops a fuel flexible model which is not only capable of predicting the cell's performance for a binary mixture but also for any multicomponent hydrocarbon mixture, in which the reaction layer is modelled as a finite volume where the conservation and constitutive equations as well as the electrochemical reactions are solved for, the model incorporates empirical interdependency relations for its microstructural properties. Also exergy production was included in modelling the hybrid plant which compared two unique configurations for the air-reheating system

A brief outline of the thesis is as follows:

Chapter 1.	A brief overview of the hydrogen economy and fuel cells with SOFCs in particular is presented
Chapter 2.	Review of SOFC modelling approaches
Chapter 3.	A detailed description of the fundamental principles, thermodynamics and kinetics of SOFC are presented
Chapter 4.	The model development for the electrode diffusion layers, electrode reaction layers, electrolyte, flow channels and interconnects along with the boundary conditions are presented
Chapter 5.	A 2D hydrogen fed isothermal model is developed to analyse the distribution of the reactant species in the electrodes and the flow channels, the model is validated and the verification of the electrode as double layer is also carried out.
Chapter 6.	A 2D multicomponent fed non-isothermal model is developed to analyse the flexibility in fuel choice by using any multicomponent hydrocarbon mixture as fuel, also, the impact of direct internal reforming and water-gas shift chemical reactions on the cell performance is studied.
Chapter 7.	A hybrid SOFC-Gas turbine model is developed to simulate the integrating properties of SOFCs with gas turbines under steady state conditions, the impact on performance and efficiency on the system model is studied. Exergy analysis to determine the sources of irreversibility’s in the system was also carried out.
Chapter 8.	The key conclusions are presented here and future research direction is recommended.

CHAPTER2 : Literature Review

2.1 Introduction

The major attractive features of solid oxide fuel cells (SOFCs) are their good fuel flexibility, quiet operation, lower emissions and higher efficiency, due to its high temperature operation. They could incorporate designs that utilises their thermal output to further increase efficiency such designs include gas turbine hybrid systems, auxiliary power units (APU), stationary/non stationary electricity generation applications and in combined heat and power systems[38-41]. These benign features have spurned lots of research interests on SOFCs in recent years, focussing mainly on improving its performance and studying its characteristics at reduced operating temperatures. The main technological motivation in this direction is that the design and material requirements are simplified and cheaper, reduced corrosion rates, improved durability, rapid start-up and shut down times, easier heat management, less complicated sealing techniques and improved stack life[32, 42].

Mathematical modelling is an important research tool that aims at providing detailed insight, while reducing the high cost, time and effort associated with experimentation[43]. Modelling SOFCs aim at predicting, optimising and controlling the fuel cell behaviour[44] while also providing a better understanding of the complex coupling of electrochemical processes and transport phenomena going on within the cell.

In the last decade, numerous modelling studies on SOFCs has focused on simulation processes based on physical principles; such simulations are described as physical models, these models successfully translate the electrochemical reactions processes, the ionic properties, electronic properties and the gas transport processes into numerical models by developing physical and analytical equations to represent them[45]. There are a great number of SOFC physical models found in the literature; most of the models focus on operability, performance, optimisation, design, heat management, material selection and controller design of the cell[46-48].

These models could broadly be classified into electrode and cell/stack models. The electrode models usually involve detailed studies on the processes going on in the electrodes so as optimise and improve the electrode performances while the cell/stack models aims at predicting and optimising the entire cell performance using information obtained from the electrode models by carrying out sensitivity studies. Usually, the research objectives determine the complexity and physical dimensions of the model[49], also, depending on the purpose and needs of the model, the simulations (electrode and cell /stack) could be further characterised by:

Levels of dimensionality: This ranges from zero dimensions (0-D) to three dimensions (3-D), each with its unique features. 2-D and 3-D models are usually associated with cell design modelling by providing detailed knowledge of the internal behaviours of the cell/stack while lower dimension models usually aim to analysis and solve at system levels such as in the prediction of performance characteristics for steady state or transient simulations [45].

Micro or Macro scale[50]: Micro models considers the microscopic scale behaviour in the model. The models can be of a particular component conducted at atomistic level, they are usually limited to specific phenomenon been analysed for example, in the treatment of electrodes. The microstructural properties are taken into consideration, in which the electrodes are treated as been made up of ionic conducting particles, electronic conducting particles and pore spaces through which the species diffuses. In contrasts, macro scale models conduct investigation at the molecular level, such treatment deals mainly with the operational behaviour of the cell

Steady state or dynamic: Depending on whether any of the following would be included in the model: starting up, shutting down, heating up, cooling up, the simulations could be a dynamic model (if they are included) or a steady state model (if they are not included).

System level: here, the integration of the SOFC model as a component in larger systems such as in hybrid systems can be assessed by simulating at system level. Usually such models involve both energy and exergy analysis

A review of electrodes and cell/stack models found in literature in the context of the above characterisation (1-4) is carried out in the remaining part of this chapter.

2.2 Electrode modelling

Electrode models are developed primarily with the aim of studying and optimising the performance of the electrodes, this is usually carried out by investigating the structural properties of the electrodes either in micro models or macro models simulations. In the micro modelling approach, the electrochemical reaction layer is treated as a discrete volume made up of the three phases of ionic conducting particles to conduct oxygen ions, electronic conducting particles to conduct electrons and the pore spaces to transport the reactant gas[51], the electrochemical reactions could be modelled to occur throughout the electrode[52] or in a thin reactive layer close to the electrolyte [53]. The aim of these microscopic models is to understand the complex phenomena occurring in the electrodes as it relates to the micro structural properties such as the porosity, pore size, permeability and tortuosity factor with a view to improving the SOFC performance. In contrast, macro models treats the electrodes as consisting only of electronic conducting particles and pores, defining the electrochemical reaction as occurring exclusively at the electrode/electrolyte boundary interface.

Literature suggests that electrode micro-modelling can roughly be categorised under thin film models[54], random resistor network models[55-58] and random packing sphere models[59, 60].

The random packing sphere model is said to be the most used and appropriate for modelling[61], the application of this modelling theory was used by Costamagna et al[59] to develop a micro model simulation, their model was a one-dimension SOFC electrode with random packing sphere electrode model, in which they accounted for the electronic and ionic transport in the entire electrode. They subsequently developed a relationship for evaluating the active surface area of the composite electrode. In developing the relationship, they used the earlier model proposed by Bouvard et al[62], emphasis was placed on the electrode thickness, as very thin electrode thickness reduces the electrochemical active area. However, a very thick electrode layer increases the ohmic losses. The model failed to account for the concentration losses in the cell despite their importance.

Chan et al[60] also applied the electrode microscopic model with random packing sphere theory in developing their one dimension micro scale anode- supported SOFC model, in which they established a relationship between the electrochemical reactions and the gas transport properties. All three major forms of polarisation were considered in their model, their results show that the polarisation losses are a function of the particle size and that a relationship between the anode thickness and the particle size exist. However, their model assumed the exchange current density to be a constant which in reality should be dependent on the temperature and reactant concentration.

Xia et al[63] then went on to improve the model, in which the exchange current density was defined to reflect its microscopic sense by considering it as a function of the reactant and product concentration. Ni et al[64] studied how the particle sizes affect the cell performance. They used the random packed sphere theory micro scale modelling approach, the model investigates the mass transport and electrochemical reactions phenomena occurring in the anode. Enhanced cell performance achieved by modifying the microstructures of the electrode was demonstrated by the model.

Also Chan et al[65], Chen et al[66] and Deseure et al[67] applied the electrode microscopic model with random packed sphere theory to simulate their individual SOFC cathode model. Chen et al[66] later went on to developed a mechanistic model that studies the oxygen reduction phenomena at the cathode/ electrolyte (LSM/YSZ) interface, their model also considered all three forms of polarisation. They went on to establish a relationship linking all the processes occurring in the cathode. Parametric results from their model showed that when the particle size ratio is high, the fraction of YSZ in the composite cathode needs to be increased to lower the polarisation resistance. Chan et al[65] also considered all the forms of polarisation in the cathode, the model considers oxygen reduction mechanisms, grain interior and boundary effects on the total resistance. They also studied the effect of TPB length on the ionic/electronic particle size ratio and the volume fraction.

Desuere et al[67] developed a composite cathode model comparable to those developed by Chan et al[65] and Chen et al[66]; their model ignored the ohmic losses in the cell while accounting for the activation and concentration. They carried out simulations to predict optimum design parameters; such as the kinetic and structural/geometric parameters.

Macroscopic models of electrodes considers the electrochemical reaction sites as a dimensionless boundary interface between the electrode and the electrolyte, Lehnert et al [68], Yakabe et al[69], Suwanwarangkul et al[70], Tseronis et al[71] and Grigoruk et al[72] simulated macro models which studied the mass transport profile of species in the porous anode.

The models developed by Lehnert el al[68], Yakabe et al[69] and Grigoruk et al[72] used the dusty gas equations in modelling the mass transport processes in the anode while Suwanwarangkul et al[70] compared Ficks (FM) model, dusty-gas (DGM) model and the Stefan-Maxwell (SMM) model for binary and ternary system flows in the anode. Their finding reveal that the dusty gas model in which the Knudsen diffusion effect were considered is the most appropriate model to describe the gas transport phenomena in SOFC anodes.

Tseronis et al[71] also carried out comparison studies on the three different models in a bid to predict the species concentration profile, he compares a 2D DGM against a 2D SMM and 1D models, their studies show that a combination of mass transport models might be the most appropriate in describing the flow phenomena in the SOFC; their combination of DGM in describing the flow in the porous medium (anode) and SMM in describing the flow in the channel gave the best cell performance

The models discussed above [68-72] only predicts concentration losses in the anode, however to effectively predict the performance of a SOFC, all the forms of losses (activation, ohmic and concentration) have to be considered.

Damm et al [73] developed a macro model that considered the heat and gas transport properties in the SOFC anode, the temperature difference between the gas and solid phase was estimated using a scaling analysis, however, the simulation results showed negligible temperature difference between the gas and solid states.

Yuan et al[74] used a 3-D CFD approach to model the reforming and transport processes in a composite SOFC anode, results obtained showed that internal reforming in the anode occurs mainly in regions close to the fuel channel and that the species transport and temperature distribution profiles in the cell are dependent on both the electrochemical and chemical (reforming and water-shift gas) reactions in the cell.

Electrode models found in the majority of literature have used either the micro modelling approach (reaction site is defined as the entire electrode) or the macro modelling approach (reaction site is defined as a boundary interface between the electrode and electrolyte). However, it is widely agreed in the literature that the electrochemical reaction site extends from the boundary interface to a distance of about 20µm into the electrode [68, 75-78], under such considerations, the reaction sites can be considered as a distinct layer. As such, the electrodes are modelled as composites; having two layers referred to as the diffusion/support layer (responsible for diffusion of species to the reaction site and provides structural support) and reaction layer (where the electrochemical reaction occurs)[53, 75, 79, 80], these composite electrode models serves as a connecting link between the micro and macro modelling approaches.

Hussain et al[80] developed a fuel flexible multi-component model that is expected to predict the species distribution for any reformate gas. A composite layer electrode structure was used. The model considered the electrochemical reactions in the reaction layer and water-shift gas reaction in the support layer. The reforming properties of the reaction were neglected in the model.

Farhad et al[81] also developed a one-dimensional micro-model of a composite anode electrode consisting of a substrate layer and a functional layer. Their model predicts the electrochemical performance for a hydrocarbon fuelled anode. Mass transport, ionic and electron transport process were considered in the model but the momentum and energy transport terms were neglected. The effect of some microstructural parameters on cell performance was considered. The parameters investigated includes the volume fraction, porosity and particle size

2.3 Cell modelling

Cell models are developed primarily with the aim of predicting and optimising the performance of the entire cell by carrying out sensitivity and parametric studies. The cell performance is greatly influenced by the oxidising and reducing reactions occurring in the reaction sites, the chemical reactions of steam reforming and water-shift gas which occurs in both electrode layers, the transportation of species to the reaction sites in the electrodes, the transportation of oxide ions from the cathode reaction layer through the electrolyte to the anode reaction layer and the transportation of electrons through the diffusion and reaction layers of the electrodes.

Electrode models discussed above in section 2.3 are models of particular cell components usually conducted at the atomistic (micro) or molecular (macro) level. The information obtained by such specific model studies are usually limited to the exact phenomenon or aspect studied, thus providing limited insights on the performance and characteristics of the entire cell, however the results play an important role in the development, analysing and design considerations of cell models as they provide useful data for the development of the cell models[82].

Cell models can also be categorised into micro and macro cell models based on the treatment of the electrodes, although most cell models available in literature used the macro modelling approach, Hussain et al [35], Jeon D.P[83] and Nam et al [75] all simulated their cell with the micro modelling approach. Hussain et al[35] developed a two dimension fuel flexible SOFC model that predicts the cell performance at various design and operating conditions, they assumed the exchange current density value to be a constant, although the model considered a multicomponent mixture in the electrode, the micro scale modelling approach was used only in the reaction zone layer, thereby neglecting the microstructural properties in the diffusion layers of their cell model, this was included in models developed by Jeon D. P[83] and Nam et al[75] in which micro scale modelling was carried out in the entire electrode, however, both models only considered binary mixtures in the anode, thus neglecting the fuel flexibility characteristic of SOFCs.

Ferguson et al[84] developed a 3-D simulation of an SOFC model which predicts the behaviour of the voltage, temperature and the current distribution when some parameters were varied. Their model consists of interconnects, electrode layers, electrolyte layer and flow channels. Electrochemical reaction was modelled to occur at the electrode/electrolyte interface (macro scale), the heat source is made up of the ohmic heat and the heat produced by the chemical reactions in the anode. Furthermore, the model was used as a design tool to analyse the cell efficiency. The analysis was carried out by studying the cell efficiency at different flow configurations and different geometric designs with the aim of identifying the flow configuration and geometric design that provides the best cell performance. The effect of rib width and electrode thickness on efficiency were also studied. Results showed that the counter-flow design for a planar geometry gave the most efficient set up when hydrogen was use as fuel and that the planar geometry had less ohmic losses compared to the tubular geometry.

Kim et al[85] used a 1-D empirical analysis to simulate a SOFC operating at intermediate temperature between 923K and 1073K, the model analyses the concentration polarisation through the porous electrode for a hydrogen fed SOFC. The effect of activation polarisation in the Tafel limit was also studied, the model ignored the effect of electrode microstructure and that of heat transfer equations on its performance.

The 3-D intermediate temperature SOFC model developed by Iwai et al[86] solves for multicomponent gas transport, temperature distribution, electronic and ionic transport. The reforming and water-shift gas reactions were also considered in the model. The model assumes the oxidation of CO and H_2 in the electrochemical reaction. However, the model failed to include the Knudsen diffusion term in the gas transport equations.

Chinda et al[87] simulated a 2-D model that can simultaneously solve mass, energy transport equation, chemical and electrochemical reactions, they included the effect of electrode microstructure and operating conditions on the performance analysis of the cell. Although energy transport equations were considered in the model, its radiation component was ignored.

In SOFC modelling, the radiation component of the heat transfer equations is somewhat controversial. Some authors argue that due to the operating temperatures of SOFCs, the thermal radiation emitted from the solid components of the SOFC constitute a significant part of the total heat transfer in the cell. [82]. Authors who agreed with this and included thermal radiation components in their heat transfer models include Costamagna and Honegger[88], Ota et al[89], Aguiar et al[90], Xue et al[91], Damm and Fedorov[46], Daun et al[92] and Sanchez et al[93], Kee et al[94]. On the other hand, many other authors ignored the radiation component of their heat transfer model due to three main reasons: First, the researchers completely ignored the heat transfer equations and assumed a uniform temperature throughout the cell (isothermal modelling) [69, 95], this was disputed by Burt et al[96] whose studies showed that ignoring radiation heat transfer leads to the prediction of un-even temperature gradients in SOFC stacks[96]. Second, very thin channel walls were assumed[97] and third, due to the high cost of computation when radiation heat transfer is considered[98].

Costamagna and Honegger[88] considered radiation heat transfer as a boundary condition between the cell and the surrounding, they neglected the radiative transport within the electrode and electrolyte layer.

In models developed by Damm et al[46] and Aguiar et al[90] radiative heat transfer within the electrode and electrolyte layer as well as surface to surface radiation within the channels were considered. Damm et al [46] argues that radiation from the stack to the environment are of critical importance for effective thermal management of high temperature stacks, this view was also taken by Aguiar et al[47] who argues that about 79% of the total heat transfer in a SOFC with an external reformer is due to the radiation emitted between the solid components of the cell and the reformer.

Although Daun et al[92] considers radiative heat transfer in their model, results obtained led them to conclude that radiative heat transfer component can safely be excluded from SOFC modelling equations as they have negligible effect on the cell's overall heat transfer.

The governing equations used in modelling SOFCs are highly complex and non-linear, making it very difficult to obtain exact analytical solutions; these equations are usually solved by using computational fluid dynamics (CFD) methods to convert them into sets of numerical solvable equations. The most commonly used CFD techniques in modelling SOFCs are the finite-element method (FEM) and the finite-volume method (FVM).

Hussain et al[35], Nam et al[75],Ferguson et al[84] and Lehnert et al[68] simulated their models with FVM based in-house developed codes, Commercial codes based on FVM such as STAR-CD, FLUENT, and PHOENICS have also been used by numerous authors in developing their models.

Recknagle et al[97], Yakabe et al[98] and Liu et al [99] used the FVM software package "STAR-CD" for their model simulations, FLUENT was used by Ackmann et al [100], Autissier et al[101] and Danilov et al[102] in their SOFC models, although less popular, PHOENICS have also been used by Beale et al[103] in conjunction with FLUENT in solving governing equations of flow, heat, mass transfer and electrochemistry in their model.

Anderson et al[76] employed the FEM commercial code COMSOL Multiphysics to develop an SOFC model operating at intermediate temperature, their model includes the governing equations for heat, mass, momentum and charge transport as well as the electrochemical reaction and internal reforming kinetics. Jeon et al[74],Shixue et al[53], Tseronis et al [71] all used the COMSOL Multiphysics software in developing their SOFC models.

A major challenge to using the planar geometries in SOFCs is its mechanical stability. Planar geometries are known to be susceptible to high internal stresses arising mainly from heat cycles, also since an effective high temperature gas sealing technique is required, only certain material are suitable to be used as seals; such as glass, cement or glass-ceramic. The use of such sealing materials could generate mechanical constraints, due to thermal coefficient mismatch with the other cell components thereby increasing the cells internal stress. Also, as a result of the non-homogenous temperature distribution within the cell and the very thin electrolyte layer used in planar SOFCS, further mechanical deformation of the cell components is expected which could further increase the cells stress level[98].

In the model developed by Yakabe et al[98], principal stresses in the electrolytes and the interconnectors of the cell were computed from an earlier model in which they studied temperature distribution profiles using the FEM software “ABAQUS”, their Studies show that the reduction in the fuel temperature at the cell entrance due to the rapid consumption of methane in the internal reforming reaction will result in large tensile stresses and that the co-flow configuration is a more suitable flow pattern since its temperature distribution is more even than that obtained for a counter-flow configuration, they then recommended the co-flow configuration as a useful measure to reducing the SOFCs internal stresses.

Lin et al[104] conducted studies on thermal stress in their SOFC models, the commercial FEM software “ABAQUS” was also used in characterising the thermal stress distribution in the SOFC stack, their model considered the effect of support configuration, glass-ceramic sealant, temperature gradient and thermal expansion coefficient mismatch on the stress distribution in the cell. Based on their simulation, the glass-ceramic sealant was identified as the most susceptible part of the SOFC stack to induce thermal stress.

Steady state and transient studies were conducted by Selimovic et al[105] to investigate the thermal stress distribution in a planar bipolar SOFC. The electrochemical, thermal and transport processes were coupled together in developing the model. Their analysis showed that the largest stress distribution in the cell occurred at the anode/electrolyte interface. It also revealed that the use of metallic interconnector improves the temperature distribution and consequently reduces thermal stresses.

The two most common SOFC geometric designs used in the literature are the tubular SOFC (T-SOFC) and planar SOFC (P-SOFC). The T-SOFC design is used by authors like Campanari et al[106], Ota et al[89] and Xue et al[91] in their models while the P-SOFC design was used in models by quite a number of researchers [68, 69, 71, 83, 98, 107-109].

Ferguson et al[84] and Stiller et al[110] carried out simulations on both configurations, however, their studies was focussed more on parametric analysis than comparative. The models take into account the chemical reactions, mass conservation, heat transfers; both models used methane gas as the fuel.

Zhang et al[111] did a comparative study between T-SOFC and P-SOFC configuration, a 3-D steady state numerical model that accounts for internal reforming and water shift reaction for both designs was described, their findings indicate that the more significant losses on the P-SOFC configuration were the ohmic losses in the electrolyte and the activation losses. For the T-SOFC configuration, the ohmic losses in the cathode were the most significant. The studies further revealed that the current density distribution is strongly dependent on the location of the major ohmic losses in the cell. The ratio of ohmic heat to the overall heat generated in the cell was much higher in T-SOFC than in P-SOFC, this difference is higher in the counter-flow design than in the co-flow design. The P-SOFC configuration are more compact than the T-SOFC thus they suffer from less ohmic and concentration losses. However, thermal gradients are typically higher especially in cases when internal reforming is considered. On the other hand, the current path lengths in T-SOFCs are longer than in P-SOFC, this tends to limit their performance.[112]

The state-of-the-art planar SOFC are generally manufactured in three designs: electrolyte supported, cathode supported and anode supported SOFCs. The electrolyte supported design comprises of a thick electrolyte usually between 120-200µm, they usually operate at high temperature around 1000°C as they are known to produce high ohmic losses at low temperature. The latter design has a thick cathode or anode depending on whether it is cathode or anode supported usually between 400-800 µm and a thin electrolyte between 8-20 µm. The electrode designs (cathode and anode) have less ohmic losses in the electrolyte due to its thinness. However, concentration losses are quite significant because of gas diffusion resistance in the electrodes due to its thickness [50, 113].

Chan et al[114] showed with their polarisation model of a SOFC that the performance of an anode supported cell is superior to that using a cathode as the support,

Patcharavorachot et al[107] carried out an electrochemical study of a planar SOFC with the aim of investigating the role of support structures at when the SOFC is operated at intermediate temperatures, results obtained demonstrate that the anode supported SOFC gives better performance that the electrolyte or cathode supported. Subsequently, many researchers have developed models on anode supported SOFCs.

Yuan et al[115] developed a 3-D model of a planar anode supported SOFC to investigate the transport processes in the cell, the model considers a binary fuel mixture in the anode (H_2 +H_2O) and air in the cathode, the electrochemical reactions were assumed to occur only at the electrode/electrolyte interface.

Shi et al[116] also developed a 2-D isothermal mechanistic model of an anode supported SOFC based on the button cell geometry, they also assumed a binary fuel mixture in the anode. They treated the reaction layer as a boundary condition. Their model considered all the forms of polarisation.

Paradis et al[117] used an anode supported theoretical model to investigate the internal reforming reaction process and their transport model, they considered multi-component mixture in the anode, yet treated the electrochemical process as occurring in the electrode/electrolyte interface.

Zhu et al[118] developed a 3-D model for a planar anode supported cell with co-flow configuration, although the model considered multi-component mixture in the anode. However, momentum and energy equations were not taken into account with an isothermal assumption over the whole cell, also the reaction zone layer was treated as a boundary condition.

More recently, a number of authors such as Hussain et al[35], Ho et al[79, 113], Jeon et al[83, 108] have developed numerical models predicting the performance of planar anode supported SOFC, the novel feature of their models is the consideration of the reaction zone layers as finite volumes, having a distinct layer different from the diffusion layers of the electrodes.

2.4 System level modelling

The high operating temperature of SOFC is said to impose several technological constraints on its materials, while at the same time making the cell very suitable for co-generation and/or coupling with hybrid systems due to significant amount of high quality heat output.

A hybrid system usually refers to the integration of a fuel cell in some other form of heat engine of which the gas turbine (GT) is the most commonly investigated. The integration of SOFCs with GTs and other conventional devices such as combined heat and power systems, heat exchangers and compressors has been very successful in terms of improved energy efficiencies since the SOFC-GT hybrid system are known to reach efficiencies of 85%[119].

Studies on the modelling of SOFC hybrid systems are gradually increasing, a good number of these studies focuses on the energy and/or exergy balance analysis of the system, so as to evaluate the distribution and location of the thermodynamic inefficiencies and irreversibility present in the system. Most of the hybrid system models in literature are 0-D models, here the fuel cell component is treated as a dimensionless box, nevertheless, this approach is suitable for hybrid SOFC simulations where the study emphasis is on the interaction of the fuel cell and the rest of the system and the contribution of the SOFC to the overall system performance [120].

The pioneers in the field of SOFC modelling and their integration with gas turbines are Harvey and Richter[121-123], the earliest known SOFC-GT system was proposed by them in 1993, they improved on the model by incorporating internal reformer in the cycle.

Calise et al[119] carried out simulations and exergy analysis on a hybrid SOFC-gas turbine system, they solved for the energy and exergy balance for each component and for the entire system, they went on to calculated the base electrical efficiency as 60% which increased to 70% when heat recovery setup was considered.

Gogoi et al[124] developed an analytical model that provides the energy and exergy based performance analysis of an SOFC-GT-steam turbine (ST) combined cycle power plant, parametric studies were carried out on the variation of compressor pressure ratio (CPR), fuel flow rate (FFR) and air flow rate (AFR), the optimum boiler pressure was found to be at 40bar with 50% additional fuel burning.

In the paper presented by Chan et al[38], a natural gas fed hybrid SOFC power generating system was presented. The cases studied analysed the effect of operating pressure and fuel flow rate on performance of components and the overall system, the hybrid SOFC-GT system achieved an electrical efficiency of 60% and the entire system (including waste recovery) was about 80% efficient.

In a later study carried out by Chan et al[125], they carried out different levels of modelling on the earlier built model, this included the fuel cell model, fuel stack model and the integrated system, the improved system consist of an integrated reformer, SOFC stack and other gas turbine component. The developed hybrid system achieved an electrical efficiency of 60%.

Palsson et al[126] studied the integration of a GT hybrid system with a SOFC, their results show that the pressure ratio has large impact on performance and that electrical efficiency of more than 65% can be achieved at low pressure ratio.

2.5 Simulation of solid oxide fuel cells

Multiphysics simulation entails the interaction and coupling between two or more physical disciplines. The phenomena associated with these disciplines are usually described by a set of partial differential equations which are solved for the corresponding physical phenomena occurring in the defined physical domain. A thorough comprehensive analysis of SOFCs phenomena requires an effective multidisciplinary approach. The operation of an SOFC depends on the complex intertwining between different multiphysics such as mass transport, heat transport, momentum transport, and charge transport all taking place simultaneously and been tightly coupled. The different phenomena occurring in the cell can be described based on different scale structure: micro-, meso- and macro scales. The micro and meso scale aim at understanding the detailed phenomena occurring in each component while the macro scale is more related to empirical analysis such as using computational fluid dynamics. Predictions from the micro and meso scale modelling are then used in developing the empirical macro scale model,

The main features used in simulating each of the physical domains in the model are itemised in Table 2.1 and discussed below:

Table 2.1: Physical phenomena taking place within the SOFC and their spatial scale.

PHENOMENON	MECHANISM	LAYER	SPATIAL SCALE
Mass Transport	Molecular	Channels	Macroscale
	Ionic/Electronic	Electrodes	Microscale
	Molecular	Electrodes	Mesoscale
Momentum Transport	Any	Channels, Electrodes	Macroscale
Species Transport	Convection	Channels, Electrodes	Macroscale
	Ordinary diffusion	Channels, Electrodes	Macroscale
	Knudsen diffusion	Electrodes	Mesoscale
Heat Transport	Convection	Channels, Electrodes	Macroscale
	Diffusion	Overall	Mesoscale
	Radiation	Cell surfaces	Macroscale
Reaction Kinetics	Reduction-Oxidation	Reaction zone (TPB)	Microscale
	Reforming	Anode	Mesoscale
	Water shift gas	Anode, Fuel channel	Mesoscale
Charge Transport	Ionic	Electrolyte	Microscale
	Ionic/Electronic	Electrodes	Microscale

PHENOMENON	MECHANISM	LAYER	SPATIAL SCALE
	Electronic	Interconnect	Microscale

2.5.1 Mass transport modelling

Mass transport in flow channels and porous electrodes is considered important in enhancing the performance of the fuel cell, due to the structure of the flow channels and porous electrodes, the pressure, velocity and species distribution need to be studied using mass transport equation. Generally in SOFCs, mass transfer is due to convection, ordinary or molecular and Knudsen diffusion, while convection and ordinary diffusion is used in describing the diffusion process in the channels, the species diffusion through the porous electrode could be described by either the ordinary or Knudsen diffusion. Ordinary diffusion is known to be dominant for large pore sizes and at high system pressure. If the frequency of collision between the molecules and the pore wall is high, then the Knudsen diffusion term becomes significant and needs to be taken into consideration.

In SOFC literature, there is a wide range of models used in describing the diffusion phenomenon in SOFC electrodes and channels of which the most established ones are either through the Ficks model [59, 84, 86, 106, 127, 128] or the Maxwell-Stefan model[101, 129, 130], some other authors use more complex models like the modified Maxwell-Stefan model [35, 41, 91] or the Dusty-gas model[131, 132].

Tseronis et al[71] and Cayan et al[133] combined different diffusion method in their model. Suwanwarangkul et al[70] reported a comparison between the three major approaches, they concluded that the choice of approach is case sensitive and that the DGM is most appropriate at high current density and for multicomponent systems while the SMM gives a good approximation for binary systems. Although mass transport phenomena in SOFCs significantly affects the cell performance, its consideration was completely neglected in models developed by Costamagna et al[88] and Stiller et al[110].

2.5.2 Momentum transport modelling

Gas flow velocities in SOFCs are affected by chemical reactions, mass transfer, temperature change and density changes occurring in the cells[44]. They are characterised by very slow flow motion which justifies the common practice of assuming laminar flow in the gas channels [134]. Flow velocity profiles are modelled by the momentum conservation equation. Despite the importance of velocity variation inside flow channel, momentum conservation was not incorporated in the model developed by Ferguson et al[84], since they assumed a zero velocity in the electrodes and constant within the flow channels.

Some other researchers [37, 135, 136] didn’t consider the momentum conservation in their model. Although, many comprehensive models in literature include the momentum conservation in their model [58, 76, 83, 91, 127, 137, 138].

Bhattacharyya et al[139] compared models having momentum conservation equation with those not having the equations, they found that changes in velocity especially on the cathode side of the flow channel has a significant effect on cell performance and that neglecting momentum balance equations in steady state consideration causes computation errors especially at high current densities. Vast majority of simulations agree in the use of Navier-Stokes equations to model the momentum conservation in the gas channels and the Darcy equation for the porous electrodes [79, 98, 115]. The connection between Navier stokes and Darcy equation with the Darcy-Brinkman approach is described later chapter Four.

2.5.3 Heat transport modelling

Heat transport modelling is of vital importance in the design and development of SOFCs, due to the close coupling of temperature fields to the electrochemical reaction rates, reaction kinetics, electrode overpotentials, ohmic resistances, operating voltage, fuel utilisation and flow fields. Furthermore, an accurate thermal analysis is essential for the prediction, optimisation, assessing and mitigating thermo-mechanical degradation of the cell[73].

Although some researchers assumed an isothermal system in their model [35, 68, 71, 75, 107, 140], a good number of authors accounted for heat transfer components in theirs.

A common assumption found in predictive thermo-fluidic models of SOFCs is the assumption of local thermal equilibrium (LTE) between the gas and solid components within the porous electrode [76, 79, 141], the validity of this assumption was proved by

Damm et al[73]; they were able to predict the temperature difference between the solid and gas phase in the SOFC, their model assumed the local temperature between both phases was not in equilibrium (local temperature non-equilibrium (LTNE) approach), the difference in value obtained was found to be small enough to be tolerated, this finding was collaborated in a study by Andersson et al[142], who used the same method to determine the temperature difference between gas and solid phases, which they found to be negligible.

Heat transfers within SOFCs usually occur through convection (between the solid components and the gas streams), conduction (within the porous and solid structures), diffusion and radiation. Among literature, there are little or no discrepancies on the need to model the convective and conductive contribution, on the other hand, the need to model the diffusive and radiation effect on thermal analysis of SOFCs is quite controversial.

2.5.4 Electrochemical reaction modelling

The electrochemical reaction which occurs inside of the fuel cell is known to be the driving force of the cell performance. These reactions occur at the reaction layers also called the triple phase boundary (TPB). Some authors consider this reaction zone layers as mathematical surfaces, thus treating them as boundary conditions [69, 76, 87, 114, 134, 143], the justification for this assumption is that the reaction sites are spread thinly into the electrodes a distance of about 10µm[76, 144].

However, other authors consider the reaction zone layer as finite volumes, defining an active surface area per unit volume of the electrode as the region where the electrochemical reaction occurs [35, 79, 83, 108, 113]. Authors who considered this region as finite volume usually agree that this layers thickness ranges between 10-50µm. The high operating temperature of SOFC offers possibilities of internal reforming (see next section), unlike in many other types of fuel cells, carbon monoxide (CO) is not poisonous, but can be oxidised along with H_2 in the electrochemical reactions. Under such considerations, only a very small fraction of the CO is actually oxidised as it mostly participate in the water-gas shift reactions than in the electrochemical reactions[44].

Nevertheless, a good number of authors [68, 69, 145-147] still considered CO oxidation in their model. Although most [40, 59, 71, 78, 83-85, 89, 114] ignored the occurrence of CO oxidation due to the dominance of H_2 over CO in charge transfer chemistry.

The SOFC simulations developed by Aloui and Halouani[148] compared performances when only H_2 was oxidised with the oxidation of syngas (H_2 and CO), results obtained showed that the direct oxidation of syngas gives slightly better cell performance than using only H_2 fed.

2.5.5 Reforming and shift reaction modelling

Reforming reactions enables the production of oxidisable fuels like H_2 and CO from hydrocarbons such as methane or natural gas. This reaction occurs predominately between 873K and 1273K; offering good thermal compatibility with SOFC operations. As such, heat needed for the endothermic reforming reaction can be supplied by the SOFC [44]. Hydrocarbon reforming can either occur before the SOFC (external reforming) or inside the SOFC (internal reforming).

Two forms of internal reforming exist: direct (DIR-SOFC) and indirect (IIR-SOFC) internal reforming. In DIR-SOFC, the hydrocarbon is fed into the cell through the anode flow channel, the chemical reforming reactions occurs in the anode electrode layers (diffusion and reaction) while for the IIR-SOFC, the reformer is placed separately but still in thermal contact with the anode electrodes.

On the other hand, the exothermic water-shift gas reaction occurs when CO reacts with water to generate H_2 (more fuel for the oxidising reactions) and CO_2, the shift reaction is assumed to take place in electrode layers and fuel channel.

Chanda et al[87], Aguiar et al[40], Iwai et al[91], Ho et al[113, 149], Haberman and Young[150] and other researchers in [47, 68, 109, 151, 152] included DIR-SOFC in their models while Aguiar et al[153] and Dokamaingam et al[37, 154] used IIR-SOFC in theirs. A few others like Hussain et al [35, 80] only considered the water shift gas reaction in their model.

2.6 Current issues in SOFC modelling.

SOFC models are developed by using computational fluid dynamics (CFD) methods to solve the transport equations; these solutions are then coupled to an electrochemical model[155].

Table 2-1 compares some models in the literature; the criteria used for the comparison are the modelling methodologies and the particular physics been considered.

Majority of the compared models [35, 69, 75, 79, 83, 150, 156, 157] were carried out at the cell level; of which most analysed at the macro scale level.

The finite volume method (FVM) is preferred for discretisation by most of the authors.

All the models compared included governing equations for the mass transport. Charge transport models were also included by most of the papers except those who models only investigated the electrodes. Quite a few neglected momentum transport [75, 87, 90, 150] and energy transport [35, 69, 75].

Parametric studies were carried out by most authors [75, 79, 83, 87, 90, 156, 157] aimed at performance optimisation but validation with experimental data is rare.

The models that considered energy transport equations included convective heat transfer and ignored the radiation component in their simulations.

DIR-SOFC was considered by all the papers that used hydrocarbons as their fuel.

For flow configuration; co-flow and counter-flow were mainly found in literature, with most authors modelling with co-flow configuration.

0-D to 3-D modelling techniques can be found in literature, in 0-D modelling, the SOFC is considered as a black box, they are usually used in system modelling where the SOFCs are integrated in other heat engines to improve work output and efficiencies. I-D are useful when variations along flow directions are been studied, while 2-D are needed when connections between flow channels and electrodes are important, 3-D is usually used to obtain detailed knowledge of the performance characteristics of the SOFC [45, 158]

Table 2-2: Comparison of some SOFC models found in literature

Paper number		**1**	**2**	**3**	**4**	**5**	**6**	**7**	**8**	**9**	**10**	**11**
Paper reference number		[156]	[75]	[79]	[69]	[35]	[90]	[157]	[87]	[83]	[150]	[38]
Dimensions	0-D											
	1-D					x						
	2-D						x		x	x	x	x
	3-D	x	x	x	x			x				
Fuel	Hydrogen	x		x				x		x		
	Methane		x		x	x	x		x		x	x
	Gas mixture											
	Other											
Discretisation	FDM											
	FVM	x	x	x	x	x	x		x		x	x
	FEM							x		x		
Flow configuration	co-flow	x	x	x		x	x	x	x	x	x	x
	counter-flow		x		x		x					
	cross flow											
Level of modelling	Cell	x	x	x	x	x		x		x	x	
	Stack						x		x			x
	System											x
Modelling scale	micro model			x		x			x	x		
	macro model	x	x		x		x	x			x	x
Governing equations	Mass	x	x	x	x	x	x	x	x	x	x	x
	Energy	x		x			x	x	x	x	x	x
	Momentum	x	x	x	x	x		x		x		x
	charge	x	x	x		x	x	x	x	x	x	x
Heat transfer consideration	convection	x	x				x	x	x	x	x	x
	Radiation						x					
Reforming type	External											
	DIR		x				x		x		x	x
	IIR											
Validation with Exp. data	yes					x			x			
	no	x	x	x	x		x	x		x	x	x
Parametric study	Yes	x	x	x		x	x	x	x	x		
	no				x						x	

Most of the studies in SOFC modelling use the well-known or so called “state of the art” materials in their analysis, new studies need to be carried out to assess alternative materials and to study the effect of these materials on cell efficiencies, cell degradation, performance improvement etc.

The table below categories the selected models from Table 2-2 into the cell types, objectives, methodology and the limitations of the models.

Table 2-3: Detailed comparison of selected models

Author	**Cell type**	**Objective**	**Method**	**Limitations**
Wang et al (1)	PSOFC	To study the influence of operating conditions and anode structure by predicting the temperature distribution, species concentration, current density and over potentials	FVM in solving the conservation laws of mass, momentum, energy and electric charge for both co-flow and counter-flow cases	-model not validated with experimental data -Knudsen diffusion is neglected -concentration heats was ignored -Electrochemical reactions were modelled as a boundary interface -Ohmic overpotential is ignored -Exchange current density is assumed constant. -model parameters were neither determined from empirical relations nor from experiments or literature -solves for only binary mixtures
Nam et al (2)	Micro PSOFC	To develop a detailed micro-scale prediction of the electrochemical processes in the entire SOFC	Experiments on electrochemical reaction kinetics with defined TPB length were used to model the activation overpotentials, gas phase transport was calculated by	-The momentum of gaseous species was assumed negligible -Solves only for binary mixtures -Electrochemical reactions were modelling as occurring in the entire electrode surface -Concentration overpotential was ignored

			the dusty-gas model	-Convective fluxes were included in the electrodes -conversation of energy was not included in the model
Thinh et al (3)	Micro PSOFC	To develop an anode supported SOFC with composite electrode in which the internal reforming of methane and steam is included	Equations describing transport, chemical and electrochemical processes for mass, momentum, species and energy are solved using a Star-CD commercial package	- the ohmic heat source terms are not included in the energy model -the heat source term from activation and concentration losses are not included -The kinetics for the methane reforming reaction rate assumes a first order for methane and zero order for the other components in the reaction -it assumes a constant for the exchange current density and reactive surface area
Yakabe et al (4)	PSOFC	To estimate the concentration polarisation in the anode	FVM was used in solving the conservation of mass equation in which Darcy's law was used in modelling the gas flow	-Electrochemical reaction modelled as a boundary interface -it uses oxygen pressure difference to calculate the concentration overpotential in the anode -ignored all other overpotential terms and the energy balance equations
Hussain et al(5)	PSOFC	To develop a fuel flexible SOFC model with a finite reaction layer and incorporate micro characteristics of the cell	FVM in solving the mass, momentum and charge equations to predict the cell performance at various operating and design conditions	-Failed to use empirical relations to model the microstructural parameters -Ignored the heat transfer equations -only accounted for the water-gas shift reaction (ignored steam reforming reaction)

				-exchange current densities were assumed constant
Aguiar et al (6)	Dynamic PSOFC	To develop a dynamic planar anode supported SOFC with internal reforming	Using mass and energy balances and an electrochemical model to predict the cell performance at several temperatures and fuel utilisation	- The kinetics for the methane reforming reaction rate assumes a first order for methane and zero order for the other components in the reaction -heat arising from the electrochemical reactions are not included
Andersson et al (7)	PSOFC	To investigate the influence of ion and electron transport resistance	Governing equations for heat, mass, momentum and charge transport as well as the kinetics for electrochemical and reforming reactions	-The effect of species concentration(pressure) was not included in the exchange current density term -micro structural characteristics were not included

Although there are many thermal models in literature, most of them are at the cell level, there is a need for further developments in stack and system level modelling, there is also a need for more models (micro models) that relates the microstructure, geometry and material properties as they are quite rare in literature.

There are very limited studies which focuses on how the interdependent microstructural properties affect the chemical reactions and mass transport processes in the cell, also the reactive surface area, porosity, particle size, and electrode thickness are known to have conflicting effect on the cell performance. More research studies is needed to fully understand and predict this behaviour.

Electrochemical heating is also not fully available in open literature although they are quite important in developing models. The Joule heating effect which are usually quite large due to the high ionic resistance of YSZ and the heat due to the activation overpotential because of the large cathode activation overpotentials must be accounted for in the model for an accurate energy balance.

The pressure gradients in the electrodes and the momentum balance equations are ignored without justification in most modelling studies

To model SOFC's taking into account the above mentioned needs, the thermodynamics and kinetics of SOFC must be fully understood and this is discussed in details in the next chapter.

2.7 Conclusions.

SOFC models found in the literature are classified broadly into electrode level, cell level or system level models. The choice of what level to carry out simulations depends on the aim of the study and the components been considered. However, irrespective of the model level, the approach could either be micro-scale or macro-scale.

A review of SOFC models has been undertaken. A variety of modelling approaches have been used in their simulations, these approaches can be summarised under four concepts and will be discussed briefly:

- Electrochemical reaction sites

In the macro-scale approach, the electrochemical reaction is assumed to occur in the boundary interface between the electrolyte and the electrode. The justification for this assumption is the thinness of the region. This assumption leads to a simplification of the model since the conservation equations in the region will not be considered, the chemical reactions will also not be considered and the effect of the electrochemical reactions on the electrode kinetics is ignored. The micro-scale approach is to treat the reaction layer as a finite volume in which the electrochemical reactions occur in a distinct reaction layer.

- Electrode treatment.

In the macro-scale approach, the electrode is considered as been made up only of electronic particles and the pore size, most of the models that used this approach assumed parameters without any interdependency relationship between them. The micro-model treats the layers as been made up of three phases: ion conducting, electronic conducting and the pore size, as a result interdependency relationships between the micro-structural parameters are considered in developing the model. Due to the complexity of this approach, most studies limited this approach to electrode level models; although recently Nam et al[75] used this approach in a cell level model.

- Fuel flexibility

It is widely agreed that an important characteristic of the SOFCs are its fuel flexibilities, been able to use hydrocarbons and carry out internal processing of the fuels. Most of the macro-scale models used hydrocarbon in their model and considered internal reforming processes, they were able to do this successfully due to the minimal complexities in their model as a result simplifications in the electrochemical reaction and electrode treatments. However, very few micro-models included multi-component mixtures; rather binary mixtures were mostly used.

- System level models

It is only recently that interest in system level modelling is gaining interest, a number of the existing models have studied SOFC integration with basic cycles and only studying for the energy changes regarding efficiency and specific work output, a few others studied the exergy destroyed in the system, however, very few combined the studies.

Different aspects and approaches to SOFC modelling have been undertaken in literature, however, the models either made some assumptions to simplify the simulation process or had limitations (some of which has been discussed above), therefore the unique contribution of this thesis is to produce a comprehensive micro scale SOFC model . The key features of this present model are listed as follows:

- Micro-Scale: The micro-scale modelling approach is used in the simulation for both all the components; in which the micro-structural parameters are modelled to depend on each other.

- Fuel Flexibility: The micro-scale model is able to simulate any hydrocarbon based fuel made up of a multi-component mixture. The reforming and water-shift gas reactions were considered to occur in the anode

- The electrochemical reaction is modelled to occur only in the distinct electrode reaction layer. As such, the conservation equations and the chemical reactions are considered in this layer

- A total heat transfer model is developed, in which all the exothermic and endothermic reactions are considered, also the heat properties of the irreversibility's (overpotentials) in the cell are considered. (a number of the reviewed literature didn't consider overpotential heat properties)

- The Knudsen diffusion term due to the frequency of collision between the gas molecules and the pore walls is included in the mass transfer model.

- System level studies for both the energy and exergy analysis in complex cycle configurations involving more than three heat exchanging components. Two unique configurations were developed and their effect on efficiencies and exergy destruction were examined.

CHAPTER3 : Thermodynamics and Kinetics of SOFCs

3.1 Introduction

The engineering and operation of a SOFC entails a multidisciplinary approach in which knowledge of thermodynamics, kinetics, heat transfer, mechanical design, material science and fluid mechanics are necessary. Of these, the thermodynamics and kinetics of the cell are of fundamental importance in SOFC modelling and operation: thermodynamics concerns the reaction process under certain conditions while the kinetics is connected to the catalytic effect of electrodes on the electrochemical reaction[159].

This chapter describes the fundamental thermodynamic and kinetic principles of SOFC operations. The thermodynamic principles are used in solving the energy conversion processes in the SOFC, while its kinetics describes the irreversibility's present in the SOFC.

The definitions of some of the terms used in describing the thermodynamic model are presented in section 3-2, the relationships used in calculating the reversible cell voltage (Nernst voltage) is presented in section 3-3, after which the thermodynamics of integrating SOFCs in hybrid systems is developed in section 3-4. The last section describes electrode kinetics of SOFCs and the irreversibility's present in SOFCs operation.

3.2 Basic definitions

Fuel utilisation factor

Fuel utilisation factor U_f is defined as the ratio of the amount of fuel that is electrochemically oxidised to the maximum available fuel entering the anode. In most cases the fuel is H_2, however, CO could be included in some instance. The equation can be expressed as:

$$U_f = \frac{\dot{N}_{fuel,utilised}}{\dot{N}_{fuel,in}} \tag{3-1}$$

Air utilisation factor

Air utilisation factor U_a is defined as the ratio of oxygen that is electrochemically reduced to the oxygen present in the inlet air stream at the cathode, the equation can be expressed as

$$U_a = \frac{\dot{N}_{o_2,utilised}}{\dot{N}_{o_2,in}} \tag{3-2}$$

Excess air coefficient

SOFC usually operate with air at the cathode inlet instead of pure oxygen. The air supplied would normally have excess air coefficient greater than one $(\lambda > 1)$, this coefficient is defined as the ratio of oxygen in the air stream to that needed for a stoichiometric reaction, Equation (1-3) shows that the oxygen is half the hydrogen in the inlet stream for a stoichiometric balance of the hydrogen oxidation reaction, this can be expressed as:

$$\lambda_{air} = \frac{2.\dot{N}_{o_2,in}}{\dot{N}_{H_2,utilised}} \tag{3-3}$$

3.3 Reversible cell voltage

The ideal performance of a reversible fuel cell can be described thermodynamically by the first and second laws of thermodynamics. The reversibility of the fuel cell is presupposed on the assumption that the chemical energy of the reactants in the anode and cathode are converted into electrical energy and remains in equilibrium at each stage of the conversion. A schematic of a reversible fuel cell is shown in Fig 3-1, the total enthalpy to the cell delivered by the reactants is $\sum n_0 H_0$ and that of the products of the electrochemical reaction leaving the cell is$\sum n_i H_i$, the heat released by the cell is Q_{fc} and the work done is W_{fc}

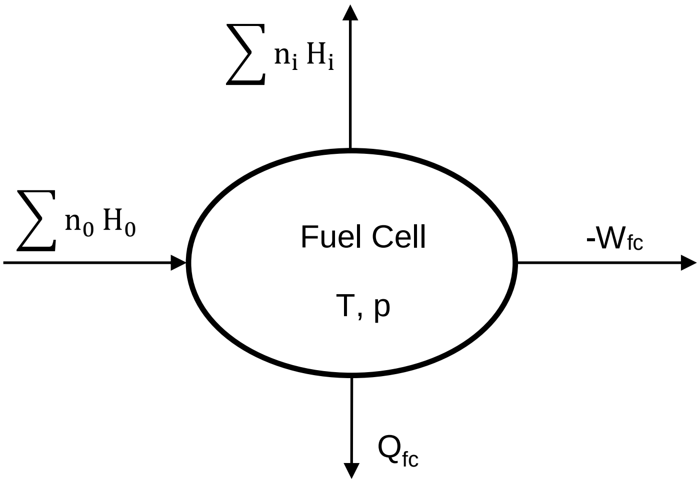

Figure 3-1: Reversible fuel cell and its system boundaries

The mathematical expression of the first law of thermodynamics is expressed as:

$$Q_{fc} + W_{fc} = \Delta H_r \tag{3-4}$$

The second law of thermodynamics which applies for a reversible heat transfer process yields the following expression:

$$\Delta S = \frac{Q_{fc}}{T_{fc}} = 0, \qquad Q_{fc,rev} = T_{fc}\Delta S \tag{3-5}$$

Combining Equations (3-4) and (3-5) yields the reversible specific work of the fuel cell $W_{fc,rev}$ which is equal to the Gibbs free energy of the reaction ΔG_r [21]

$$W_{fc,rev} = \Delta G_r = \Delta H_r - T_{fc}\Delta S \tag{3-6}$$

The reversible cell efficiency $\eta_{fc,rev}$ is defined as the ratio of the Gibbs free energy to the enthalpy

$$\eta_{fc,rev} = \frac{\Delta G_r}{\Delta H_r} = \frac{\Delta H_r - T_{fc}\Delta S}{\Delta H_r} = 1 - \frac{T_{fc}\Delta S}{\Delta H_r} \tag{3-7}$$

The reversible power of the cell $P_{fc,rev}$ is defined as the product of the specific work and the reactant molar flow rate $\dot{n}$

$$\mathrm{P}_{fc,rev} = \dot{n}W_{fc,rev} \tag{3-8}$$

The fuel cell is considered to be an electrical device, thus the reversible power can be further expressed as

$$\mathrm{P}_{fc,rev} = \mathrm{E}_{fc,rev}i \tag{3-9}$$

Where $\mathrm{E}_{fc,rev}$ the reversible is cell voltage and i is the current.

According to Faradays law, the current is a function of the molar flow electrons molar flow rate, this can be expressed as:

$$i = -\dot{n}_{el}Fj_i \tag{3-10}$$

F is the faraday constant and $\dot{n}_{el}$ is the number of moles of the electrons and j_i is the reactant flux per unit area. Combining Equations (3-8), (3-9) and (3-10) yields:

$$\dot{n_f}W_{fc,rev} = \mathrm{E}_{fc,rev} \,.\, -\dot{n}_{el}F \tag{3-11}$$

Substituting the expression for $W_{fc,rev}$ from Equation (3-6) yields:

$$\mathrm{E}_{fc,rev} = \frac{\dot{n}_f \Delta G_r}{-\dot{n}_{el}Fj_i} \tag{3-12}$$

The ratio between molar flow of electrons and the molar flow of reacted fuels can be defined as the number of electrons released during the oxidising process. Thus the reversible voltage can be expressed as

$$E_{fc,ref} = \frac{-\Delta G_r}{n^{el}F} \tag{3-13}$$

This is the fundamental equation that describes the reversible cell voltage for an ideal fuel cell. When the influence of fuel utilisation (changes in partial pressure of reactant components in the system) [160, 161] is considered, the reversible cell voltage is similar to the Nernst Voltage E_N (or open circuit voltage E^{ocv}) and defined as

$$\mathrm{E}^{ocv} = \mathrm{E}_N = \frac{-\Delta G_r^0(T)}{n^{el}F} - \frac{R_gT}{n_{el}F}\, In \left[\prod_i (p_i^0)^{v_i}\right] \tag{3-14}$$

Where $-\Delta G_r^0(T)\ is$ the molar Gibbs function at standard conditions, defined at $T_0 = 298K$ and $P_0 = 1atm,\ p_i^0$ are the partial pressure of reactants and products in the bulk flows, R_g is the universal gas constant, T is the operating temperature and v_i is the stoichiometric coefficient. The first term on the right side of Eq. (3-12) $\left(\frac{-\Delta G_r^0(T)}{n_{el}F}\right)$ is called the standard electrochemical cell voltage (E^0) and is defined for a pure hydrogen-steam mixture as[76, 106]

$$E^0 = 1.271 - 2.73110^{-4}T \tag{3-15}$$

In practice, E_N represents the open circuit voltage of the cell since the concentration of the reactant gases at the reaction boundary is the same as that of the bulk stream i.e. there is no current flow from or to the electrode, the open circuit voltage (Nernst voltage) for an overall H_2-O_2 fuel cell reaction (Equation (3-16)) is shown in Equation below in Equation (3-15):

$$H_2(g) + \frac{1}{2}O_2(g)\ \leftrightarrow H_2O(g) \tag{3-16}$$

$$E^{ocv} = E^0 - \frac{R_gT}{2F}\ In\left(\frac{p_{H_2O}}{p_{H_2}p_{O_2}^{1/2}}\right) \tag{3-17}$$

It is also expressed in terms of the reactant mole fractions as:

$$E^{ocv} = E^0 - \frac{R_gT}{2F}\ In\left(\frac{x_{H_2O}}{x_{H_2}x_{O_2}^{1/2}}\right) - \frac{R_gT}{4F}\ In\left(\frac{p_o}{p}\right) \tag{3-18}$$

According to Equation (3-6) the temperature dependent Gibbs free energy is not equal to the enthalpy of the reaction as there are some irreversible losses in the reaction due to an entropy change, based on the stoichiometry of the reactions, the changes in enthalpy and entropy are calculated as follows:

$$\Delta H(T) = \sum_i v_i.\left(h_f + \int_{T^0}^{T} c_p\, dT\right) \tag{3-19}$$

$$\Delta S(T) = \sum_i v_i.\left(s_f + \int_{T^0}^{T} c_p\, dT\right) \tag{3-20}$$

Where v_i is the number of moles of species, h_f and s_f are the enthalpy and entropy of formation of species i at standard conditions (1 atm, 298K).

For the hydrogen oxidation process, the enthalpy is the difference between the heats of formation of products and reactants, it can be expressed as:

$$\Delta H = h_{f,H_2O} - h_{f,H_2} - {}^{1}\!/_{2}\, h_{f,O_2} \tag{3-21}$$

Similarly, the entropy is the difference between entropies of products and reactants expressed as:

$$\Delta S = s_{f,H_2O} - s_{f,H_2} - {}^{1}\!/_{2}\, s_{f,O_2} \tag{3-22}$$

Where $h(J\,mol^{-1})$ and $s(J\,mol^{-1}K^{-1})$ are the enthalpies and entropy values respectively. While the subscripts $H_2O\,, H_2\ and\ O_2$ are the values for water, hydrogen and oxygen respectively. The values at standard conditions are presented in Table (3-1) and the reversible oxidation reactions for common SOFC fuel at standard conditions are also tabulated in Table 3-2

Table 3-1: Enthalpies and Entropies of Formation of Fuel Cell Reactants [162].

	$h_f\,(kJ\,mol^{-1})$	$s_f(kJ\,mol^{-1}K^{-1})$
H_2	0	0.13066
O_2	0	0.20517
$H_2O(g)$	-241.98	0.18884

Table 3-2: Enthalpies, Entropies and Gibbs Free Energy for Fuel Cell Reactants Oxidation Processes[162]

	$\Delta H^0(kJ\,mol^{-1})$	$\Delta S^0(kJ\,mol^{-1}K^{-1})$	$\Delta G^0(kJ\,mol^{-1})$
$H_2 + {}^{1}\!/_{2}\,O_2 \rightarrow H_2O$	-241.82	-44.37	-228.59
$\mathrm{CO} + {}^{1}\!/_{2}\,O_2 \rightarrow CO_2$	-282.99	-86.41	-257.23
$\mathrm{CH_4} + 2O_2 \rightarrow 2H_2O + CO_2$	-802.31	-5.13	-800.68

The specific heat capacity c_p is also defined as a function of temperature (Figure 3-2) and an empirical relationship may be used in approximating as follows[162]:

$$c_{pi} = a_i + b_i T + c_i T^2 \tag{3-23}$$

Where a, b and c are empirical coefficients shown in Table 3-3

Table 3-3: Coefficients for Temperature Dependency of c_p [162]

	a	b	C
H_2	28.91404	-0.00084	2.01E-06
O_2	25.84512	0.01287	-3.90E-06
$H_2O(g)$	30.62644	0.009621	1.18E-0.6

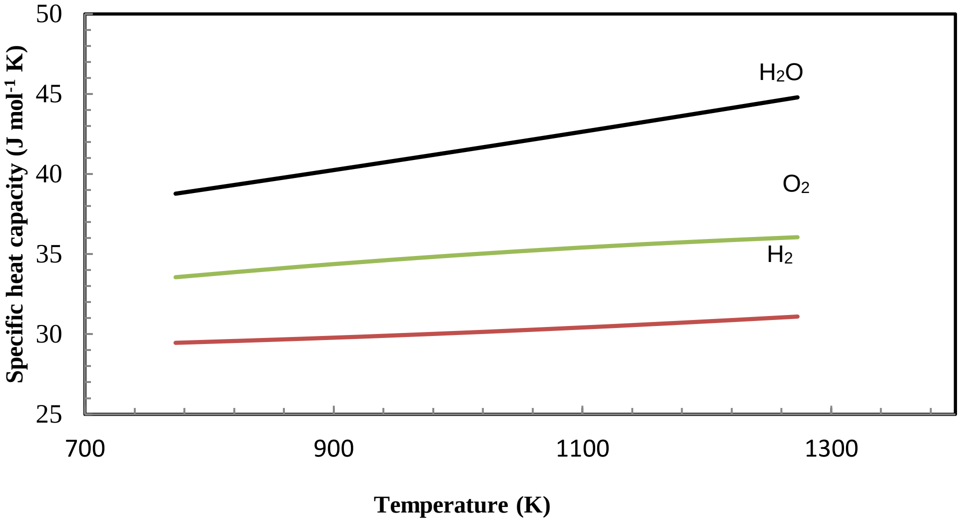

Fig 3-2: Temperature dependent specific heat capacity

The Nernst voltage at varying pressures may be expressed as a function of operating temperature and reactant concentration, it can therefore be calculated using Equation (3-23), the results obtained are shown below in Figures 3.3-3.6

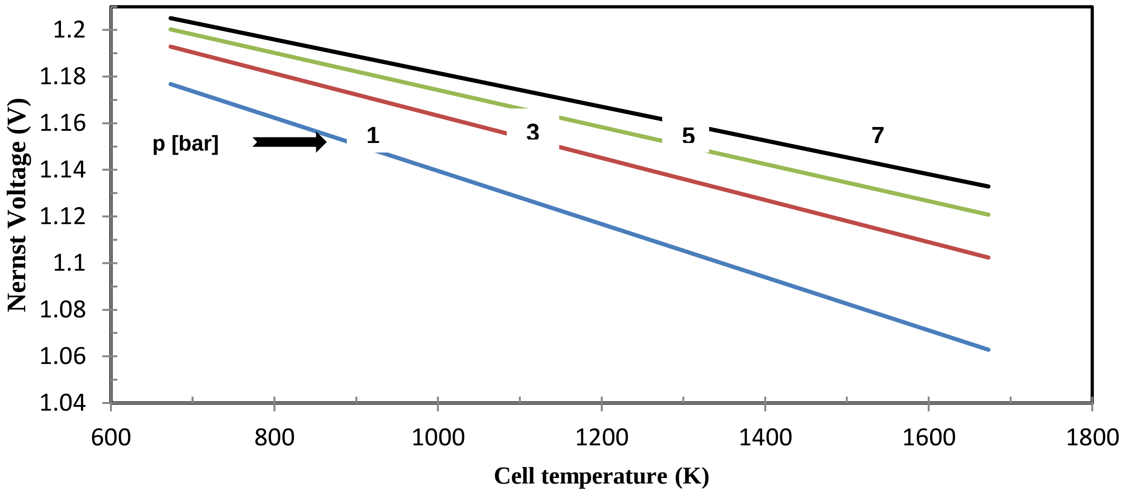

Figure 3-3: Nernst voltage at different states of operating pressure and temperature

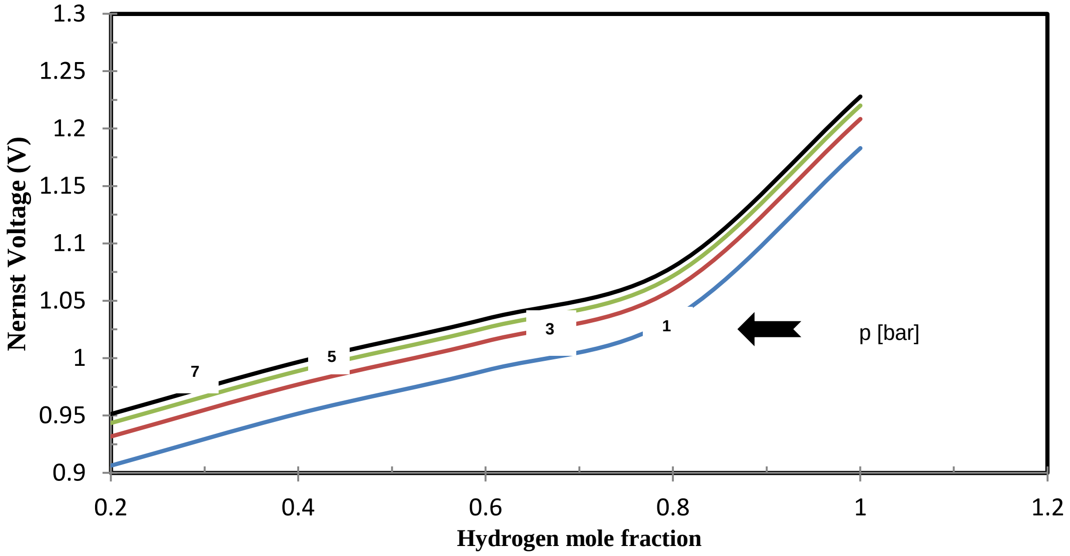

Figure 3-4: Nernst voltage as a function of hydrogen mole fraction and operating pressure

3.4 Thermodynamics of SOFC systems.

A SOFC- hybrid system is any power generating system that allows the integration of a SOFC in a heat engine cycle [163].They can be described as a unit consisting of a number of SOFCs electrically connected together into stacks. The stacks can be made to supply the depleted fuel and air from the SOFC to a combustor for afterburning before been passed on to the heat engine or made to supply its exhaust gases directly into the heat engine. Whatever system the SOFC-hybrid uses, it always associated components such as pumps, fans, heat exchangers, compressors etc. Figure (3-5) shows generic possibility of integrating the SOFC with a heat engine.

The primary goal in any power producing system is to maximize net-work output and system efficiency; these can be achieved thermodynamically by the energy and exergy analysis of the entire system. The first law of thermodynamics describes the conservation qualities of energy; and that the total energy of a system can only be converted from one form to another but can never be destroyed. However, its ability to produce work gives rise to a loss in its energy quality (irreversibility). The energy quality is an indication of the exergy value. Thus, Exergy can be defined as the maximum amount of work obtainable from a substance when it moves from its state to a state which is in reversible equilibrium with the environment[164]. The concept of exergy allows the determination of irreversibility's (thermodynamic losses) and the true quality (converting fully into work) of the different energy forms. Thus the exergy analysis method is a supplement to energy analysis of any system, at the same time providing the means to quantify and analyse the levels of irreversibility's in the system[165].

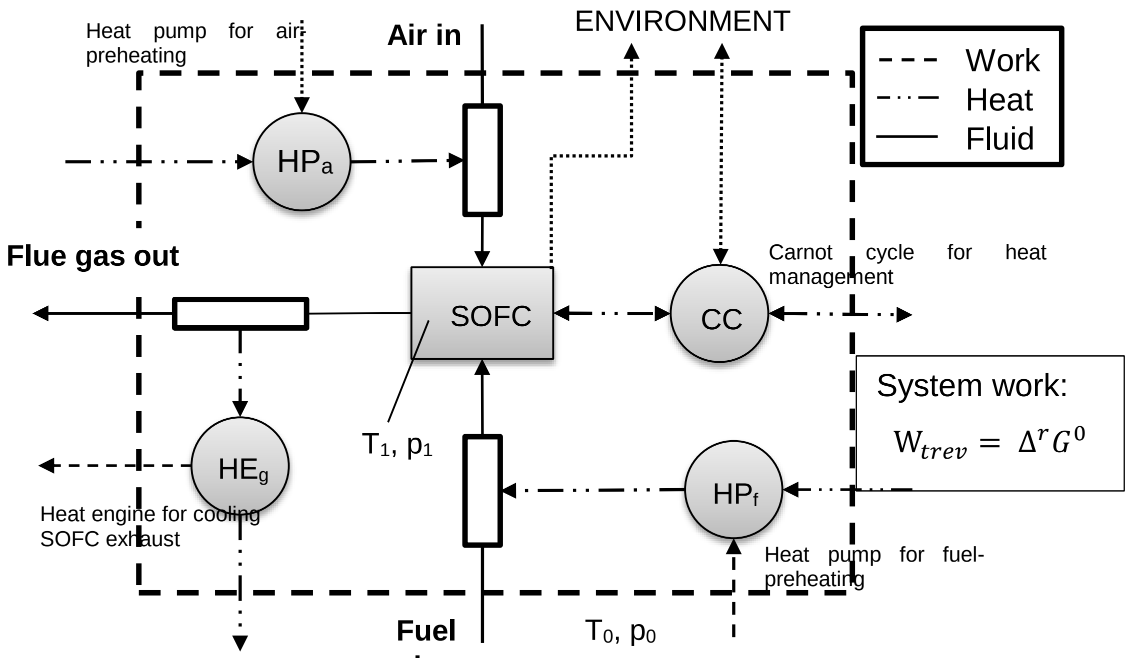

Figure 3-5: A typical fuel cell-heat engine hybrid system[160]

Where $HP_a$is the air preheating heat pump, HP_f is the fuel preheating heat pump, HP_g is the SOFC exhaust cooling heat engine and CC is the Carnot cycle

As earlier stated and shown in Fig 3-1, a reversible system is one in which the process is in thermodynamic equilibrium with surrounding environment. Figure 3-5 shows a typical reversible SOFC-heat engine. The fuel and air enters the system at state 0 (T_0, p_0), work is done on the fluids by the reversible heat pumps HP_f (fuel) and HP_a (air) to bring them to the thermodynamic state of the fuel cell (T_1, p_1), the exhaust gases from the SOFC is brought from its state(T_1, p_1) back to the environmental (T_0, p_0) by the reversible heat engine HE_g. The heat engine HP_g delivers reversible work which gives the exergy of the SOFC exhaust in the state(T_1, p_1). Lastly the Carnot cycle CC is used in exchanging heat reversibly between the SOFC and the surrounding. The thermodynamic relationship for the work and heat expression for each component is expressed below.

The reversible work delivered by the SOFC defined in Equation (3-6) is

$$w_{fc,rev} = \Delta G_r = \Delta H_r - T_{fc}\Delta S \tag{3-24}$$

And the reversible heat from the fuel cell is expressed as:

$$q_{fc,rev} = T_{fc}\Delta S \tag{3-25}$$

The heat source of the Carnot cycle is the fuel cell $(q_{fc,rev})$, the reversible work of the CC is defined as

$$w_{cc,rev} = q_{fc,rev}.\left(1 - \frac{T_0}{T_{fc}}\right) = T_{fc}\Delta S.\left(1 - \frac{T_0}{T_{fc}}\right) \tag{3-26}$$

$$q_{cc,rev} = q_{fc,rev} = T_0\Delta S \tag{3-27}$$

The reversible heat needed to raise the temperature of the fuel is produced by the heat pump HP_f and is defined as

$$q_{ff,rev} = h_{ffc} = w_{HP_f,rev} + q_{HP_f,rev} \tag{3-28}$$

Where h_{ffc} is the enthalpy of the fuel heating process, $w_{HP_f,rev}$ is the work done by the heat pump. The fuel pump HP_f is supplied with heat $q_{HP_f,rev}$ from the environment and with the work done $w_{HP_f,rev}$ which is the exergy ex_f of the fuel heat pump, thus the reversible work done by the heat pump is given as

$$w_{HP_f,rev} = ex_f = h_{ffc} - T_0 . S_{ffc} \tag{3-29}$$

where
$$h_{ffc} = c_p(T_1 - T_0) \tag{3-30}$$

$$S_{ffc} = c_p In \frac{T_1}{T_0} - R \frac{p_1}{p_0} \tag{3-31}$$

Thus the exergy of the heat pump can be given as

$$ex_f = c_p(T_1 - T_0) - T_0 \left(c_p In \frac{T_1}{T_0} - R \frac{p_1}{p_0} \right) \tag{3-32}$$

Equation (3-29) to (3-32) gives the definition of the exergy of the fuel heat pump. Equations (3-33) and (3-34) gives the expressions for the exergy of the air heat pump and the exhaust gas heat pump respectively.

$$w_{HP_a,rev} = ex_a = h_{afc} - T_0 . S_{afc} \tag{3-33}$$

$$w_{HP_g,rev} = ex_g = h_{gfc} - T_0 . S_{gfc} \tag{3-34}$$

The Equations (3-29), (3-33) and (3-34) describes the physical exergy of the components under considerations, these equations are valid in determining the exergy if the processes only involve thermal interactions with the environment. As seen from Equation (3-32), the physical exergy is made up of a temperature component and a pressure component.

When the processes involves both heat transfer and an exchange of substances with the surroundings[164], the chemical exergy term are then included. The expression for the chemical exergy is given as:

$$ex_{ch} = RT_0 In \frac{p_0}{p_{00}} \tag{3-35}$$

Where p_0 is the pressure of the environment which is the initial state in this case and p_{00} which is the partial pressure of the substance under consideration as a component of the atmosphere.

The total work of the reversible fuel cell hybrid system of Figure (3-7) is thus given as

$$w_{sys,rev} = W_{fc,rev} + w_{cc,rev} + w_{HP_f,rev} + w_{HP_a,rev} + w_{HP_g,rev} \tag{3-36}$$

A simpler process can be defined such that it replaces the heat pumps HP_f, HP_a and HP_g with heat exchangers is shown in Figure 3-6. The replacement is possible because the heat pumps only heat up air and fuel for HP_f and HP_a while HP_g cools the flue gas, but their total reversible work is negligible.

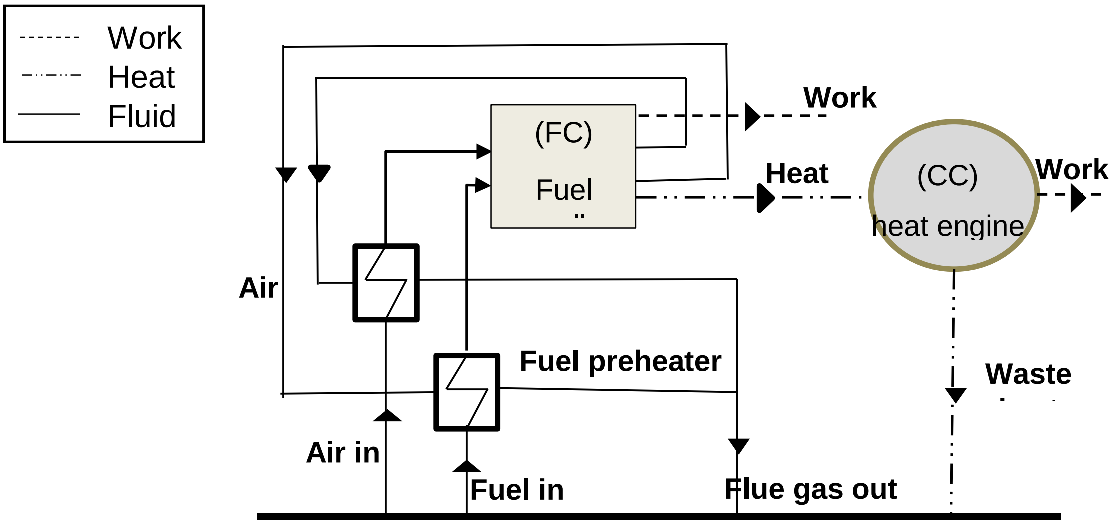

Figure 3.6: A simplified fuel cell-heat engine hybrid system[160]

This simplified cycle is however not reversible; since heat capacities are no longer constant as they are a function of the temperature of the component they pass through leading to changes the reaction enthalpy $\Delta H(T,p)$,. The system efficiency of the simplified hybrid cycle is defined as

$$\eta_{sys} = \frac{\sum w}{LHV} \tag{3-37}$$

The fuel cell in both cases (Figure 3-5 and 3-6) operates reversibly, but the Carnot cycle in the simplified cycle is not completely reversible since a small amount of the waste heat from the fuel cell is used in heating up the air and the fuel. A key benefit of the simplified cycle is its ability to describe the operations of a real cycle from this simple model by the use of exergetic efficiencies. The exergetic efficiency is thus defined as

$$\eta_{ex} = \frac{w_{real}}{w_{rev}} \tag{3-38}$$

3.5 Electrode kinetics in SOFCs

The electrochemical reactions in fuel cells occur simultaneously on the anode and cathode reaction layers, i.e in equations (1-1) to (1-6) in Chapter 1. Due to the gases involved in the electrochemical reactions, the electrodes have to be sufficiently porous to allow the flow of the gases to the reaction sites and their products from the sites.

3.5.1 Butler-Volmer kinetics

The rate of the electrochemical reaction is dependent on the activation barrier which has to be overcome by the charge when it moves from the electrode reaction layer to the electrolyte or vice visa. Electrical current is generated by the electrons released or consumed in the electrochemical reaction process. As the electrons or ions flow, through the circuit, current is generated, the current generated per unit area is known as the current density. Faraday describes the relationship between the current density, the charge transferred and the rate of consumption or generation of species per unit area. The expression has already been shown in Equation (3-10)

An electrochemical reaction normally involves either the oxidation and the reduction of the species, the oxidation process entails the production of electrons while the reduction process consumes electrons, when the process is in equilibrium (i.e. No net electric current is been generated), both the processes are occurring at equal rates

$$Ox + ne^{-} \leftrightarrow Rd \tag{3-39}$$

Where Ox is the oxidation process, ne^- is the net electron generated/consumed and Rd is the reduction process.

The consumption of the species during the reaction is a function of their surface concentration, thus the flux for both reactions of can be written or

$$i_f = k_f C_{Ox} \tag{3-40}$$

$$i_b = k_b C_{Rd} \tag{3-41}$$

The difference between the electrons released and those consumed gives the net current generated:

$$i = n_{el} F \left(k_f C_{Ox} - k_b C_{Rd} \right) \tag{3-42}$$

Where k_f and k_b are the forward (oxidation) and backward (reduction) reaction rate coefficient, C_{Ox} and C_{Rd} are the surface concentration of the oxidised and reduced species respectively. When the reaction is at equilibrium i.e. the rate of the forward reaction is equal to the rate of the backward reaction i.e both proceeding simultaneously; the net current then is zero. The reaction rate in this condition is expresses as the exchange current density. Its coefficient can be expressed as a function of the Gibbs free energy and is given as

$$k = \frac{k_B}{h} \exp\left(\frac{-\Delta G}{RT} \right) \tag{3-43}$$

Where k_B is the Boltzmann constant and h is the Planck's constant. The Gibbs free energy is made up of both chemical and electrical terms, thus for a reduction reaction:

$$\Delta G = \Delta G_{ch} + \alpha_{Rd} F \emptyset \tag{3-44}$$

And for an oxidation process

$$\Delta G = \Delta G_{ch} - \alpha_{Ox} F \emptyset \tag{3-45}$$

Where "ch" is the chemical component of the Gibbs free energy, α is the transfer coefficient and $\emptyset(V)$ is the potential.

The forward and backward reaction rate coefficients of Eq. (3-42) are then represented respectively as:

$$k_f = k_{0,f}\, C_{Ox} \exp\left(\frac{-\alpha_{Rd} F \emptyset}{RT}\right) \quad (3\text{-}46)$$

$$k_b = k_{0,b}\, C_{rd} \exp\left(\frac{\alpha_{Ox} F \emptyset}{RT}\right) \quad (3\text{-}47)$$

By introducing into Eq. (3-42), the expression for the net current density is obtained

$$i = nF\left\{k_{0,f} C_{Ox} \exp\left(\frac{-\alpha_{Rd} F \emptyset}{RT}\right) - k_{0,b} C_{rd} \exp\left(\frac{\alpha_{Ox} F \emptyset}{RT}\right)\right\} \quad (3\text{-}48)$$

At equilibrium, the net current is zero, although the forward and backward reaction proceeds simultaneously, the current density for which this happens (i.e. forward and backward reactions are equal) is called the exchange current density

$$i_0 = n_{el} F k_{0,f}\, C_{Ox} \exp\left(\frac{-\alpha_{Rd} F \emptyset_{eq}}{RT}\right) = n_{el} F k_{0,b} C_{rd} \exp\left(\frac{\alpha_{Ox} F \emptyset_{eq}}{RT}\right) \quad (3\text{-}49)$$

Where i_0 is the exchange current density and $\emptyset_{eq}$ is the equilibrium or reversible potential.

By combining the above equations, a relationship between the current density and polarisation is obtained. This equation is the known as the Butler-Volmer (B-V) equation

$$i = i_o\left\{exp\left(\frac{\alpha_{Rd} F \eta}{RT}\right) - exp\left(\frac{-\alpha_{Ox} F \eta}{RT}\right)\right\} \quad (3\text{-}50)$$

Where η is the polarisation defined as the difference between the electrode potential and the equilibrium potential. The B-V equation for the anode and cathode reaction in a SOFC is expressed as:

$$i_a = i_{o,a}\left\{exp\left(\frac{\alpha_{Rd,a} F \eta_a}{RT}\right) - exp\left(\frac{-\alpha_{Ox,a} F \eta_a}{RT}\right)\right\} \quad (3\text{-}51)$$

$$i_c = i_{o,c}\left\{exp\left(\frac{\alpha_{Rd,c} F \eta_c}{RT}\right) - exp\left(\frac{-\alpha_{Ox,c} F \eta_c}{RT}\right)\right\} \quad (3\text{-}52)$$

The polarisation η is expressed as:

$$\eta_a = E_a - E_{eq,a} \; for\ the\ anode \tag{3-53}$$

$$\eta_c = E_c - E_{eq,c} \; for\ the\ cathode \tag{3-54}$$

Where $E_{eq,a} = 0$ and $E_{eq,c} = E^{ocv}$ and E_a and E_c are the electric potential difference in the anode and cathode respectively and are defined as

$$E_a = \emptyset_{s,a} - \emptyset_{i,a} \tag{3-55}$$

$$E_c = \emptyset_{s,c} - \emptyset_{i,c} \tag{3-56}$$

Hence, $\emptyset_{s,a}$ and $\emptyset_{s,c}$ are the electric potentials of the electronic conducting phase in the anode and cathode; and $\emptyset_{i,a}$ and $\emptyset_{i,c}$ are the electric potentials of the ionic conducting phase.

3.6 Electrode polarisation

As current is generated in the SOFC, the voltage across its terminal $E^{cell}$is less than that corresponding to the reversible running at open circuit conditionsE^{ocv} this drop in voltage reflects a decrease of the conversion efficiency of chemical energy into electrical energy. The major reason for the voltage losses is due to the polarisation phenomena that occur in the fuel cell. Polarisation depends on the load which the cell is subjected; its main sources are activation, concentration and ohmic polarisation. Figure 3-9 shows a typical cell polarisation curve, it also shows the contribution of the individual polarisation to the overall cell voltage, thus the cell voltage E^{cell} is calculated as

$$E^{cell} = E^{ocv} - (\eta_{act} + \eta_{conc} + \eta_{ohm}) \tag{3-57}$$

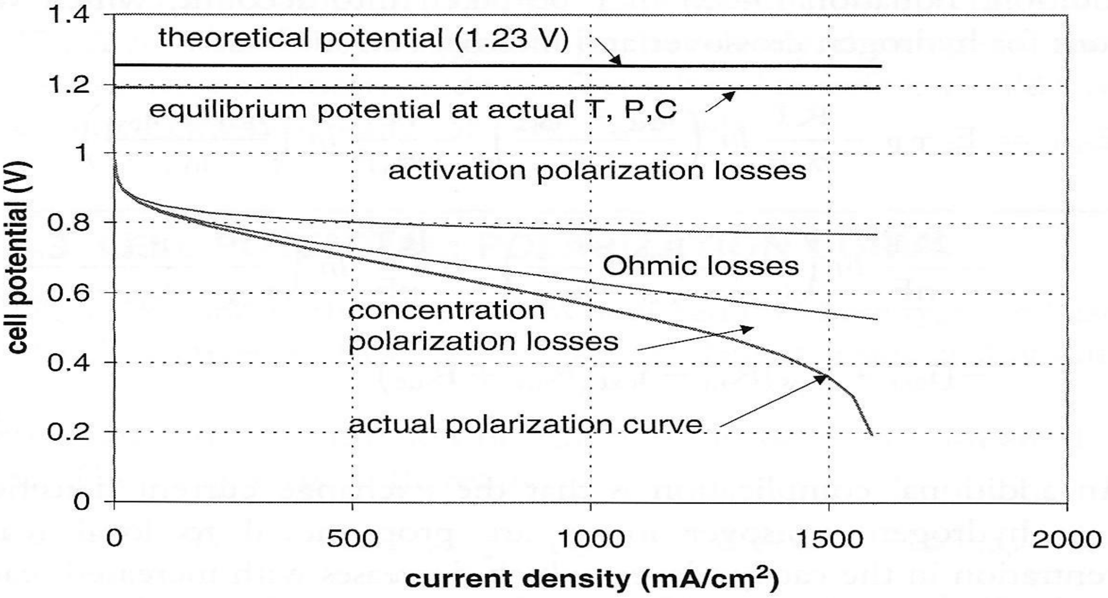

Figure 3-7: Voltage losses in a fuel cell and the resulting polarisation curve [166]

3.6.1 Activation polarisation

The activation polarisation is associated with the sluggishness of the electrode kinetics in the electrochemical reactions. The activation polarisation is high at low currents because then the reactants must first overcome the energy barrier called the activation which is needed to drive the electrochemical reactions at the reaction layer. These losses occur in both the anode and the cathode side; however, oxygen reduction in the cathode side requires much higher polarisation due to its much slower reaction rate than hydrogen oxidation[76].

The expressions for the activation polarisation are as the same as those expressed in equations (3-53) to (3-56)

The B-V expression in Eq. (3-51) and (3-52) provides the relationship between the current density and the activation polarisation in the reaction sites, thus given the current density of the cell, the solution to the equations provides the corresponding activation polarisation in the anode and cathode reaction sites.

3.6.2 Concentration polarisation

Concentration polarisations represent the voltage reduction associated with concentration difference of the reactant species through the electrodes as a result of the mass diffusion process. The concentration losses are depends on the reactant gases involved and the thickness of the layers through which the gases diffuse, as such concentration of the gas species at the reaction layer will be different from the concentration at the entrance into the cell. (Bulk flow). The expression for the concentration overpotential in the anode and cathode is given respectively by the following equations:

$$\eta_{conc,a} = \frac{RT}{nF}\ In\left(\frac{p_{H_2}^{b}p_{H_2O}^{r}}{p_{H_2O}^{b}p_{H_2}^{r}}\right) \tag{3-58}$$

$$\eta_{conc,c} = \frac{RT}{nF}\left(\frac{p_{O_2}^{b}}{p_{O_2}^{r}}\right) \tag{3-59}$$

Where the first term refers to the concentration polarisation on the anode while the second term is the expression for the cathode side, the superscripts “b” and “r” refers to the gas channel and the reaction zone respectively.

if the reaction layer is defined as a boundary interface between the electrolyte and the electrode, the relationship for the partial pressures at the is expressed as[85]:

$$p_{H_2}^{r} = p_{H_2}^{b} - \frac{iRTl_a}{2FD_{H_2-H_2O}^{eff}} \tag{3-60}$$

$$p_{H_2O}^{r} = p_{H_2O}^{b} + \frac{iRTl_a}{2FD_{H_2-H_2O}^{eff}} \tag{3-61}$$

$$p_{O_2}^{r} = p - \left(p - p_{O_2}^{b}\right)exp\left(\frac{iRTl_c}{4FD_{O_2-N_2}^{eff}}\right) \tag{3-62}$$

Zhao and Virkar[167] also defined the partial pressure relationship for a SOFC when the reaction zone is treated as a finite volume (i.e. composite electrode):

$$p_{H_2}^{r} = \frac{l_{a,2}}{D_{H_2-H_2O}^{eff(2)}}\left[\frac{p_{H_2}^{b}D_{H_2-H_2O}^{eff(2)}}{l_{a,2}} - \frac{iRTl_a}{2FD_{H_2-H_2O}^{eff(1)}} * \left(\frac{D_{H_2-H_2O}^{eff(2)}}{l_{a,2}} + \frac{D_{H_2-H_2O}^{eff(1)}}{l_{a,1}}\right)\right] \tag{3-63}$$

$$p_{H_2O}^r = \frac{l_{a,2}}{D_{H_2-H_2O}^{eff(2)}}\left[\frac{p_{H_2}^b D_{H_2-H_2O}^{eff(2)}}{l_{a,2}} + \frac{iRTl_a}{2FD_{H_2-H_2O}^{eff(1)}} * \left(\frac{D_{H_2-H_2O}^{eff(2)}}{l_{a,2}} + \frac{D_{H_2-H_2O}^{eff(1)}}{l_{a,1}}\right)\right] \tag{3-64}$$

$$p_{O_2}^r = p_{O_2}^b - \frac{\left(\frac{iRTl_c}{2FD_{O_2-N_2}^{eff}}\right)\left[\left(p - p_{O_2}^b\right)\left(l_{c(1)}D_{O_2-N_2}^{eff(1)} + l_{c(2)}D_{O_2-N_2}^{eff(2)}\right) + \left(\frac{p - p_{O_2}^b}{p}\right)\left(\frac{iRTl_c}{4F}\right)\right]}{pl_{c(1)}D_{O_2-N_2}^{eff(1)}} \tag{3-65}$$

Where l is the electrode layer thickness, D_{a-b}^{eff} is the effective diffusion coefficient of reactants a and b, and the superscripts (1) and (2) are the electrode diffusion and reaction layers respectfully

3.6.3 Ohmic polarisation

Ohmic polarisation is the voltage loss within the cell caused by the resistance to the flow of ions through the electrolyte and resistance to the flow of electrons and ions in the electrodes. Ohms law is used to describe the relationship between voltage loss and current density as:

$$\eta_{ohm} = \left(ASR_{contact} + ASR_{bulk}\right) . i \tag{3-66}$$

Where

$$ASR_{bulk} = \rho_k l_k \tag{3-67}$$

Where, ASR_{bulk} is the bulk area specific resistance, ρ_k is the resistivity of the materials s and l_i is the length of the electron or oxide ion path which is usually simplified by assuming it is the thickness of the cell component normal to the electrode-electrolyte interface.

The contact resistance is sometimes ignored in studies because there are limited theoretical models in the literature to determine the resistance. The state-of-the-art materials usually used in an SOFC are: NI-YSZ for the anode, YSZ for the electrolyte, YSZ-LSM for the cathode. However, in recent studies, researchers are trying to find other alternative materials that could improve the performance of the cell such as high chromium steel for the interconnect materials.

CHAPTER4 : Model Development

4.1 Introduction

This chapter develops a comprehensive numerical model for the simulation of SOFCs which describes the performance of the cell. The basic operating principle of a SOFC involves a complex interrelation of physical and chemical phenomenon which occurs simultaneously within several SOFC components, this phenomenon are described by governing equations that takes into considerations the unique nature of the components considered and the specific assumptions made. To successfully develop mathematical relations that describe the phenomenon occurring in each component, the SOFC mathematical model is split into a set of smaller sub models, the resulting sub models are

- Electrode diffusion model;
- Electrode reaction model;
- Electrolyte model;
- Channel model
- Interconnect model.

The physical phenomena and constitutive equations used in developing the model for each sub domain are summarised in Table (4-1).

In this chapter, the physical computational domain and the major assumptions are presented in section 4-1, then the conservation equations governing the processes in the electrode diffusion model are presented in section 4-2. The equations governing the processes in the electrode reaction model, electrolyte model, channel and interconnect model are then developed in sections 4-3, 4-4, 4-5 and 4-6 respectively. Section 4-7 defines the boundary conditions needed to develop the model, finally the thermo-physical expressions to model the transport coefficients and thermodynamic properties of the reactant gases are described in section 4.8

Table 4-1: Summary of main features of sub models for SOFC model

Sub model	Phenomena	Constitutive Equation/ States
Electrode Diffusion	Mass transport	Ideal gas
	Momentum transport	Darcy-Brinkman
	Species transport	Modified Stefan-Maxwell
	Energy transport	Fourier
	Chemical reaction	Reforming, Water-gas shift
	Charge transport	Ohms
Electrode Reaction	Mass transport	Ideal gas
	Momentum transport	Darcy-Brinkman
	Species transport	Modified Stefan-Maxwell
	Energy transport	Fourier
	Chemical reaction	Reforming, Water-gas shift
	Electrochemical reaction (Redox)	Nernst, Butler - Volmer
	Charge transport	Ohms
Electrolyte	Energy transport	Fourier
	Charge transport	Ohms
Channel	Mass transport	Ideal gas
	Momentum transport	Darcy-Brinkman
	Species transport	Stefan-Maxwell
	Energy transport	Fourier
Interconnect	Charge transport	Ohms
	Energy transport	Fourier

4.2 Computational domain and major assumptions

Figure 4-1 shows the physical domain of the SOFC consisting of nine sub-domains:

- the anode side interconnector (AI),
- the anode fuel flow channel (ACH),
- nickel gas diffusion electrode (ADL),
- nickel-yttria stabilised zirconia(Ni-YSZ) anode reaction layer (ARL),
- yttria stabilised zirconia (YSZ) electrolyte,
- yttria stabilised zirconia-lanthanum strontium manganite (YSZ-LSM) cathode reaction layer (CRL),
- lanthanum strontium manganite (LSM) cathode diffusion layer,
- the cathode air flow channel (CCH)
- Cathode side interconnector (CI).

Figure 4-1a shows a three dimensional representation of the physical domain while Figure 4-1b shows the computational domain which is a cross sectional representation of the SOFC.

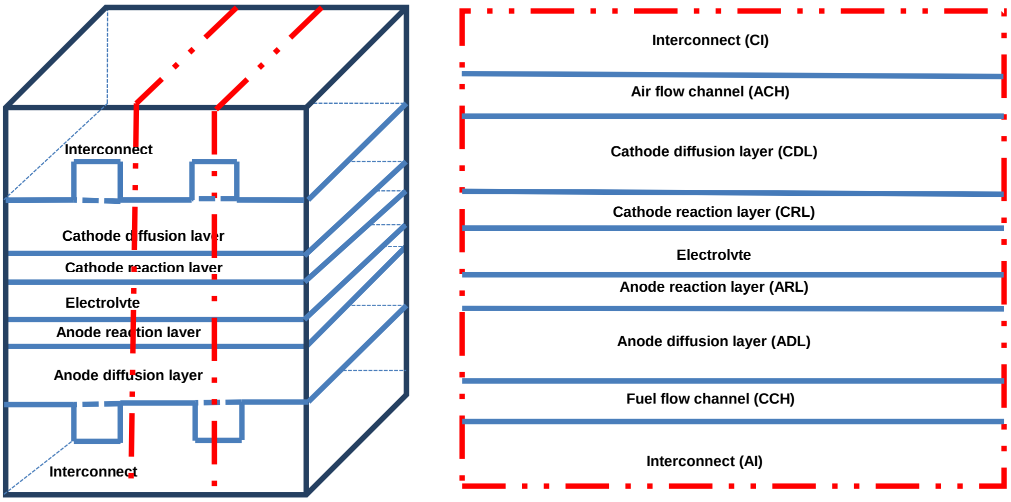

(a) **(b)**

Fig 4-1 (a) 3-D schematic illustration of a unit SOFC, (b) cross sectional view of symmetric portion representing the computational domain

4.2.1 Model assumptions

- steady state conditions is assumed in the model simulations
- The electrochemical reactions are assumed to take place only in the electrode reaction layers since the model considers them as distinct regions from the diffusion layers [35, 113]
- Convective and diffusive flux are used in modelling species transport in the channels
- Diffusive flux is used in modelling species transport in both diffusion and reaction layers[85]
- The gas mixtures are treated as ideal
- The electrolyte is treated as a dense non-porous solid
- Only H_2 oxidation is considered in the electrochemical reactions[87].

4.3 Electrode diffusion model

The electrode diffusion sub model describes the flow of reactants and products from the channels to the electrode reaction layer where the electrochemical reactions take place. This model also describes the chemical reaction of hydrocarbon reforming and the resultant water-shift gas reaction that occurs in the layer. The processes to be modelled in this layer are the transport of species to reaction layer along with the chemical reactions (internal reforming and water-shift gas). Also, transport of energy due to heat conduction, convection and heat generated/consumed during the electrochemical and chemical reactions need to be modelled. The conservation equations for the processes in the diffusion layers are the conservation of mass, both in terms of the total mass and species mass, conservation of energy in terms of the sensible enthalpy, the momentum conservation equation or Newton's second law and conservation of charge. The following section describes these phenomena in more details.

4.3.1 Conservation of mass

Consider a control volume element $(dxdydz)$ as shown in Figure 4-2. The mass balance within the volume element for species i can be described by the following relation:

$$\begin{Bmatrix} Rate\ of\ mass \\ accumulation \\ or\ depletion \end{Bmatrix} = \begin{Bmatrix} rate\ of \\ mass\ inlet \end{Bmatrix} - \begin{Bmatrix} rate\ of \\ mass\ outlet \end{Bmatrix} + \begin{Bmatrix} rate\ of production \\ or\ consumption \\ of\ species\ i \end{Bmatrix} \quad (4\text{-}1)$$

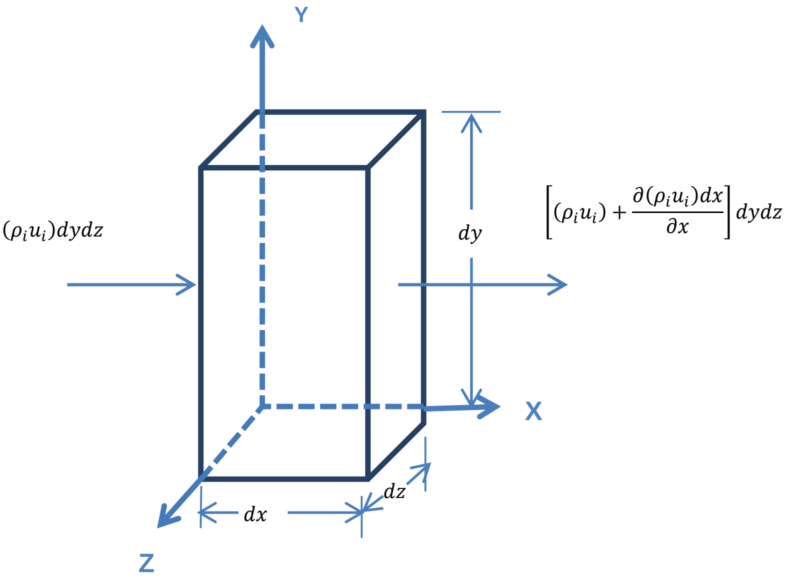

Figure 4-2: Control volume showing the mass flux of species i

The conservation statement for the three mutually perpendicular surfaces $x, y\ and\ z$ can be expressed mathematically as

$$\begin{aligned}\frac{\partial(\rho_i dxdydz)}{\partial t} = (\rho_i u_i dydz) - \left(\rho_i u_i + \frac{\partial(\rho_i u_i)dx}{\partial x}\right)dydx \\ + (\rho_i v_i dxdz) - \left(\rho_i v_i + \frac{\partial(\rho_i v_i)dy}{\partial y}\right)dxdx \\ + (\rho_i w_i dxdy) - \left(\rho_i w_i + \frac{\partial(\rho_i w_i)dz}{\partial z}\right)dxdy + r_i\end{aligned} \tag{4-2}$$

In compact form, Equation (4-2) can be written as

$$\frac{\partial(\rho_i)}{\partial t} + \nabla.(\rho_i u) = r_i \tag{4-3}$$

Invoking the steady state assumption Equation (4-3) can be written as:

$$\nabla.(\rho_i u) = r_i \tag{4-4}$$

Where $\rho_i$the density of the species is i , u is the bulk motion velocity and r_i is the volumetric mass source or sink. The ideal gas law is used to define the fluid density ρ_i due to the high operating temperatures of SOFCs:

$$\rho_i = \frac{pW}{RT} \tag{4-5}$$

Where p, W and T are the pressure, mixture molecular weight and the temperature respectively, while R is the universal gas constant.

4.3.2 Conservation of species

The mass balance of the species in the electrode backing layer can be obtained by applying the mass conservation law on each species to the control volume described in Figure (4-2). The species balance can thus be described by the following equation

$$\begin{Bmatrix} Rate\ of \\ accumulation \\ or\ depletion\ of \\ species\ i \end{Bmatrix} = \begin{Bmatrix} Inlet\ rate \\ of\ species\ i \end{Bmatrix} - \begin{Bmatrix} Outlet\ rate \\ of\ species\ i \end{Bmatrix} + \begin{Bmatrix} rate\ of production \\ or\ consumption \\ of\ species\ i \end{Bmatrix} \tag{4-6}$$

Using the mathematical expression developed in Equation (4-2) and invoking the steady state assumption, the species mass balance can be expressed in compact form as

$$\nabla.(\rho_i u \nabla x_i) + \nabla.j_i = r_i \tag{4-7}$$

Where x_i is the mole fraction of species i, j_i is the mass diffusive flux vector of species i and r_i is the source or sink term.

Since the diffusion layer is porous, the porosity has to be accounted for in the species balance, thus Equation (4-7) can be re-written as

$$\varepsilon\nabla.(\rho_i u \nabla x_i) + \nabla.j_i = r_i \tag{4-8}$$

Where ε is the porosity of the electrode diffusion layer.

Equation (4-8) is called the species continuity equation, the first term on the left represents the convective fluxes, the second term represents the diffusive fluxes while the last term is the flux due to the chemical reaction. The convective flux is assumed negligible relative to the diffusive flux in the electrode layer [71], thus the species continuity equation reduces to

$$\nabla.j_i = r_i \tag{4-9}$$

The mass diffusive flux vector can be written explicitly as[168]:

$$j_i = j^c + j^p + j^g + j^T \tag{4-10}$$

Where j^c represents ordinary diffusion term, j^p is the pressure diffusion term, j^g is the body force term and j^T the thermal diffusion term.

The mass diffusive flux j_i is dependent on conditions such as temperature, pressure, reactant concentration and microstructural properties of the material under consideration [110, 169, 170]. There are three major models for obtaining the diffusional flux, these are: Ficks law, Stefan Maxwell equation or Dusty-gas model. Although Ficks laws and the Dusty-gas equations are still been used[79, 132, 169, 170], the Stefan-Maxwell model is still the most widely employed[35, 93, 128, 171] and it gives the most general and convenient approach for describing multicomponent mass transport[172], furthermore, the Stefan-Maxwell model can be modified to include the Knudsen diffusion term which accounts for the effect of collision between the gas molecules and the pore wall.

Modified Stefan-Maxwell equations for multicomponent systems

The Stefan-Maxwell model for a multicomponent system having n species is given as[70]:

$$c_g \nabla x_i = \sum_{j=1, j\neq i}^{n} \frac{x_j j_i - x_i j_j}{D_{ij}} \tag{4-11}$$

Where c_g is the concentration of the gas mixture, j_i is the diffusive flux of i and D_{ij} is the binary diffusion coefficient. For an n component system, the diffusive flux of each species depends on the concentration gradient of the remaining $(n-1)$ species, thus the diffusive flux consistency condition imposed to close the system is expressed as

$$j_n = -\sum_{i=1}^{n-1} j_i \tag{4-12}$$

The ordinary diffusion coefficient for a species n in a multicomponent gas mixture is given by [173, 174]

$$D_{i,m} = \frac{1 - x_i}{\sum_{j\neq i}\left(\frac{x_j}{D_{ij}}\right)} \tag{4-13}$$

Curtis and Bird[175] studied diffusive flux in multicomponent mixtures and they propose the mass flux vector as

$$j_i = -D_i^T \nabla In\, T - \rho_i \sum_{j=1}^{n} D_{ij}\, d_j \tag{4-14}$$

Where D_i^T is the thermal diffusion coefficient, D_{ij} is the diffusion coefficient matrix and d_j is the diffusion driving force expressed as:

$$d_j = \nabla x_j + \left(x_j - w_j\right)\frac{\nabla p}{p} \tag{4-15}$$

The relationship between the mole fraction x_j and the mass fraction w_j by given by the following equations:

$$x_j = \frac{w_j}{M_j} M_n \qquad M_n = \sum\nolimits_i \left(\frac{w_i}{M_i}\right)^{-1} \tag{4-16}$$

The diffusion model for SOFC electrodes takes into consideration only ordinary diffusion j^c which is due to the concentration gradient, as all the other diffusion processes j^p, j^g, j^T are assumed negligible compared to that of ordinary diffusion, however, the ordinary diffusion either for binary systems or multicomponent systems occurs simultaneously with the Knudsen diffusion[168]. Knudsen diffusion term becomes significant when the frequency of the collision between the pore wall and the gas molecules increases; this only happen when the mean free path of the gas molecules is larger than that of the pore sizes. Hence, when the Knudsen diffusion effect is included, Equation (4-11) becomes

$$c_g \nabla x_i = \sum_{j=1, j\neq i}^{n} \frac{x_j j_i - x_i j_j}{D_{ij}} + \frac{j_i}{D_{Kn,ij}} \tag{4-17}$$

Where D_{ij} is the ordinary diffusion coefficient and $D_{Kn,ij}$ is the Knudsen diffusion coefficient

Both diffusion term can be combined and corrected with some geometric factors that accounts for both the porosity and the tortuosity of the medium [106, 129] to give an effective diffusion coefficient expressed as:

$$D_{ij}^{eff} = \frac{\varepsilon}{\tau}\left(\frac{1}{D_{ij}} + \frac{1}{D_{Kn,ij}}\right)^{-1} \tag{4-18}$$

Where ε and τ are the porosity and tortuosity of the porous media respectively, they are defined as [176, 177]:

$$\varepsilon = 1 - \frac{volume\ occupied\ by\ solid}{total\ volume} \tag{4-19}$$

$$\tau = \frac{actual\ path\ lenght}{point - to - point\ lenght} \tag{4-10}$$

The ordinary diffusion coefficients are modelled by the empirical correlation developed by Fuller et al, and is given as[178]:

$$D_{ij} = \frac{0.001434T^{1.75}}{pM_{ij}^{1/2}\left[V_i^{1/3} + V_j^{1/3}\right]^2} \tag{4-11}$$

Where

$$M_{ij} = 2\left[(1/M_i) + \left(1/M_j\right)\right]^{-1} \tag{4-12}$$

Where D_{ij} is in $\left({}^{m^2}/_{s}\right)$, T is temperature in K, p is pressure in bar, M_i and M_j is the molar mass in $\left({}^{kg}/_{kmol}\right)$ and V_i and V_j are the Fuller et al. diffusion volume.

The Knudsen diffusion coefficients are defined by the kinetic theory of gases as [179]:

$$D_{Kn,ij} = \frac{2d_{pore}}{3}\sqrt{\frac{2RT}{\pi M_{ij}}} \tag{4-13}$$

Where d_{pore} is the mean pore diameter and R is the universal gas constant in $(J\ mole^{-1}K^{-1})$.

The pore diameter depends on the particle diameter and is expressed by the equation[75]:

$$d_{pore} = \frac{2}{3}\frac{\varepsilon}{1-\varepsilon}d_p \tag{4-24}$$

The modified Stefan-Maxwell equation which takes into account the Knudsen diffusion term can then be expressed in the original form of the Stefan-Maxwell equation given in Equation (4-11) as:

$$c_{gas}\nabla x_i = \sum_{j=1, j\neq i}^{n} \frac{x_j j_i - x_i j_j}{D_{ij}^{eff}} \tag{4-25}$$

Formulation of the modified Stefan-Maxwell equations

It is more convenient to express Equation (4-25) in an $(n-1)$ matrix form[180] as it will be otherwise difficult to obtain a numerical solution for the implicit relationship between the mole fraction and molar fluxes.

Recalling Equation (4-12) since only $(n-1)$ term is independent

$$j_n = -\sum_{i=1}^{n-1} j_i$$

Equation (4-25) can then be written as:

$$c_g\nabla x_i = -F_{ii}j_i - \sum_{j=1, j\neq 1}^{n-1} F_{ij}j_j \tag{4-26}$$

Where F_{ii} and F_{ij} are defined by

$$F_{ii} = \frac{x_i}{D_{in}^{eff}} + \sum_{k=1, k\neq 1}^{n} \frac{x_k}{D_{ik}^{eff}} \tag{4-27}$$

$$F_{ij} = -x_i\left(\frac{1}{D_{ij}^{eff}} - \frac{1}{D_{in}^{eff}}\right) \tag{4-28}$$

Equation (4-25) can be expressed in $(n-1)$ dimensional matrix form as:

$$c_g(\nabla x) = -[F](j) \tag{4-29}$$

Where $[F]$ is a square matrix of order $(n-1)$

$$\begin{bmatrix} F_{11} & F_{12} & \cdots & F_{1,n-1} \\ F_{21} & F_{22} & \cdots & F_{2,n-1} \\ \vdots & \vdots & \cdots & \vdots \\ F_{n-1,1} & F_{n-1,2} & \cdots & F_{3,n-1} \end{bmatrix} \tag{4-30}$$

With elements given in Equations (4-26) and (4-27). The column matrix (j) is given as

$$\begin{pmatrix} j_1 \\ j_2 \\ \vdots \\ j_{n-1} \end{pmatrix} \tag{4-31}$$

And (∇x) is a column matrix defined as:

$$\begin{pmatrix} \nabla x_1 \\ \nabla x \\ \vdots \\ \nabla x_{n-1} \end{pmatrix} \tag{4-32}$$

If we multiply Equation (4-28) with the inverse of $[F]$, we obtain

$$c_g[F]^{-1}(\nabla x) = -[F]^{-1}[F](j) \tag{4-33}$$

This simplifies to:

$$(j) = -c_g[F]^{-1}(\nabla x) \tag{4-34}$$

Since $[F]^{-1}[F] = 1$

Chemical reaction kinetics

The SOFCs inlet fluid is usually made up of all or some of the following species:

$H_2, H_2O, CO, C0_2$, CH_4 in the anode stream
O_2, N_2, in the cathode stream

The source term r_i in Equation (4-7) represents the production/consumption rate of the species as a result of the chemical reaction taking place in the diffusion layer, since no reaction occurs in the cathode stream, therefore, its source term r_i is zero. If the reactant gas in the anode stream is a hydrocarbon such as natural gas, rather than hydrogen, reforming reaction and water gas shift reactions would take place in the anode diffusion layer. These reactions (for methane) are given as follows:

Methane steam reforming reaction

$$CH_4 + H_20 \leftrightarrow 3H_2 + CO \tag{4-35}$$

Water gas shift reaction

$$CO + H_20 \leftrightarrow H_2 + CO_2 \tag{4-36}$$

The reaction rates for the above reactions are given as [68, 87, 150, 151]

$$R_r = k_{rf} p_{CH_4} p_{H_2O} - k_{rb} \left(p_{H_2}\right)^3 p_{CO} \tag{4-37}$$

$$R_s = k_{sf} p_{CO} p_{H_2O} - k_{sb} p_{H_2} p_{CO_2} \tag{4-38}$$

Where R_r and R_s are the methane reforming reaction rate and water-gas shift reaction rate, k_{rf} and k_{rb} are the forward and backward reaction rate constants for the reforming reaction while k_{sf} and k_{sb} are the forward and backward reaction rate constants for the water-shift gas reaction respectively.

Equation (4-37) and (4-38) can be expressed in terms of mole fraction as

$$R_r = p^2 \left[k_{rf} x_{CH_4} x_{H_2O} - p^2 k_{rb} \left(x_{H_2}\right)^3 x_{CO}\right] \tag{4-39}$$

$$R_s = p^2 \left[k_{sf} x_{CO} x_{H_2O} - k_{sb} x_{H_2} x_{CO_2}\right] \tag{4-40}$$

Where p is the total pressure.

The reverse reaction rate constant k_{rb} and k_{sb} can be determined from the equilibrium constants for both reactions, it is defined as a function of temperature and obtained using the following empirical relations [35, 52]

$$k_{rq} = \frac{k_{rf}}{k_{rb}} = 1.0267 \times 10^{10} \times exp(-0.2513\zeta^4 + 0.3665\zeta^3 + 0.5810\zeta^2 - 27.134\zeta + 3.2770)[Pa^2] \quad (4\text{-}41)$$

$$k_{sq} = \frac{k_{sf}}{k_{sb}} = exp(-0.2935\zeta^3 + 0.6351\zeta^2 - 4.1788\zeta + 0.3169)[Pa^2] \quad (4\text{-}42)$$

where $\zeta = \frac{1000}{T(K)} - 1$ (4-43)

The forward reaction rates for the methane reforming and water-shift gas reactions are given as

$$k_{rf} = 2395exp\left(-\frac{231266}{RT}\right)[mol\, m^{-3}Pa^{-2}s^{-1}] \quad (4\text{-}44)$$

$$k_{sf} = 0.0171exp\left(-\frac{103191}{RT}\right)[mol\, m^{-3}Pa^{-2}s^{-1}] \quad (4\text{-}45)$$

The source term r_i for each species in the anode diffusion layer is calculated as follows:

$$r_{CH_4} = -M_{CH_4}R_r \quad (4\text{-}46)$$

$$r_{H_2} = M_{H_2}(3R_r + R_s) \quad (4\text{-}47)$$

$$r_{CO} = M_{CO}(R_r - R_s) \quad (4\text{-}48)$$

$$r_{H_2O} = M_{H_2O}(R_r + R_s) \quad (4\text{-}49)$$

$$r_{CO_2} = M_{CO_2}R_S \quad (4\text{-}50)$$

4.3.3 Conservation of momentum

The momentum balance within a control volume $(dxdydz)$ shown in Figure 4-3 can be described by the following equation

$$\begin{Bmatrix} \text{Rate of momentum} \\ \text{accumulation} \\ \text{or depletion of} \\ \text{species } i \end{Bmatrix} = \begin{Bmatrix} \text{rate of} \\ \text{species } i \\ \text{momentum} \\ \text{inlet} \end{Bmatrix} - \begin{Bmatrix} \text{rate of} \\ \text{species } i \\ \text{momentum} \\ \text{outlet} \end{Bmatrix} + \begin{Bmatrix} \text{sum of forces} \\ \text{acting on} \\ \text{system} \end{Bmatrix} \tag{4-51}$$

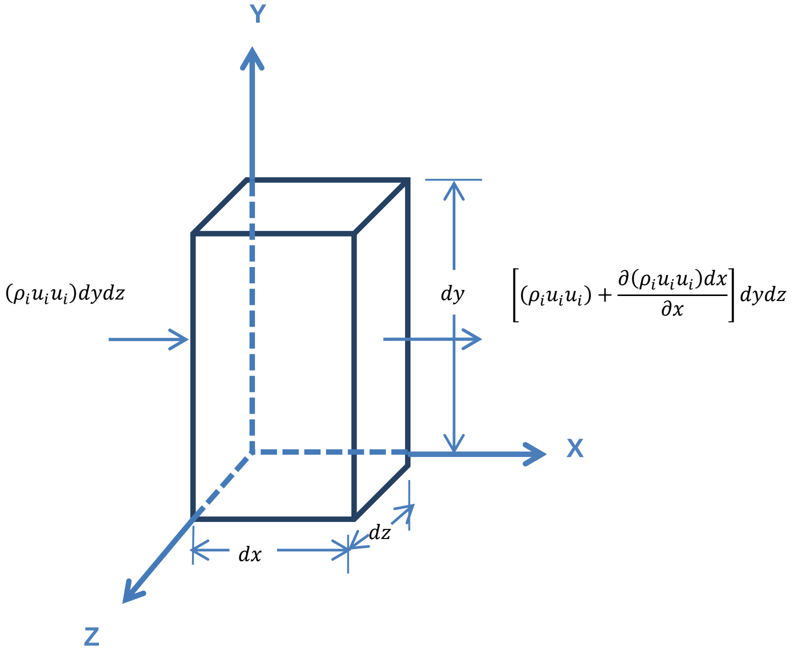

Fig 4-3: Control volume element showing the momentum flux of species i

The above conservation statement for the three mutually perpendicular surfaces $x, y \text{ and } z$ can be expressed mathematically as

$$\begin{aligned} &\frac{\partial(\rho_i u_i dxdydz)}{\varepsilon \partial t} \\ &= \left(\frac{\rho_i}{\varepsilon} u_i u_i dydz\right) - \left(\frac{\rho_i}{\varepsilon} u_i u_i + \frac{\partial(\rho_i u_i u_i)dx}{\varepsilon \partial x}\right) dydx \\ &+ \left(\frac{\rho_i}{\varepsilon} v_i v_i dxdz\right) - \left(\frac{\rho_i}{\varepsilon} v_i v_i + \frac{\partial(\rho_i v_i v_i)dy}{\varepsilon \partial y}\right) dxdx \\ &+ \left(\frac{\rho_i}{\varepsilon} w_i w_i dxdy\right) - \left(\frac{\rho_i}{\varepsilon} w_i w_i + \frac{\partial(\rho_i w_i w_i)dz}{\varepsilon \partial z}\right) dxdy \\ &+ \rho \vec{f} + \nabla . \vec{\tau} \end{aligned} \tag{4-52}$$

Where $\nabla.\vec{\tau}$ is the shear stress tensor and $\vec{f}$ are the body forces which includes gravity, electromagnetic and inertia forces.

Equation (4-52) can be written in compact form after invoking the steady state condition as

$$\nabla.\left(\frac{\rho}{\varepsilon}uu\right) = \rho\vec{f} + \nabla.\vec{\tau} \tag{4-53}$$

The Darcy-Brinkman equation[76] is used to describe the momentum balance in the porous electrode diffusion layers by including an additional term to the Darcy equation to account for the viscous transport in the momentum balance, the Darcy-Brinkman equation is shown as

$$\nabla.\left(\frac{\rho}{\varepsilon}uu\right) = -u\frac{\mu}{K} + \rho\vec{f} + \nabla.\vec{\tau} \tag{4-54}$$

Where μ is the fluid viscosity and K is the permeability of the electrode diffusion layer

In SOFC, both oxidant and fuel gases obey Newton's law of viscosity, where the shear force is varies with the negative of the local velocity gradient, thus the shear stress tensor may be written as[168]:

$$\vec{\tau} = \frac{\mu}{\varepsilon}[\nabla\vec{u} + (\nabla\vec{u})^T] - \left[p + \left(\mu u - \frac{2}{3\varepsilon}\mu\right)(\nabla.\vec{u})\right]\vec{I} \tag{4-55}$$

Where ε is the porosity, μu is the coefficient of bulk velocity, μ is the dynamic velocity of the fluid and $\vec{I}$ is the identity matrix, $\begin{bmatrix}1 & 0 & 0\\ 0 & 1 & 0\\ 0 & 0 & 1\end{bmatrix}$. However, bulk viscosity is known to be negligible under typical SOFC conditions such as low flow rates and laminar flow i.e. $\mu u \approx 0$ Thus Equation (4-55) reduces to

$$\vec{\tau} = \frac{\mu}{\varepsilon}[\nabla\vec{u} + (\nabla\vec{u})^T] - \left[p + \left(\frac{2}{3\varepsilon}\mu\right)(\nabla.\vec{u})\right]\vec{I} \tag{4-56}$$

The momentum conservation equation for a fluid flowing though the electrode diffusion layer may be expressed from Equation (4-55) and (4.56) as

$$\nabla.\left(\frac{\rho}{\varepsilon^2}uu\right) = -u\frac{\mu}{K} + \rho\vec{f} + \nabla.\left(\frac{\mu}{\varepsilon}[\nabla\vec{u} + (\nabla\vec{u})^T] - \left[p + \left(\frac{2}{3\varepsilon}\mu\right)(\nabla.\vec{u})\right]\vec{I}\right) \tag{4.57}$$

The flow velocities u expressed in Equations (4-52) through to Equation (4-57) are the averaged velocity; this allows the velocity field to be described as a continuous field across the pores and the solid matrix by which the flow can be described by the same velocity.

4.3.4 Conservation of energy.

The conservation of energy for a fluid contained in the control volume $(dxdydz)$ of Figures (4-4) can be written as follow:

$$\left\{\begin{matrix} rate\ of \\ internal\ and \\ kinetic\ energy \\ accumulation \end{matrix}\right\} = \left\{\begin{matrix} net\ rate\ of \\ internal\ and \\ kinetic\ energy \\ by \\ convection \end{matrix}\right\} - \left\{\begin{matrix} net\ rate\ of \\ internal\ and \\ kinetic\ energy \\ by \\ conduction \end{matrix}\right\} + \left\{\begin{matrix} net\ rate \\ of\ work\ done \\ by\ system \\ on \\ surroundings \end{matrix}\right\} \tag{4-58}$$

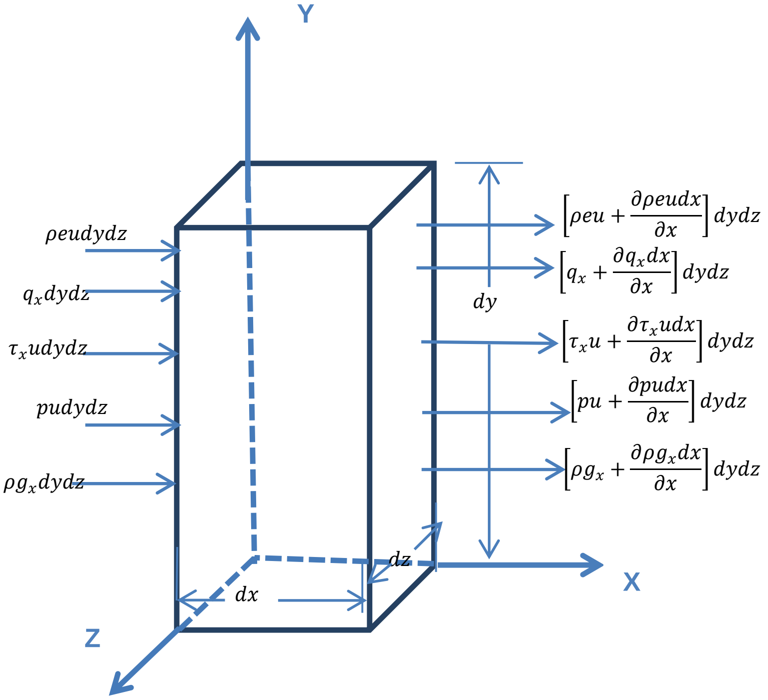

Fig 4-4: Control volume element showing the Energy fluxes in the x direction

The above conservation statement for the three mutually perpendicular surfaces $x, y\ and\ z$ can be expressed mathematically as

$$
\begin{aligned}
\frac{\partial(\rho edxdydz)}{\partial t} = & \left(\frac{\partial(\rho eu)}{\partial x}dydz\right) - \left(\frac{\partial(\rho ev)}{\partial y}dxdz\right) - \left(\frac{\partial(\rho ew)}{\partial z}dydz\right) \\
& - \left(\frac{\partial q_x}{\partial x}dxdydz\right) - \left(\frac{\partial q_y}{\partial y}dxdydz\right) - \left(\frac{\partial q_z}{\partial z}dxdydz\right) \\
& - \left(\frac{\partial \tau_x u}{\partial x}dxdydz\right) - \left(\frac{\partial \tau_x v}{\partial y}dxdydz\right) - \left(\frac{\partial \tau_x w}{\partial z}dxdydz\right) \\
& - \left(\frac{\partial(pu)}{\partial x}dxdydz\right) - \left(\frac{\partial(pv)}{\partial y}dxdydz\right) \\
& - \left(\frac{\partial(pw)}{\partial z}dxdydz\right) - \rho ug_x dxdydz - \rho vg_y dxdydz \\
& - \rho wg_z dxdydz + r_e
\end{aligned} \tag{4-59}
$$

Where r_e is the heat source term, q is the heat flux and e is the specific energy which is the sum of the kinetic energy $\left(\frac{1}{2}u^2\right)$ associated with the fluid motion and the internal energy (U) related to the random internal and translational motion of the molecules

$$
e = \left(\frac{1}{2}u^2 + U\right) \tag{4-60}
$$

Equation (4-59) can be written in compact form after invoking the steady state assumption as

$$
\left[\rho u.\nabla\left(\frac{1}{2}u^2 + U\right)\right] = -\nabla.q - \nabla.(\tau.u) + \nabla.(pu) + \nabla.(\rho ug) + r_e \tag{4-61}
$$

The term on the left hand side of Equation (4-61) is the rate of energy input per unit volume by convection, while on the right hand side, the first term is the rate of energy input by conduction; the second term is the rate of work done on the fluid by viscous forces; the third term is the rate of work done on the fluid by pressure forces; the fourth term is the rate of work done on fluid by gravitational forces and the last term is the heat source due to the heat generated/consumed as a due to the joule heating effect and from chemical reactions.

Neglecting the kinetic energy, gravitational potential energy and the work done by viscous stresses as their contribution to the energy balance in a SOFC electrode is negligible, Equation (4-61) reduces to

$$\rho \mathrm{u}.\nabla U = -\nabla.q - \nabla.(pu) + r_e \tag{4-62}$$

According to Bird and Stewart[168], the heat flux q for a multicomponent fluid is given as:

$$q = q^c + q^d + q^x \tag{4-63}$$

Where $q^c,\ q^d,\ q^x$ are the heat fluxes by conduction, heat flux by each diffusing species and the heat flux related to the concentration driving force usually described as the diffusion-thermo effect or Dufour effect respectively. The Dufour effect is usually quite small thus can be ignored. Equation (4-63) now reduces to:

$$q = q^c + q^d \tag{4-64}$$

According to Fourier's law, the heat flux due to conduction for the electrode diffusion layer can be expressed in terms of temperature gradient as

$$q^c = -k_{dl}^{eff}\nabla T \tag{4-65}$$

This describes the molecular transport of heat by conduction in an isotropic media, Expanding Equation (4-64) for a multicomponent mixture, the heat flux becomes

$$q = -k_{dl}^{eff}\nabla T + \sum_{i=1}^{n} h_i\, j_i \tag{4-66}$$

Where k_{dl}^{eff} is the effective thermal conductivity in the layer, h_i is the specific absolute enthalpy of species i and j_i is the species molar diffusive flux. Substituting Equation (4-65) in Equation (4-62)

$$\rho \mathrm{u}.\nabla U + \nabla.(pu) = -\nabla.\left[-k_{bl}^{eff}\nabla T + \sum_{i=1}^{n} h_i\, j_i\right] + r_e \tag{4-67}$$

Replacing $\nabla.(pu)$ with $\rho u\ \nabla.\left(\frac{p}{\rho}\right)$, Equation (4-67) becomes

$$\mathrm{\rho u}.\nabla\left(U+\left(\frac{p}{\rho}\right)\right) = -\nabla.\left[k_{bl}^{eff}\nabla T+\sum_{i=1}^{n}h_i\,j_i\right]+\ r_e \qquad (4\text{-}68)$$

From basic thermodynamic relations, enthalpy $H = U + \left(\frac{p}{\rho}\right)$, the above equation thus becomes:

$$\mathrm{\rho u}.\nabla H\ =\ -\nabla.\left[k_{bl}^{eff}\nabla T+\sum_{i=1}^{n}h_i\,j_i\right]+\ r_e \qquad (4\text{-}69)$$

Substituting $H = \sum_{i=1}^{n} x_i h_i$ into the equation

$$\mathrm{\rho u}.\nabla\left(\sum_{i=1}^{n}x_i h_i\right)\ =\ -\nabla.\left[k_{bl}^{eff}\nabla T+\sum_{i=1}^{n}h_i\,j_i\right]+\ r_e \qquad (4\text{-}70)$$

The term on the left hand side can be further expressed as

$$\mathrm{\rho u}.\nabla\left(\sum_{i=1}^{n}x_i h_i\right)=\ \mathrm{\rho u}.\left(\sum_{i=1}^{n}x_i\nabla h_i\right)+\ \mathrm{\rho u}.\left(\sum_{i=1}^{n}h_i\nabla x_i\right) \qquad (4\text{-}71)$$

Recalling the species mass balance equation from Equation (4-7)

$$\nabla.(\rho u\nabla x_i) =\ r_i -\ \nabla.j_i \qquad (4\text{-}72)$$

Using the thermodynamic relation $(\nabla h_i = c_{pi}\nabla T)$ and inserting Equation (4-72) into Equation (4-71)

$$\mathrm{\rho u}.\nabla\left(\sum_{i=1}^{n}x_i h_i\right)=\ \mathrm{\rho}c_p\mathrm{u}.\nabla\mathrm{T}+\ \left(\sum_{i=1}^{n}h_i[r_i-\ \nabla.j_i]\right) \qquad (4\text{-}73)$$

Replacing the term on the left of the energy equation (4-70) with the above equation

$$\rho c_p \mathrm{u}.\nabla \mathrm{T} + \sum_{i=1}^{n} h_i r_i - \sum_{i=1}^{n} h_i \nabla . j_i = -\nabla.\left(k_{dl}^{eff} \nabla T\right) - \nabla.\sum_{i=1}^{n} h_i\, j_i + r_e \tag{4-74}$$

The second term on the right hand side of the above equation can be written as

$$\nabla.\sum_{i=1}^{n} h_i\, j_i = \sum_{i=1}^{n} h_i \nabla . j_i + \sum_{i=1}^{n} j_i \nabla . h_i \tag{4-75}$$

Substitute Equation (4-75) into Equation (4-74) and using$\left(\nabla h_i = c_{pi} \nabla T\right)$, the energy equation becomes

$$\rho c_p \mathrm{u}.\nabla \mathrm{T} + \sum^{n} h_i r_i = -\nabla.\left(k_{dl}^{eff} \nabla T\right) - \sum^{n} c_{pi} j_i \nabla T + r_e \tag{4-76}$$

Recalling the assumption that the diffusive flux is the primary mode of species transport in the diffusion layers, thus the convective flux is negligible, the energy equation becomes

$$\sum_{i=1}^{n} c_{pi} j_i \nabla T = -\nabla.\left(k_{bl}^{eff} \nabla T\right) + r_e - \sum_{i=1}^{n} h_i r_i \tag{4-77}$$

In terms of the species continuity relation, the above energy equation can be expressed as

$$\sum^{n} c_{pi} \rho_i u_i \nabla T = -\nabla.\left(k_{dl}^{eff} \nabla T\right) + r_e - \sum^{n} h_i r_i \tag{4-78}$$

Where c_{pi} is the specific heat capacity of species i at constant pressure, ρ_i is the density of species i, $\sum_{i=1}^{n} h_i r_i$ is the heat generated or consumed due to the chemical reaction taking place on the diffusion layer and r_e is the energy source term which is the heat generated due to the ohmic resistance when electronic current passes through the diffusion layer called joule heating and is defined as

$$r_e = \sigma_{dl}^{eff} \nabla^2 \phi_s \tag{4-79}$$

Where σ_{dl}^{eff} is the electronic conductivity, ϕ_s is the electronic potential.

The effective thermal conductivity of the diffusion layer k_{bl}^{eff} is defined as[76]

$$k_{bl}^{eff} = \varepsilon k_f + (1 - \varepsilon) k_s \tag{4-80}$$

Where k_f is the thermal conductivity of the fluid mixture in the layer and k_s is the thermal conductivity of the solid phase of the diffusion layer.

4.3.5 Conservation of electronic charge.

Electronic charge is produced when electrons migrate through the solid phase of the electrode diffusion layer, the conservation statement for electric charge in the control volume$(dxdydz)$ shown in Figure (4-5) can be written as:

$$\left\{\begin{matrix} rate\ of \\ accumulation \\ of\ electric \\ charge \end{matrix}\right\} = \left\{\begin{matrix} Inlet\ rate \\ of\ current \end{matrix}\right\} - \left\{\begin{matrix} Outlet\ rate \\ of\ current \end{matrix}\right\} + \left\{\begin{matrix} rate\ of production \\ or\ consumption \\ of\ electric \\ charge \end{matrix}\right\} \tag{4-81}$$

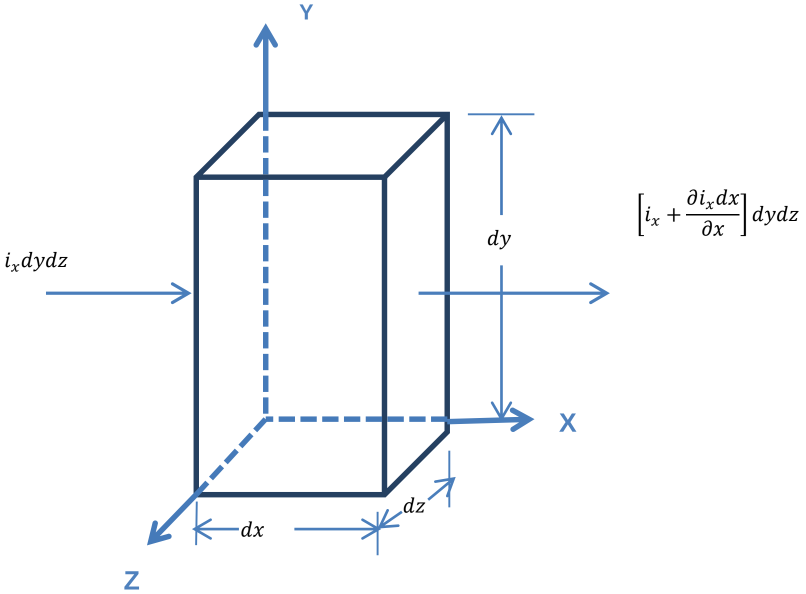

Fig 4-5: Control volume element showing the current density in the x direction

The conservation statement as applied to three mutually perpendicular surfaces $x, y\ and\ z$ can be expressed mathematically as

$$\begin{aligned}\frac{\partial(idxdydx)}{\partial t} = {} & (i_x dydz) - \left(i_x + \frac{\partial i_x}{\partial x}\right) dydz \\ & + \left(i_y dxdz\right) - \left(i_y + \frac{\partial i_y}{\partial y}\right) dxdz \\ & + (i_z dxdy) - \left(i_z + \frac{\partial i_z}{\partial z}\right) dxdy \\ & + r_c dxdydz \end{aligned} \tag{4-82}$$

Equation (4-81) simplifies to

$$\frac{\partial i}{\partial t} = -\frac{\partial i_x}{\partial x} - \frac{\partial i_y}{\partial v} - \frac{\partial i_z}{\partial z} + r_c \tag{4-83}$$

Recalling the steady state assumption, the above equation can be expressed in compact form as

$$\nabla.(i_e) = r_c \tag{4-84}$$

Where i_e is the electronic current density and r_c is the source term, but since there is no production or consumption of electric charge in the diffusion layer, Equation (4-84) becomes

$$\nabla.(i_e) = 0 \tag{4-85}$$

The current density vector i_e is related to the electric field V and conductivity σ by Ohms law as:

$$i_e = \sigma_{s,dl}^{eff} V \tag{4-86}$$

Where the voltage V equals the negative gradient of the potential at a specific point within the field

$$V = -\nabla \phi_s \tag{4-87}$$

Substituting Equation (4-86) and (4-87) into Equation (4-85) gives

$$\nabla.\left(-\sigma_{s,dl}^{eff} \nabla \phi_s\right) = 0 \tag{4-88}$$

Where σ_{dl}^{eff} is the effective electronic conductivity in the diffusion layer defined as

$$\sigma_{s,dl}^{eff} = \frac{(1-\varepsilon)}{\tau}\sigma_{dl} \tag{4-89}$$

Where ε and τ are the porosity and tortuosity of the porous diffusion layer respectively and σ_{dl} is the electronic conductivity of the diffusion layer material.

4.4 Electrode reaction model

The electrode reaction layers are relatively thin regions in the order of 20µm where the electrochemical reaction occurs, they are treated as composite electrodes as they are made up of three phases: electron conducting phase for the transport electrons, ionic conducting phase for the transport of ions and pores through which the reactant gases diffuse[81], in addition to hosting the electrochemical reactions, they are also responsible for the transport of reactant gases and their products to and from the electrolyte to the diffusion layer.

Various authors[56, 59, 66, 78, 181-183] have investigated different approaches with different levels of complexity to modelling the electrode reaction layer, most common among these models are the thin film models, random resistor network models, macroscopic porous electrode models and the random packing sphere models.

The thin film models [54, 183, 184] for composite electrodes are based on the theory that all the co-existing phases (electronic,ionic and gas) form a continous path from the electrolyte to the diffusion layer, in which case, the pores are treated as straight channels, in this model the reaction layer is treated as a thin film, thus presenting the very disordered structure of real electrodes (observed in experimentation) as a very ordered structure[78].

In the random resistor network[55, 57, 185], the composite electrode is modelled to as been made up of dense grains of electronic conducting particles and ionic conducting particles packed firmly together so that their centres occupy the nodes of a continous lattice, the lattice is modelled based on the theory the the spherical particles are equal sized and are randomly prescribed as ionic particles or electronic particles in the lattice.

The resistor network model are only approximations of real composite electrodes [186] and its use are limited to small sized specimen due to the high computation cost[75].

On the other hand, the random packing sphere model[59, 60, 75] is modelled such that the composite electrodes is made up of discrete particles of ionic conductors and electronic conductors randomly packed together and that current is conducted from one particle to another through the neck formed between them.

This modelling approach allows the macro-scale predictions of electrochemical processes in electrodes to be made, and at the same time, preserve the important micro-structural properties of the electrode.

Both the random packing sphere model and the resistor network model are referred to the as the Monte Carlo method due to the randomness of the conducting particles.

The macroscopic porous electrode modelling approach[35, 187] assumes that the composite electrode is made up of randomly packed ionic and electronic particles by which current is transmitted from particle to particle through necks formed by contact between them. This approach does not take into considerations the actual geometric sizes of the component partices instead it describes them as continous average quantities, thus this approach is sometimes described as an approximation of the Monte Carlo methods[78].

Sieve Sunde[78] describes the Monte Carlo approach to modelling as superior to the other ones because of its ability to predict salient experimental features. Hence the model developed uses the random packing sphere (Monte Carlo) approach in the reaction layer. The micro structure of the reaction layer modelled as a random packing system is shown in Figure (4-6a) while the geometric details for the tripple phase boundary is shown in (4-6b)

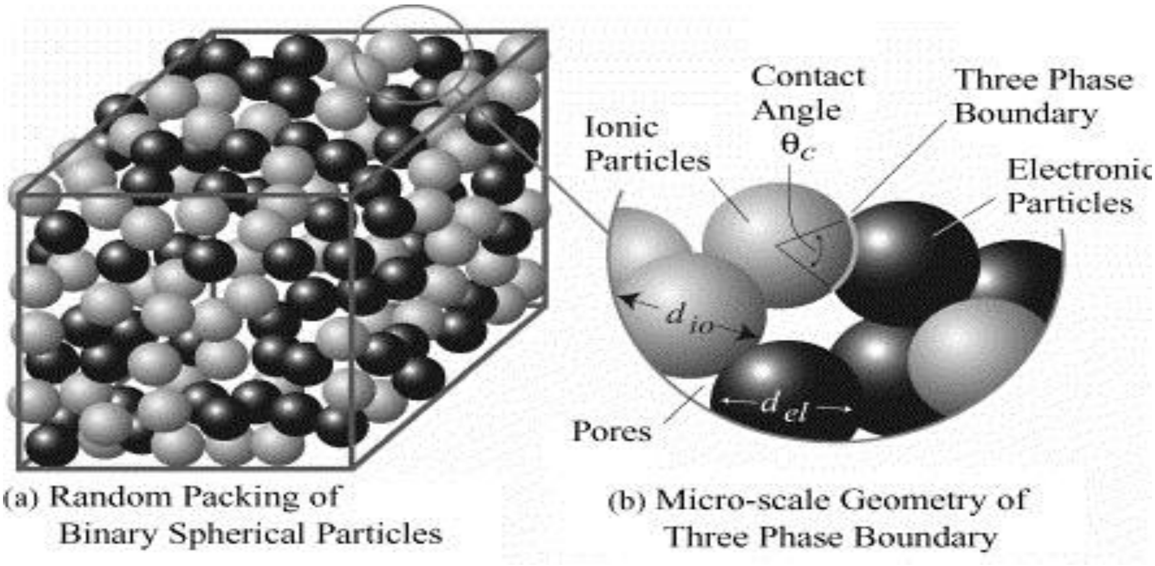

Fig 4-5: Micro-structural modelling as random packing system of binary spherical particles[75]

The processes to be modelled in the reaction layers are the transport of species to and from the electrolyte, also the chemical reactions (reforming and water-shift gas), the electrochemical reactions, the transport of ions and electrons and the transport of energy.

The governing equations of the processes in the reaction layers are the conservation of mass, both in terms of the total mass and species mass, conservation of energy in terms of the sensible enthalpy and the momentum conservation equation or Newton’s second law. These equations are similar to those already developed for the diffusion layers except for the source term. The following section details these phenomena in the different sub-models in more details.

4.4.1 Conservation of species

The conservation equation governing the transport of species in the electrode reaction layer is similar to that developed in diffusion layer model, it can be expressed as:

$$\nabla . j_i = r_{ri} \tag{4-90}$$

Where the species source term r_{ri} accounts for the rate of consumption/production of species due to the electrochemical and chemical reactions.

$$r_{ri} = r_{ec} + r_i \tag{4-91}$$

Where r_{ec} the source is term due to the electrochemical reactions and r_i is that due to the chemical reactions. The source term due to the chemical reactions have already been defined in Equations (4-35) to (4-39) and the modified Stefan-Maxwell equation in equation (4-14) is used in modelling the species diffusion in the reaction layer, the outstanding task is to obtain an expression for the source term r_{ec} due to the electrochemical reaction.

According to Faradays law (Equation (3-10)) which relates the rate of electrochemical reaction to the volumetric current density as

$$i_v = -nF\, r_{ec} \tag{4-92}$$

Where $n_{el}$the number of electrons transferred and F is the faraday constant. The volumetric current density produced in the reaction layer is defined by the Butler-Volmer equation (Equations (3-46) and (3-47)) and expressed as

$$i_v = A_v i_{o,} \left\{ exp\left(\frac{\alpha F\eta}{RT}\right) - exp\left(\frac{(1-\alpha)F\eta}{RT}\right) \right\} \tag{4-93}$$

Where α is the transfer coefficient, A_v is the reactive surface area per unit volume and i_o is the exchange current density normally expressed as [76, 90]

$$i_{o,} = \frac{RT}{n_{el}F} A_{electrode} exp\left(\frac{-E_{electrode}}{RT}\right) \tag{4-94}$$

Where A is the pre-exponential factor and E is the activation energy.

From Equation (4-92), the species source term due to the electrochemical reaction can be expressed as

$$r_{ec} = \frac{v_i i_v}{nF} \tag{4-95}$$

Where v_i is the stoichiometric coefficient of the species in the reaction.

Reactive surface area per unit volume (A_v)

The reactive surface area is a key micro-structural parameters governing the electrochemical performance of the reactive layers, the larger the reaction sites, the smaller the activation losses[75]. In micro-scale modelling such as the random packing sphere model, the reactive surface area per unit volume is formed by contacts of percolated ionic particles and electronic particles and is expressed as:[75, 83, 108]

$$A_v = \pi d_c N_t n_{io} n_{el} \frac{Z_{io} Z_{el}}{Z} P_{io} P_{el} \tag{4-96}$$

Where d_c is the neck diameter, N_t is the density of all the particles, n_{io} and n_{el} are the fractions of ionic and electronic conducting particles respectively, Z_{io} and $Z_{el}$are the average co-ordinating numbers for the ionic and electronic particles respectively, Z is the average coordination number for random packing systems of spherical particles and P_{io} andP_{el} are the probabilities of the respective conducting particles to belong to the percolated cluster of the same phase.

The above parameters used in defining the reactive surface area per unit volume can be calculated as follows:

The neck diameter is given as:

$$d_c = sin\left(\frac{\theta}{2}\right) \min\left(d_{p,io} d_{p,el}\right) \tag{4-97}$$

Where θ is the contact angle between the ionic and electronic conducting particles while $d_{p,io}$ and $d_{p,el}$ are the respective particle diameters.

The number density of all the particles is given by:

$$N_t = \frac{1 - \varepsilon}{(\pi/6) d_{p,el}^3 \left(n_{el} + (1 - n_{el}) \left({d_{p,io}}/{d_{p,el}}\right)^3\right)} \tag{4-98}$$

Similarly, the number fraction is given by

$$n_{el} = \frac{\left({d_{p,io}}/{d_{p,el}} \right)^3 \varphi_{el}}{1 - \varphi_{el} + \left({d_{p,io}}/{d_{p,el}} \right)^3 \varphi_{el}}$$

(4-99)

$$n_{io} = 1 - n_{el}$$ (4-100)

Where φ_{el} is the volume fraction of the electronic conducting particles.

The average total coordinating number (number of contacts with other particles) for the electronic and ionic particles are given as:

$$Z_{el} = 3 + \frac{Z - 3}{n_{el} + (1 - n_{el}) \left({d_{p,io}}/{d_{p,el}} \right)^2}$$

(4-101)

$$Z_{io} = 3 + \frac{Z - 3 \left({d_{p,io}}/{d_{p,el}} \right)^2}{n_{el} + (1 - n_{el}) \left({d_{p,io}}/{d_{p,el}} \right)^2}$$

(4-102)

The probability of the conducting particle belonging to the percolated cluster is given by

$$P_{el} = \left[1 - \left(\frac{4.236 - Z_{el-el}}{2.472} \right)^{2.5} \right]^{0.4}$$ (4-103)

$$P_{io} = \left[1 - \left(\frac{4.236 - Z_{io-io}}{2.472} \right)^{2.5} \right]^{0.4}$$ (4-104)

Where

$$Z_{el-el} = n_{el}\frac{Z_{el}^2}{Z} \quad (4\text{-}105)$$

$$Z_{io-io} = n_{io}\frac{Z_{io}^2}{Z} \quad (4\text{-}106)$$

4.4.2 Conservation of electronic charge

The conservation of electronic charge in the electrode reaction layer can be adapted from the already derived equation for diffusion layer given in Equation (4.85) as

$$\nabla.(i_e) = i_{v,a} \quad \text{For the anode reaction layer} \quad (4\text{-}107)$$

$$\nabla.(i_e) = -i_{v,c} \quad \text{For the cathode reaction layer} \quad (4\text{-}108)$$

Using Ohms law relation, the current density i_e can be expressed in terms of the electronic potential, thus the above equations become

$$\nabla.\left(-\sigma_{s,rl}^{eff}\nabla\phi_s\right) = i_{v,a} \quad \text{For the anode reaction layer} \quad (4\text{-}109)$$

$$\nabla.\left(-\sigma_{s,rl}^{eff}\nabla\phi_s\right) = -i_{v,c} \quad \text{For the cathode reaction layer} \quad (4\text{-}110)$$

Where $\sigma_{s,rl}^{eff}$ is the effective electronic conductivity in the reaction layer and is defined as:

$$\sigma_{s,rl}^{eff} = \varphi_{el}\frac{(1-\varepsilon)}{\tau}\sigma_{s,rl} \quad (4\text{-}111)$$

Where ε is the porosity, τ is the tortuosity, φ_{el} is the volume fraction of the electronic conducting particle and $\sigma_{s,rl}$ is the electronic conductivity of the electron conducting particle

4.4.3 Conservation of ionic charge

By analogy to the modelling equations developed for electronic charge, the equations for the ionic charge in the reaction layers can be expressed as:

$$\nabla.(i_i) = i_{v,a} \quad \text{For the anode reaction layer} \quad (4\text{-}112)$$

$$\nabla.(i_i) = -i_{v,c} \quad \text{For the cathode reaction layer} \tag{4-113}$$

Similarly, applying Ohms law, the above equations become

$$\nabla.\left(-\sigma_{i,rl}^{eff}\nabla\phi_i\right) = i_{v,a} \quad \text{For the anode reaction layer} \tag{4-114}$$

$$\nabla.\left(-\sigma_{i,rl}^{eff}\nabla\phi_i\right) = -i_{v,c} \quad \text{For the cathode reaction layer} \tag{4-115}$$

Where $\sigma_{i,rl}^{eff}$ is the effective electronic conductivity in the reaction layer and is defined as:

$$\sigma_{i,rl}^{eff} = \varphi_{el}\frac{(1-\varepsilon)}{\tau}\sigma_{i,rl} \tag{4-116}$$

Where ε is the porosity, τ is the tortuosity, φ_{el} is the volume fraction of the electronic conducting particle and $\sigma_{i,rl}$ is the electronic conductivity of the ionic conducting particle.

4.4.4 Conservation of energy

The principle of energy conservation in the electrode reaction layer is similar to that already developed in the diffusion layer (Equation (4-78)) except for the source term and is expressed below assuming local thermal equilibrium exists between the porous matrix and the fluid as

$$\sum_{i=1}^{n} c_{pi}\rho_i u_i \nabla T = -\nabla.\left(k_{rl}^{eff}\nabla T\right) + r_e - \sum_{i=1}^{n} h_i r_i \tag{4-117}$$

Where k_{rl}^{eff} is the effective thermal conductivity of the layer and is defined as[35]

$$k_{rl}^{eff} = \varepsilon k_f + (1-\varepsilon)[\varphi_{el}k_{el} + (1-\varphi_{el})k_{io}] \tag{4-118}$$

Where k_f is the thermal conductivity of fluid in the layer, φ_{el} is the volume fraction of the electronic conducting particles, k_{el} and k_{io} are the thermal conductivities of the electronic conducting particles and the ionic conducting particles respectively. $\sum_{i=1}^{n} h_i r_i$ represents the heat source from the chemical reaction in the anode reaction layer while r_e is the energy heat source term in both reaction layers, they can be expressed as

$$r_e = \sigma_{s,rl}^{eff}\nabla^2\phi_s + \sigma_{i,rl}^{eff}\nabla^2\phi_i + \frac{i_v}{n_e F}Q_{elec}A_v + i_v(\eta_{act} + \eta_{conc})A_v \qquad (4\text{-}119)$$

The term $(\sigma_{s,rl}^{eff}\nabla^2\phi_s)$ represents the Joule heating effect due to resistance created by the passage of electronic currents through reaction layer, the second term $(\sigma_{i,rl}^{eff}\nabla^2\phi_i)$ represents the joule heating effect due to the resistance created by the passage of ionic currents through the reaction layer, the third term $\left(\frac{i_v}{n_e F}Q_{elec}A_v\right)$ [127, 188] represents the reversible heat generated due to the electrochemical reactions, lastly, $i_v(\eta_{act} + \eta_{conc})A_v$ are the irreversible heat generated due to the electrochemical reactions.

4.4.5 Conservation of momentum

The momentum conservation in the reaction layers is obtained from the already derived equations for the diffusion layer given in Equation (4-56) and can be expressed as

$$\nabla.\left(\frac{\rho}{\varepsilon_{rl}^2}uu\right) = -u\frac{\mu}{K_{rl}} + \rho\vec{f} + \frac{\mu}{\varepsilon_{rl}}[\nabla\vec{u} + (\nabla\vec{u})^T] - \left[p + \left(\frac{2}{3\varepsilon_{rl}}\mu\right)(\nabla.\vec{u})\right]\vec{I} \qquad (4\text{-}120)$$

Where ε_{rl} is the porosity in the reaction layer and $K_{rl}$is the permeability of the reaction layer

4.5 Electrolyte model

The electrolyte layer is a completely dense solid with negligible porosity that impedes the flow of gases through it. As a result of the electrochemical reaction occurring at the cathode reaction layer, oxide ions (O^{2-}) are produced and migrate through the electrolyte to the anode reaction layer, ensuring the transport of mass and charge, and heat released, but there is no production or consumption of ions. The processes that needs to be modelled in this layer are the oxide ion transfer which simultaneously enforces mass and charge transfer and the energy transfer, thus this model considers the conservation of charge accounting for the mass and charge transport and the energy conservation which accounts for the joule heating effect due to the resistance created by the flow of ions in the electrolyte layer.

4.5.1 Conservation of ionic charge

The conservation of ionic charge in the dense electrolyte layer can be calculated as

$$\nabla.(i_i) = 0 \tag{4-121}$$

Where(i_i) is the current density and it is described by Ohm's law as

$$i_i = -\sigma_{i,ele}\nabla\phi_i \tag{4-122}$$

Where $\sigma_{i,ele}$ is the ionic conductivity of the electrolyte layer and $\nabla\phi_i$ is the ionic potential of the ion conducting electrolyte layer.

4.5.2 Conservation of energy

The heat transfer in the electrolyte is only due to conduction, thus the conservation of energy equation in the layer can be expressed as

$$\sum_{i=1}^{n} c_{pi}\rho_i u_i\nabla T = -\nabla.(k_e\nabla T) + r_e \tag{4-123}$$

Where the heat source term is the joule heating effect due to the resistance of passage of ionic currents through the electrolyte and is given by

$$r_e = \sigma_{i,e}\nabla^2\phi_i \tag{4-124}$$

4.6 Channel model

The channel sub model describes the flow of reactants and products along the SOFC channels. The reactant gases enter the cell through the channel inlet and are driven to the electrodes where the electrochemical reactions take place, the products of the anode side electrochemical reaction exit the electrodes into the channel and mix with the unreacted gases in the channel from where they are evacuated through the channel outlet.

The processes that need to be modelled in the channels are the transport of species to and from the electrode diffusion layer, also the water-shift gas reaction and the transport of energy as a result of heat convection and species diffusion along with the heat generated/consumed due to the chemical reaction. The conservation equations governing the processes in the flow channels are the conservation of mass, in terms of the total mass and species, conservation of energy in terms of the sensible enthalpy and the momentum conservation equation or Newton's second law. The following section describes these phenomena in more details

4.6.1 Conservation of mass

The mass conservation equation in the flow channels is expressed as

$$\nabla.(\rho_i u) = r_i \tag{4-125}$$

Where r_i is the mass source or sink term.

4.6.2 Conservation of species

The conservation of species in the flow channels is given by

$$\nabla.(\rho_i u \nabla x_i) + \nabla.j_i = r_i \tag{4-126}$$

Where $\nabla.j_i$ is the ordinary diffusion flux of the species which could either be in a binary gas mixture or a multicomponent gas mixture, the diffusion modeling is carried out using the Stefan-Maxwell equations

4.6.3 Conservation of momentum

The momentum conservation equation for the fluids flowing through the channel may be expressed as

$$\nabla.(\rho uu) = -u\mu + \rho\vec{f} + \nabla.\left(\mu[\nabla\vec{u} + (\nabla\vec{u})^T] - \left[p + \left(\frac{2}{3}\mu\right)(\nabla.\vec{u})\right]\vec{I}\right) \tag{4-127}$$

4.6.4 Conservation of energy

The conservation of energy in the flow channels is given by

$$\sum_{i=1}^{n} c_{pi}\rho_i u_i \nabla T = -\nabla.\left(k_f \nabla T\right) + r_e \tag{4-128}$$

Within the flow channels, the heat sources may be neglected since there is no generation of heat in the channels as the reaction sites are located in the electrodes.

4.7 Interconnect model

The interconnector also referred to as current collector or bipolar plate is an all solid layer usually made from metals or ceramic that is situated between individual cells, its purpose is to connect the individual cell in the stack in series so that the generated electricity can be combined. The phenomena occurring in the interconnectors are similar to those occurring in the electrolyte; however unlike the electrolyte it is electrons that flow through it. The processes that needs to be modelled in this layer are the electrons transfer which simultaneously enforces mass and charge transfer and the energy transfer, thus this model considers the conservation of charge accounting for the mass and charge transport and the energy conservation which describes the joule heating effect due to resistance to electrons flow.

4.7.1 Conservation of electronic charge

The conservation of electronic charge in the interconnect layer can be calculated as

$$\nabla.(i_s) = 0 \tag{4-129}$$

Where(i_e) is the current density and it is described by Ohm's law as

$$i_s = -\sigma_{s,int} \nabla \phi_e \tag{4-130}$$

Where $\sigma_{s,int}$ is the electronic conductivity of the interconnect and $\nabla \phi_e$ is the electronic potential of the interconnect layer.

4.7.2 Conservation of energy

The interconnect is in contact with the electrodes and the reactant gas on one side and with the surrounding on the other side, thus heat transfer by conduction occurs with the electrodes while heat transfer by convection occurs with the gas and the surroundings on the other side. Also, radiation is expected to play an important role[16, 90, 146] in the energy equations, even though some authors[92] reports negligible radiation effect on the overall temperature distribution, thus the conservation of energy equation in the interconnect layer is expressed as:

$$\sum_{i=1}^{n} c_{pi} \rho_i u_i \nabla T = -\nabla.(k_e \nabla T) + \in (T_{amb}^4 - T^4) + r_e \tag{4-131}$$

Where $\in \sigma(T_{amb}^4 - T^4)$ is the surface-to-ambient radiation and r_e is the joule heating effect due to the resistance of passage of electronic currents through the interconnect and is given by

$$r_e = \sigma_{s,int} \nabla^2 \phi_e \tag{4-132}$$

4.8 Boundary and interfacial conditions

The specifications of the boundary conditions are needed to generate accurate results from the model calculations. The boundary and interface conditions needed to complete the formulation of the SOFC model are shown in Figure (4-6). The locations for the internal boundaries are represented as I1, I2…I10, while those for the external boundaries are represented as E1, E2…E4.

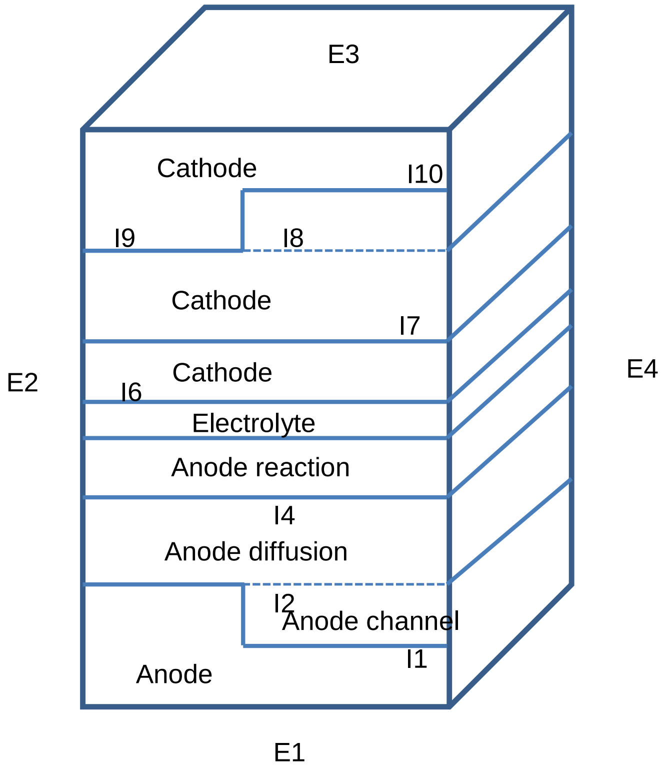

Figure 4-7: Two dimensional schematic of the boundary and interfacial conditions of SOFC model

4.8.1 Interconnect

The interconnect is responsible for the migration of electrons to and from the electrodes, this ensures continuity of electric current at the electrode/interconnect boundary

- Anode side

The current on the anode side interconnect is collected on the outer surface E1. Thus a zero voltage (ground) boundary condition is prescribed at the outer interconnect surface

$$\phi_s = 0 \tag{4-133}$$

- Cathode side

The electric potential boundary on the cathode interconnects side E3 closes up the electric circuit and defines the operating cell voltage. The boundary condition is prescribed as

$$\phi_s = V_{cell} \tag{4-134}$$

The boundary conditions applicable at the interconnect external boundaries E1, E3 are insulated both electrically and thermally, thus the following conditions apply

$$\boldsymbol{n}.\boldsymbol{i} = 0 \tag{4-135}$$

$$\boldsymbol{n}.\boldsymbol{Q} = 0 \tag{4-136}$$

The interface between the interconnect and the fluid in the channel I1 and I10 are also electrically insulated, but the heat flux at the interface is expressed as

$$\boldsymbol{n}.\boldsymbol{Q} = h\left(T_{I,n} - T_{gas}\right) \tag{4-137}$$

Where $T_{I,n}$ is the interface temperature, T_{gas} is the temperature of the reactant gas mixture in the flow channel and h is the average heat transfer coefficient, which is determined from the Nusselt number[93]

4.8.2 Flow channels

- Inlet

The inlet conditions for the velocity, mass fraction and inlet pressure at flow channel inlets are prescribed as

$$u = u_{in} \tag{4-138}$$

$$x_i = x_{i,in} \tag{4-139}$$

$$p = p_o \tag{4-140}$$

Outlet

The outflow boundary conditions at channel outlet are defined as laminar conditions and prescribed as

$$p = p_o \tag{4-141}$$

A convective flux boundary condition is imposed on the channel outlet; this is based on the assumption that the diffusive flux term is negligible at the outlet:

$$\boldsymbol{n}.\left(-\rho \nabla x_i D_{ij}\right) = 0 \tag{4-142}$$

Wall

A no-slip boundary condition is applied at the channel walls which implies the fluid velocity is zero at the walls

$$u = 0 \tag{4-143}$$

4.8.3 Electrode diffusion

The electrode diffusion layers are in contact with the electrode reaction layer on one side, and with the reactant gases and interconnect on the other side, the external boundaries E2 and E4 are insulated, thus the equations for the electrical, thermal and species transport conditions for these boundaries are respectively

$$\boldsymbol{n}.\boldsymbol{i_s} = 0 \tag{4-144}$$

$$\boldsymbol{n}.\boldsymbol{Q} = 0 \tag{4-145}$$

$$\boldsymbol{n}.\boldsymbol{J} = 0 \tag{4-146}$$

The internal boundary I4 and I7 represents the interface between the diffusion layer and the reaction layer, the boundary conditions for these interfaces are continuous flux for electronic potential, species and heat transport, while insulated boundary condition holds for the ionic potential over the interface, these conditions are expressed mathematically as

$$(\boldsymbol{n}.\boldsymbol{i_s})|_{\boldsymbol{dl}} = (\boldsymbol{n}.\boldsymbol{i_s})|_{\boldsymbol{rl}} \tag{4-147}$$

$$(\boldsymbol{n}.\boldsymbol{j})|_{\boldsymbol{dl}} = (\boldsymbol{n}.\boldsymbol{j})|_{\boldsymbol{rl}} \tag{4-148}$$

$$(\boldsymbol{n}.\boldsymbol{Q})|_{\boldsymbol{dl}} = (\boldsymbol{n}.\boldsymbol{Q})|_{\boldsymbol{rl}} \tag{4-149}$$

$$(\boldsymbol{n}.\boldsymbol{i_i})|_{\boldsymbol{dl}} = \boldsymbol{0} \tag{4-150}$$

The interface I3 and I9 are the boundaries between the diffusion layer and the interconnect, within this interface, there is continuity of electric potential and of heat flux, while insulated boundary condition holds for ionic potential and gas species, these can be expressed as

$$(\boldsymbol{n}.\boldsymbol{i_s})|_{\boldsymbol{dl}} = (\boldsymbol{n}.\boldsymbol{i_s})|_{\boldsymbol{int}} \tag{4-151}$$

$$(\boldsymbol{n}.\boldsymbol{Q})|_{\boldsymbol{dl}} = (\boldsymbol{n}.\boldsymbol{Q})|_{\boldsymbol{int}} \tag{4-152}$$

$$(\boldsymbol{n}.j)|_{\boldsymbol{dl}} = \boldsymbol{0} \tag{4-153}$$

$$(\boldsymbol{n}.\boldsymbol{i_i})|_{\boldsymbol{dl}} = \boldsymbol{0} \tag{4-154}$$

The interface I2 and I8 are in contact with the reactant gas, here, there is species flow continuity with the channel flow and insulation for the electric and ionic currents

$$\boldsymbol{n}.(\nabla.(\rho_i u \nabla x_i) + \nabla.j_i)|_{\boldsymbol{ch}} = \boldsymbol{n}.(\varepsilon\nabla.j_i)|_{\boldsymbol{dl}} \tag{4-155}$$

$$(\boldsymbol{n}.\boldsymbol{i_s})|_{\boldsymbol{dl}} = \boldsymbol{0} \tag{4-156}$$

$$(\boldsymbol{n}.\boldsymbol{i_i})|_{\boldsymbol{dl}} = \boldsymbol{0} \tag{4-157}$$

The heat flux at this interface is given by

$$\boldsymbol{n}.\boldsymbol{Q} = h(T_{I,n} - T_{gas}) \tag{4-158}$$

4.8.4 Electrode reaction

The electrode reaction layer is in contact with the diffusion layer on one side and with the electrolyte on the other, the external boundaries E2 and E4 are insulated, thus the equations for the electronic, ionic, thermal and species transport conditions for these boundaries are respectively

$$\boldsymbol{n}.\boldsymbol{i_s} = 0 \tag{4-159}$$

$$\boldsymbol{n}.\boldsymbol{i_i} = 0 \tag{4-160}$$

$$\boldsymbol{n}.\boldsymbol{Q} = 0 \tag{4-161}$$

$$\boldsymbol{n}.\boldsymbol{J} = 0 \tag{4-162}$$

The internal boundary I4 and I7 represents the interface between the reaction layer and the diffusion layer; the boundary conditions for these interfaces are analogical to those expressed for the diffusion layer in Equations (4-146) to (4-149)

The interface I5 and I6 are the boundaries between the reaction layer and the electrolyte. At these interface, since the electrolyte is non porous thus gases cannot enter the electrolyte. Also, the electronic current density is insulated at this boundary while the ionic current density is continuous, the heat flux is also continuous across this interface, these are expressed mathematically as

$$(\boldsymbol{n}.\boldsymbol{i_i})|_{\boldsymbol{rl}} = (\boldsymbol{n}.\boldsymbol{i_i})|_{\boldsymbol{ele}} \tag{4-163}$$

$$(\boldsymbol{n}.\boldsymbol{Q})|_{\boldsymbol{rl}} = (\boldsymbol{n}.\boldsymbol{Q})|_{\boldsymbol{ele}} \tag{4-164}$$

$$(\boldsymbol{n}.j)|_{\boldsymbol{rl}} = \boldsymbol{0} \tag{4-165}$$

$$(\boldsymbol{n}.\boldsymbol{i_e})|_{\boldsymbol{rl}} = \boldsymbol{0} \tag{4-166}$$

4.8.5 Electrolyte

The electrolyte is impermeable to gases, the species mass flux and electronic current density are insulated at all surfaces, but for the surfaces I5 and I6, at the top and bottom, continuity with reaction layers need to be expressed for the ionic current density flux and the heat flux, these boundary conditions are expressed in Equations (4-163) and (4-164) respectively.

4.9 Thermo-physical model

The approach to SOFC modelling is becoming increasingly sophisticated, involving detailed description of flow, thermal, chemical and electrochemical processes, the accuracy of these models is limited by the reliability of available data to predict the thermodynamic and transport properties of the reactant gases[178]

In this section, the theoretical and semi-empirical methods used in predicting the thermo-physical properties and transport coefficients of the SOFC gas mixtures are presented, these includes model equations for the momentum (dynamic viscosity) and energy (thermal conductivity) transport coefficients as well as the specific heat capacity at constant pressure

4.9.1 Dynamic viscosity, μ

The semi-empirical formula developed by Todd and Young is used to estimate the dynamic viscosity of a pure gas i is given as[178]

$$\mu_i = \sum_0^6 a_k \left(\frac{T}{1000}\right) \tag{4-167}$$

Where the unit of ($\mu = 10^{-7}\ kg/ms$). The parameters a_k are tabulated in [178] for most of the common gases used in SOFC modelling. The equation for a multicomponent gas mixture is thus given by

$$\mu_g = \sum_{i=1}^{n} x_i \mu_i \tag{4-168}$$

4.9.2 Thermal conductivity, k

The semi-empirical formula developed by Todd and Young is used to estimate the thermal conductivity of a pure gas i is given as[178]

$$k_i = \sum_0^6 b_k \left(\frac{T}{1000}\right) \tag{4-169}$$

The parameters b_k are tabulated in [178] for most of the common gases used in SOFC modelling. The equation for a multicomponent gas mixture is thus given by

$$k_g = \sum_{i=1}^{n} x_i k_i \tag{4-170}$$

4.9.3 Specific heat capacity, c_p

The semi-empirical formula developed by Todd and Young is used to estimate the thermal conductivity of a pure gas i is given as[178]

$$c_{p,i} = \sum_0^6 c_k \left(\frac{T}{1000}\right) \tag{4-171}$$

The parameters c_k are tabulated in [178] for most of the common gases used in SOFC modelling. The equation for a multicomponent gas mixture is thus given by

$$c_{p,g} = \sum^{n} x_i c_{p,i} \tag{4-172}$$

4.10 Numerical solution

The solutions of the governing equations defined in this chapter are obtained through the numerical method called the finite element method (FEM). In fuel cell modelling, the derivation of the governing and constitutive equations are not difficult in themselves, although they require a thorough understanding of the physical and chemical processes as well as certain mathematical tools. However, these equations are highly non-linear making it extremely difficult to obtain analytically exact solutions. This problem can be overcome by using approximate solutions which discretises the equations thereby converting them to a set of numerically solvable algebraic equations. The most commonly used computational technique for discretising equations are the finite difference method (FDM), finite volume method (FVM) and the finite element method (FEM). The finite element method is a computational technique which divides the spatial domain into smaller finite element sizes called finite element. Each of the element is assigned a set of characteristic equation which are then solved simultaneously thereby predicting the cells behaviour.

The steps involved in the finite element solution of a problem are:

i. Discretisation of the given domain into a collection of finite elements
ii. Derivation of element equations for all elements in the mesh
iii. Assembly of element equations to obtain the equations of the whole problem
iv. Imposition of the boundary conditions of the problem
v. Solution of the assembly equations
vi. Post processing of the results

The first three steps are the main features of the finite element method. The discretisation of the domain represents the subdivision of the complex geometries into a collection of simpler geometric domains called elements. The shape of each element depends on the complexity and dimension of the geometry. For instance, in the 2D domain structure used in this work, the domain can be divided into triangular or quadrilateral mesh element. The approximate functions (algebraic polynomials) which solves the governing equations are used over each mesh function using appropriate interpolation theory methods. These functions depends on several aspects such as geometry, number and location of the sub domains and the quantities to the interpolated. The assembly of the element equations is based on the idea that the solution is continuous at the inter-element boundaries. The obtained final system of the algebraic equations is a numerical analogy of the original mathematical model.

4.11 Developing and solving the SOFC model using COMSOL

The governing equations and boundary conditions used in this model (as described above) were discretised using the finite element method and solved for a two dimensional SOFC system using the commercial software package COMSOL Multiphysics (version 4.3a). The software is designed to solve the non-linear set of differential and algebraic equations. The model simulation was performed on a 64 bit Windows operating platform with a 16GB RAM, and Inter Core i7-2600 CPU 3.40 GHz processor. The governing equations and constitutive relations in the model were solved for stationary conditions. The general steps to developing the model are explained below:

i. **Building the SOFC geometry**: The two dimensional geometry of the SOFC was created. The geometry developed consists of seven sub-domains with each representing a distinct component in the SOFC. Each sub-domain is be assigned the appropriate governing equations which represents the physical behaviour of the domain
ii. **Adding the COMSOL module**: The COMSOL software is not only capable of solving the non-linear set of coupled differential and algebraic equations but it also has optional modules for specific applications. These modules provides the built-in physic interfaces in the particular discipline. In this study, the “Batteries and Fuel Cell Module” is applied in the SOFC model. This module provides customised physics interfaces for modelling fuel cells. These interfaces have tools and sequences for building detailed models for the operation of the fuel cell including the description of the electrochemical reactions, chemical reactions and transport properties that influence the performance of the cell.
iii. **Specify the governing equations**: The model equations which describes the physical phenomena occurring in each sub-domain were assigned using the

governing equations described in this chapter. These governing equations are already provided by the COMSOL software

iv. **Specifying the constitutive relations**: The constitutive relations used in describing the unique attributes of the model for describing the different processes such as the electrochemical and chemical reactions and the transport properties were developed as part of this work and incorporated into the model. COMSOL allows the use of user defined equations and relations (such as the Butler-Volmer equation, porosity change, specific volume per unit area) to be imported either as scalar expressions for parameters or dependent expressions for variables. A significant part of the code used in developing this model were incorporated into the software by the user, these user defined equations and relations were first tested using Excel spreadsheet as a form of pre validation.

v. **Define the boundary conditions**: To solve the governing equations and constitutive relations, the boundary conditions and initial values for all the variables are specified in the model. These values were chosen based on data from other models and experimental works in literature. Also pre validation of data used was carried out in Excel

vi. **Building the mesh**: The meshing technique is an important process in solving the problems in the finite element method described in section 4-10. The mesh enables the model geometry to be discretised into smaller units called mesh elements. This divides an initial complex problem into small elements ensuring the problem can be accurately solved. The software creates the mesh for the simulation domain. It has the option of different size levels that the user can select from (Extremely fine, Extra fine, Finer, Fine, Normal, Coarse, Coarser, Extra course, Extremely coarse). The mesh sizes do not significantly affect the results obtained, however, they will affect the time for the simulation solution to converge. In this SOFC model, “Fine” was used to create the mesh.

vii. **Create the study for solving the model**: COMSOL software has the options of different study types to be selected depending on the behaviour of the problem. The two most common studies are the “stationary study” used for a steady state situation in which the variables are not time dependent and the “time dependent study” which is used for transient simulations using a time dependent solver for computing the solution. In this SOFC model, a stationary study was chosen. In COMSOL, the solver uses a numerical technique for finding approximate solutions for the differential and algebraic equations. The Newton-Raphson method is used by COMSOL in solving the model equations. The maximum number of iterations was set to 23. The solution is considered converged when the difference between two results is less than 10^{-3} (relative tolerance) for all variables.

viii. **Create the results**: Data from the simulated model file were used for the post processing steps using other software's such Excel, Origin and Hysys

These are the major steps and methodology used in building and solving the SOFC model. The simulation time to obtain the solution was between 40 – 130 minutes depending on the complexity of the model.

4.12 Conclusions

Governing equations used in predicting the physical and chemical processes in a SOFC have been presented in this chapter, these equations include the conservation of mass and species, conservation of momentum, conservation of electric charge for the ionic and electronic conducting particles and the conservation of energy, for ease of simulating, the entire SOFC model was broken down into five sub models: electrode diffusion, electrode reaction, electrolyte, channel and interconnect models. The boundary conditions and the thermo-physical parameters used in the model are also presented.

On the anode side of the model, the conservation of mass and species equation can be developed for a binary mixture and for a multicomponent mixture, while on the cathode side; the equations were only developed for binary mixtures. In addition to the equations developed for the diffusion layer, an additional equation for the ionic potential in the reaction layers was developed since this model treats the reaction layer as a distinct finite volume.

CHAPTER5 : Isothermal SOFC model

A two dimensional, along the channel, micro-scale, steady state isothermal model is presented in this chapter. The model incorporates the distinct layer porous electrodes, solid interconnect and solid ceramic electrolyte as described in chapter 1. The steady state behaviour of the cell was determined by numerical solution of combined transport, continuity and kinetic equations. The purpose of this chapter is to explore intermediate temperature performance of hydrogen fuelled micro-SOFCs by investigating its transport and reaction characteristics. It also carried out parametric studies to investigate the effect of key operating and design parameters on the cells performance. This model gives the foundation for the optimisation of several geometric and design parameters of the cell.

5.1 Introduction

Solid oxide fuel cells (SOFCs) are encouraging candidates for energy conversion systems because of their huge potentials for power generation in stationary, portable and transport applications and their high energy conversion efficiency when compared to other fuel cells[14, 21, 52, 189]. In addition, internal reforming of hydrocarbons can be carried out in the anode and they have significantly lower emissions of sulphur oxides, nitrogen oxides and carbon dioxide compared to conventional power generation devices[76, 98, 190].

Although there has been significant advances with respect to development of new materials with improved properties and better fabrication processes in the last two decades[191], some barriers still hamper the development and commercialisation of SOFCs. The high operating temperature is the major limiting factor to using SOFCs. In order to overcome this limitation and achieve stability and economy, recent efforts are geared towards intermediate temperature SOFCs (IT-SOFCs)[23, 32], these may be achieved by either reducing the electrolyte thickness thereby reducing its ohmic resistance [115, 192, 193]; developing new electrodes with improved catalytic activities which reduces polarisation[31, 194-196] or improving the electrode microstructure which increases the electrochemical reaction area[52, 197, 198].

To compensate for the reduced cell performance associated with operating at intermediate temperatures through any of the three routes mentioned above, the use of thin film micro SOFCs are been investigated [199-202]. Amongst them, the technique of thin electrolyte is widely used for intermediate temperature SOFCs. Furthermore Yttria stabilised zirconia (YSZ) which is normally used as electrolyte for high temperature SOFCs can be used at intermediate temperatures by reducing the its thickness.

Quite a number of existing micro models found in literature are modelled with the traditional SOFC geometric structure i.e. without the electrochemical reaction layers [52, 59, 64, 65, 75, 89, 134, 203-205] whereby the consumption and generation of gaseous species are carried out at the interfaces and the governing equations are coupled only by the boundary conditions. For micro-SOFCs modelled with a distinct reaction layer, the electrochemical active layers extend from the electrode/electrolyte interfaces to the reaction layer. The gaseous species are consumed and generated within the reaction layer and the governing equations are coupled not only by the boundary conditions but also by the source or sink terms. Consequently, it is only recently that a few authors are considering micro-SOFCs with distinct reaction layers in their models [35, 79, 83, 206, 207].

5.2 Model description

5.2.1 Computational domain and assumptions

A three dimensional representation of a planar type anode supported SOFC unit is shown in Figure 4-1(a), which includes the interconnects, flow channels, diffusion layers and reaction layers on both the anode and cathode sides and a thin electrolyte layer between the reaction layers. A two dimensional presentation of the computational domain is shown in Figure 4-1b.

The model considers seven sub-domains; anode channel (ACH), anode diffusion layer (ADL), anode reaction layer (ARL), electrolyte, cathode reaction layer (CRL), cathode diffusion layer (CDL) and cathode channel (CCH). The material properties and constituent equations of each layer are listed in Table 5-1.

In addition to the general assumptions listed in Chapter 4, the model features and assumptions in this particular model are listed as follows:

- The temperature and total pressure are constant and uniform throughout the cell

- Additional resistance due to the presence of interconnector are not considered
- The reactant gases at both the anode and cathode are introduced by plug flow
- Co-flow mode of reactant gases into the flow channels is applied
- The electrode layers are made up of binary spherical particles that are randomly packed
- The spherical particles are equal sizes
- The flow in the channels is treated as laminar and incompressible
- No slip boundary condition is applied on the cell walls
- Species transport at channel outlet is by convective flux only

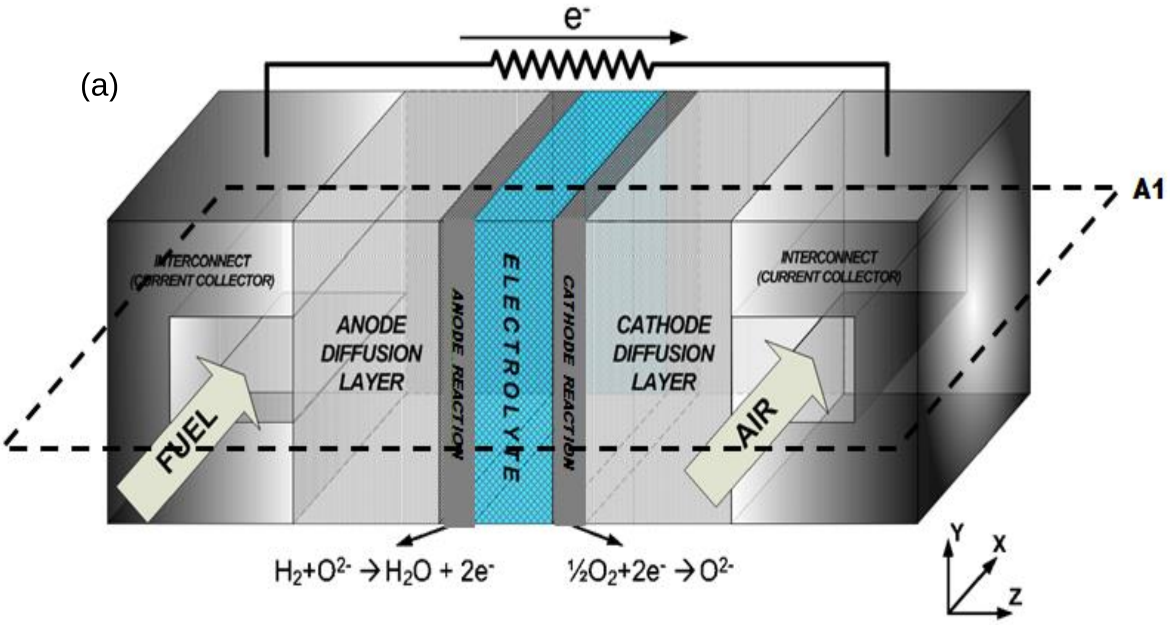

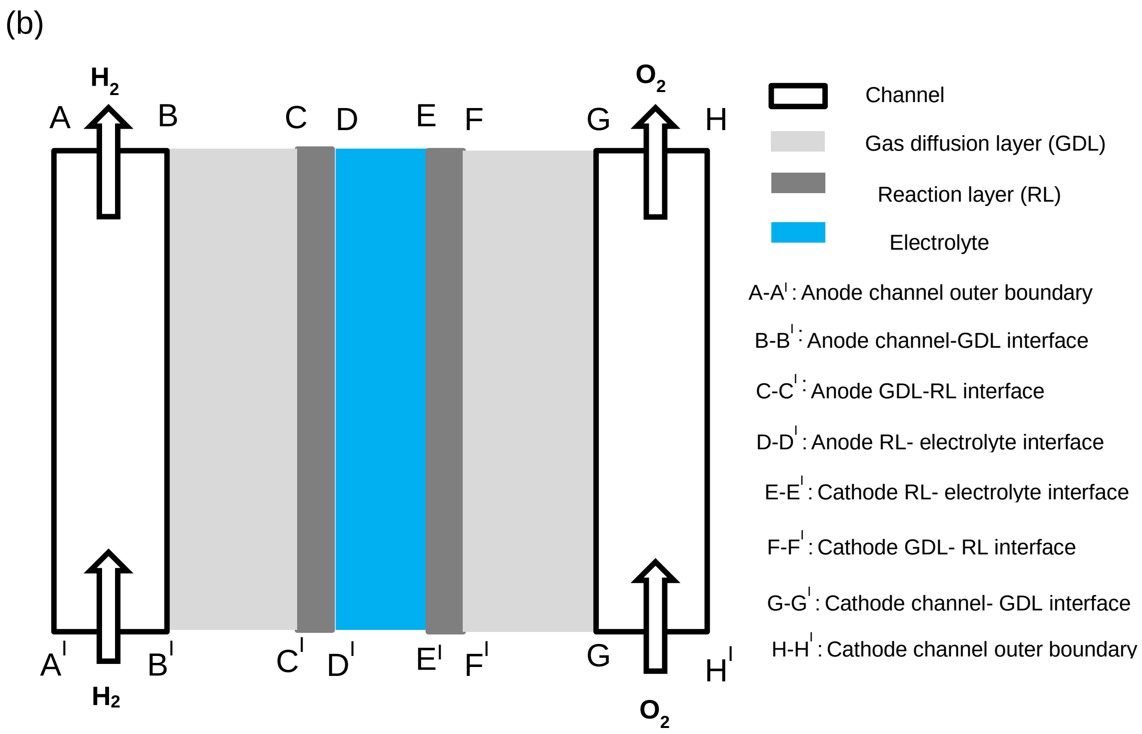

Figure 5-1: Schematic of a SOFC (a) 3D representation[71] (b) 2D computational domain A1

Table 5-1: Equations and parameters used in the simulation

Equations and parameters	Value or expression	Reference
Binary diffusion coefficient, D_{ij} $(m^2 s^{-1})$	$\frac{0.001434T^{1.75}}{pM_{ij}^{1/2}\left[V_i^{1/3}+V_j^{1/3}\right]^2}$	[35, 178]
Knudsen diffusion coefficient, $D_{Kn,ij}$ $(m^2 s^{-1})$	$\frac{2d_{pore}}{3}\sqrt{\frac{2RT}{\pi M_{ij}}}$	[35, 76]
Anode conductivity,$\sigma_{s,a}(S\,m^{-1})$	$[((9.5\times10^7)/T)exp(-1150/T)]$	[35, 76]
Cathode conductivity,$\sigma_{s,c}(S\,m^{-1})$	$[((4.2\times10^7)/T)exp(-1200/T)]$	[35, 76]
Pore diameter, d_{pore} (m)	$\frac{4}{A_0}\frac{\varepsilon}{1-\varepsilon}$	[75]
Specific surface area of solid volume, A_0	$\frac{6}{d_{p,el}}$	[75]
Kozeny constant, k_K	5	[75]
Flow permeability, (m^2)	$\frac{\varepsilon^3}{k_K{A_0}^2(1-\varepsilon)^2}$	[75]
Volume fraction, φ	0.5	[35]

Tortuosity, τ	3	
Electrode diffusion layer		
Effective electronic conductivity,$\sigma_s (S\, m^{-1})$	$\frac{(1-\varepsilon)}{\tau}\sigma_s$	[35]
Anode and cathode porosity, ε_{adl}, ε_{cdl}	0.5	[83, 108]
Diameter of spherical particle, d_{el}, d_{io} (μm)	1	[83, 108]
Electrode reaction layer		
Effective surface area, A_v (m^{-1})	$\pi d_c N_t n_{io} n_{el} \frac{Z_{io} Z_{el}}{Z} P_{io} P_{el}$	[75]
Effective electronic conductivity,$\sigma_{s,} (S\, m^{-1})$	$\varphi\frac{(1-\varepsilon)}{\tau}\sigma_s$	[35]
Effective ionic conductivity,$\sigma_{i,} (S\, m^{-1})$	$\varphi\frac{(1-\varepsilon)}{\tau}\sigma_i$	[35]
Anode and cathode porosity, ε_{arl}, ε_{crl}	0.25	[83, 108]
Diameter of spherical particle, d_{el}, d_{io} (μm)	0.5	[83, 108]
Electrolyte layer		
Electrolyte conductivity,$\sigma_{i,} (S\, m^{-1})$	$3.34 \times 10^4 exp(-1150/T)$	[35, 76]

5.2.2 Governing equations

The governing equations defined in Chapter 4 are specified to account for the particular phenomena taking place in each sub-domain as expressed in Table 5-1 after taking into consideration the assumptions listed above

Table 5-2: Governing equations used in the hydrogen fed SOFC isothermal model

Flow channels		
Conservation of mass	$\nabla.(\rho\boldsymbol{u}) = 0$	(5-1)
Conservation of momentum	$-\nabla.(\rho\boldsymbol{uu}) - \nabla.\left[-p + \Psi - \left(\frac{2}{3}\mu\right)(\nabla.\boldsymbol{u})\right]$	(5-2)
	$where\ \Psi = \mu[\nabla\boldsymbol{u} + (\nabla\boldsymbol{u})^T]$	
Conservation of species	$\rho u.\nabla w_i - \nabla.\left[\rho w_i \sum D_{ij}^{eff}(\nabla x_i - \nabla w_i)\frac{\nabla p}{p}\right]$	(5-3)
Electrode diffusion layer		
Conservation of mass	$\nabla.(\rho\boldsymbol{u}) = 0$	(5-4)
Conservation of momentum	$-\nabla.\left(\frac{\rho}{\varepsilon^2}\boldsymbol{uu}\right) - \boldsymbol{u}\frac{\mu}{k_p} - \nabla.\left[-p + \Psi - \left(\frac{2}{3\varepsilon}\mu\right)(\nabla.\boldsymbol{u})\right]$	(5-5)

	$where\ \Psi = \frac{\mu}{\varepsilon}[\nabla\boldsymbol{u} + (\nabla\boldsymbol{u})^T]$	
Conservation of species	$-\nabla.\left[\rho w_i \sum D_{ij}^{eff}(\nabla x_i - \nabla w_i)\frac{\nabla p}{p}\right] = 0$	(5-6)
Conservation of charge	$\nabla.\left(-\sigma_s^{eff}\nabla\phi_s\right) = 0$	(5-7)
Electrode reaction layer		
Conservation of mass	$\nabla.(\rho\boldsymbol{u}) = 0$	(5-8)
Conservation of momentum	$-\nabla.\left(\frac{\rho}{\varepsilon^2}\boldsymbol{uu}\right) - \boldsymbol{u}\frac{\mu}{k_p} - \nabla.\left[-p + \Psi - \left(\frac{2}{3\varepsilon}\mu\right)(\nabla.\boldsymbol{u})\right]$ $where\ \Psi = \frac{\mu}{\varepsilon}[\nabla\boldsymbol{u} + (\nabla\boldsymbol{u})^T]$	(5-9)
Conservation of species	$-\nabla.\left[\rho w_i \sum D_{ij}^{eff}(\nabla x_i - \nabla w_i)\frac{\nabla p}{p}\right] = r_i$ $where, r_{H_2} = -r_{H_2O} = \frac{i_v}{2F}\ at\ ARL$ $and\ r_{O_2} = \frac{i_v}{4F}\ at\ CRL$	(5-10)
Conservation of charge	$\nabla.\left(-\sigma_s^{eff}\nabla\phi_s\right) = i_v$ $\nabla.\left(-\sigma_i^{eff}\nabla\phi_i\right) = -i_v$ $where, i_v = A_v i_{tpb}$	(5-11) (5-12)
Electrolyte		
Conservation of charge	$\nabla.\left(\sigma_{i,ele}\nabla\phi_i\right) = 0$	(5-13)

5.2.3 Electrochemical reaction kinetics

The current densities of both the anode and cathode are modelled by the non-linear Butler-Volmer equation expressed in Eq. (4-92). However, in SOFCs, due to its operating temperatures, the mass and charge transfer phenomena occur very rapidly, thus, to account for the transfer rates, the Butler-Volmer equations need to be modified by the species concentration[90], the modified equations are given as:

$$i_{v,a} = A_{v,a} i_{o,a}\left\{\frac{c_{H_2}}{c_{H_2,ref}} exp\left(\frac{\alpha F \eta_a}{RT}\right) - \frac{c_{H_2O}}{c_{H_2O,ref}} exp\left(\frac{(1-\alpha)F\eta_a}{RT}\right)\right\} \tag{5-14}$$

$$i_{v,c} = A_{v,c} i_{o,c} \left\{ \frac{c_{O_2}}{c_{O_2,ref}} exp\left(\frac{\alpha F \eta_c}{RT}\right) - \frac{c_{O_2}}{c_{O_2,ref}} exp\left(\frac{(1-\alpha)F\eta_c}{RT}\right) \right\} \tag{5-15}$$

Where $c_{H_2,ref}$, $c_{H_2O,ref}$ and $c_{O_2,ref}$ are the reference concentrations of hydrogen, water and oxygen, n is the number of electrons transferred in the rate limiting reaction step, A_v is the reactive surface area per unit volume, α the charge transfer coefficient and η_i is the polarisation. The subscripts $i = a\ or\ c$ refers to the anode and cathode respectively.

The polarisation η_i expressed in Eq.(5-14) and Eq.(5-15) are defined as

$$\eta_a = \varphi_s - \varphi_i - \eta_A^{conc} = \varphi_s - \varphi_s + \frac{RT}{2F} In \left(\frac{p_{H_2}^b p_{H_2O}^r}{p_{H_2O}^b p_{H_2}^r}\right) \tag{5-16}$$

$$\eta_c = V^{ocv} + \varphi_i - \varphi_s - \eta_c^{conc} = V^{ocv} + \varphi_i - \varphi_s + \frac{RT}{4F} \left(\frac{p_{O_2}^b}{p_{O_2}^r}\right) \tag{5-17}$$

Where φ_s is the electronic phase potential, φ_i is the ionic phase potential and η^{conc} is the concentration polarisation.

Parameters used in developing the electrochemical model are listed in Table 5-3

Table 5-3: Electrochemical parameters used in the isothermal SOFC model

Parameters	Anode	Cathode	Reference
Charge transfer coefficient, $\boldsymbol{\alpha}$	0.5	0.5	[35, 76]
Pre-exponential factor, $\boldsymbol{A}$	6.54×10^{11}	2.35×10^{11}	[90, 107]
Activation energy, $\boldsymbol{E}$	137	140	[76, 107]
Equilibrium potential,	………..	Eq.(3-16)	Calculated
$\boldsymbol{H_2}$ reference concentration	$\frac{x_{H_2}p}{RT}$	………..	Calculated
$\boldsymbol{H_2O}$ reference concentration	$\frac{x_{H_2O}p}{RT}$	………..	Calculated
$\boldsymbol{O_2}$ reference concentration	………..	$\frac{x_{O_2}p}{RT}$	Calculated

5.2.4 Polarisation curve

The operating cell voltage of the SOFC(E^{cell}), can be expressed in terms of the open circuit voltage (OCV)(E^{ocv}), the anode side overpotential(η_A), the cathode side overpotential (η_C) and the ohmic loss in the electrolyte(η_E).

$$E^{cell} = E^{ocv} - (\eta_A + \eta_C + \eta_E) \tag{5-18}$$

where

$$\eta_A = \eta_a + (R_{arl} + R_{adl})i_v \tag{5-19}$$

$$\eta_C = \eta_c + (R_{crl} + R_{cdl})i_v \tag{5-20}$$

$$\eta_E = R_e i_v \tag{5-21}$$

Where R_i is the resistance of the layer and i_v the volumetric current density.

5.2.5 Boundary conditions

Boundary conditions has been applied at particular locations in the cell in solving the governing equations (Eq. (5-1) to Eq. (5-13)).These locations are illustrated in Figure 5-1b. The external boundaries are treated as solid walls with no-slip conditions, the composition of the gaseous species are specified at channel inlets A^{I}-B^{I} and G^{I}-H^{I}. $\emptyset_s = 0$ At B-B^{I} and $\emptyset_s = E^{cell}$ at G-G^{I} were imposed to calculate the electrical potential. The fluxes at the boundaries between the diffusion and reaction layers (C-C^{I} and F-F^{I}) are continuous for the transport of gaseous species and the electronic potential but insulated for the ionic potential. At locations D-D^{I} and E-E^{I} insulation conditions exist between the reaction layers and electrolyte for the diffusive flux and the electronic current density while continuity conditions exist for the ionic current. The pressure at the inlet and outlet was set to ambient conditions at 1atm. The detailed boundary conditions are listed in Table 5-4.

Table 5-4: Boundary conditions in the Isothermal SOFC model

Boundary (Figure 5-1b)	Condition expressions
Anode inlet (Boundary A^{I}-B^{I})	$x_{H_2} = specified, \quad x_{H_2O} = 1 - x_{H_2}$ $p_a = 1atm$
Cathode inlet (Boundary G^{I}-H^{I})	$x_{O_2} = specified, \quad x_{N_2} = 1 - x_{O_2}$ $p_c = 1atm$
Anode outlet (Boundary A-B)	$\rho u x_{H_2}.\boldsymbol{n} = 0$
Cathode outlet (Boundary G-H)	$\rho u x_{O_2}.\boldsymbol{n} = 0$
Anode flow channel – anode diffusion layer interface (Boundary B-B^{I})	$\varphi_s = 0$ $(\rho u x_{H_2} + j_{H_2}).\boldsymbol{n}\big\|_{ch} = j_{H_2}.\boldsymbol{n}\big\|_{dl}$

Boundary (Figure 5-1b)	Condition expressions
cathode flow channel – cathode diffusion layer interface (Boundary G-G^{I})	$\varphi_s = V^{cell}$ $(\rho u x_{O_2} + j_{O_2}).\mathbf{n}\big\|_{ch} = j_{O_2}.\mathbf{n}\big\|_{dl}$
Anode diffusion layer – anode reaction layer interface(Boundary C-C^{I})	$j_{H_2}.\mathbf{n}\big\|_{dl} = j_{H_2}.\mathbf{n}\big\|_{rl}$ $i_s.\mathbf{n}\|_{dl} = i_s.\mathbf{n}\|_{rl}$ $i_i = 0$
Cathode diffusion layer – cathode reaction layer interface (Boundary F-F^{I})	$j_{O_2}.\mathbf{n}\big\|_{dl} = j_{O_2}.\mathbf{n}\big\|_{rl}$ $i_s.\mathbf{n}\|_{dl} = i_s.\mathbf{n}\|_{rl}$ $i_i = 0$
Anode reaction layer – electrolyte interface (Boundary D-D^{I})	$j_{H_2} = 0$ $i_s = 0$ $i_i = i$
Cathode reaction layer – electrolyte interface (Boundary E-E^{I})	$j_{O_2} = 0$ $i_s = 0$ $i_i = i$

5.2.6 Numerical procedure.

The commercial finite element method (FEM) software COMSOL Multiphysics (version 4.3a) was used to solve the non-linear system of governing equations and boundary conditions described above. The software is designed to solve sets of coupled algebraic and differential equations. The SOFC simulation was performed on a 64 bit Windows operating platform with a 16GB ram, and Inter Core i7-2600 CPU 3.40GHz processor. The computational geometry consists of 333,742 degrees of freedom and 120,196 elements. The convergence of the numerical solutions was judged by the relative tolerance criteria of 1×10^{-3}. Figure 5-2 shows the schematic of the computational process for the isothermal SOFC model. As seen, the transport of concentrated species interface which defines the equation for the diffusion model as well as the species mass fraction is coupled to the secondary current distribution interface by the current density term. The secondary current distribution interface which describes the current as well as the potential distribution is also coupled to the free and porous media flow by the same current density term. Each of the interfaces transmits their different output parameters into other interfaces as input parameters. The conservation and constitutive equations accounting for each phenomenon in the different interfaces are then coupled and computed to develop the isothermal SOFC model.

.

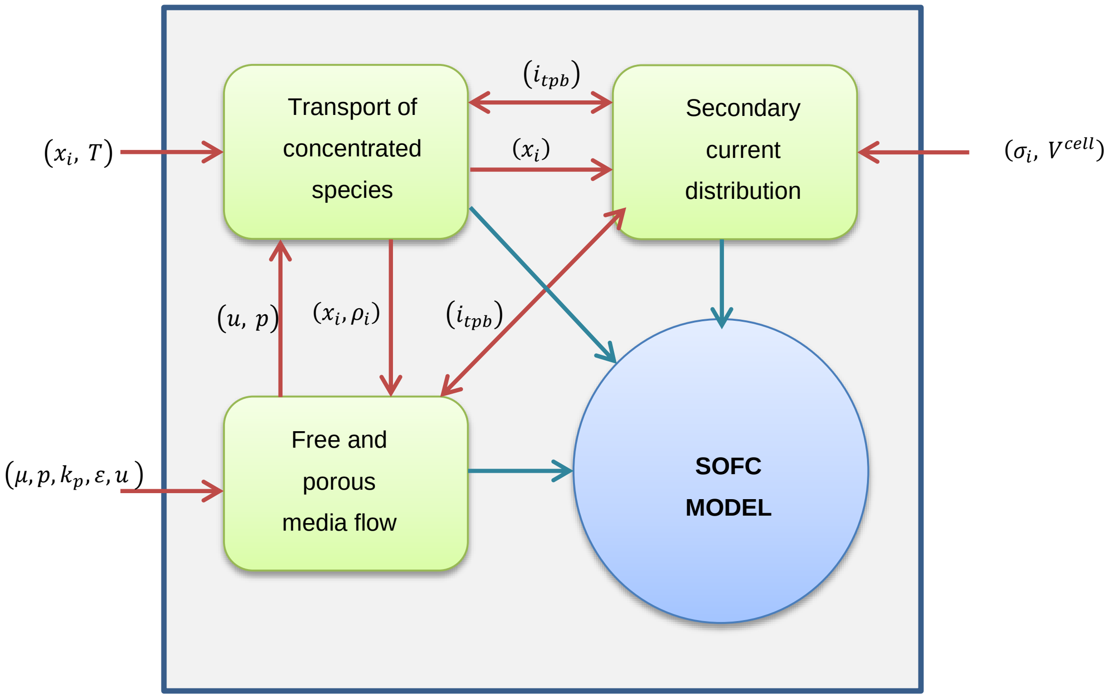

Figure 5-2: Schematic of computational process

5.3 Cell performance validation

The range of validity and accuracy of the hydrogen fed, isothermal SOFC model is determined by comparing experimental data with the numerically developed cell performance result.

To carry out the validation, experimental data from the paper “Effect of cathode current-collecting layer on unit-cell performance of anode-supported solid oxide fuel cells” by Jung et al [208] and the numerical simulation studies carried out by Jeon [83] titled “A comprehensive CFD model of anode-supported solid oxide fuel cells” is used.

5.3.1 Experimental data

The fabrication and testing processes of the experimental cell described in detail by Jung et al in their paper “Effect of cathode current-collecting layer on unit cell performance of anode supported fuel cells” [208] is recapped below.

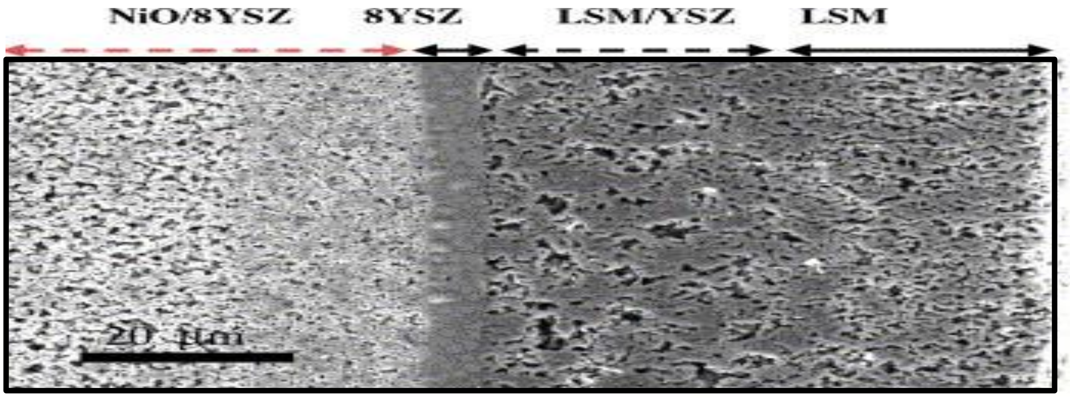

Figure 5-3: Cross-section of SEM micrograph experimental cell[208]

“The anode supported SOFC was fabricated by mixing fine yttria-stabilised zirconia (YSZ), coarse YSZ and nickel oxide (NiO) powders to produce NiO-YSZ anode substrate. The granules of NiO-YSZ composite powders were then compacted by uni-axially pressing into the anode diffusion layer. The anode reaction layer, which has the same composition as the anode diffusion layer but without the coarse YSZ powder was printed on the NiO-YSZ diffusion layer via screen printing. A YSZ electrolyte layer was then screen printed on the anode reaction layer and co fired in air at 1673K for 3hrs

The cathode powder $(La_{0.7}Sr_{0.3})_{0.95}MnO_3$ (LSM) was synthesized using a modified glycine-nitrate process. A thin layer of LSM-YSZ cathode reaction layer was then screen printed on the sintered anode/electrolyte substrate, after which the LSM cathode current collector layer was applied. All the cathode layers were co-fired at 1423K in air for 3hrs.

The current-voltage and current-power characteristics were measured with a SOFC test station at 1073K. Air was used as oxidant and moisturised hydrogen with 3% water ($97\%H_2 + 3\%H_2O$) was used as fuel”.

5.3.2 Numerical approach

Figure 5-4 compares this model simulation with that simulated by Jeon et al[83] and that obtained from the above experimental data[208] at 1073K. The parameters used for the model simulation are listed in Table 5-5. Most of the parameters used in validating the model were obtained from Jung et al[208], other parameters not provided by the experimental report were obtained from literature. The SOFC was simulated with humidified hydrogen as fuel and oxygen component of air as the oxidant, their composition is shown in Table 5-5. The COMSOL simulation results by Dong Jeon[83] was also compared.

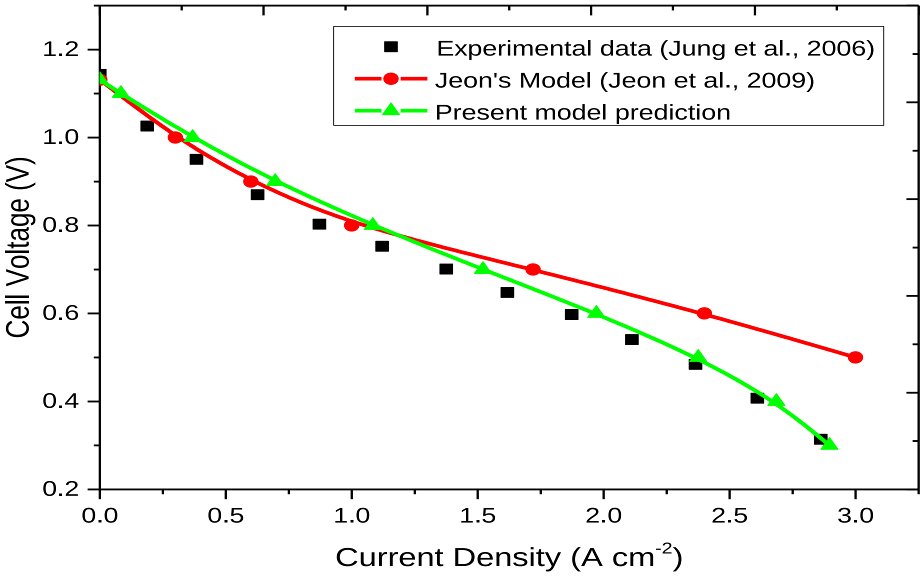

Figure 5-4: Comparison between present model predictions, simulation results of Jeon[83] and experimental results of Jung et al[208] at1073K and 1atm.

The present model predictions gives better overall agreement with the experimental results than those obtained by Jeon[83].The model simulations does not include the interconnect geometry i.e. the contact resistance between the electrodes and the interconnect. At low current densities, when the effect of the contact resistance is high, the model predictions didn't give a good fit with the experimental results, although the simulation by Jeon gave good fitting in that region as they included the interconnect effect, however, at high current densities, the present model gave better fitting than Jeon's model since the in-plane electrode resistance were included.

In other to obtain a good fit between the present simulation and the experimental data, the tortuosity value was varied; also, the diameters of the conducting particles were also assumed.

Table 5-5: Parameters used in validating the model

Parameters	**Value**
Flow channels	
Layer thickness $l_{ch}(\mu m)$	1000
Cell Length, $t_{ch}(\mu m)$	50000
Anode diffusion layer (ADL)	
Layer thickness, $l_{adl}(\mu m)$	1000
Pore diameter, $d_{pore,adl}(\mu m)$	1.4
Porosity, ε_{adl}	0.42
Volume fraction, φ_{adl}	0.4
Permeability, $K_{adl}(* 10^{-12} m^2)$	0.034
Effective conductivity,$\sigma_{adl}(S\ cm^{-1})$	1011
Anode reaction layer (ARL)	
Layer thickness, $l_{arl}(\mu m)$	20
Pore diameter, $d_{pore,arl}(\mu m)$	0.33
Porosity, ε_{arl}	0.097
Volume fraction, φ_{arl}	0.4
Permeability, $K_{arl}(* 10^{-12} m^2)$	0.034
Effective conductivity,$\sigma_{arl}(S\ cm^{-1})$	1011
Cathode diffusion layer (CDL)	
Layer thickness $l_{cdl}(\mu m)$	13
Pore diameter, $d_{pore,cdl}(\mu m)$	1.4
Porosity, ε_{crl}	0.36
Volume fraction, φ_{cdl}	1
Permeability, $K_{arl}(* 10^{-12} m^2)$	0.037
Effective conductivity,$\sigma_{arl}(S\ cm^{-1})$	152
Cathode reaction layer (CRL)	
Layer thickness $l_{crl}(\mu m)$	25
Mean particle diameter, $d_{pore,crl}(\mu m)$	2
Porosity, ε_{crl}	0.4
Volume fraction, φ_{crl}	0.587
Permeability, $K_{arl}(* 10^{-12} m^2)$	0.054
Effective conductivity,$\sigma_{arl}(S\ cm^{-1})$	93
Electrolyte (E)	
Layer thickness $l_{e}(\mu m)$	8
Effective conductivity,$\sigma_{arl}(S\ cm^{-1})$	0.047
Operating conditions	
Operating temperature, $T(K)$	1073K
Total pressure, $p(atm)$	1.0
Fuel inlet composition, x_{H_2} ; $x_{H_2 O}$	0.97; 0.03
Air inlet composition, x_{O_2} ; x_{N_2}	0.21; 0.79

5.4 Results and discussion

As stated earlier, this chapter aims at analysing the electrochemical characteristics of the cell by studying the effect of design and operating conditions on the predicted SOFC performance under isothermal conditions. In order to characterise the cell's performance, the overpotentials in the different components of the cell are first determined. The model predicts the activation and ohmic overpotential in the electrodes and electrolyte as well as the concentration overpotentials in the electrodes.

The role of support structures and the effect of key operating parameters on SOFC performance are investigated. Three basic support structure approaches are proposed in the development of planar SOFCs [107]: the anode-supported, cathode-supported and electrolyte supported SOFCs

Results obtained from the 2-D simulation of the three support structures are presented initially. After which, parametric analysis on key design parameters is carried out.

5.4.1 Role of support structures

Anode-supported SOFC

In the anode-supported SOFC, the anode layer is the thickest component, while the cathode and electrolyte are very thin. The thick anode layer helps in decreasing the ohmic resistance since thin electrolyte layers can now be used, makes them more suited for lower temperatures operation (873-1073K). This would naturally increase the ohmic overpotentials, however, the effect will be minimised by the very thin electrolyte layer used. Due to the reduced operating temperatures, cheaper materials can now be used for the interconnect rather of the expensive high chrome alloys or oxides which would normally be used for high temperature operations, this would result in reduced material and manufacturing costs[35]

The operating conditions and geometric parameters used in the simulation of the anode supported SOFC are listed in Table 5-6. The other parameters for the model are same as those listed in Table 5-1. The simulated performance of the anode supported cell is shown in Figure 5-5.

Table 5-6: Base case parameters used in simulating an anode supported SOFC

Operating temperature, $(T(K))$	1073
Total pressure, $(p(atm))$	1.0
Fuel inlet composition, (x_{H_2}, x_{H_2O})	0.7, 0.3
Air inlet composition, (x_{O_2}, x_{N_2})	0.21, 0.79
Anode diffusion layer thickness, $(l_{adl}(\mu m))$	1000
Anode reaction layer thickness, $(l_{arl}(\mu m))$	20
Electrolyte layer thickness, $(l_e(\mu m))$	10
Cathode diffusion layer thickness, $(l_{cdl}(\mu m))$	50
Cathode reaction layer thickness, $(l_{crl}(\mu m))$	20

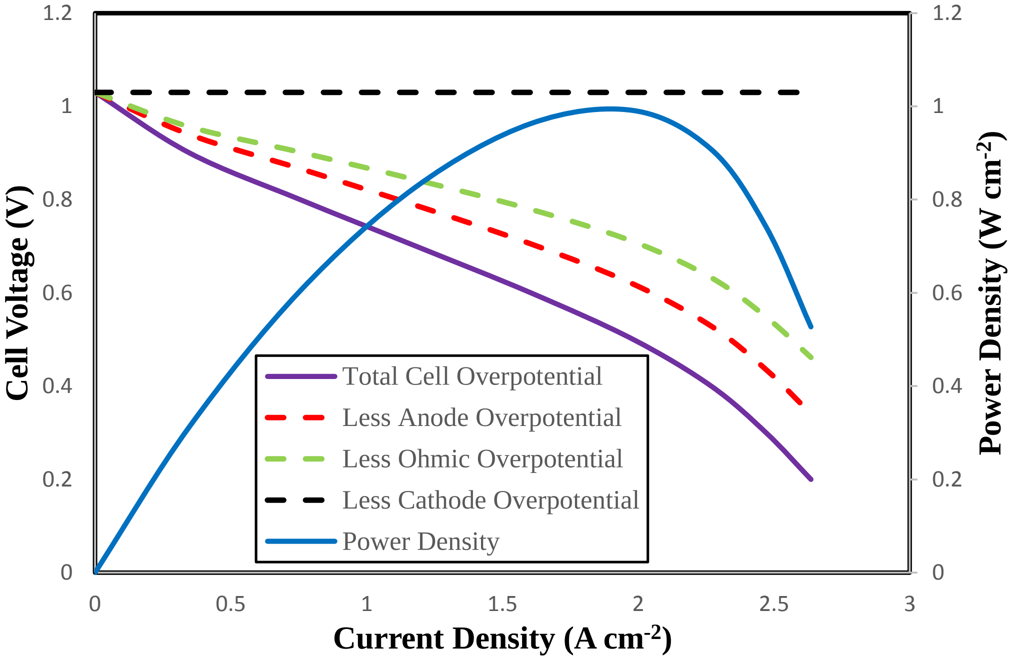

Figure 5-5: Base case performance of an anode supported SOFC at 1073K and 1 atm

The performance curves of the modelled anode-supported SOFC at isothermal conditions are shown in Figure 5-5. The figure illustrates the relationship between the cell voltage and current density on the one hand and also between the power density and the current density at 1073K. The solid lines represents to the cell voltage and power density curves. The cell voltage decreases as the current density increases due to the irreversible resistances in the SOFC, these irreversibility's are known as overpotentials. The overpotentials are represented by the dashed lines in the Figure. The overpotentials on the electrodes (anode and cathode) include activation overpotentials (resistance to the charge transfer reactions), concentration overpotentials (resistance to the flow of reactant species through the pores to the reaction sites) and ohmic overpotentials (resistance to the flow of ions and electrons in the reaction layers and the resistance to the flow of electrons in the diffusion layers). The electrolyte ovepotential include only the ohmic overpotentials due to the flow of ions in the electrolyte.

The cell voltage curve exhibits regions of activation overpotential at low current densities and concentration overpotentials at high current densities. The power density is observed to increase to a maximum of 0.99 W cm^{-2} at a current density of 1.98 A cm^{-2} and a cell voltage of 0.49V, after which it begins to decrease towards zero. SOFC's are usually designed to operate at 0.7V[47] thus based on Figure 5-5, the best operating point for the cell would be at current density of 0.87 A cm^{-2} leading to a power density of 0.84W cm^{-2} .Although the cell under study is an anode-supported one, it can be observed that the cathode overpotential represents the major losses within the cell.

To understand this observation better, the contribution of each cell component to the overall overpotentials are further investigated.

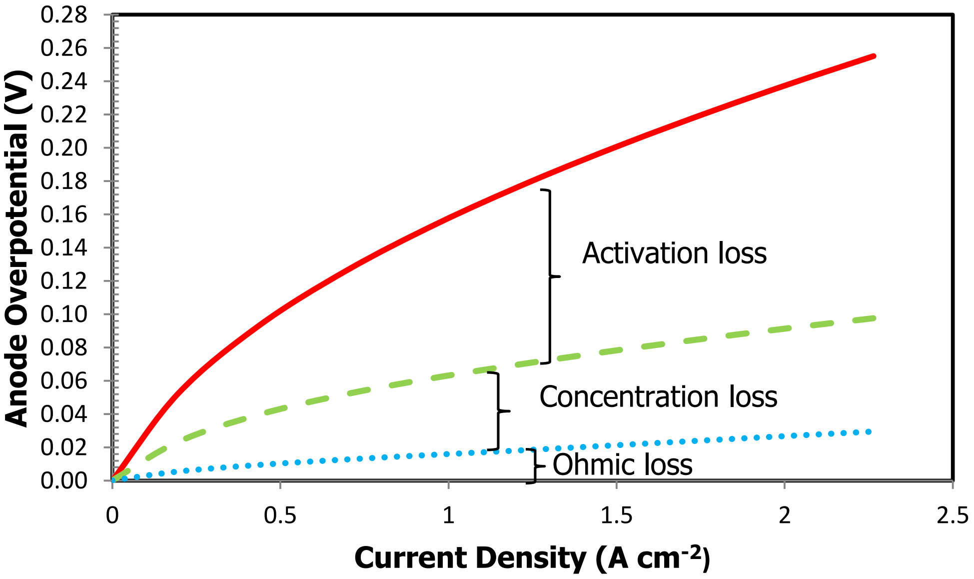

Figure 5-6: Anode Overpotential of an anode-supported SOFC at 1073K and 1atm

The anode overpotential at base condition is shown in Figure 5-6. It is clear that the activation overpotential is the most significant amongst all the overpotentials in the anode, followed by the concentration overpotential which is due to the thick electrode diffusion layer. A thick electrode layer inhibits the diffusion process by slowing down the diffusion of H_2 gas to the reaction sites which leads to a decrease in its partial pressure at the site. However, the partial pressure of H_2O simultaneously increases at the reaction site since H_2O a product of the electrochemical reaction, consequently, the concentration overpotential will be significantly large under these conditions.

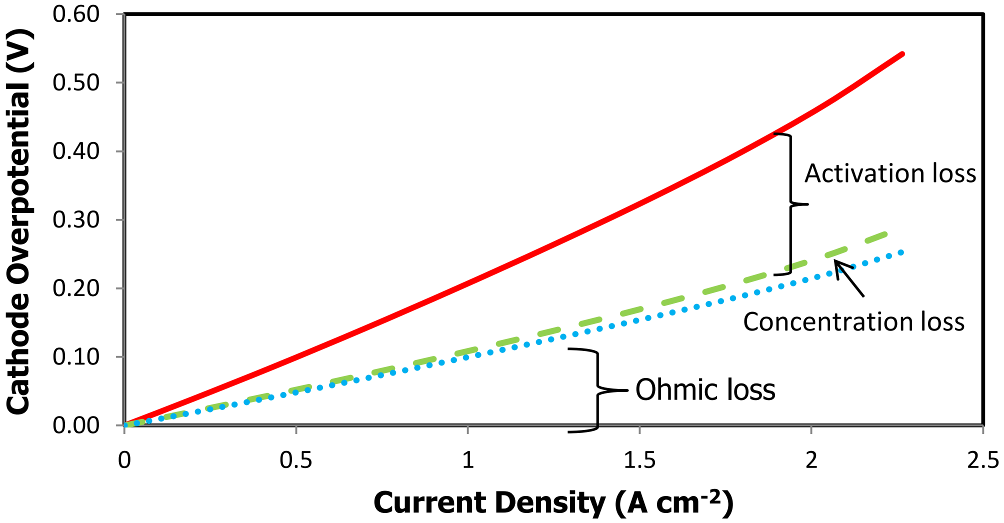

Figure 5-7: Cathode Overpotential of an anode supported SOFC at 1073K and 1atm

On the other hand, the cathode concentration overpotential is negligible small; this is due to the very thin cathode electrode layer. nonetheless, the contributions of the activation overpotential is significant as a result of the sluggish resistance of the oxygen ion transfer reaction and its low exchange current density, its ohmic overpotential is also quite high due to its low electronic conductive (conductivity is inversely proportional to the ohmic losses) and due to the presence of ions in the reaction layer. These are shown in Figure 5-7 for the cathode side overpotential.

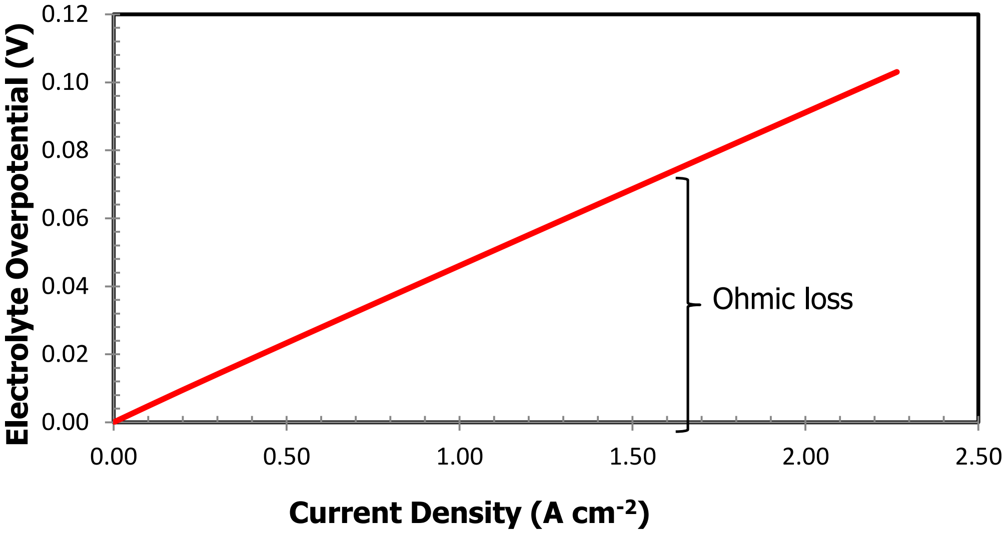

Figure 5-8: Electrolyte overpotential of an anode supported SOFC at 1073K and 1atm

The electrolyte overpotential is all ohmic as a result of the resistance to the transfer of ions in the layer, this is shown in Figure 5-8.

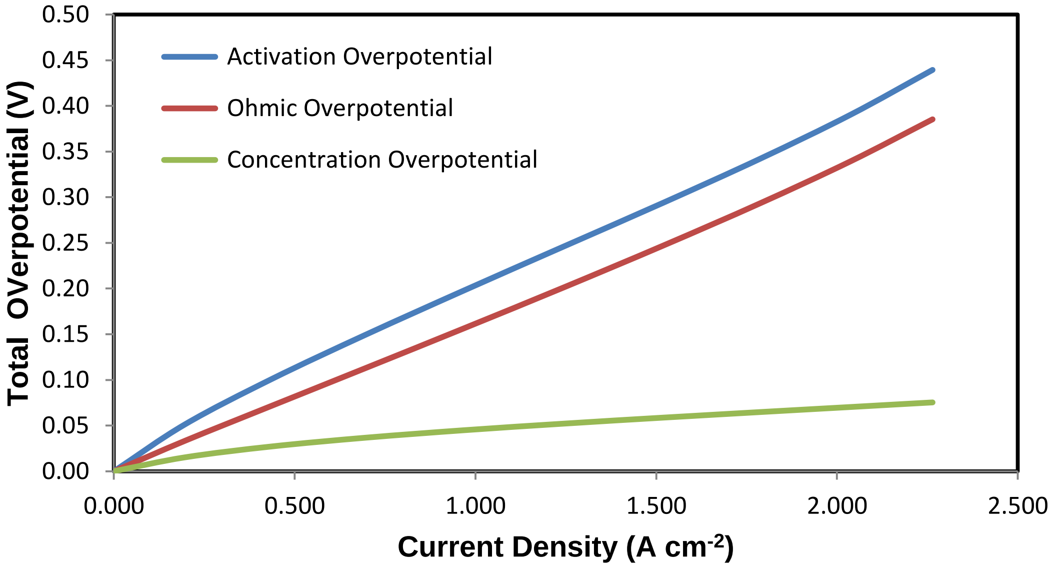

Figure 5-9: Sum total of the different overpotentials in the anode supported SOFC

Furthermore, when all the overpotential are summed together as seen in Figure 5-9, the activation overpotential remains the largest contributor to the overall cell voltage loss in anode supported SOFCs representing 48.7% of the total cell overpotential at

1.5A cm^{-2}. The ohmic overpotential is also quite significant, representing 41.5% of the total overpotential. This can be attributed to the presence of ion conducting particles in the reaction layers of the electrodes, which contributes significantly to the overall ohmic overpotential. Hence, there is a need to enhance the cells ionic conductivity either by developing new materials or altering the geometric designs in other to improve the performance of anode-supported SOFCs.

Cathode-supported SOFC

In cathode-supported SOFCs, the cathode electrode layer is the thickest component; the other layers are kept thin. Cathode supported cells are considered advantageous because of the reduced risk of carbon poisoning in thin anode layers when hydrocarbon fuel is used[209], furthermore, the risk of Ni oxidation by water is reduced in thin anode layers[210], in addition to the ohmic polarisation as a result of the thin electrolyte thickness.

The operating conditions and geometric parameters used in this simulation are listed in Table 5-7. The other parameters for the model are same as those listed in Table 5-1. The simulated performance of the cathode supported cell is shown in Figure 5-10.

Table 5-7: Base case parameters used in simulating a cathode supported SOFC

Operating temperature, $(T(K))$	1073
Total pressure, $(p(atm))$	1.0
Fuel inlet composition, (x_{H_2}, x_{H_2O})	0.7, 0.3
Air inlet composition, (x_{O_2}, x_{N_2})	0.21, 0.79
Anode diffusion layer thickness, $(l_{adl}(\mu m))$	50
Anode reaction layer thickness, $(l_{arl}(\mu m))$	20
Electrolyte layer thickness, $(l_e(\mu m))$	10
Cathode diffusion layer thickness, $(l_{cdl}(\mu m))$	1000
Cathode reaction layer thickness, $(l_{crl}(\mu m))$	20

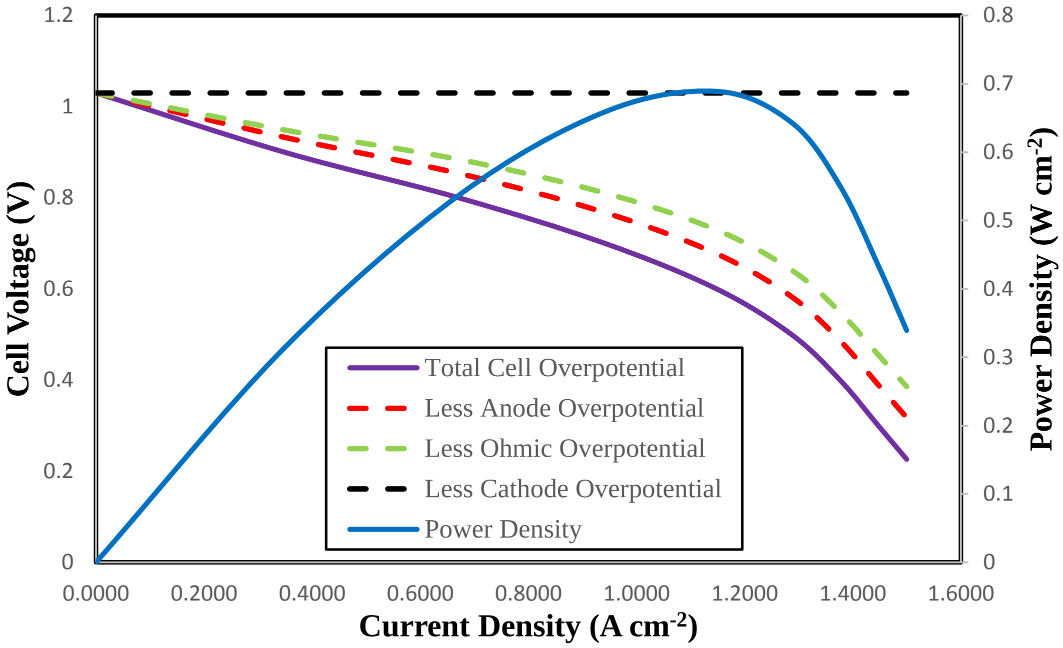

Figure 5-10: Base case performance of a cathode supported SOFC

The performance curves for the cathode-supported SOFC are shown in Figure 5-10. The figure illustrates the cell voltage versus current density and cell voltage versus power density curves at 1073K. The solid lines represent the cell voltage and power density while the dashed lines represent the contributions of the individual overpotentials.

The curve is seen to concentration overpotential at regions of high current densities. The maximum power density obtained from the curve is shown to be 0.71 W cm^{-2} at a current density of 1.16 A cm^{-2}. As seen, the most significant contributor to cell voltage loss is the cathode overpotential, which accounts for 66.7% of the total overpotential at current density of 1.00 A cm^{-2}, the cathode concentration overpotential remains quite small in comparison to the other overpotentials even though it is a cathode-supported cell, as shown below in Figure 5-11,

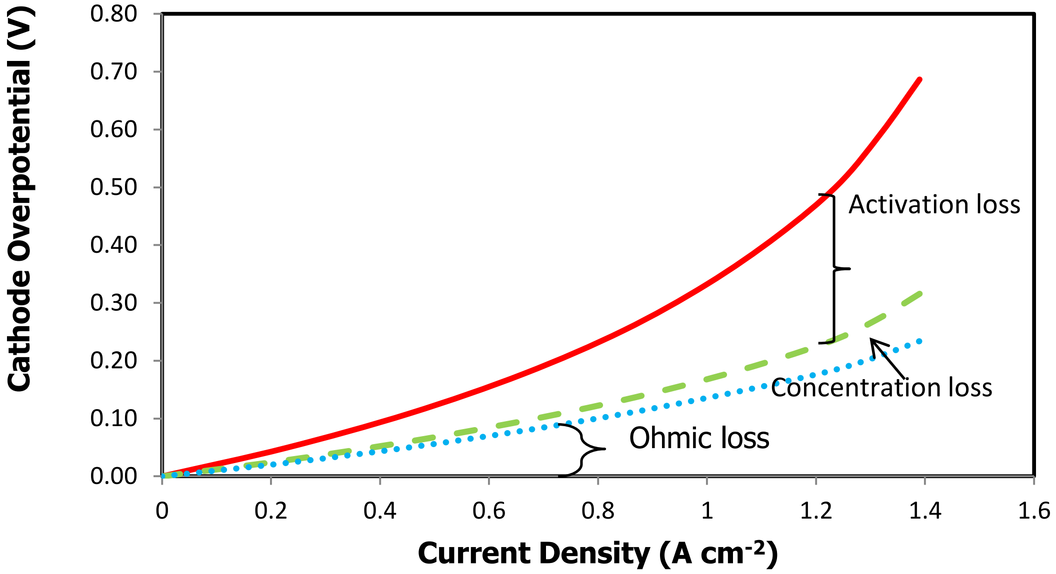

Figure 5-11: Cathode overpotential of a cathode supported SOFC

The anode and electrolyte overpotentials are relatively small due to their thin layers as shown in Figures 5-12 and 5-13 respectively.

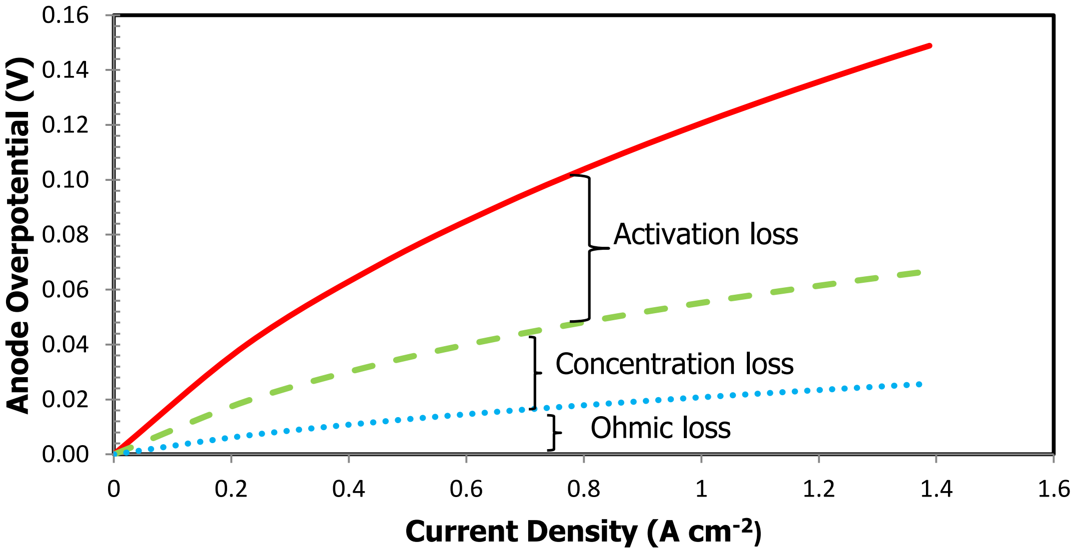

Figure 5-12: Anode overpotential of a cathode supported SOFC

The most significant contributor on the anode side is the activation overpotential.

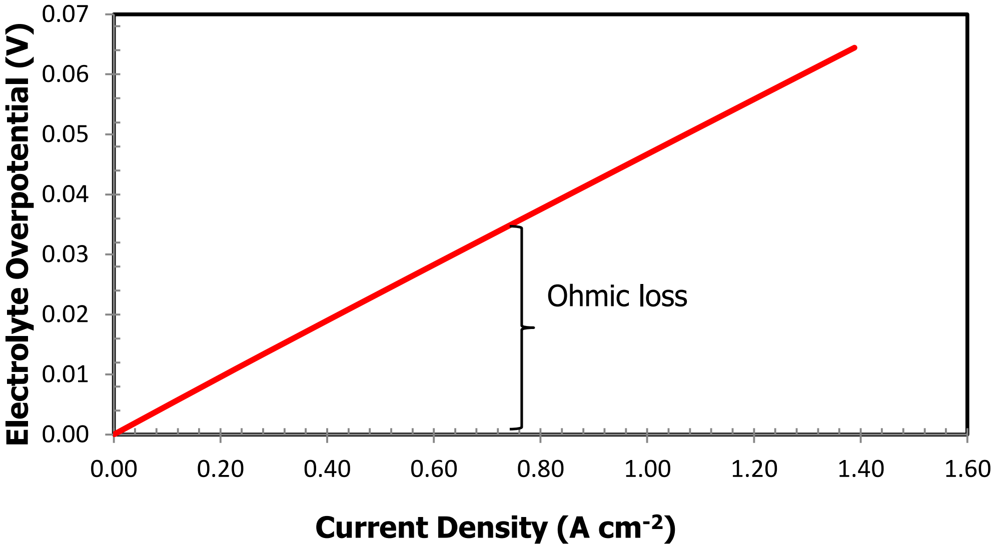

Figure 5-13: Electrolyte overpotential of a cathode supported SOFC

Furthermore, as can be seen from Figure 5-14, that the activation overpotential from both cathode and anode sides represents the largest contributor to the overall overpotential in cathode-supported SOFCs representing 53.8% of the total cell overpotential at 1.0 A cm^{-2}

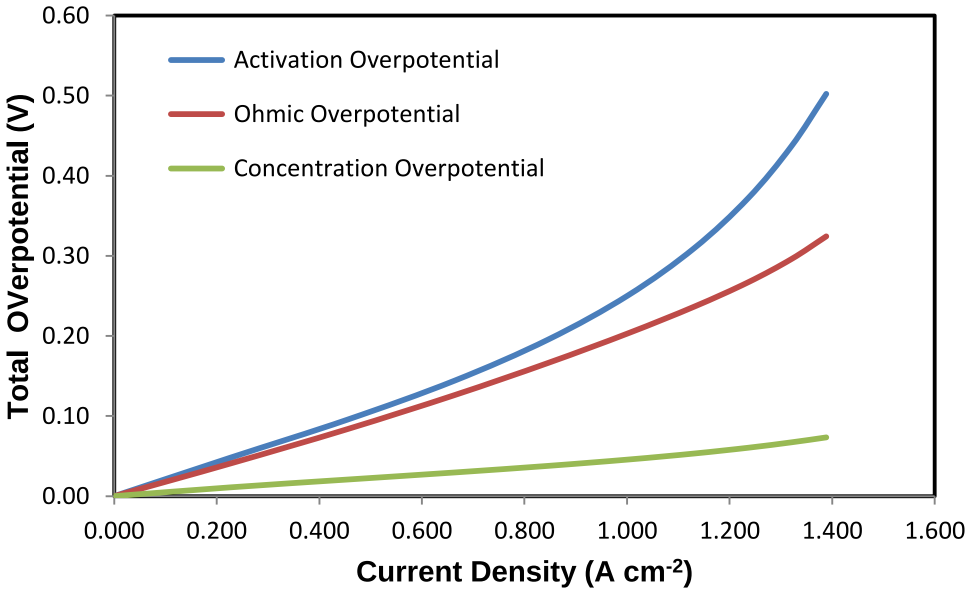

Figure 5-14: Sum total of the different overpotential in a cathode supported SOFC

Electrolyte-supported SOFC

In this simulation, the electrolyte is modelled as the thickest component while the other layers are very thin. The thick electrolyte layer usually results in high ohmic resistance due to the reduced operating temperature (1073K). Thus, more effort is focussed on high temperature operation for electrolyte-supported SOFCs in a bid to reduce the ohmic resistance [107]

The parameters used in simulating the electrolyte-supported SOFC are listed in Table 5-8, while other design parameters used are same as those used for the other support structure models and listed in Table 5-1.

Table 5-8: Base case parameters used in simulating an electrolyte supported SOFC

Operating temperature, $(T(K))$	1073
Total pressure, $(p(atm))$	1.0
Fuel inlet composition, (x_{H_2}, x_{H_2O})	0.7, 0.3
Air inlet composition, (x_{O_2}, x_{N_2})	0.21, 0.79
Anode diffusion layer thickness, $(l_{adl}(\mu m))$	50
Anode reaction layer thickness, $(l_{arl}(\mu m))$	20
Electrolyte layer thickness, $(l_e(\mu m))$	1000
Cathode diffusion layer thickness, $(l_{cdl}(\mu m))$	50
Cathode reaction layer thickness, $(l_{crl}(\mu m))$	20

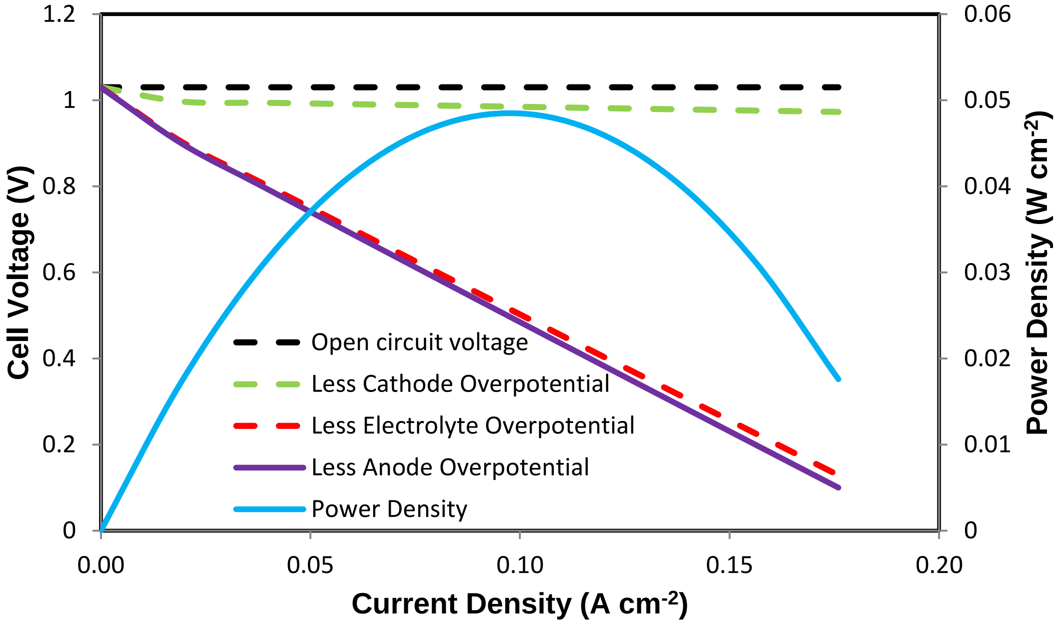

Figure 5-15: Base case performance of an electrolyte supported SOFC at1073K and 1atm

The performance of the electrolyte supported SOFC is shown in Figure 5-15 illustrating the variations of cell voltage and power density against the current density. Again, the solid line represents the cell voltage and power density, while the dashed lines represent the overpotentials. It can be seen that the cell performance exhibits only ohmic overpotentials at regions of low and high current densities, and does not exhibit either activation or concentration overpotentials, indicating their negligible contribution in electrolyte supported SOFC's

The maximum power density obtained from the electrolyte supported SOFC operating at 1073K is 0.053W cm^{-2} at current density of 0.12 a cm^{-2}. Furthermore, that the largest contributor to cell voltage loss is the ohmic overpotential in the electrolyte; whereas the anode and cathode overpotentials are totally negligible in the overall cell performance.

The extremely high ohmic overpotential in the electrolyte which accounts for about 98.3% of the total cell overpotential can be attributed to the temperature dependent ionic conductivity in the electrolyte, hence the need to operate electrolyte-supported SOFC at high operating temperature so as to reduce the ionic conductivity and consequently the ohmic overpotential.

Performance comparison with different support structures.

Figure 5-16 shows the performance comparison with the different support structures (anode, cathode and electrolyte supported). As can be seen in the figure, the anode-supported SOFC's performance is much better than those of the cathode-supported and electrolyte supported. The anode supported cell has higher power densities and its current density range is wider than the others, this implies it would have a smaller cell area than the others with the consequent reduction in manufacturing cost.

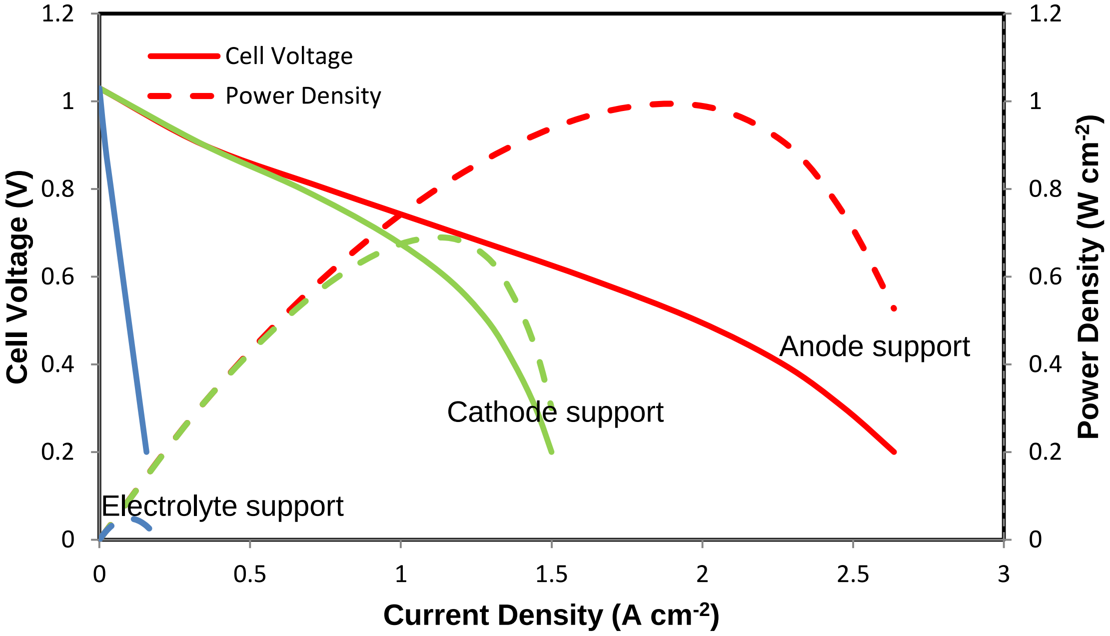

Figure 5-16: Performance comparison of the different support structures at 1073K and 1atm

From simulation results expressed in Figure 5-16, it can be seen that the electrode-supported SOFCs displays better cell performance than electrolyte supported, in addition, the electrolyte- supported SOFCs are usually operated at high operating temperature in order to reduce its high ohmic overpotentials which consequently means it requires expensive alloys as interconnectors, thereby increasing material and manufacturing cost. On the other hand, the anode supported SOFCs exhibits the best performance at reduced operating temperature. Operating SOFC's at reduced temperature allows many of the material-related problems to be resolved. Thus, anode supported design of SOFCs holds more potentials for the commercialisation process for planar SOFCs. Therefore, the next section further investigates the effect of geometric parameters and operating conditions on the performance of an anode-supported SOFC.

5.5 Parametric studies

A parametric analysis is carried out in order to investigate the sensitivity of the simulated model, this is done by studying the effect of varying operating conditions and the geometric features on the performance of the simulated 2-D anode supported SOFC.

5.5.1 Effect of temperature

The performance curves for an anode supported SOFC at varying operating temperatures is shown in Figure 5-18. Anode supported SOFCs are usually operated at temperatures between 873K and 1073K, described as the intermediate temperature operation, as such, this temperature range will be used in examining its effect on cell performance. Furthermore, all other parameters used in the simulation are kept constant.

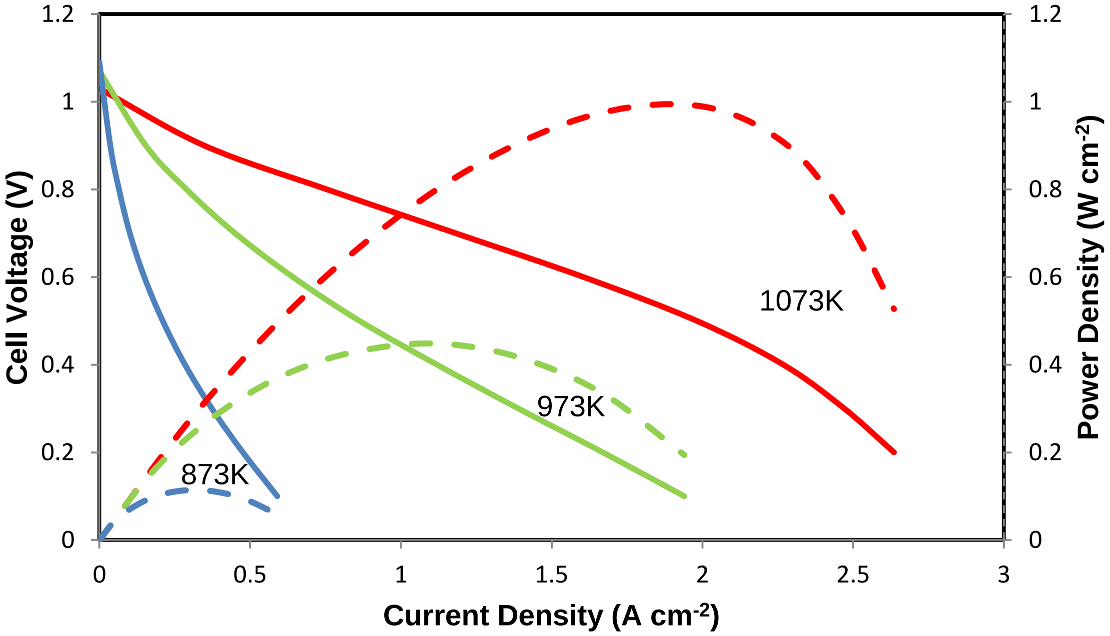

Figure 5-17: Effect of inlet temperature on cell performance

It can be seen from Figure 5-17 that the cell performance improves as the operating temperature is increased, with the maximum power density increasing from 0.049 W cm^{-2} at 873K (at a current density of 0.1 A cm^{-2} and a cell voltage of 0.5V) to 0.51W cm^{-2} at 973K (at a current density of 0.55 A cm^{-2} and a cell voltage of 0.55V) and to 0.99 W cm^{-2} at 1073K (at a current density of 1.96 A cm^{-2} and a cell voltage of 0.45V). The increasing operating temperature leads to a reduction of the open circuit voltage (i.e. the cell voltage at zero current density) and an increase the limiting current density (i.e. the current density at zero cell voltage).

The improved cell performance at increased operating temperature is not only due to the increased rate of electrochemical reaction at the reaction sites (due to the higher operating temperatures), but also due to the effect of temperature dependence of the individual overpotentials in the cell as shown in Figures 5-18 (a-c)

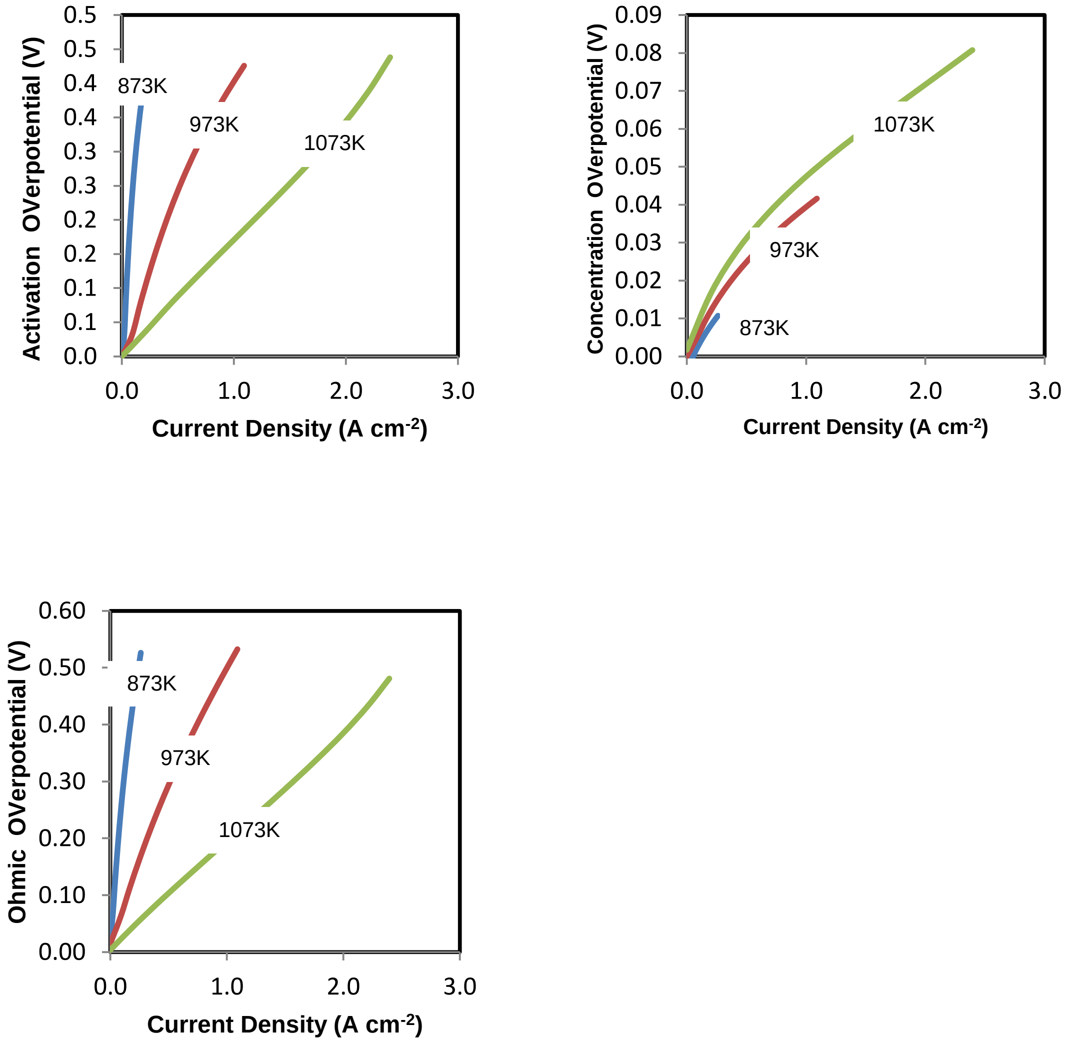

Figure 5-18: Effect of inlet operating temperature on (a) Activation Overpotential (b).Concentration overpotential (c) Ohmic Overpotential.

The ohmic polarisation is temperature dependent due to the thermally activated dependence of YSZ in both reaction layers and the electrolyte; as a result, the higher the temperature, the higher the conductivity which in then reduces the ohmic overpotentials and consequently improves cell performance as shown in Figure 5-18c.

The activation overpotential is also thermally activated, this is reflected in the exchange current density which is temperature dependent, as such when the operating temperature is high, the activation overpotential gets lowered. The reduced activation overpotential leads to improvement in the cell performance, as shown in Figure 5-18a

On the other hand, the concentration overpotential is weakly dependent on the operating temperature; this is reflected through the temperature dependence of the partial pressures of the reactant gases H_2 and O_2 at the reaction sites as well as through the effective diffusivities. The binary diffusion coefficients are proportional to $T^{3/2}$ using the Fuller diffusion model(see Table 5-1) this reduces the mass diffusion resistance in the thick anode thereby increasing the concentration overpotential when the operating temperature is increased; as seen in Figure 5-18b.

Thus, the improvement on cell performance of the anode-supported SOFC at increasing temperature is primarily due to the reduced ohmic and activation overpotentials.

As earlier discussed, there are many advantages to reducing the operating temperature of SOFCs in terms of cost and ease of manufacturing, however as seen in Figure 5-18, there is a corresponding drop in cell performance when this is done, thus the need to enhance the ionic conductivity in the electrodes and electrolyte in order to effectively operate SOFCs below 1073K.

5.5.2 Effect of pressure

The effect of operating pressure on cell performance is shown below, the pressure is varied from 0.5 atm to 3 atm while all other parameters are kept at base conditions.

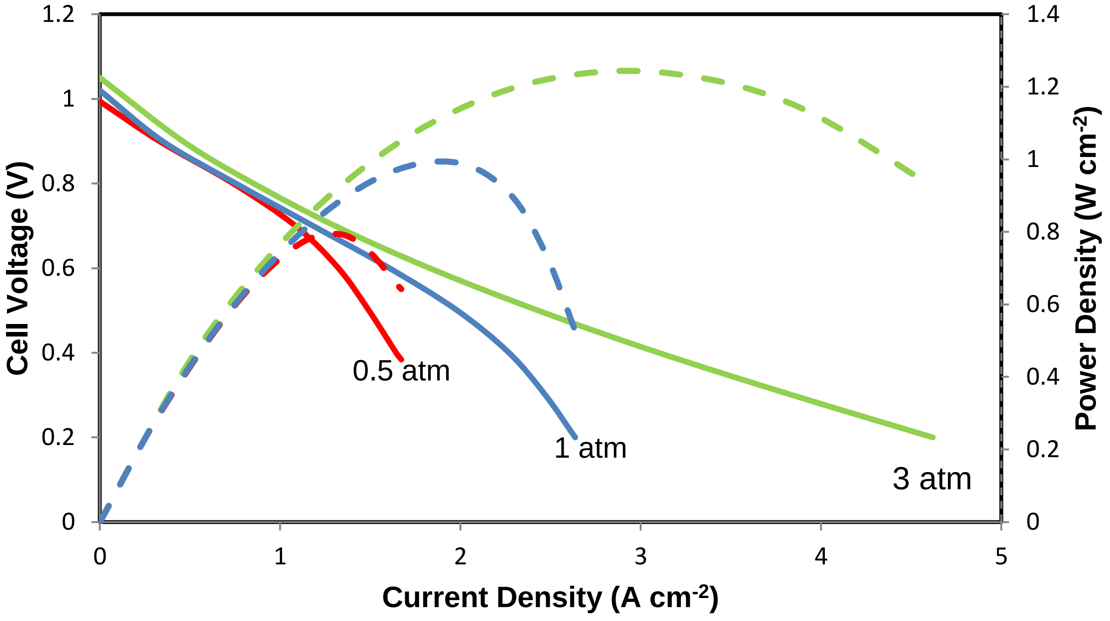

Figure 5-19: Effect of operating pressure on cell performance.

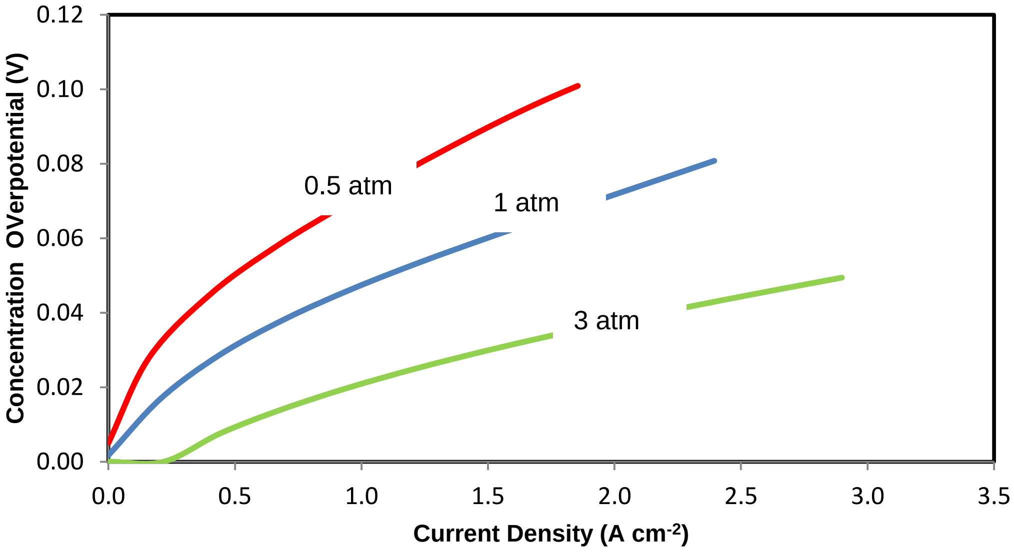

Figure 5-20: Effect of operating pressure on concentration overpotential

It is observed from Figure 5-19 that when the operating pressure is increases, the cell performance improves. This is due to increased reactant concentration at the reaction layer due to the ease with which the fuel and oxidant diffuses, this will then lead to an increase in the electrochemical reaction and mass diffusion rates, causing a reduction in the concentration overpotential as shown in Figure 5-20 and hence enhanced cell performance. Also, at high operating pressures, the open circuit voltage increases, resulting in the minimisation of the activation overpotential which also results in improved cell performance.

Increasing the operating pressure of anode-supported SOFCs may seem a viable option to increasing its performance, however it also results in a number of constraints such as material selection limitations, gas sealing problems and issues with mechanical strength[21]; these have to be taken into consideration before increased pressure could be an option.

5.5.3 Effect of SOFC geometric parameters on overpotentials

The impact of the individual cell component thickness on overpotential is analysed here. Figure 5-21 shows the variation of the anode side overpotential with the ARL thickness (L_{arl}) at 0.7V when all the other geometric parameters are kept constant. Significant reduction in anode overpotential is observed when L_{arl} is increased from 5µm to 14µm, this may be attributed to the increase in the reactive surface area, which enhances the electrochemical reaction rate and consequently reduces the overpotential. However, the anode overpotential is seen to increase with further increases in the ARL thickness. This is due to the increase in concentration and ohmic polarisation which sets in due to the thicker ARL. Also, at thicker diffusion layers, a reduction in concentration of the species are expected, this leads to higher activation polarisation. Thus the optimum thickness of the ARL is set at 14µm.

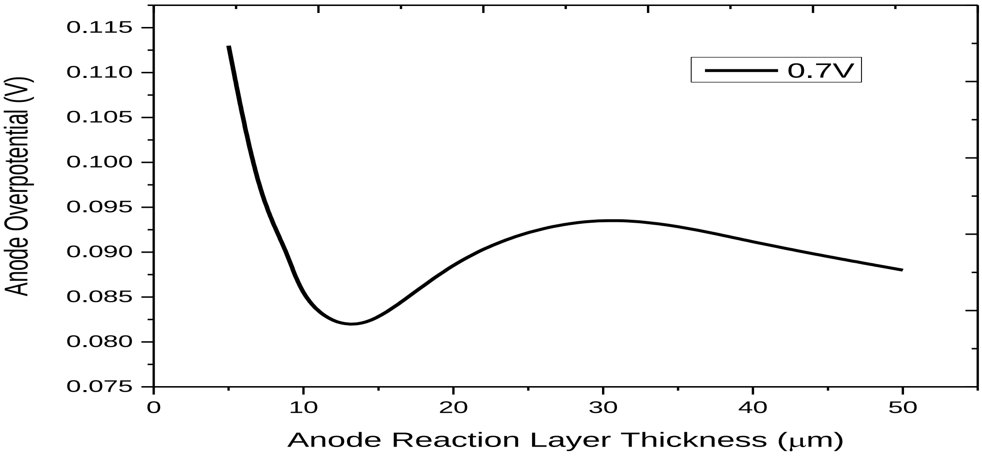

Figure 5-21: Effect of anode reaction layer thickness on anode overpotential

The relationship between anode overpotential and the anode diffusion layer thickness (L_{adl}) is presented in Figure 5-22 for diffusion layer thickness ranging between 500 and 3000μm while all the other geometric parameters are kept constant. The profound effect of the thickness on polarisation is clearly seen in the figure above. Increased thickness increases the resistance of the gaseous species through the diffusion layer resulting in increased concentration polarisation. It is thus important to make the layer as thin as possible, although from the view point of cell support and mechanical ruggedness, the lower limit of 500μm is suitable.

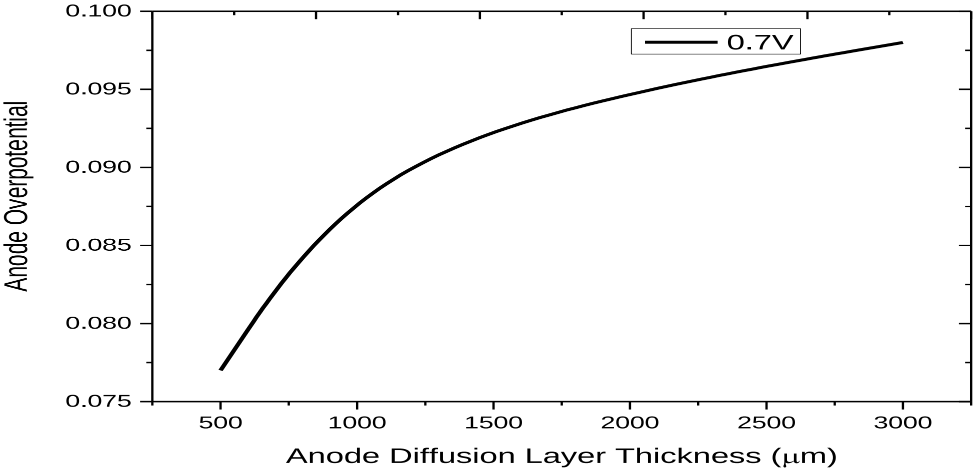

Figure 5-22: Effect of anode diffusion layer thickness on anode overpotential

The cathode overpotential is probably the most important component of the total SOFC overpotential as it accounts for about 60% of the total overpotential at large current densities (see Figure 5-5). The CRL thickness is an important factor affecting the overpotential. Figure 5-23 shows the variation of the cathode overpotential with the CRL thickness (L_{crl}). A reduction in the overpotential is observed when the L_{crl} is increased from 5 to 10µm, further increases in L_{CRL} increases the overpotential. This is because of an increase in the activation overpotential resulting from the reduced concentration of O_2 at the layer and the increased ohmic overpotential due to the thicker layer. Therefore, the optimum L_{crl} is set at 10µm.

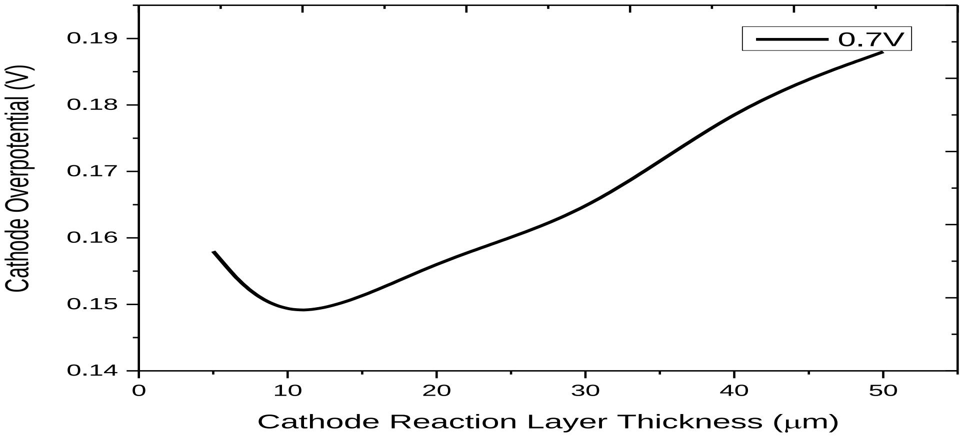

Figure 5-23: Effect of cathode reaction layer thickness on cathode overpotential

Figure 5-24 shows the effect on cathode overpotential of cathode diffusion layer thickness between 20 and 200µm, increasing the thickness does not have any significant effect on overpotential as it remains constant, based on the insignificant contribution of concentration overpotential even at the higher limit of 200µm. The optimum thickness is arbitrarily set at 85µm.

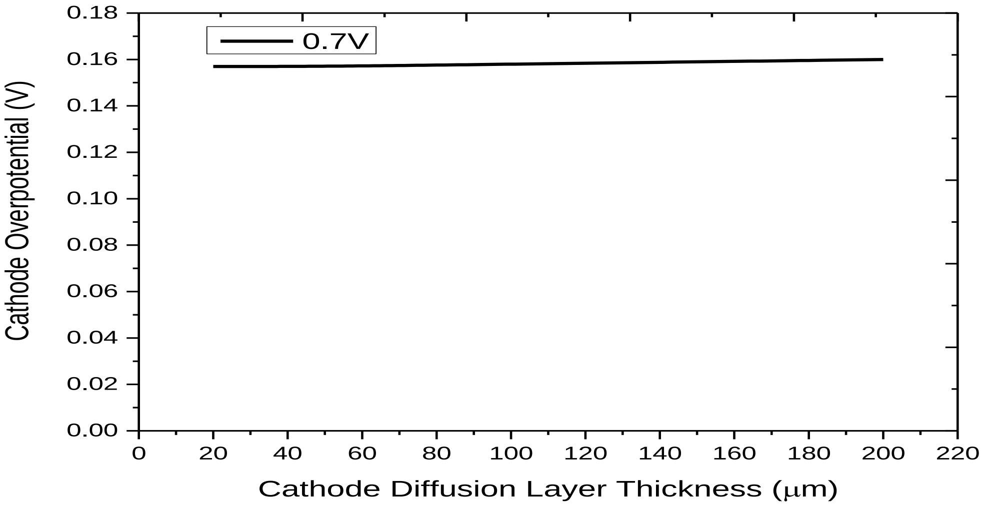

Figure 5-24: Effect of cathode diffusion layer thickness on cathode overpotential

The impact of electrolyte thickness on the electrolyte overpotential is presented in Figure 5-25. The electrolyte thickness is varied from 5- 50µm while all other geometric parameters are kept constant. The profound effect of electrolyte layer thickness on the overpotential is clearly seen. This is due to the increased ohmic overpotential as the thickness is increased, thus making the electrolyte layer as thin as possible is important, although from the viewpoint of ease of fabrication, probably the lower limit is about 10µm

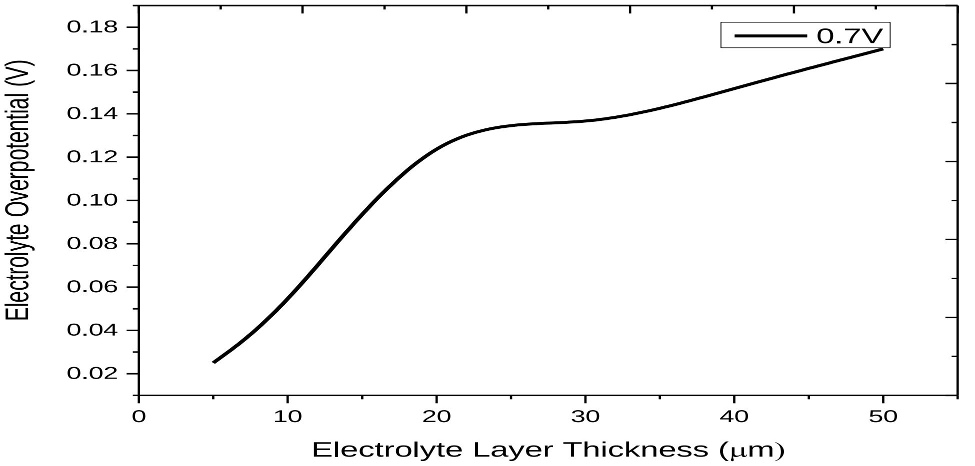

Figure 5-25: Effect of electrolyte layer thickness on electrolyte overpotential

5.6 The optimised cell

A comparison of the base case simulated cell and the optimised cell based on geometric parameters is presented in Figure 5-26. The optimised geometric parameters are tabulated in Table 5-9

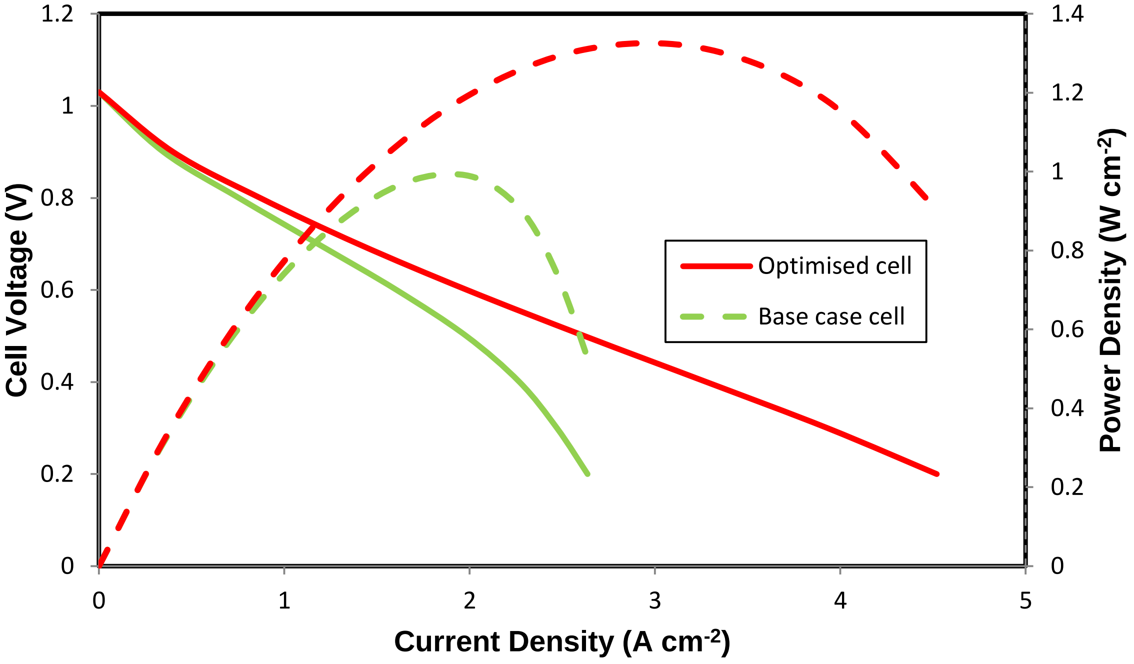

Figure 5-26: Performance comparison of optimised and base case cell

Table 5-9: Optimised geometric parameters used in simulating the anode supported SOFC

Anode diffusion layer thickness, $(l_{adl}(\mu m))$	500
Anode reaction layer thickness, $(l_{arl}(\mu m))$	14
Electrolyte layer thickness, $(l_e(\mu m))$	10
Cathode diffusion layer thickness, $(l_{cdl}(\mu m))$	80
Cathode reaction layer thickness, $(l_{crl}(\mu m))$	10

The optimised cell exhibits a maximum power density of 1.32 W cm^{-2} while that of the base case simulated cell was 0.99W cm^{-2}, signifying a 20% reduction in the total cell overpotential at a current density of 2.4 A cm^{-2}. However, it should be noted that it was only the geometric parameters that were varied to optimise the cell. Clearly further performance gains are to be expected when the microstructural parameters are varied. This will be carried out in Chapter 6.

5.7 Conclusions

The solution obtained from the numerical implementation of the two dimensional, along the channel, microscale, steady state, isothermal SOFC model is presented. The electrochemical model is first validated with measured experimental data and simulated data published in literature by measuring the cell performance. The developed model is then used to predict the performance of three different support structures, namely anode-supported, cathode supported and electrolyte supported. At intermediate temperature conditions, the anode supported SOFC exhibits the best performance amongst all three support structures.

Considering the individual cell voltage losses, for the anode-supported SOFC, it was found that the cathode ohmic overpotential was the single largest contributor, followed by the cathode activation and the electrolyte ohmic overpotentials. On the other hand, the cathode activation overpotential is the largest contributor in the cathode-supported SOFC while the electrolyte ohmic overpotential was the overwhelming largest contributor for the electrolyte supported SOFC, accounting for 98% of the total cell overpotential.

Following, the two dimensional anode-supported SOFC developed was used to study the effect of key operating condition and design conditions on the performance of cell, with the aim of probing the robustness of the model as an optimisation tool. It was found that reducing temperature below 1073K results in significant drop in the SOFC performance while at the same time, reduced temperatures leads to reduction the material and manufacturing costs. Increasing the operating pressure was observed to increase the SOFC performance considerably; however a number of constraints such as material selection and mechanical rigidity could limit this. In addition, the effect of varying geometric parameters on SOFC performance was studied, it was found that the individual layer thickness has profound effect on the overpotentials. Optimum values were obtained for each layer thickness with a view to optimising the cell.

Finally, the optimised layer thicknesses obtained were then used to simulate the optimised SOFC performance. It was found that the optimised cell was considerably better than the base case cell accounting for a 20% reduction in the overall cell overpotential.

CHAPTER6 : Non-Isothermal SOFC model

This chapter describes the development of a two dimensional, along the channel, steady state anode supported intermediate temperature planar SOFC model with direct internal reforming model characteristics on the binary spherical particles electrode structure. The model incorporates the distinct layer porous electrodes, solid ceramic electrolyte and flow channels as described in chapter 1. The model takes into consideration the micro-scale transport, energy transport, steam reforming reactions, water-shift gas reaction and electrochemical reactions occurring in the cell. The impact of thermal considerations, internal reforming, changes in inlet temperatures and the effect of micro-structural parameters on the performance of the steady state cell are also investigated. Optimisation studies are also carried out on the microstructural parameters in the reaction layers of the electrodes.

6.1 Introduction

SOFCs are one of the more prominent fuel cells due to their potential for high energy efficiency and their ability to convert the chemical energy in hydrocarbons into electrical energy. This process involves the heat transfer between different reaction processes occurring in the cell such as the endothermic methane steam reforming reaction (MSR), exothermic water-gas shift reaction (WGS) and the electrochemical reaction. As a result of heat transferred during the operation of the SOFC, thermal management is important due to the effect of temperature on material properties, chemical kinetics and phase transfer parameters [44, 113]. Therefore, it is useful to incorporate a heat transfer model that accounts for various heat transfer processes in both the solid structures and flow channels of the cell.

Numerous mathematical models have been developed which accounts for heat transport and aims at fully understanding its coupling to the species and momentum transport occurring in the cells [46, 91-93, 97, 157, 211].

Ackmann et al[100] simulated a planar SOFC model in which the energy equations were incorporated and coupled to the mass transport equations, their heat transfer model accounted for the heat convection in the channel and conduction in the electrodes and electrolyte while ignoring the heat transfer by radiation and heat transfer by convection in the electrodes.

Models developed by Anderson et al[76], Nagel et al[211] and Damm et al[212] improved on previous heat transfer models by assuming local thermal equilibrium between the gas and solid in the electrodes leading to a single conductive-convective governing equation describing the heat transfer in the electrodes.

Jeon's[83] model studied the potential gain due to temperature increasing inside the cell, they did this by comparing the difference between isothermal cell performances and non -isothermal cell, their model confirms a significant gain in potential between the isothermal and non-isothermal models at high current density confirming the importance of non-isothermal modelling of SOFCs.

The ability of SOFCs to reform hydrocarbons such as methane or natural gas into hydrogen within the anode[14] is a key feature of SOFCs, this reaction is known to occur predominantly at temperatures between 873K and 1173K[44] making it compatible with intermediate temperature SOFCs. The heat required for the endothermic reforming reaction is provided by the exothermic electrochemical reactions in the cell.

Aguiar et al[47] studied the performance of an anode supported SOFC with direct internal reforming for co-flow and counter-flow configuration, their result shows that the counter-flow configuration gives rise to a high temperature gradient and an uneven current density distribution.

Morel et al[136] also studied the direct internal reforming process of methane by developing a combined heat and mass transport SOFC model. The model takes considered the mass transport along the channel and diffusion through the porous electrode as proposed by Lennart et al[68] while the kinetics of the chemical reactions are expressed as a function of temperature from the Arrhenius law as described by Ackmann[100].

Klein et al[151] presented a 2D model in which the effect of the mole fraction ratio of steam to methane on reforming and shift kinetics were studied.

Yuan et al[74] also developed a 3D model in which they studied the effect of hydraulic diameter, the permeation length ratio and the permeation rate ratio on the transport processes and chemical reactions occurring in the cell.

In the 1D model developed by Yingwei et al[213], they observed that direct internal reforming has significant effect on the cell temperature, the anode gas composition distribution, solid temperature gradient and the current density along the cell length direction.

6.2 Model description

6.2.1 Computational domain and assumptions

The computational domain is the same as that described for the isothermal hydrogen fed SOFC model in Chapter 5. The assumptions also remain the same as in Chapter 5 except that the temperature distribution throughout the cell is no longer uniform and local thermal equilibrium is assumed between the gas and solid phases of the porous electrodes in this model.

In addition to the equations listed in Table 5-1, the equations used in modelling the water-shift gas reaction and steam reforming reaction in the electrode layers are listed in Table 6-1

Table 6-1: Equations for the chemical reactions in the hydrocarbon fed non-isothermal model

Anode electrode diffusion and reaction layers	
$\boldsymbol{\zeta}$	$\frac{1000}{T(K)} - 1$
Equilibrium constant for the steam reforming reaction $\left(\boldsymbol{k_{rq}} = \frac{\boldsymbol{k_{rf}}}{\boldsymbol{k_{rb}}}\right)$	$1.0267 \times 10^{10} \times exp\begin{pmatrix} -0.2513\zeta^4 + 0.3665\zeta^3 \\ +0.5810\zeta^2 - 27.134\zeta + 3.2770 \end{pmatrix}$
Equilibrium constant for the water-shift gas reaction $\left(\boldsymbol{k_{sq}} = \frac{\boldsymbol{k_{sf}}}{\boldsymbol{k_{sb}}}\right)$	$exp\begin{pmatrix} -0.2935\zeta^3 + 0.6351\zeta^2 \\ -4.1788\zeta + 0.3169 \end{pmatrix}[Pa^2]$
Forward reaction rate constant for the steam reforming reaction $(\boldsymbol{k_{rf}})$	$2395exp\left(-\frac{231266}{RT}\right)$
Forward reaction rate constant for the water-shift gas reaction $(\boldsymbol{k_{sf}})$	$0.0171exp\left(-\frac{103191}{RT}\right)$
Reaction rates for methane reforming $(\boldsymbol{R_r})$	$k_{rf}p_{CH_4}p_{H_2O} - k_{rb}\left(p_{H_2}\right)^3 p_{CO}$
Reaction rates for methane reforming $(\boldsymbol{R_s})$	$k_{sf}p_{CO}p_{H_2O} - k_{sb}p_{H_2}p_{CO_2}$

6.2.2 Governing equations

The governing equations for the non-isothermal hydrocarbon fed SOFC model are summarised in Table 6-2:

Table 6-2: Governing equations used in the hydrocarbon fed non-isothermal SOFC model

Flow channels		
Conservation of mass	$\nabla.(\rho\boldsymbol{u}) = 0$	(6-1)
Conservation of momentum	$-\nabla.(\rho\boldsymbol{u}\boldsymbol{u}) - \nabla.\left[-p + \Psi - \left(\frac{2}{3}\mu\right)(\nabla.\boldsymbol{u})\right]$ $where\ \Psi = \mu[\nabla\boldsymbol{u} + (\nabla\boldsymbol{u})^T]$	(6-2)
Conservation of species	$\rho u.\nabla w_i - \nabla.\left[\rho w_i \sum D_{ij}^{eff}(\nabla x_i - \nabla w_i)\frac{\nabla p}{p}\right]$	(6-3)
Conservation of energy	$\rho_i c_{p,i}\boldsymbol{u}\nabla T - \nabla(k_i \nabla T) = S_T$	(6-4)
Electrode diffusion layer		
Conservation of mass	$\nabla.(\rho\boldsymbol{u}) = 0$	(6-5)
Conservation of momentum	$-\nabla.\left(\frac{\rho}{\varepsilon^2}\boldsymbol{u}\boldsymbol{u}\right) - \boldsymbol{u}\frac{\mu}{k_p} - \nabla.\left[-p + \Psi - \left(\frac{2}{3\varepsilon}\mu\right)(\nabla.\boldsymbol{u})\right]$ $where\ \Psi = \frac{\mu}{\varepsilon}[\nabla\boldsymbol{u} + (\nabla\boldsymbol{u})^T]$	(6-6)
Conservation of species	$-\nabla.\left[\rho w_i \sum D_{ij}^{eff}(\nabla x_i - \nabla w_i)\frac{\nabla p}{p}\right] = r_i$ $where, r_{H_2} = M_{H_2}(3R_r + R_s)\ at\ ADL$ $r_{CH_4} = -M_{CH_4}R_r\ at\ ADL$ $r_{CO} = M_{CO}(R_r - R_s)\ at\ ADL$ $r_{H_2O} = M_{H_2O}(R_r + R_s)\ at\ ADL$ $r_{CO_2} = M_{CO_2}R_S\ at\ ADL$	(6-7)
Conservation of charge	$\nabla.\left(-\sigma_s^{eff}\nabla\phi_s\right) = 0$	(6-8)
Conservation of energy	$\rho_i c_{p,i}\boldsymbol{u}\nabla T - \nabla(k_i \nabla T) = S_T$	(6-9)
Electrode reaction layer		
Conservation of mass	$\nabla.(\rho\boldsymbol{u}) = 0$	(6-10)

Conservation of momentum	$-\nabla.\left(\frac{\rho}{\varepsilon^2}\boldsymbol{uu}\right)-\boldsymbol{u}\frac{\mu}{k_p}-\nabla.\left[-p+\Psi-\left(\frac{2}{3\varepsilon}\mu\right)(\nabla.\boldsymbol{u})\right]$ $where\ \Psi=\frac{\mu}{\varepsilon}[\nabla\boldsymbol{u}+(\nabla\boldsymbol{u})^T]$	(611)
Conservation of species	$-\nabla.\left[\rho w_i\sum D_{ij}^{eff}(\nabla x_i-\nabla w_i)\frac{\nabla p}{p}\right]=r_i$ $where, N_{H_2}=-N_{H_2O}=\frac{i_v}{2F}\ at\ ARL$ $r_{H_2}=M_{H_2}(3R_r+R_s)\ at\ ARL$ $r_{CH_4}=-M_{CH_4}R_r\ at\ ARL$ $r_{CO}=M_{CO}(R_r-R_s)\ at\ ARL$ $r_{H_2O}=M_{H_2O}(R_r+R_s)\ at\ ARL$ $r_{CO_2}=M_{CO_2}R_S\ at\ ARL$ $and\ N_{O_2}=\frac{i_v}{4F}\ at\ CRL$	(6-12)
Conservation of charge	$\nabla.\left(-\sigma_s^{eff}\nabla\phi_s\right)=i_v$ $\nabla.\left(-\sigma_i^{eff}\nabla\phi_i\right)=-i_v$ $where, i_v=A_v i_{tpb}$	(6-13) (6-14)
Conservation of energy	$\rho_i c_{p,i}\boldsymbol{u}\nabla T-\nabla(k_i\nabla T)=S_T$	(6-15)
Electrolyte		
Conservation of charge	$\nabla.\left(\sigma_{i,ele}\nabla\phi_i\right)=0$	(6-16)
Conservation of energy	$\rho_i c_{p,i}\boldsymbol{u}\nabla T-\nabla(k_i\nabla T)=S_T$	(6-17)

In this non-isothermal model, the heat source term S_T originates from the following heat sources:

Electrochemical reactions – (ref :Eq. (1-1) and (1-2)) taking place in the reaction layer due to the amount of heat consumed/ generated due to the change in enthalpy in the reaction.

Chemical reactions – (ref: Eq. (1-15) and (1-16)) occurs in the anode diffusion layer and reaction layers and is due to the heat consumed/generated due to the reforming and shift-gas reactions

Ohmic polarisation – otherwise called joule heating, is the heat generated as a result of ionic and electric currents passing through the electrodes

Activation and concentration polarisation – is the heat generated due to the activation and concentration polarisations.

It is important to note that the hydrogen oxidation reaction is endothermic whereas the oxygen reduction reaction is exothermic. In addition to the source terms given in Chapter 5, the heat source term location and their respective expressions are listed in Table 6-3 and Table 6-4 respectively.

Table 6-3: Heat source term in different computational domain

ADL	ARL	electrolyte	CRL	CDL
$s_T^{rs} + s_T^{eo}$	$s_T^{ac} + s_T^{rs} + s_T^{l} + s_T^{er} + s_T^{eo}$	s_T^{l}	$s_T^{ac} + s_T^{l} + s_T^{eo}$	s_T^{sc}

Note: The unit for each source term is (W m^{-3})

Table 6-4: Heat source term and their expressions

Source term	**Expression**	**Domain**
Heat sources due to electronic ohmic resistance $\boldsymbol{s_T^{eo}}$	$\frac{i^2}{\sigma_s^{eff}}$	Anode diffusion layer, Cathode diffusion layer, Anode reaction layer, Cathode reaction layer.
Heat sources due to electronic ohmic resistance $\boldsymbol{s_T^{io}}$	$\frac{i^2}{\sigma_l^{eff}}$	Anode reaction layer, cathode reaction layer, electrolyte
Heat sources due to activation and concentration overpotentials $\boldsymbol{s_T^{ac}}$	$i.A_v.\left[\eta_{act,a} + \eta_{conc,a}\right]$	Anode reaction layer, cathode reaction layer

Heat sources due to chemical reactions $\boldsymbol{s_T^{rs}}$	$R_i.\Delta H_{ref}^0$	Anode diffusion layer, Anode reaction layer
Heat sources due to the electrochemical reactions $\boldsymbol{s_T^{er}}$	$\frac{Q_{elec}\,.\,i_a.A_v}{2F}$	Anode reaction layer
Heat source term $\boldsymbol{Q_{elec}}$	$-\Delta H_{f,H_2o} - 2FV$	

6.2.3 Thermal parameters

The effective specific heat capacity and thermal conductivity depends on the volume fraction of the individual species within each domain. The computational expression for the effective thermal conductivity and specific heat capacity in the porous diffusion and reaction layers are listed in Table 6-5, while the thermal and material parameters used in the model are listed in Table 6-6

Table 6-5: Effective conductivity and specific heat capacity expressions in various cell layers

	Reaction layer	**Diffusion layer**	**Electrolyte**
$\boldsymbol{k^{eff}}$	$\varepsilon_{rl}k_g + (1-\varepsilon_{rl})k_s$	$\varepsilon_{dl}k_g + (1-\varepsilon_{dl})k_s$	k_s
$\boldsymbol{c_p^{eff}}$	$\varepsilon_{rl}c_{p,g} + (1-\varepsilon_{rl})c_{p,s}$	$\varepsilon_{dl}c_{p,g} + (1-\varepsilon_{dl})c_{p,s}$	$c_{p,s}$

Where *g* is the gas phase and *s* is the solid phase

Table 6-6: Thermal and material properties used in the model

	Thermal conductivity $\boldsymbol{\left({}^{J}/_{kgK}\right)}$	**Specific heat capacity** $\boldsymbol{\left({}^{J}/_{kgK}\right)}$	**Density** $\boldsymbol{(kg/m^3)}$	**Reference**
Anode	11	450	3310	[50, 76]
Cathode	6	430	3030	[50, 76]
Electrolyte	2.7	470	5160	[50, 76]

Gas species and mixtures	$\sum_{0}^{6} b_k \left(\frac{T}{1000}\right)^k$	$\sum_{0}^{6} c_k \left(\frac{T}{1000}\right)^k$	$\frac{p\sum_i x_i M_i}{RT}$	[76, 178]
	$k_g = \sum_{i=1}^{n} x_i k_i$	$c_{p,g} = \sum_{i=1}^{n} x_i c_{p,i}$		

6.2.4 Boundary conditions

In addition to the boundary conditions listed in Chapter 5, the temperatures at the anode and cathode inlets are defined as T_a^0 and T_c^0 (K) respectively. Also, the heat transfer at the interface between the gas flow channels and the electrode diffusion layer is pure convection and is given as

$$S_T^i = h_i(T_{dl} - T_{ch}) \tag{6-18}$$

Where T_{dl} and T_{ch} are temperatures of the diffusion layer and flow channels respectively. h_i is the convective heat transfer coefficient which is computed from the Nusselt numbers (Nu) and depends on the gas properties, channel geometry and flow characteristics[87]. Since laminar flow is assumed, the convective heat transfer can be calculated using a constant Nusselt number of 3.66 [44, 47] and the channel hydraulic diameter[41]. Thus the convective heat transfer can be calculated by the following equation: [47, 58]

$$h_i = Nu\frac{k_i}{d_h}$$

Where d_h is the hydraulic diameter given by

$$d_h = \frac{2.W.H_{ch}}{W + H_{ch}}$$

Where W is the cell width and H_{ch} is the channel height.

6.2.5 Numerical procedure

The numerical procedure used in this study is based on the same principles as that described in Chapter 5, including the energy equations which accounts for the temperature distribution, the fully coupled equations are solved according to the computational process shown schematically in Figure 6-1 below.

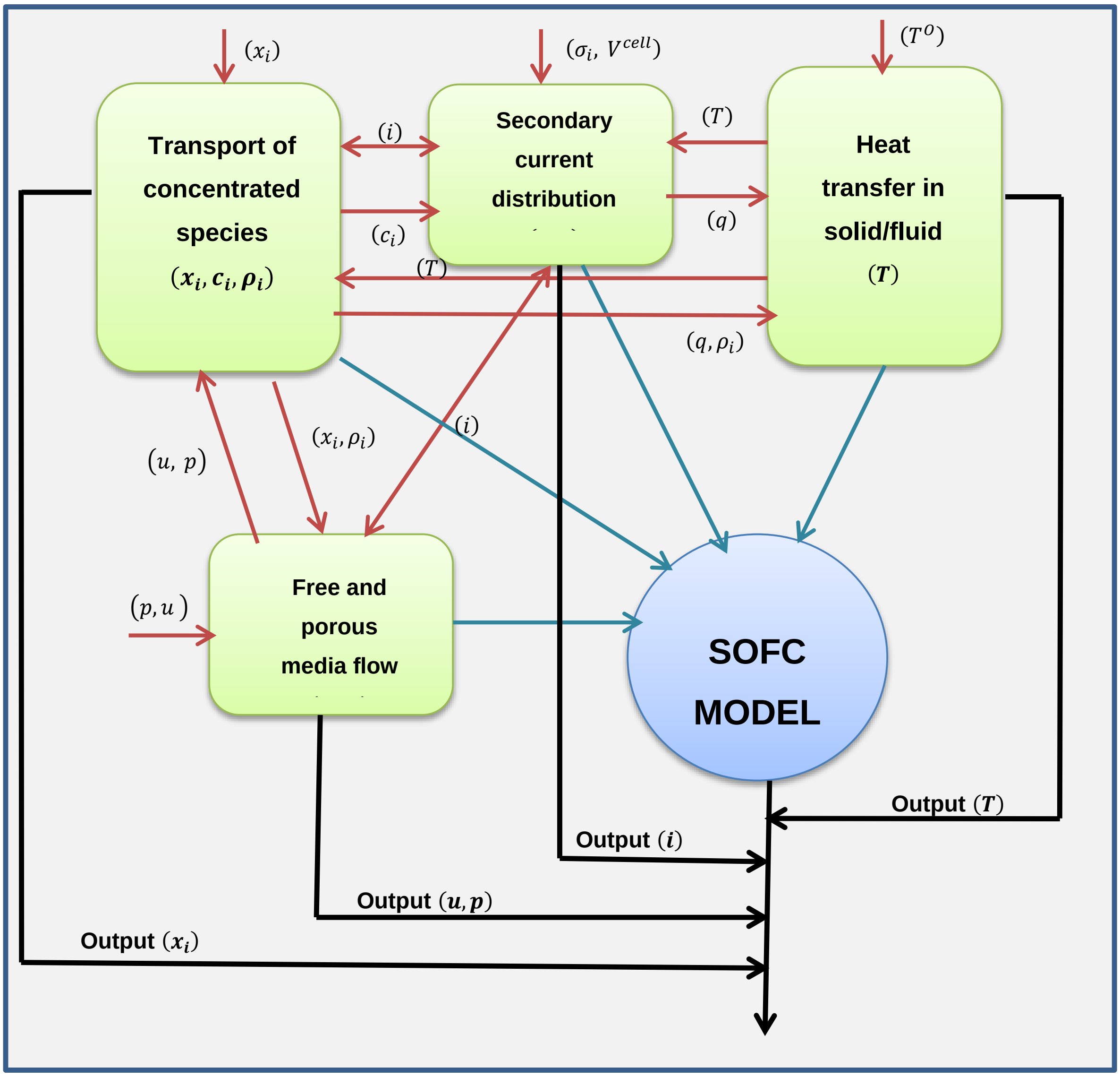

Figure 6-1: Schematic of the computational process for the non-isothermal model

6.3 Non-Isothermal cell performance validation

In order to validate the model, the performance of the non-isothermal anode-supported SOFC is compared with the experimental results of Zhao and Vicker[167] as shown in Figure 6-2.

6.3.1 Experimental procedure

The fabrication and testing processes of the experimental cell described by Zhao and Vicker[167] in the paper "Dependence of polarisation in anode-supported solid oxide fuel cells on various cell parameters" are recapped here.

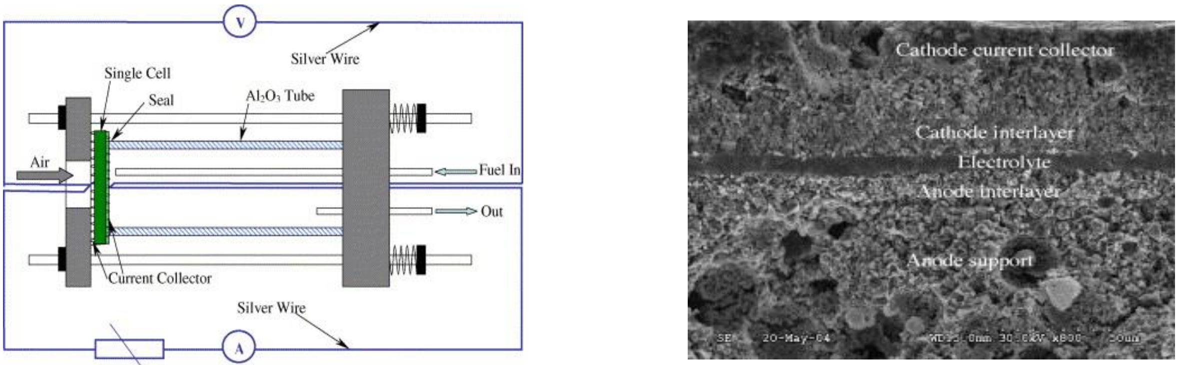

(a) (b)

Figure 6-2: Description of experimental cell: (a) schematic of single cell testing apparatus (b) cross-section of an SEM micrograph of one cell.[167]

"The anode supported SOFC was fabricated by mixing 70 wt.% NiO and 30 wt.% YSZ to which carbon powder was added. A thin layer of NiO + YSZ, which is the anode reaction layer, was drop-coated on one of the surface. After drying, a thin layer of YSZ electrolyte was drop-coated on the same surface. The resulting pellets were sintered in air at 1673K for 2hrs. After sintering, a thin layer of LSM + YSZ containing 50 wt.% LSM and 50 wt.% YSZ cathode reaction layer was then painted on the YSZ layer. The cell was fired at 1473K for 2hrs. After firing a layer of LSM cathode current collector was applied. The entire cell was then heated to 1373K.

The experimental test rig is shown in the schematic in Figure 6-2a, in which silver wires were connected to silver meshes pressing against the LSM cathode current collector and Ni +YSZ anode support layer. The cell is heated to 1073K while circulating with a mixture of 10%H_2 + 90%H_2O on the anode side and air on the cathode side.

The electrochemical performance of the cell is tested at 873K, 973K and 1073K using a mixture of 97%H_2 + 3%H_2O as fuel and air as oxidant. The cell performance were characterised by current-voltage curves. The microstructure of the fracture surface of the cell (Figure 6-2b) is characterised after testing by scanning electron microscopy (SEM)"

6.3.2 Numerical approach

Figure 6-3 compares the above experimental results with the results simulated by the model. The properties and operating conditions used in the model are listed in Table 6-7. All the parameters used in validating the model were obtained from Zhoa and Vicker[167] except those given with references.

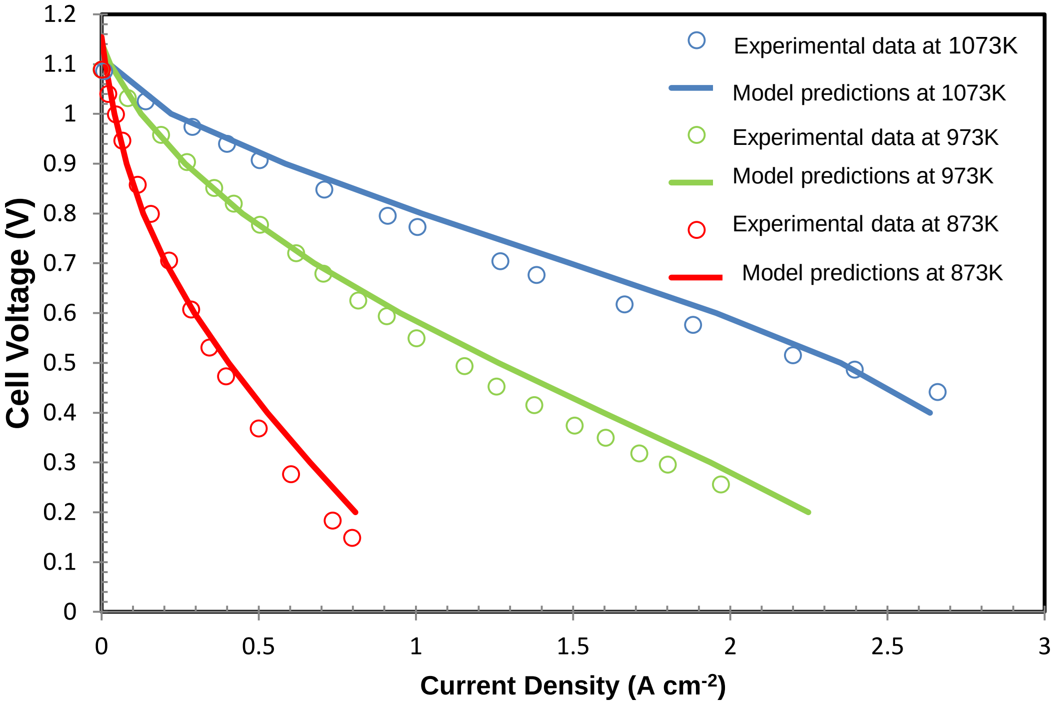

Figure 6-3: Validation of Non-isothermal model

Table 6-7: Parameters used for model validation and in simulating the model

Parameters	Validation	Simulation
Flow channels		
Layer thickness $l_{ch}(\mu m)$	1000	1000
Cell Length, $t_{ch}(\mu m)$	50000	50000
Anode diffusion layer (ADL)		
Layer thickness, $l_{adl}(\mu m)$	1000	1000
Mean particle diameter, $d_{p,adl}(\mu m)$	1 [83, 108]	1
Porosity, ε_{adl}	0.48	0.5

Volume fraction, φ_{adl}	0.55	1
Anode reaction layer (ARL)		
Layer thickness, $l_{arl}(\mu m)$	20	20
Mean particle diameter, $d_{p,arl}(\mu m)$	0.5 [83, 108]	0.5
Porosity, ε_{arl}	0.23	0.25
Volume fraction, φ_{arl}	0.55	0.5
Cathode diffusion layer (CDL)		
Layer thickness $l_{cdl}(\mu m)$	50	50
Mean particle diameter, $d_{p,cdl}(\mu m)$	1 [83, 108]	1
Porosity, ε_{crl}	0.45	0.5
Volume fraction, φ_{cdl}	1	1
Cathode reaction layer (CRL)		
Layer thickness $l_{crl}(\mu m)$	20	20
Mean particle diameter, $d_{p,crl}(\mu m)$	0.5 [83, 108]	0.5
Porosity, ε_{crl}	0.26	0.25
Volume fraction, φ_{crl}	0.475	0.5
Electrolyte (E)		
Layer thickness $l_e(\mu m)$	8	10
Operating conditions		
Operating temperature, $T(K)$	873K, 973K, 1073K	1073K
Total pressure, $p(atm)$	1.0	1.0
Fuel inlet composition, x_{H_2} ; x_{H_2O}	0.97; 0.03	0.7, 0.3
Air inlet composition, x_{O_2} ; x_{N_2}	0.21; 0.79	0.21; 0.79

6.4 Effect of temperature on fuel cell performance

The predicted performance curves obtained using the isothermal and non-isothermal models for the operating temperature from 873 to 1073K is shown in Figure 6-4. The difference in performance between the isothermal and the non-isothermal performance is defined as the potential gain due to temperature increasing η_H[83]. The potential gain is an indication of how much the heat generation and transfer processes in the cell affects its performance. The cell performance improves as the inlet operating temperature increases from 873K to 1073K, also the potential gain is observed to increase considerably as the operating temperature increases, due to the increased rate of reaction at increased temperatures.

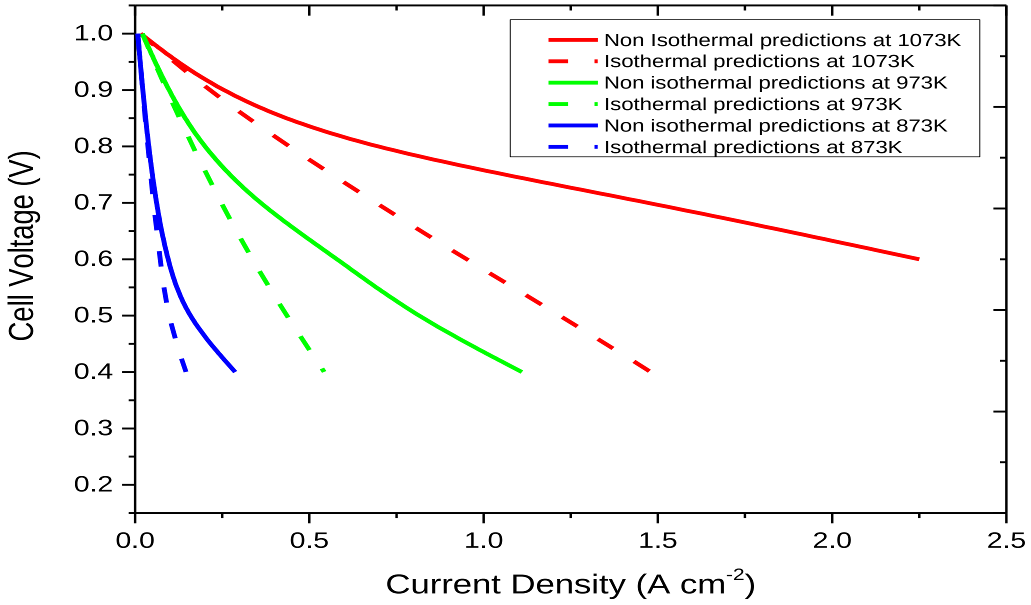

Figure 6-4: Comparison of isothermal and Non-isothermal predictions.

The potential gain due to temperature increasing at 1073K is observed to increase from 7.5% at 0.5 A cm^{-2} to 34% at 1.0 A cm^{-2} and more significantly as the current density increases to 90% at 1.5 A cm^{-2} which is consistent with the simulation results of Jeon [83]

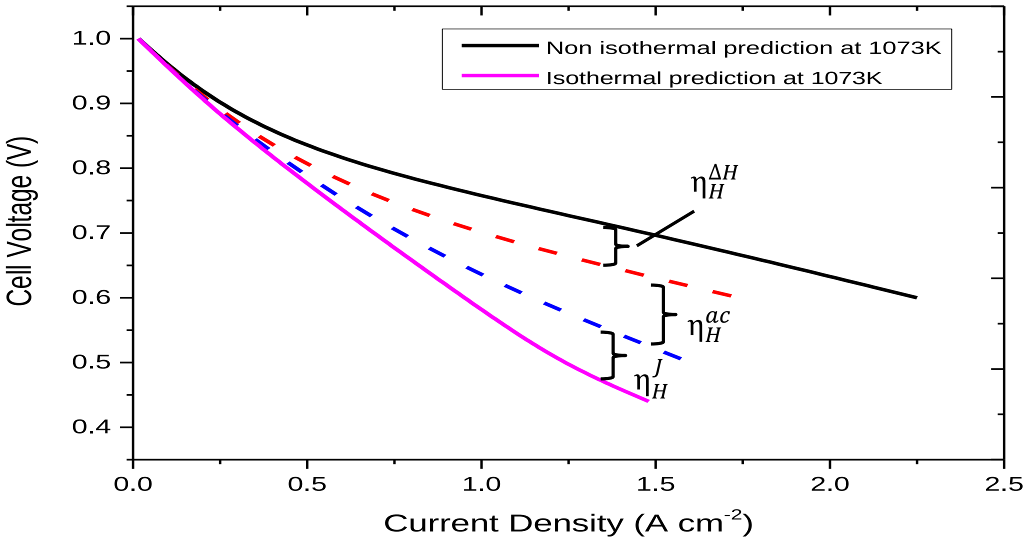

Figure 6-5: Potential gain at 1073K.

The effect of individual heat source on potential gain is shown in Figure 6-5. The contribution caused by joule heating (η_H^j) is observed to have the most effect accounting for 34.3% of the total potential gain at 1.0 A cm^{-2}, this is due to the presence of ionic conducting particles in the reaction layers of both the anode and cathode electrodes thereby increasing the ohmic polarisation of the cell. The rest of the potential gain is evenly divided between the reversible and irreversible processes occurring in the reaction layers. The reversible heat source is due to the electrochemical reactions ($\eta_H^{\Delta H}$) located in the anode reaction layer accounting for 31.7% of the total potential gain at 1.0 A cm^{-2}, while the irreversible heat source due to irreversibilites associated with overcoming the energy barrier (activation) and diffusion of species (concentration) (η_H^{ac}) accounts for 31.08% of the total potential gain at 1.0 A cm^{-2}.

6.5 Velocity profile in flow channels

The gas velocity profile within the fuel channel and air channel in the SOFC at different cell voltages are shown in Figure 6-6 and 6-7 respectively

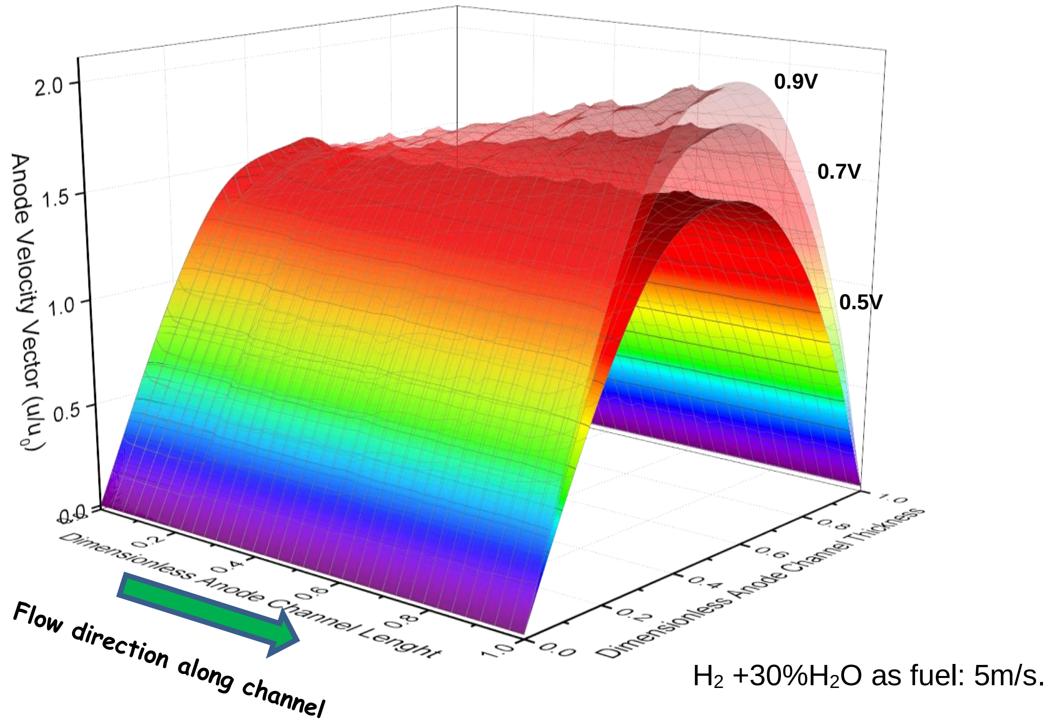

H_2 +30%H_2O as fuel: 5m/s.

Figure 6-6: Velocity vector in anode flow channel

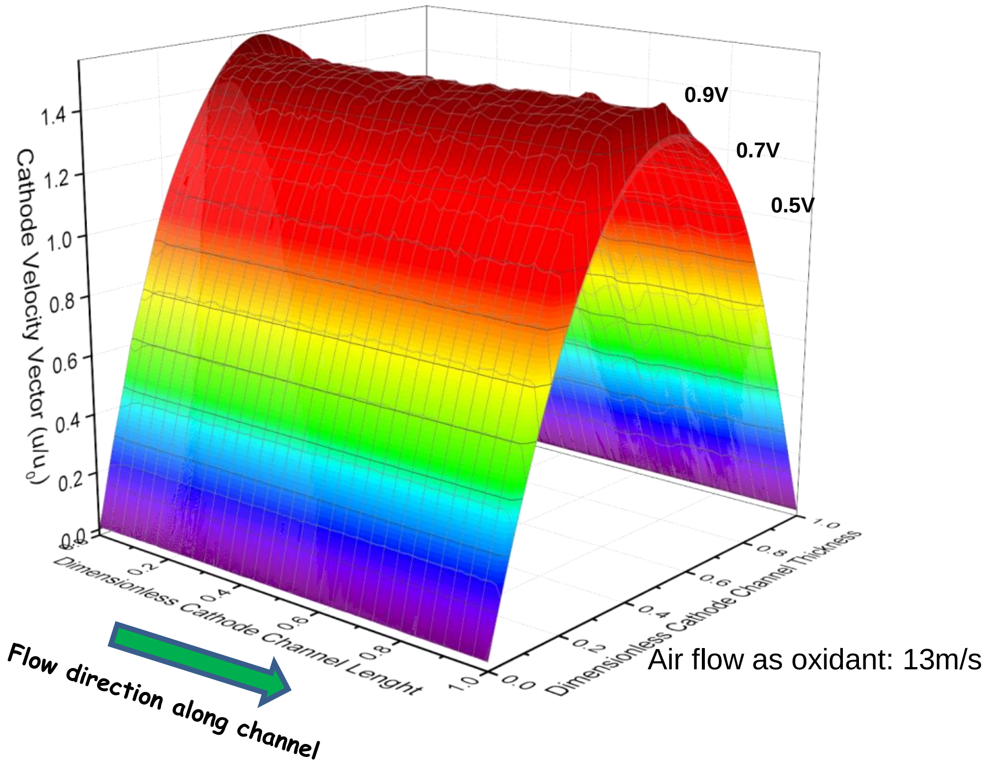

Air flow as oxidant: 13m/s

Figure 6-7: Velocity vector in cathode flow channel

The velocity is seen to increases along the centre of the channels, this is due to its volumetric expansion as a result of the decreasing density caused by the increase in cell temperature along the main flow direction (Figure 6-24). The fuel velocity is observed to increase along the channel, with its gradient steepness increasing as the operating voltage increases, this is as a result of the expansion of the gaseous fuel species due to increasing temperature accros the channel (see Figure 6-24) and H_2O generated from the oxidation reaction in the anode reaction layer. However, on the cathode side, O_2 is consumed in the reduction reaction. This leads to a reduction in the air velocity in the channel. At the same time, the expansion of the oxidant due to increasing temperature across the channel increases the air velocity. Overall, the reduction and the increase balances out leading to no noticable velocity changes along the flow channel for all the operating voltage studied as seen in Figure 6-7.

6.6 Pressure profile in cell

The total pressure distribution in the electrode-electrolyte structure of the cell is shown in Figure 6-8.

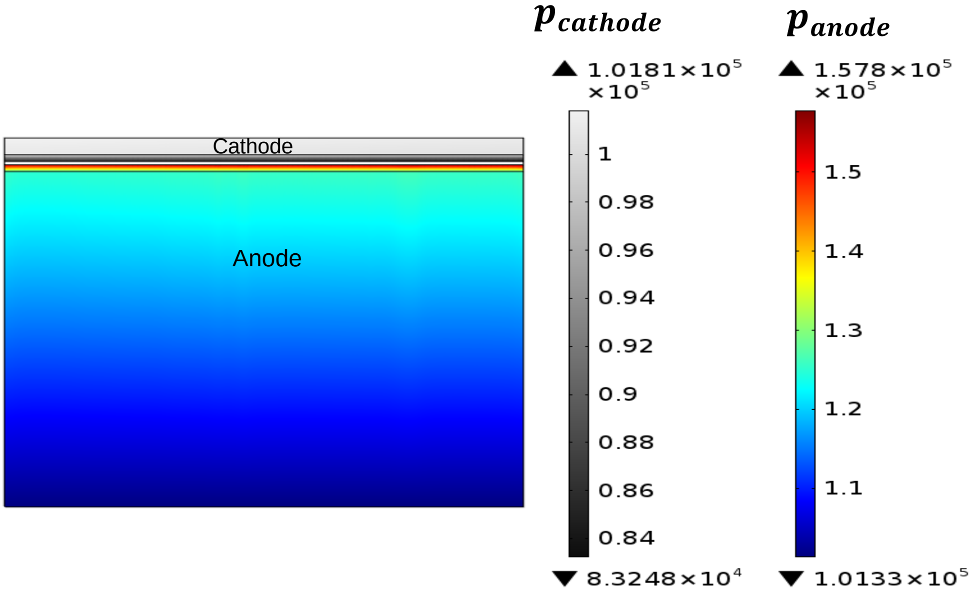

Figure 6-8: Total pressure distribution in electrodes.

The total pressure is constant in the flow channels and varies within the electrode layers, this can be clearly observed in Figure 6-9, where a total pressure rise is observed in the anode side reaction layer/electrolyte interface, whereas a drop in the total pressure is noticed in the cathode side/electrolyte interface.

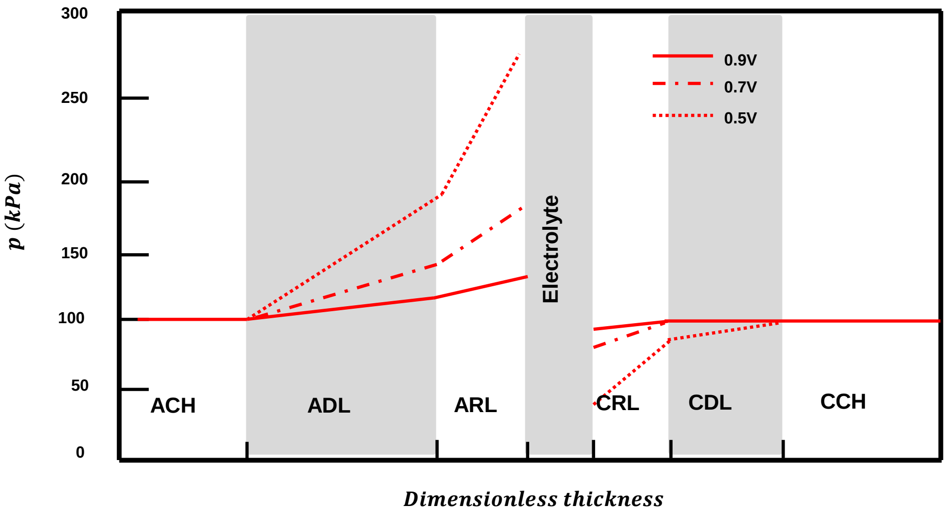

Figure 6-9: Spatial distribution of total pressure through thickness

Due to the electrochemical reaction, hydrogen is spent and water is produced in the anode reaction layer (ARL), this gives rise to a steep positive pressure gradient induced by the difference in the Knudsen diffusivities of hydrogen and water. The produced water vapour usually requires a larger pressure gradient than that required by hydrogen to transport the same amount due to its smaller Knudsen diffusivity $(k_{d,h_2} = 1.123e - 4\, m^2 s^{-1},\ k_{d,h_{2o}} = 3.75e - 5\, m^2 s^{-1}\, at\ 1073K)$, thus the water produced will accumulate in the anode due to its slower diffusion rate, hindering the transport of the hydrogen molecules resulting in a rise in pressure. At the CRL, the pressure gradient is due to the consumption of the oxygen molecules without releasing any product, this aids the diffusion of oxygen molecules from the channel towards the electrolyte resulting in a drop in pressure.

6.7 Additional model verification using phenomena predictions

The present model not only predicts the electrochemical performance of the SOFC (see cell voltage – current density validation curves in Figures 5-4 and 6-3 for isothermal and non-isothermal models respectively) but can also predict various processes and flow profiles in the different layers of the cell.

This section deals with the prediction of mole fraction, temperature and current density profiles occurring in the different components of the cell when hydrocarbon reforming reactions are considered. The results obtained from this model for these profiles are generally consistent with those in literature, thereby providing additional validation for the simulations.

The fuel composition for the 30% pre-reformed natural gas used in simulating the reforming reactions is tabulated in Table 6-8. All other parameters used were from the base case simulation in Table 6-7

Table 6-8: Species mole fraction[68]

Component	Mole fraction
CH_4	0.171
CO	0.029
H_2O	0.493
H_2	0.263
CO_2	0.044

The heat generated due to the chemical reactions within the anode diffusion and reaction layers (tabulated in Table 6-4) are expressed by the reaction rate as

$$S_T^{rs} = R_i \Delta H_{ref}^0$$

$$S_T^{rs} = S_T^r + S_T^s \tag{6-19}$$

$$S_T^r = R_r(-\Delta H_r^0) \tag{6-20}$$

$$S_T^s = \left(R_r(-\Delta H_s^0)\right) \tag{6-21}$$

ΔH_r^0 is the enthalpy from the reforming reaction whose value at 1073K is 242 (kJ mol^{-1}) [87], ΔH_s^0 is the enthalpy from the water-gas shift reaction which equals (-38 kJ mol^{-1}) at 1073K and ε is the porosity of the anode layer.

Figure 6-10 compares the performance of the SOFC when reforming and water-gas shift reactions are considered to when they are not considered in the model simulations. In the simulations that didn't consider the reactions, the same 30%

reformed hydrocarbon was introduced in the cell, only the electrochemical oxidation of hydrogen at the reaction layer was considered in the model, while the simulations with chemical reactions considered both the reforming and water-shift gas reactions in addition to the electrochemical oxidation of oxygen

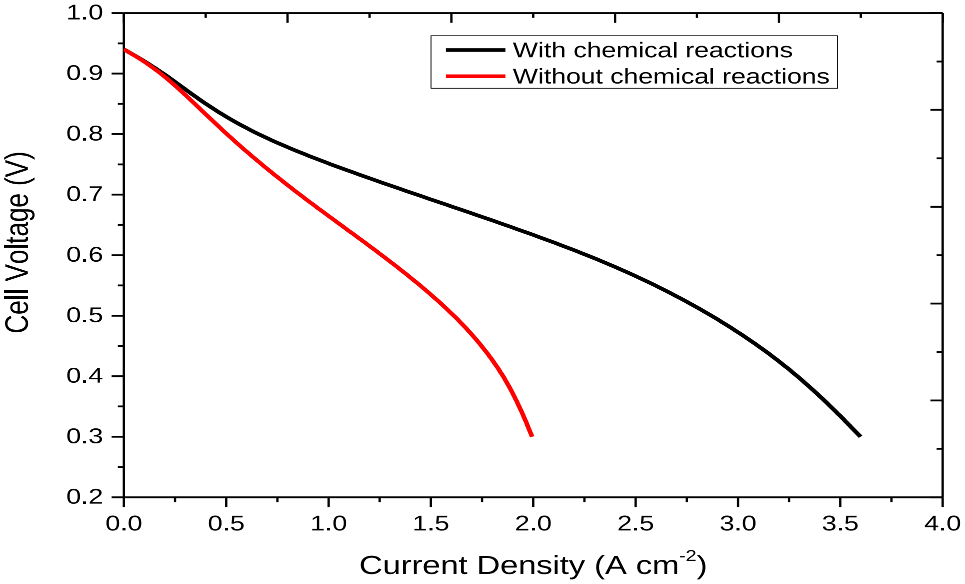

Figure 6-10: Performance comparison between when chemical reactions are considered and when they are not considered. Operating at 1073K, 1atm

As observed, there is significant improvement on the SOFC performance when the reforming and water-gas shift reactions are considered in the model. The subsequent section will analyse gaseous species distribution in both cases.

6.7.1 Species Distribution

No chemical reactions considered

Cross sectional distributions of the species in the anode diffusion layer of an anode supported SOFC is presented in Figure 6-11. The fuel composition is listed in Table 6-8 above. The operating temperature and pressure are set at 1073K and 1 atm. The reforming and water-gas shift reactions are not considered for this analysis.

The x-axis of Figures 6-11 to 6-14 represents the dimensionless cell length where 0 represents the entrance and 1 represents the exit; the y-axis represents the dimensionless anode diffusion layer thickness with 0 representing the channel/diffusion layer boundary and 1 representing the diffusion layer/reaction layer boundary. The z-axis represents the species mole fraction within the physical domain. As seen, the mole fraction of H_2 decreases by 42.3 %(0.26 to 0.15) at 0.7V, while that of H_2O increases by 22.4% (0.49 to 0.60) also at 0.7V, along the layer thickness (from the channel end towards the reaction layer end). This significant variation is due to the proximity of the anode reaction layer to the diffusion layer, wherein the electrochemical oxidation of H_2 occurs, this result in the consumption of H_2 and the production of H_2O. The slight variation noticed in the mole fraction of the other non-reacting species (CH_4, CO_2 and CO) along the diffusion layer thickness is mainly due to the multi-component diffusion occurring in the layer, in which the mole fraction (concentration) of one species depends on the mole fraction (concentration) of the other (n-1) species. The mole fraction variation along the cell channel length is also presented in the Figures 6-11 and 6-12, it is again observed that the species varies along the cell length, since there are no chemical reactions occurring in the diffusion layer for this particular case, the variations are very slight and are due only to the multi-component diffusion within the layer. In this situation, the mole fraction of H_2 decreased by 5.8% (0.26 to 0.245) while that of H_2O increased by 8.1% (0.49 to 0.53).

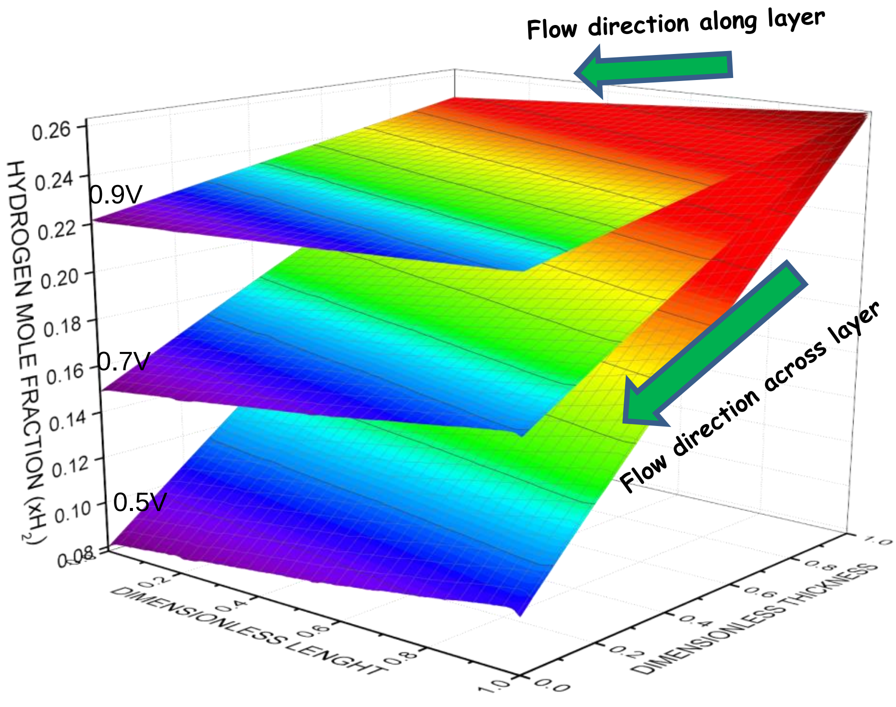

Figure 6-11: Mole fraction distribution of H_2 without chemical reaction.

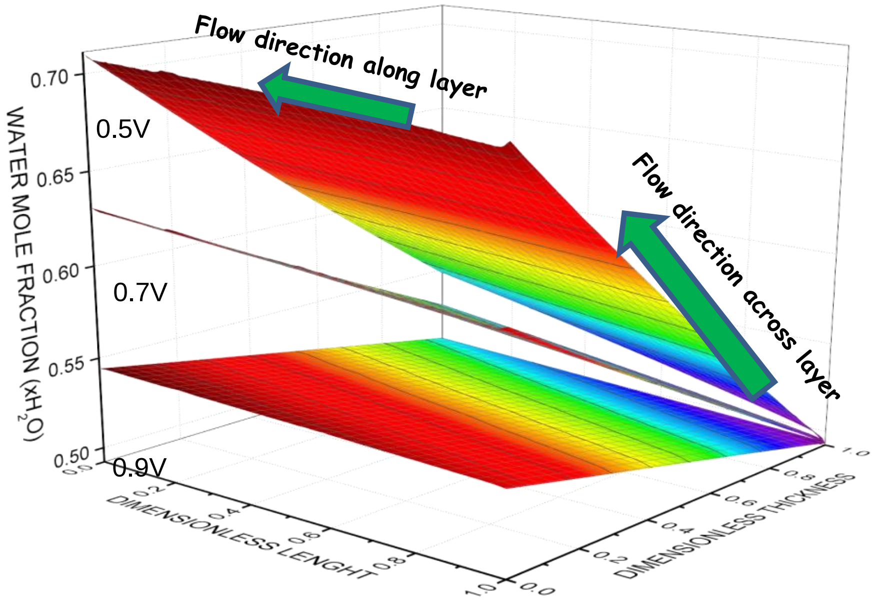

Figure 6-12: Mole fraction distribution of H2O without chemical reaction

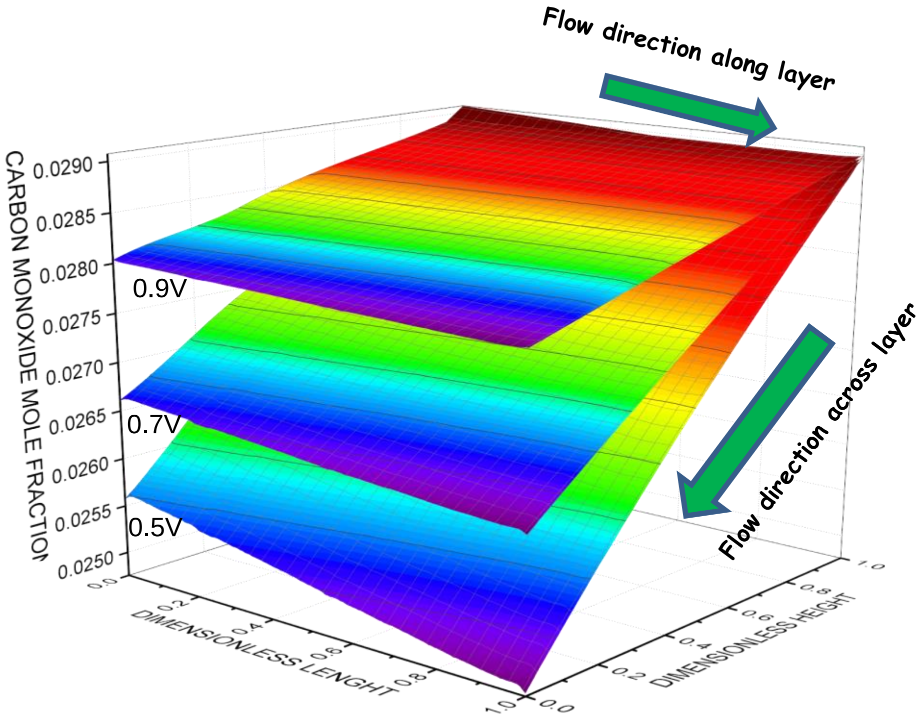

Figure 6-13: Mole fraction distribution of CO without chemical reactions.

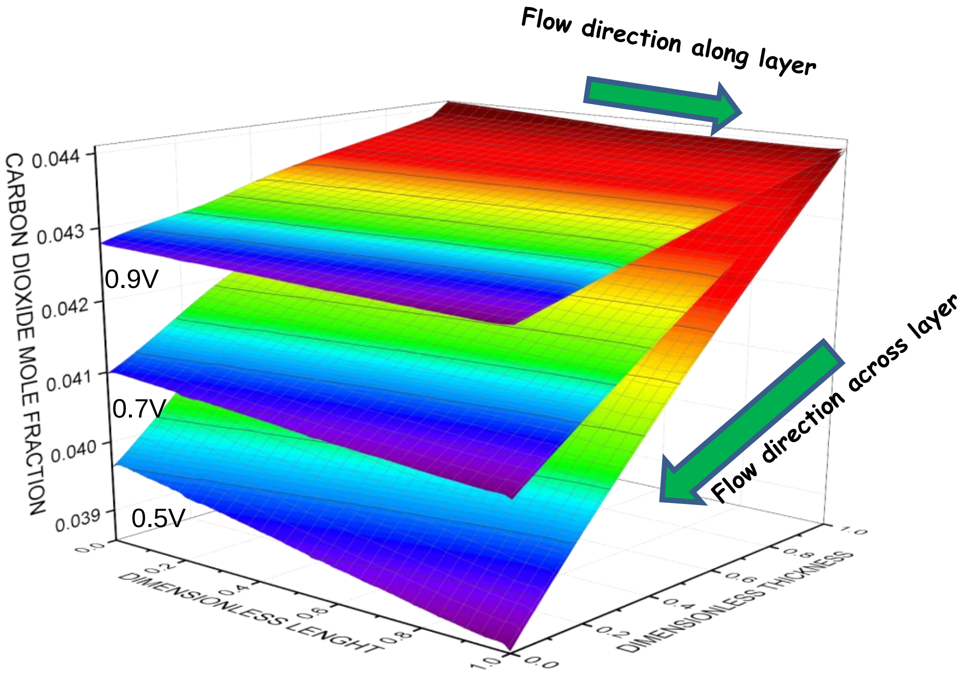

Figure 6-14: Mole fraction distribution of CO_2 without chemical reactions

Figures 6-11 and 6-14 also present the mole fraction distribution of the individual species within the anode diffusion layer when the cell voltage is varied from 0.9 to 0.5V. It is clear that the mole fraction of H_2 reduces with reducing cell voltage, while that of H_2O increases when the cell voltage is reduced. Reducing the cell voltage (increasing the current density) increases the consumption of H_2 at the reaction layer which consequently leads to the increase in the production of H_2O.

Chemical reactions considered

The effect when the chemical reaction (direct reforming and water-gas shift) are included on the distribution of the species in the anode diffusion layer at 0.7V is shown in Figures 6-15 to 6-19. The x-axis represents the dimensionless cell length where 1 represents the entrance and 0 represents the exit; the y-axis represents the dimensionless anode diffusion layer thickness with 1 representing the channel/diffusion layer boundary and 0 representing the diffusion layer/reaction layer boundary while the z-axis represents the species mole fraction within the physical domain. The impact of direct reforming reaction, water-shift gas reaction and the electrochemical oxidation of H_2 on the mole fraction distribution are studied.

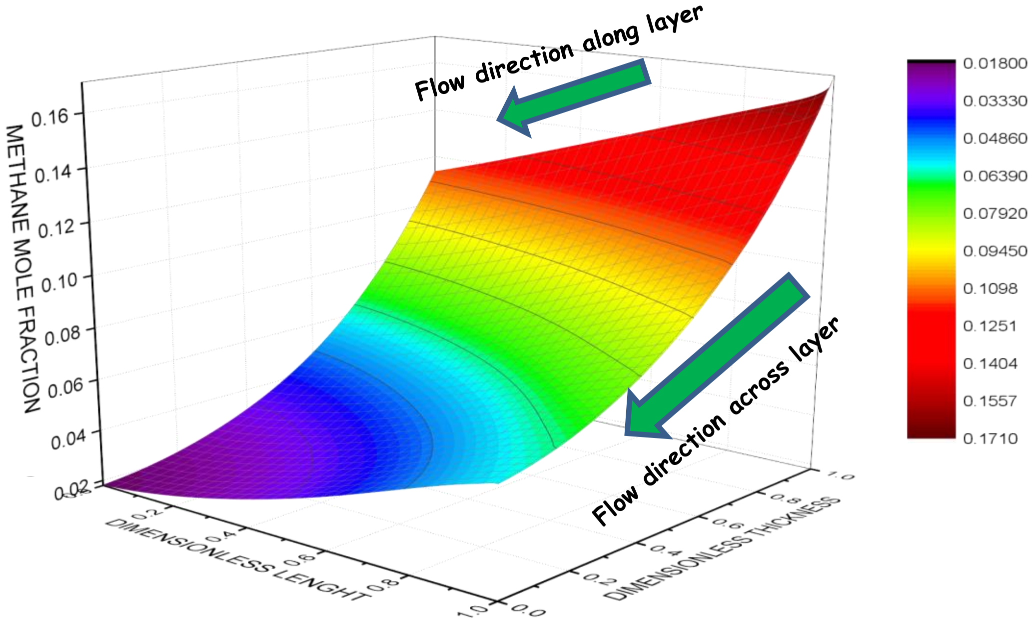

Figure 6-15: Mole fraction distribution of CH_4 considering chemical reactions.

Figure 6-15 shows the effect of steam reforming reaction on the mole fraction distribution of methane. As seen, at the regions close to the inlet into the diffusion layer (x=1, y=1), there is rapid consumption of methane leading to the production of H_2 and CO. This leads to an initial increase in the mole fraction of H_2 up to a certain thickness (when most of the methane is consumed), consequently, the mole fraction of H_2O decreases for that same thickness as shown in Figures 6-16 and 6-17 respectively.

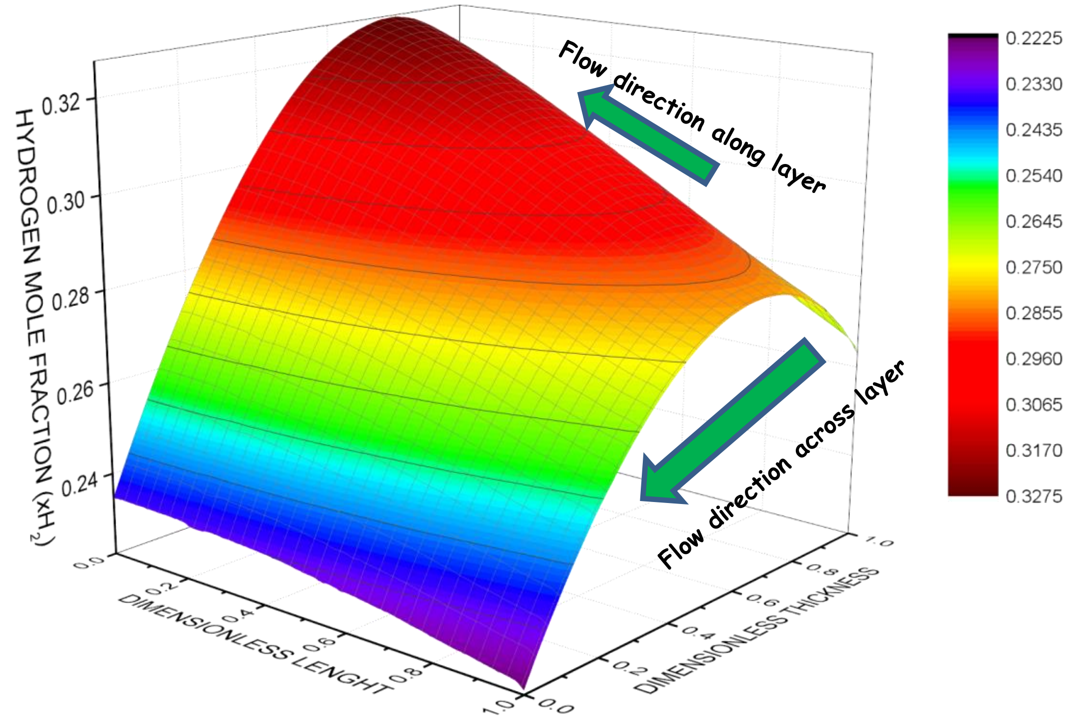

Figure 6-16: Mole fraction distribution of H_2 considering chemical reactions.

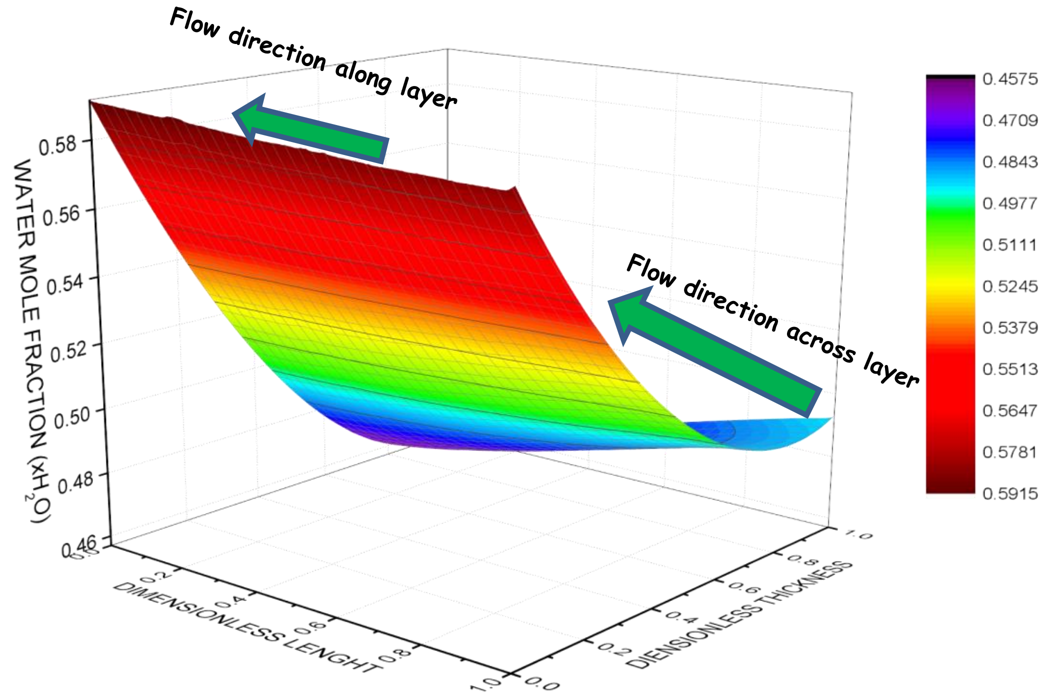

Figure 6-17: Mole fraction distribution of H_2O considering chemical reactions

This is due to the production of 3 moles of H_2 for every mole of H_2O consumed through the steam reforming reaction (see Equation 4-24) and the production of 1mole of H_2 for each mole of H_2O consumed through the water-gas shift reaction (see Equation 4-25). Once most of the methane has been consumed, the H_2 oxidation reaction becomes more rapid, proceeding at a higher rate than the steam reforming and water-gas shift reactions, this leads to a decrease in the H_2 mole fraction and an increase in the H_2O mole fraction.

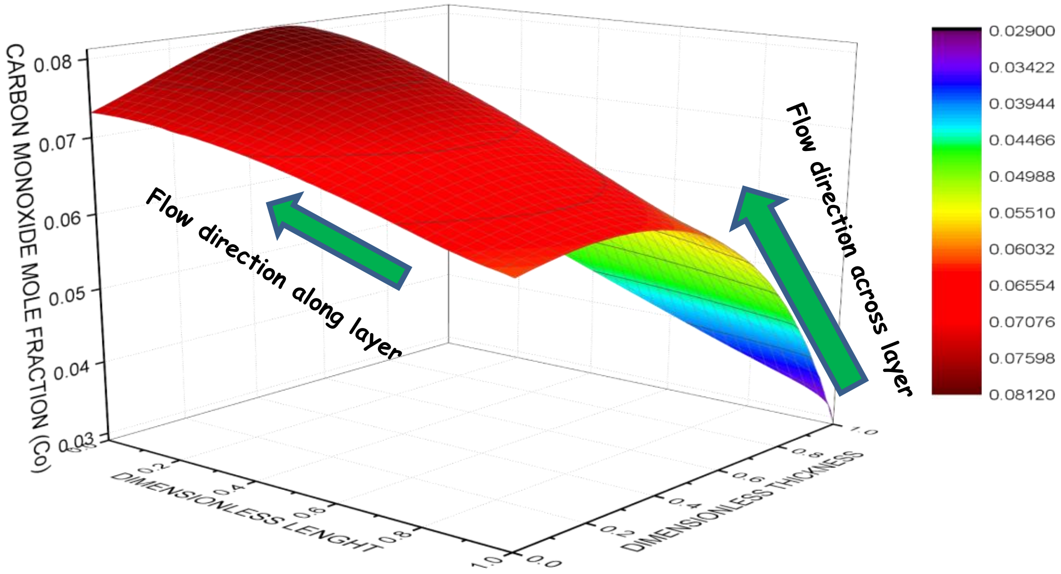

Figure 6-18: Mole fraction distribution of CO considering chemical reactions.

The slight initial increase in CO mole fraction noticed in Figure 6-18 is due to the comparatively higher rate of production of CO from the steam reforming reaction than its consumption rate in the water-gas shift reaction; also CO_2 is produced from the water-gas shift reaction, leading to its increasing mole fraction as shown in Figure 6-19

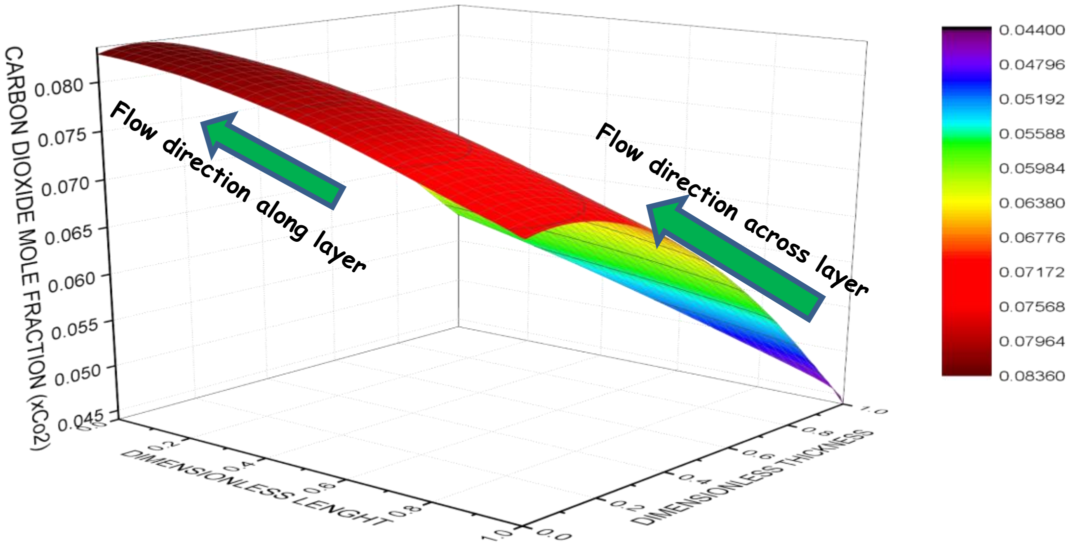

Figure 6-19: Mole fraction distribution of CO_2 considering chemical reactions.

The slight decrease in mole fraction noticed towards the exit of Figures 6-18 and 6-19 is as a result of multicomponent diffusion due to the faster rate of the electrochemical reaction over those of the steam reforming and water-gas shift reactions.

The mole fraction distribution of O_2 in the cathode diffusion layer at varying voltages from 0.9V to 0.5V is shown in Figure 6-20, due to its small thickness (50µm) compared to that of the anode diffusion layer (1000µm), its variation along the thickness is very slight. At 0.7V, O_2 mole fraction reduces by 7.9% (0.21- 0.193). This trend is seen in all three cell voltages as the O_2 mole fraction reduces with reducing cell voltages. On the other hand, a considerable reduction in mole fraction is noticed along the cell length, in the same case of 0.7V, the mole fraction reduced by 11% (0.21 – 0.187)

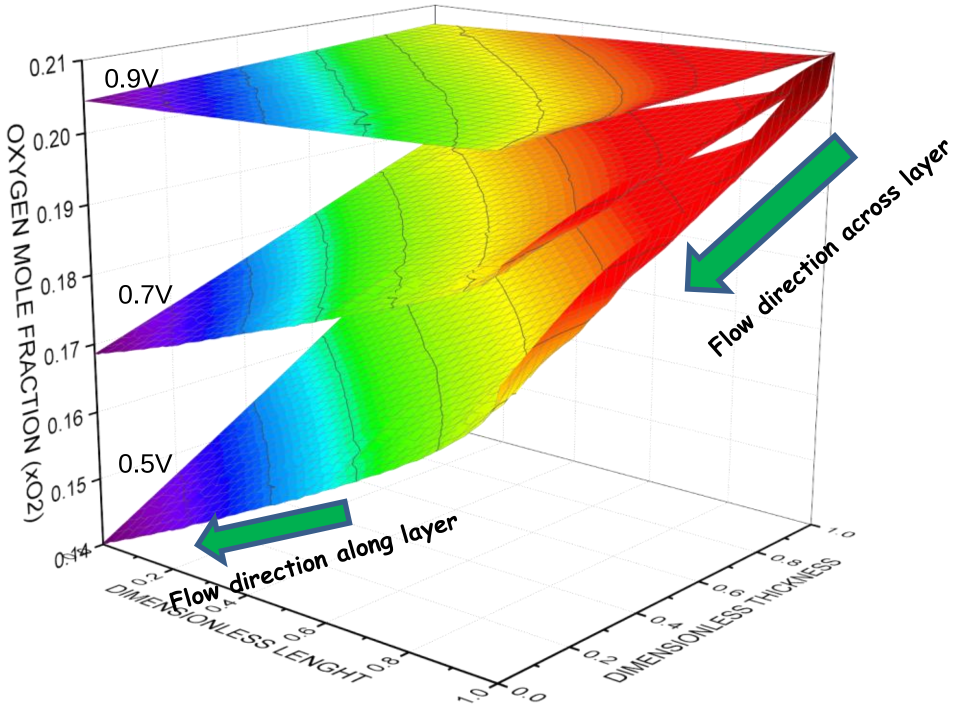

Figure 6-20: Mole fraction distribution of O_2 considering chemical reactions

The mole fraction distribution of H_2 and H_2O in the anode reaction layer at 0.7V is shown in Figures 6-21 and 6-22 respectively. The x axis represents the dimensionless cell length where 1 represents the inlet and 0 the outlet while the y axis represents the dimensionless thickness with 1 representing the reaction layer/electrolyte boundary and 0 representing the diffusion layer/reaction layer boundary.

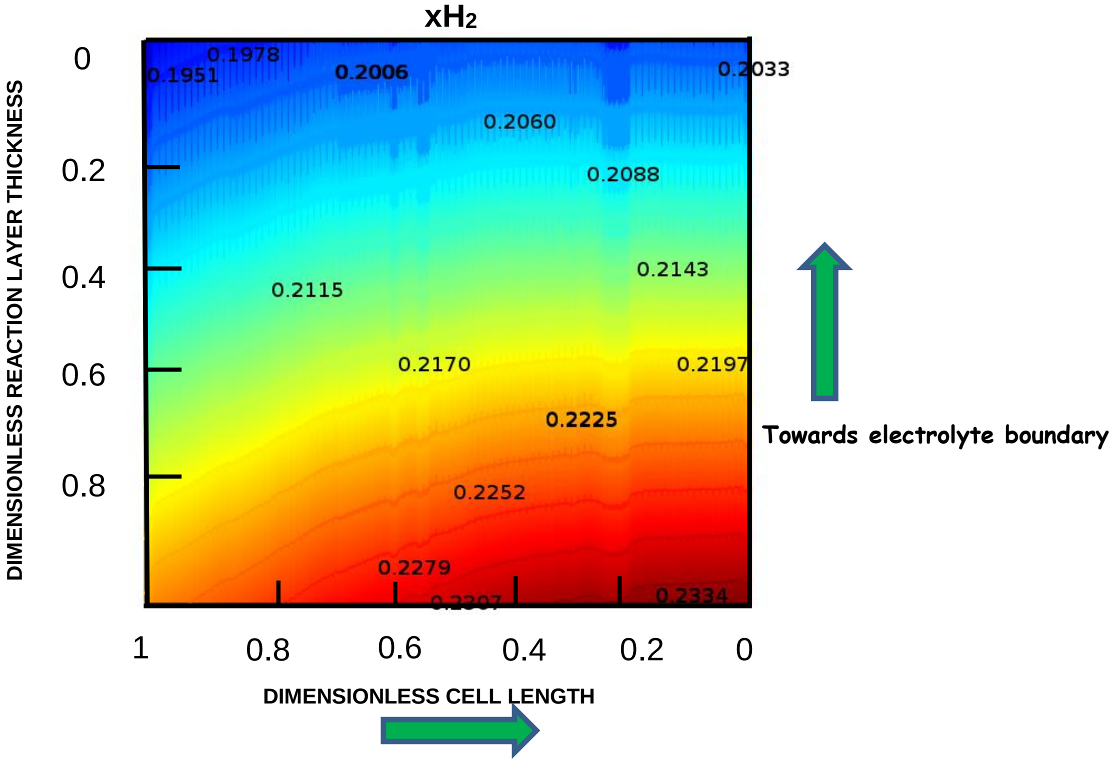

Figure 6-21: Mole fraction distribution of H_2 in ARL.

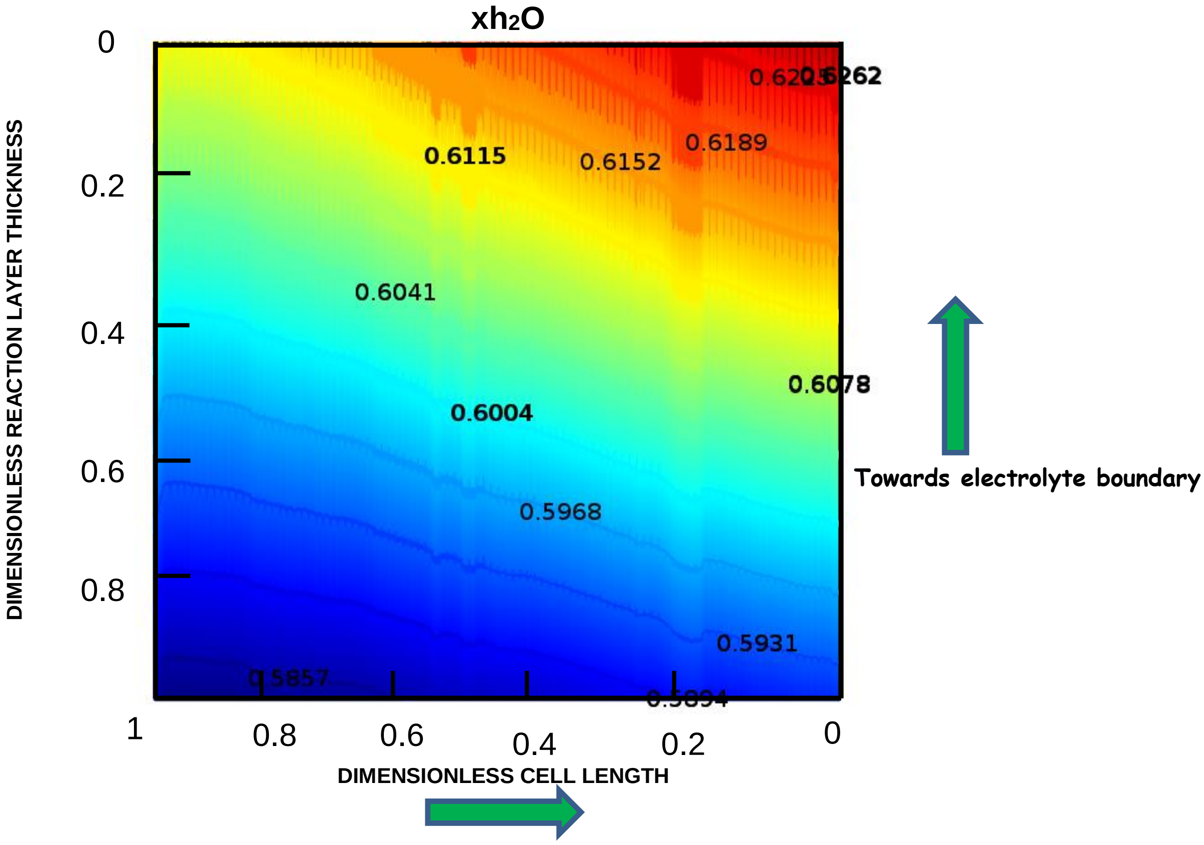

Figure 6-22: Mole fraction distribution of H_2O in ARL

Due to the oxidation reaction of H_2 in this layer, the mole fraction of H_2 decreases while that of H_2O increases along the thickness of the anode reaction layer towards the boundary with the electrolyte. However, the depletion and increment of the species are not so significant when compared to those in the diffusion layer, this can be attributed to the much smaller thickness of the reaction layer when compared to that of the diffusion layer. Similarly, the mole fraction distribution of O_2 at 0.7V is shown in Figure 6-23, also due to the electrochemical reduction of O_2 in the layer, consumption of the species occurs, leading to a decrease in the mole fraction along the layer thickness (towards the boundary with the electrolyte), but unlike in the anode layer, the depletion is more significant than in the diffusion layer because the relatively small thickness of the cathode diffusion layer.

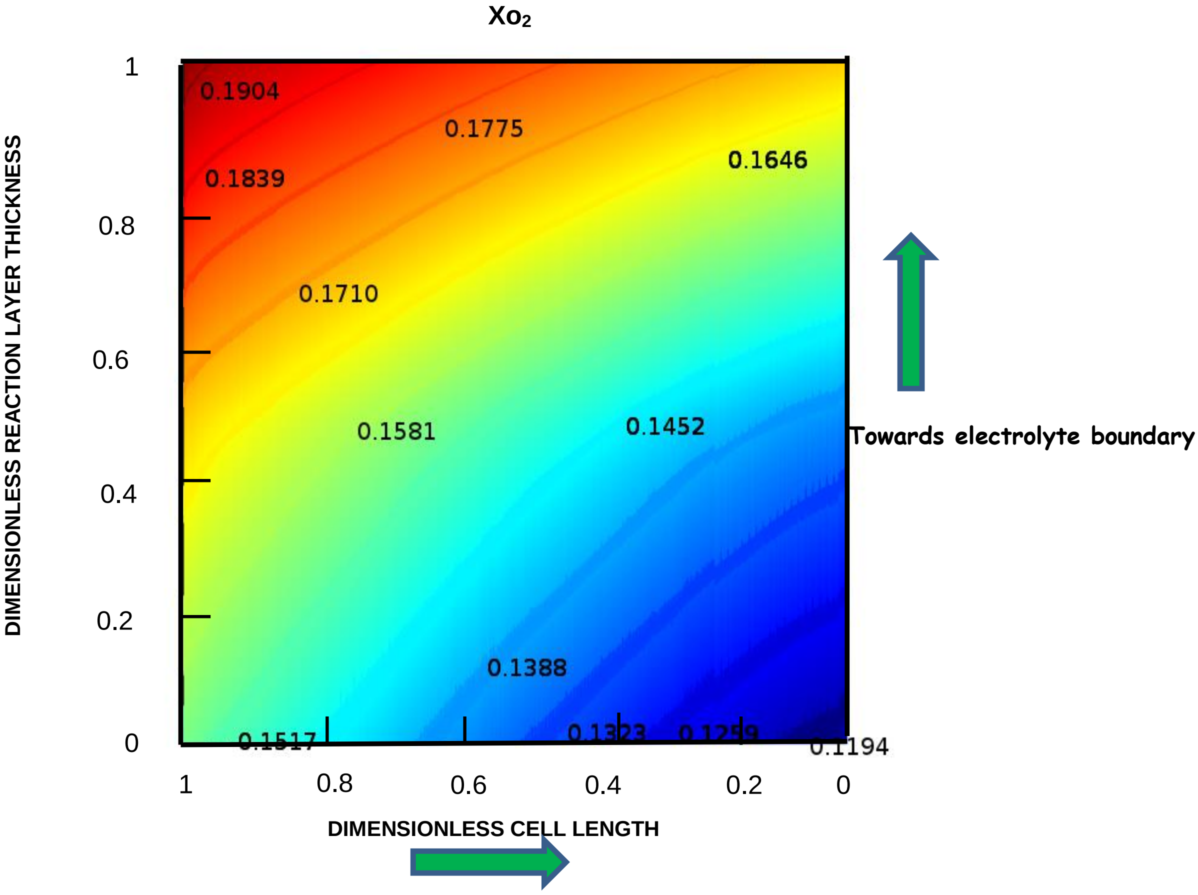

Figure 6-23: Mole fraction distribution of O_2 in CRL

6.7.2 Temperature distribution

The temperature distribution in the SOFC is presented in Figure 6-24 while the individual profiles in PEN structure, fuel and air channel are shown in Figure 6-25. The operating conditions are set at 0.7V, 1073K and 1atm. It is noticed that the cell temperature varies significantly along its main flow direction (cell length) with the maximum temperature occurring at the outlet. The high temperature variation is as a result of the heat generated by the enthalpy change due to the electrochemical reaction, the ohmic, concentration and activation polarisations within the PEN structure as well as by the water-gas shift reactions occurring in the anode and fuel channel. On the other hand, heat is consumed by the endothermic reforming reaction occurring on the anode.

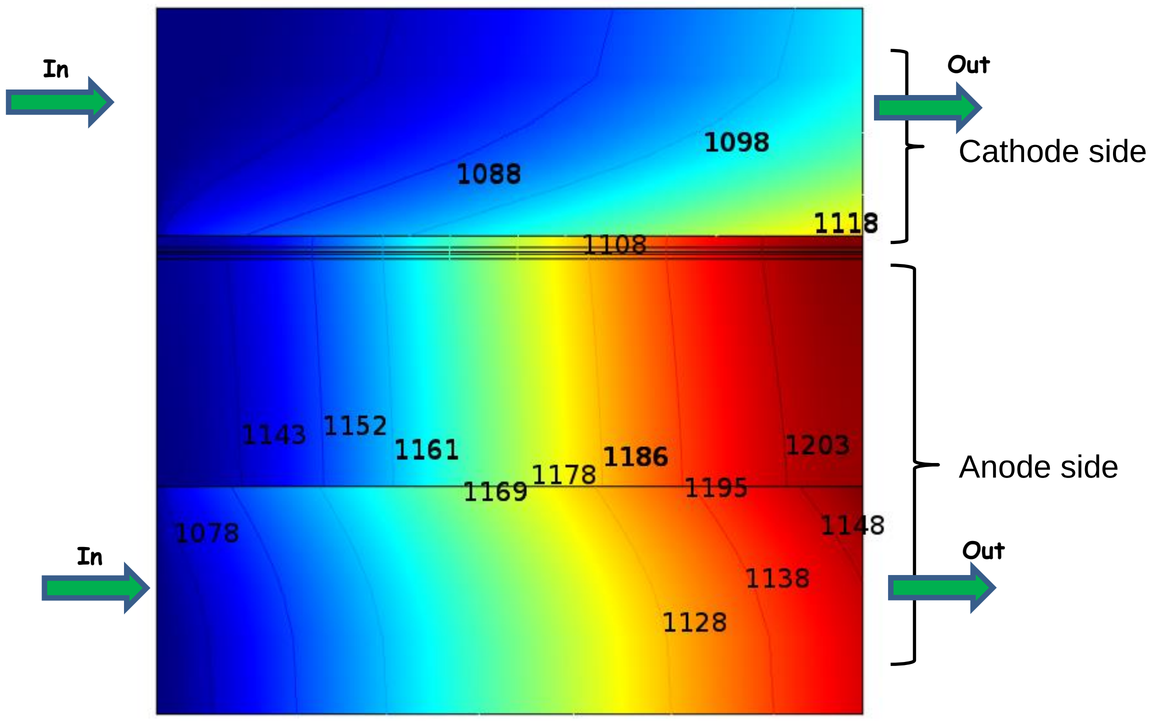

Figure 6-24: Temperature distribution in SOFC.

It is worth noting that all the enthalpy process in the cell is modelled to occur on the anode reaction layer [214], therefore the only heat generation terms on the cathode side is due to the activation, concentration and ohmic polarisation, coupled with the cooling effect of the air in supressing the increasing temperature due to the electrochemical reactions. This ensures that the cathode channel temperature is much lower than that of the anode channel temperature.

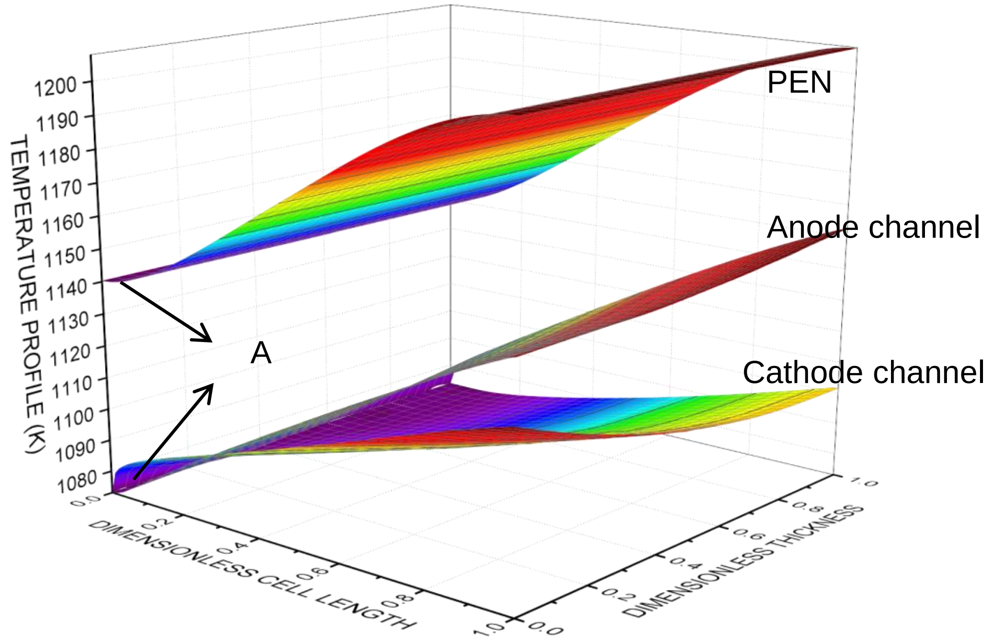

Figure 6-25: Temperature profile in the individual components of the SOFC.

A significant local cooling effect is usually reported at the entrance of the cell [47, 79, 86, 149]; these authors attribute this to the rapid consumption of methane at the cell entrance during the reforming reaction. However, this study reports a very slight local cooling (see A in Figure 6-25) due to the significant initial quantity of heat generated from the relatively large electrochemical active area-to-volume ratio. This is responsible for the much lower percentage of heat consumed in the methane reforming reaction, accounting for only 29% of the total heat produced compared to 45% as reported by Aguiar et al[47].

The temperature variations noticed across the SOFC thickness are negligible; this can probably be attributed to the reforming reaction occurring throughout the anode, the strong multicomponent diffusion of the species, the high thermal conductivity of the SOFC components and the high inlet velocity of the species.

The temperature of the SOFC PEN structure is noticed to be significantly higher than that in the fuel channel because of the exothermic electrochemical reaction occurring in the PEN structure, the thick anode electrode layer which increases the heat generated by the concentration polarisation and the high heat transfer coefficient between the fuel channel and the electrode layer.

The maximum and minimum temperatures in the SOFC are 1207 and 1073K respectively, leading to a cell's maximum temperature difference of 134K. This large thermal gradient across the various layers of the SOFC is caused by the non-uniform heat generated in the cell and has to be carefully monitored to avoid any thermally induced failures in the cell.

6.7.3 Current density distribution

The local current density distribution at 0.7V is presented in Figure 6-26. As seen, the current density profile corresponds to the temperature distribution profile of Figure 6-25, in which there is a slight decrease near the entrance which is attributed to the effect of the reforming reaction and an increase further down as the fuel flows which is attributed to the consumption of hydrogen resulting in a decrease in its molar fraction while its variation along its thickness is negligible.

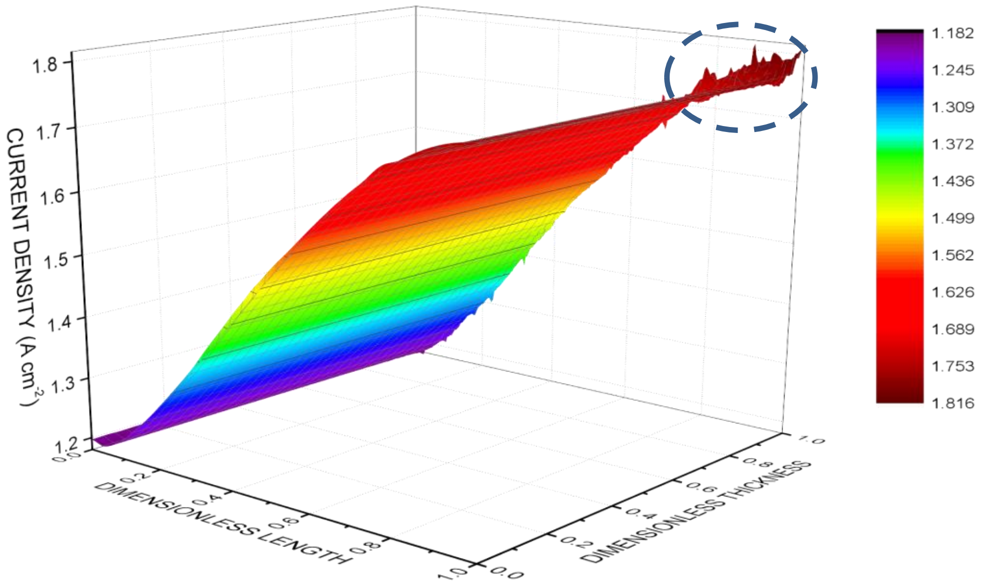

Figure 6-26: Current Density profile in SOFC.

The current density distribution profile shows that it is indicative of the electrochemical reaction rates in cell, which on its own is strongly dependent on the temperature distribution (i.e the current density maps the temperature distribution in the cell). However, near the cell outlet, the current density distribution is seen to decrease slightly due to the effect of fuel depletion at that region. The circled region at the top right of the figure shows a region of instability, this is due to the tolerance value for the simulation which was set at $1\ x\ 10^{-3}$. If the tolerance value is increased the region will become stable, however, the computational time will increase significantly.

6.8 Micro-structural parametric studies of the reaction layers

6.8.1 Mean particle diameter

The dependence of SOFC performance on the mean particle diameter of the reactive layers in the anode and cathode sides is shown in Figures 6-27 and 6-28 respectively. As seen, smaller particle diameter generally leads to better cell performance due to the increasing length of the triple phase boundary (TPB) which increases the reactive surface area thereby enhancing the electrochemical reaction rate. Also, the activation polarisation is reduced when the particle diameter is reduced since the exchange current density is proportional to the TPB length. However, the effect on cell performance of reducing the particle diameter on the anode side is not as significant as that on the cathode side due to the relatively smaller contribution of the anode activation polarisation to the total cell polarisation as compared to that of the cathode activation polarisation.

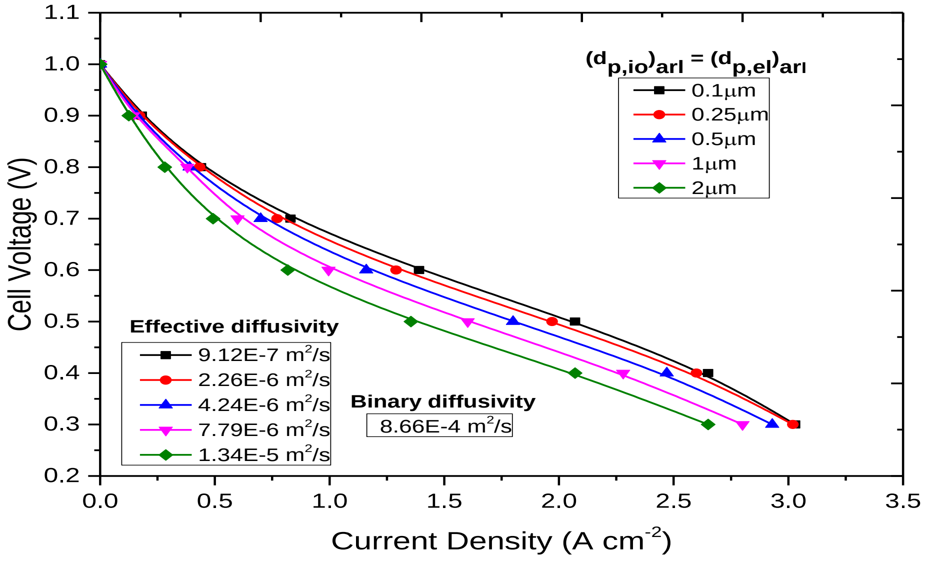

Figure 6-27: Effect of Anode reaction layer particle diameter on performance.

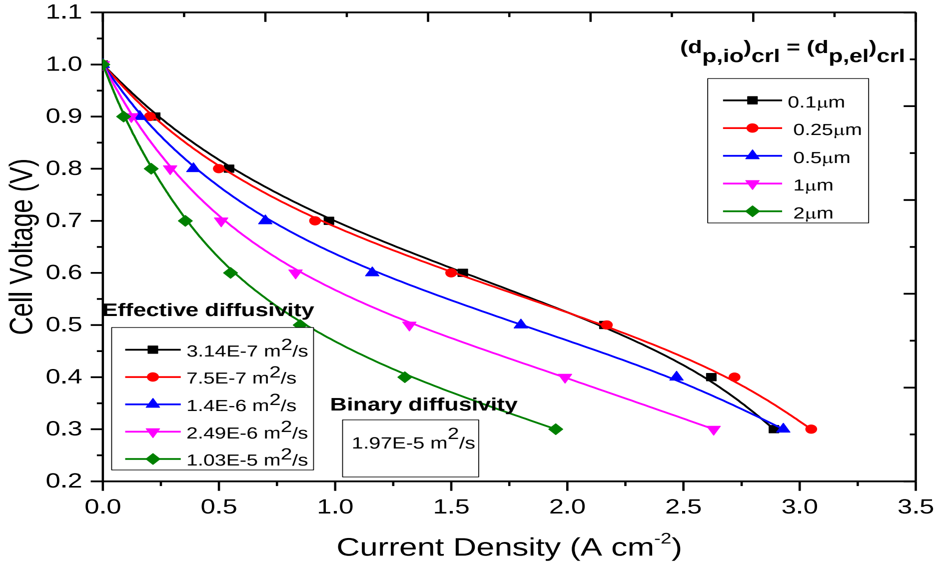

Figure 6-28: Effect of Cathode reaction layer particle diameter on performance.

This result is consistent for the different particle diameters studied except at *0.1µm* in which the above trend is observed at low current densities, however, at high current densities, a lower cell performance than in larger particle diameters is observed. Very small particle diameter implies reduced pore size which inhibits the Knudsen diffusion process thereby decreasing the effective conductivity both on the ARL and CRL, thus resulting in increased concentration polarisation. Equations 4-13 and 4-96 respectively indicates that when the particle diameter is reduced by half, the Knudsen diffusivity falls by half, the reactive surface area (TPB) is doubled and the permeability is reduced by one-fourth. This is more obvious on the anode side due to the thick anode diffusion layer in which the effect of concentration polarisation is more significant. However, on the cathode side which has a very thin diffusion layer, the lower performance at high current density is due to oxygen depletion.

6.8.2 Porosity

The dependence of cell performance on the porosity of the reaction layers is considered in Figures 6-29 and 6-30. Increasing the porosity leads to an increase in the void fraction and a decrease in the solid fraction of the electrode reaction layers, this subsequently reduces the reactive surface area available for the electrochemical reaction, In addition, porosity influences the ionic and electronic conductivities of the reaction layers as an increase in their porosity results in a decrease of their effective conductivities, resulting in increased ohmic overpotentials. However, at the same time, the concentration overpotential is reduced due to the increased mass transport rate caused by increasing the diffusivity (Knudsen and binary) and flow permeability values. For instance, an increase in the porosity from 0.25 to 0.35 results in a decrease of the reactive surface area by 13.25% but increases the Knudsen diffusivity by 38%, the effective binary diffusivity by 53.4% and the flow permeability by 72.7%, assuming all other microstructural parameters are constant.

Thus, in cell regions with significantly thick diffusion layers, the mass transport is expected to be the limiting factor in cell performance as shown in Figure 6-29 in which an anode reaction layer porosity of 0.25 at a current density of 2 A cm^{-2} results in a concentration overpotential of 0.14 V for an anode diffusion layer thickness of 1000µm. Therefore, increasing the anode reaction layer porosity results in improved cell performance due as a result of the reduced concentration overpotential. On the other hand, negligible cathode concentration overpotential is observed when the cathode reaction layer porosity is increased due to the much smaller cathode diffusion layer thickness of 50µm, thus the reactive surface area length becomes limiting since increasing the cathode porosity reduces the cell performance as a result of the smaller reactive surface area as shown in Figure 6-30.

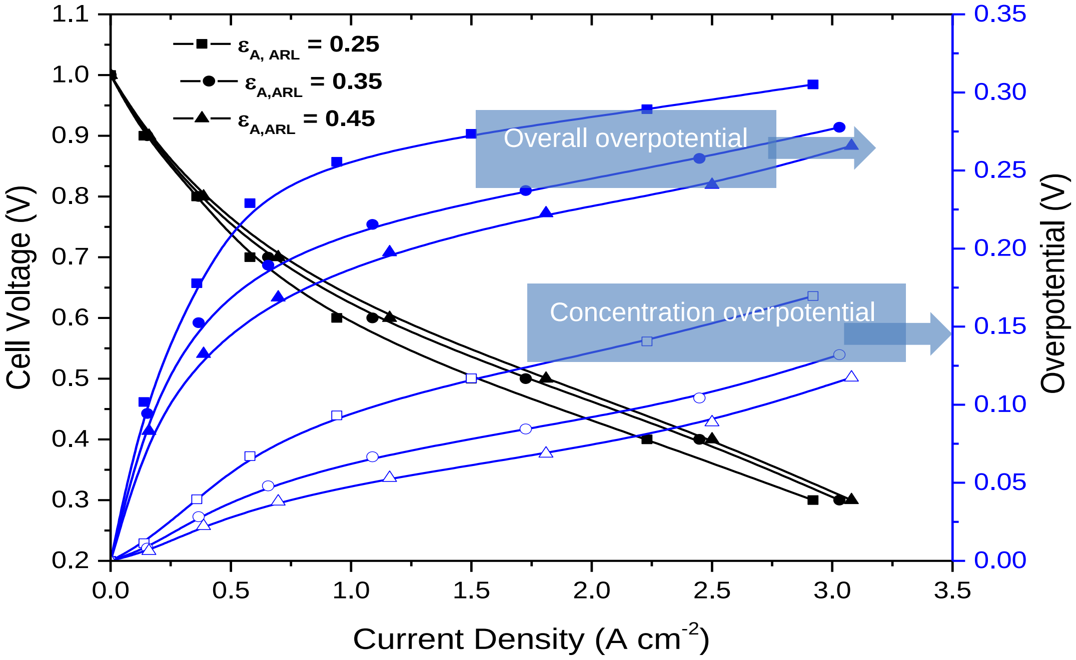

Figure 6-29: Effect of Anode reaction layer porosity on performance.

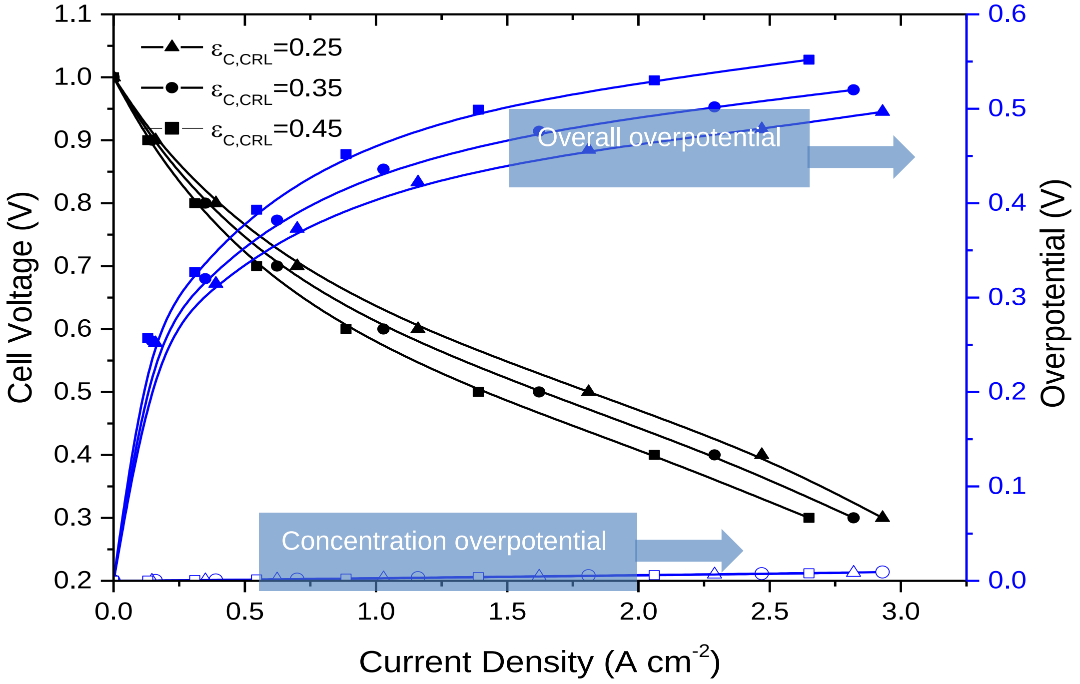

Figure 6-30: Effect of Cathode reaction layer porosity on performance.

Consequently, it is not advisable to reduce porosity to achieve a larger reactive surface area length because of the resultant reduction on the mass transport; rather it might be more advisable to reduce the particle diameter instead

6.8.3 Volume fraction of electronic phase

The composition of the electronic and ionic phases in the reaction layers and their effect on cell performance is studied in this section. The volume fraction of the electronic conducting particle is varied while the other operating and design conditions are kept at base conditions. The optimum composition is one that would provide percolation of both the electronic and ionic phases[75], gives the largest reactive surface area in the reaction layers while having the least effect on the ionic and electronic conductivity of the electrodes.

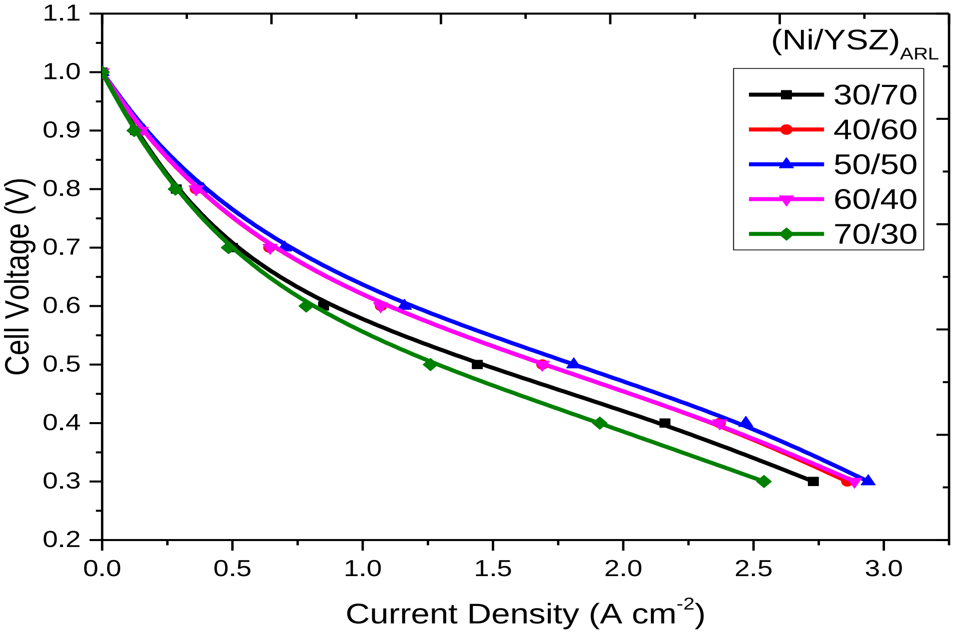

Figure 6-31: Effect of Anode reaction layer volume fraction on performance.

The effect of anode composition on cell performance is shown in Figure 6-31, as seen, performance increases when the Ni fraction in the reaction layer increases from 0.3 through to 0.5, however it starts to decrease at further increases from 0.5 through to 0.7. This indicates that the best cell performance for the anode composition is reached when the volume fraction of the electronic and ionic phases are equal at 0.5, which is consistent with the theoretical observations of Hussain et al [35]. When the Ni fraction is 0.5, the YSZ fraction becomes equal to the Ni fraction resulting in the largest possible reactive surface area and consequently the best cell performance. Also, the conductivities of the reaction layers are dependent on the volume fraction of Ni, increasing the Ni fraction beyond 0.5 increases the layers effective electronic conductivity but decreases its effective ionic conductivity which leads to increased ohmic polarisation thereby decreasing cell performance.

However, as shown in Figure 6-32 for the cathode composition, the performance curves for the volume fraction of LSM at 0.4 and 0.5 are almost identical, indicating that the best performance is obtained when the volume fraction is between 0.4 and 0.5 $(0.4 < \emptyset < 0.5)$

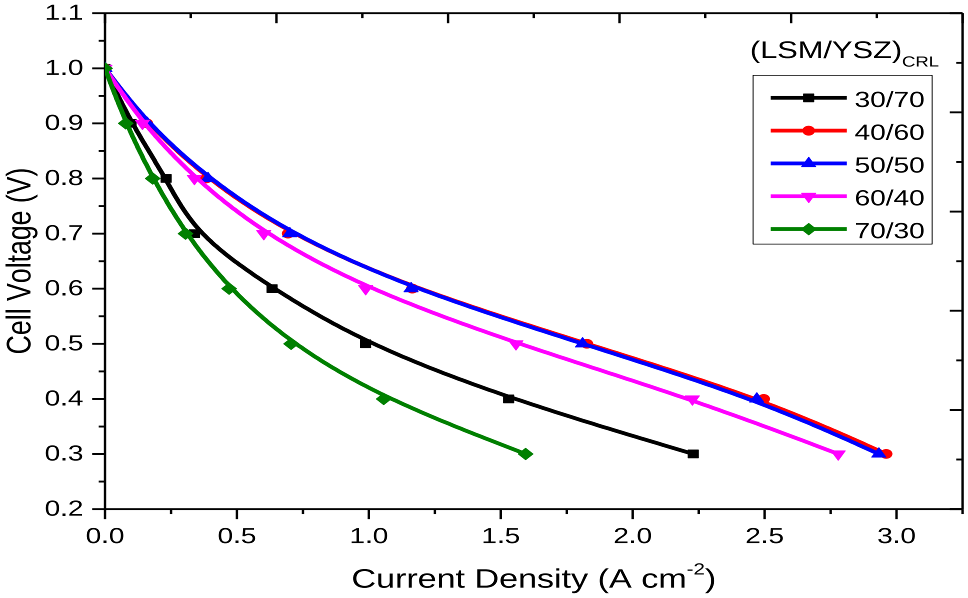

Figure 6-32: Effect of Cathode reaction layer volume fraction on performance.

This was then further investigated in Figure 6-33 where the cell current density is plotted against the LSM volume fraction. The figure shows that for the cathode volume fraction composition, the best cell performance is reached when the LSM volume fraction is 0.45, which is in agreement with the results obtained by Costamagna et al [59]

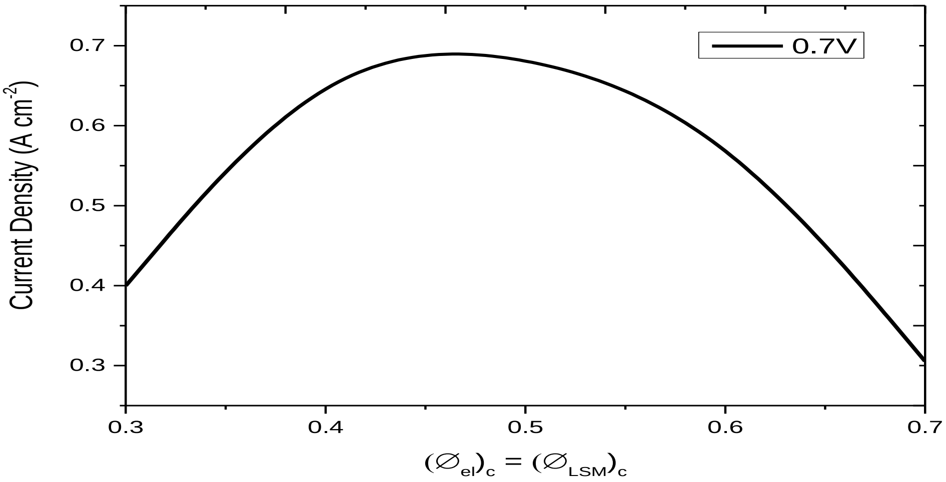

Figure 6-33: Effect of Cathode reaction layer composition on current density.

6.8.4 Tortuosity

The dependence of cell performance on the tortuosity of the SOFC is studied in this section. The tortuosity is varied while the other parameters and design conditions are kept at base condition. Increasing the tortuosity decreases the cell performance as depicted in Figure 6-32.

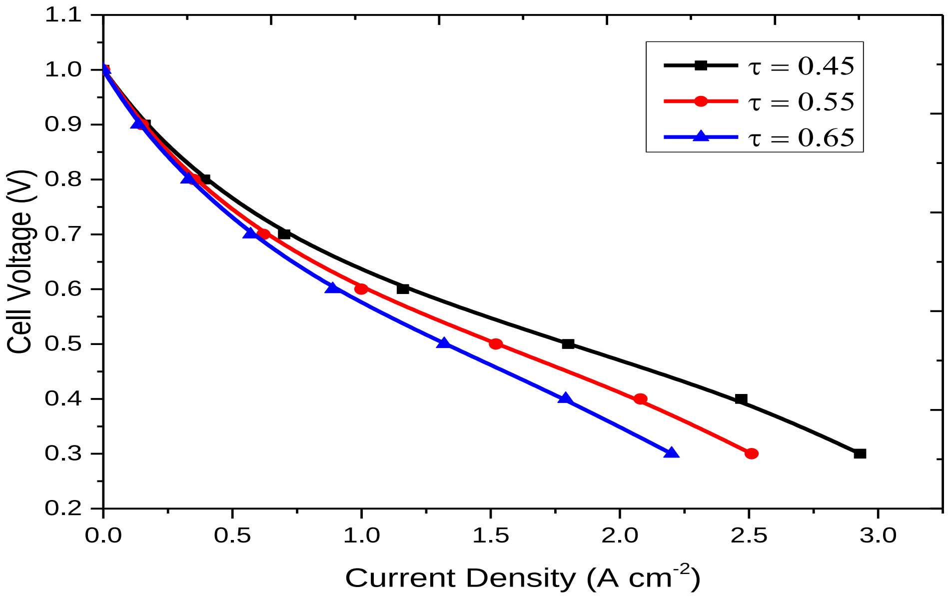

Figure 6-34: Effect of electrode tortuosity on performance.

When the tortuosity is increased, the length of the tortuous path through which the species diffuses increases, thereby creating additional resistance to the diffusing reactant species resulting in a reduction in the concentration of reactants in the reactant layers. This decreases electrochemical reaction rate and increases the concentration ovepotential. Moreover, the effective ionic and electronic conductivities are dependent on the tortuosity, as an increase in the tortuosity decreases their value, resulting in increased ohmic overpotential, thereby decreasing cell performance.

6.9 Conclusions

This chapter presented the solutions obtained from the numerical simulation of the two dimensional, microscale, steady state non-isothermal SOFC model. The model was first validated with experimental data from open literature. The effect of key operating conditions on the cell performance was studied, the operating conditions studied were the inlet temperatures, inlet flow velocities and inlet pressures.

A comparison between the cell performance when isothermal conditions were used and when non-isothermal conditions were used was carried out, results shows that the performance significantly improved when non-isothermal conditions were used, this was measured as the potential gain due to temperature rising. The effect of individual heat source on potential gain was also carried out, studies revealed that the contribution of joule heating, reversible heat sources and irreversible heat sources were approximately evenly distributed. The velocity profile and pressure profile increases in the anode compartments due to the expansion of the fuel gas (due to temperature rising) and the generation of H_2O from the oxidation reactions, however the velocity profile on the cathode side was about constant while the pressure profile decreased due to the consumption of O_2 in the reduction reaction.

The developed model was used in different phenomena predictions in the SOFC when reforming and water-gas shift reactions were considered in the anode electrodes. Performance comparison when the chemical reactions are considered and when they are not was carried out, showing significant improvement on performance with the reactions been considered. The different phenomena predictions carried out were the mole fraction distribution of species with and without chemical reactions considerations, temperature distribution profiles within the cell and the current density distribution.

Finally, micro-structural parametric studies on both anode and cathode reaction layers was carried out. The effects of the mean particle diameters, porosity, volume fraction of electronic phase and the tortuosity on SOFC performance were all individually studied with a view to obtaining their optimum values and increasing the overall cell performance.

CHAPTER7 : SOFC Hybrid System Modelling

This chapter presents the work of a steady-state thermodynamic numerical model of a hybrid solid oxide fuel cell (SOFC) - gas turbine (GT) cycle. The hybrid system consists of a zero dimensional internal reforming planar SOFC stack model, air compressor, fuel compressor, gas turbine, power turbine, recuperators, mixers, seperators and a heat recovery steam generator (HRSG). Individual thermodynamic models for each component were developed to evaluate the plants thermal energy efficiency and exergy production with a view to assessing the systems efficiencies distribution of irreversibility's or exergy destruction in the system. Parametric studies were also carried out to study the effect of system pressure, fuel utilisation factor, component efficiencies and turbine inlet temperatures on the plants efficiency.

7.1 Introduction

SOFCs have the potential to achieve higher electricity production efficiency as a result of the high quality heat it exhausts. Previous chapters have shown that pressurised SOFCs increases the overall cell performance with an increase in the output current density. This improved performance allows the SOFC to be integrated into a hybrid system, using the high energy exhaust heat from the SOFC to power the heat engine. The heat engine also serves the purpose of increasing the fluid temperatures to the inlet operating conditions of the SOFC. A hybrid system in this case refers to a fuel cell and heat engine combination. Gas turbines (GT) are one of the most commonly investigated heat engines [215, 216], although the sterling engine, steam turbines and diesel engines have also been investigated.

A number of studies have been carried out investigating the combination of SOFCs and gas turbine cycles.

Massardo et al[217] investigated the performance of an internal reforming solid oxide fuel cell (IRSOFC) and GT combined cycle, their developed model simulates the hybrid system at steady state operation, the model analyses only the energy efficiency to rate the performance.

Ameri et al[218] also simulated an atmospheric SOFC and GT hybrid system in which they assessed the effect of several operating conditions on the system performance.

Other studies on simulation and performance studies of SOFC hybrid systems have been reported by Chan et al[38, 125], Burbank et al[219], Yang et al[220], Chinda et al[39]. These studies have emphasised on the plant efficiency and specific work output for a particular system configuration.

Some other authors carried out comparative performance studies on different flow configurations. A study by Tucker et al[221] compared three different configuration designs on the basis of efficiency, operability issues and component integration while Zhang et al[222] compared two different air re-heating methods; they compared both configurations on the basis of operating pressure, operating temperature and efficiencies of the gas turbine components.

It is only recently that a few authors have begun to incorporate exergy studies as part of the hybrid cycle performance studies. Exergy studies are the application of second law of thermodynamics in assessing the irreversibility's in hybrid system.

Haseli et al [215], Sreeramulu et al[119], Calise et al[119] and Granovskii et al[223] all included exergy analysis in their model.

Calise et al [119] carried out a detailed exergy analysis on a coupled SOFC-GT plant by using exergy analysis to study the distribution of efficiency defects in each component while Granovskii et al[223] used exergy analysis in comparing two different SOFC-GT configurations, they then calculated their efficiency and compared the performance.

7.2 Different configurations of practical gas turbine cycles

A simple gas turbine unit is shown in Figure 7-1. Air enters at state 1 through the air compressor (AC), where it is pressured to state 2, after which it passes to the combustor (C). Energy is supplied in the combustor by adding fuel into the air stream, the resultant hot gasses at state 3 expands in the gas turbine (GT). In order to achieve network output from the system $(P_t - P_c)$, the turbine must produce more gross work output than that required to power the compressor and overcome the mechanical transmission losses.

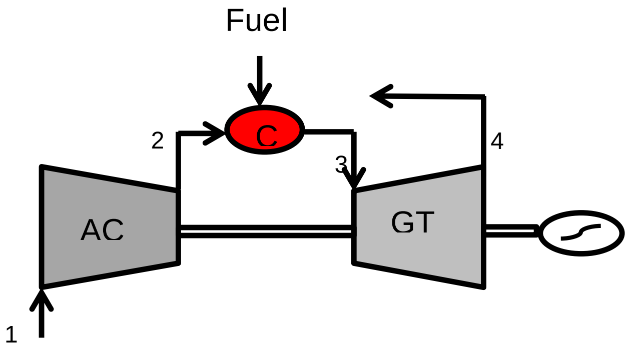

Figure 7-1: Simple gas turbine plant

The recuperated gas turbine unit is presented in Figure 7-2 in which the hot exhaust gases leaving the power turbine is passed through a heat exchanger, where the heat from the gases is used to raise the temperature of air leaving the compressor , the heat exchanger in this case is called a recuperator (R).

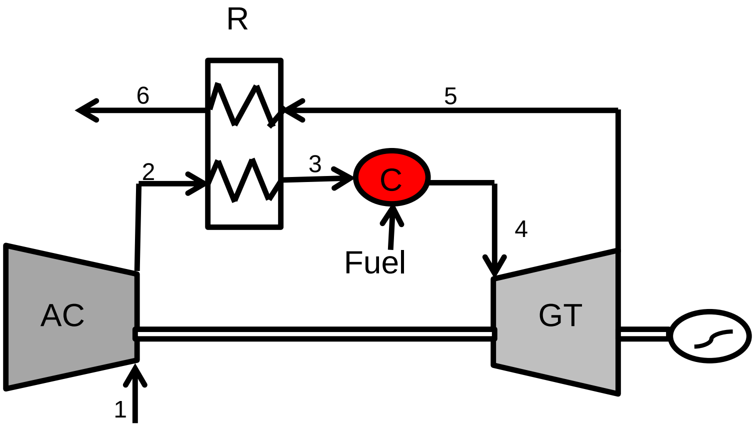

Figure 7-2: Recuperated gas turbine plant

The intercooled recuperated gas turbine unit is shown in Figure 7-3, in which the compression of the inlet air is carried out in two stages (AC1 and AC2) with an intercooler (IC) between the compressors, as such, the work input to the compressor for a given pressure ratio and mass flow is reduced, consequently leading to improved gas turbine performance.

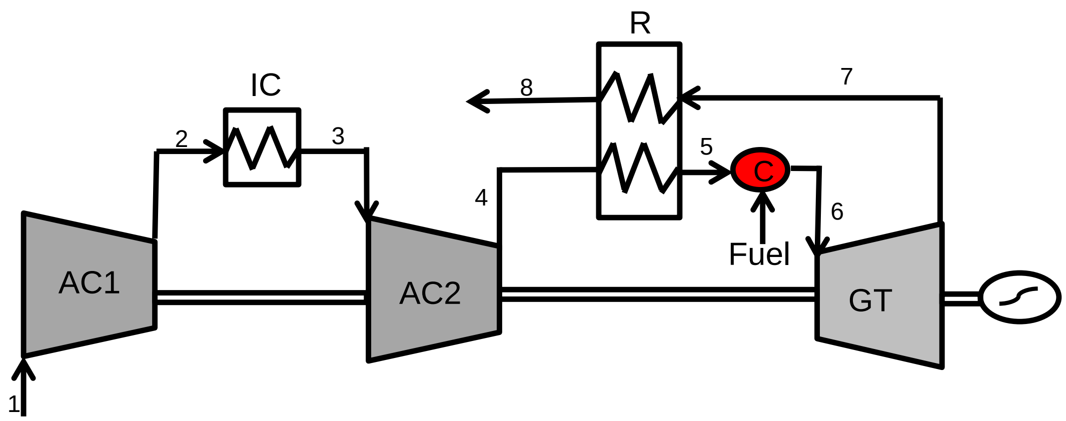

Figure 7-3: Recuperated gas turbine plant with intercooling

7.3 Thermodynamic analysis of the gas turbine plant components

The thermodynamic performance of each component highlighted above will be analysed in this section. The first law of thermodynamics which analyses the energy changes and the second law which deals with the exergy changes will be employed for the steady state flow in the cycle.

7.3.1 Compressor

The isentropic efficiency of the air compressor is given as:

$$\eta_c = \frac{h_{2s} - h_1}{h_2 - h_1} = \frac{c_{p,a}(T_{2s} - T_1)}{c_{p,a}(T_2 - T_1)} \tag{7-1}$$

The ideal temperature of air at the outlet of the compressor can be determined from the following isentropic relationship

$$\frac{T_{2s}}{T_1} = \left(\frac{p_2}{p_1}\right)^{\gamma-1/\gamma} \tag{7-2}$$

Carrying out an energy balance for the compressor, the work required for the compressor to produce a compression ratio of r_p is given by

$$\dot{W}_c = \dot{m}_1(h_2 - h_1) \tag{7-3}$$

The entropy balance equation for the compressor can be expressed as

$$\dot{m}_1 T_0 S_1 - \dot{m}_1 T_0 S_2 - S_{gen} \tag{7-4}$$

Hence the entropy generation rate for the compressor can be expressed as

$$S_{gen} = I_{compressor} = \dot{m}_1 T_0 (S_2 - S_1) \tag{7-5}$$

Where T_0 is the external environmental temperature and S is the entropy value of the state under consideration, I is the irreversibilites. S_{gen} is also known as the exergy destruction rate in the compressor.

The equations expressed above apply also for the second stage compressor (AC2) in Figure 7-3.

7.3.2 Recuperator

The recuperator effectiveness for Figure 7-2 is defined to allow for the calculation of the temperature difference necessary for the transfer heat, it is described as

$$\epsilon_R = \frac{T_3 - T_2}{T_6 - T_2} \tag{7-6}$$

Using the energy balance equation, the exhaust temperature of the cycle may be obtained:

$$m_2(h_3 - h_2) = m_6(h_6 - h_7) \tag{7-7}$$

Also, the entropy balance equation for the recuperator may be expressed as

$$\dot{m}_2 T_0 S_2 - \dot{m}_3 T_0 S_3 + \dot{m}_7 T_0 S_7 - \dot{m}_8 T_0 S_8 + S_{gen} \tag{7-8}$$

Thus, the entropy generation rate within the recuperator is expressed as

$$S_{gen} = I_{recuperator} = T_0[\dot{m}_2(S_3 - S_2) - \dot{m}_7(S_7 - S_8)] \tag{7-9}$$

7.3.3 Intercooler

The work input to the compressors when intercooling is considered as described in Figure 7-3 is given by

$$\dot{W}_c = \dot{m}_1[(h_2 - h_1) + (h_4 - h_3)] \tag{7-10}$$

The intercooler entropy balance equation can be expressed as

$$\dot{m}_2 T_0 S_2 - \dot{m}_2 T_0 S_3 - S_{gen} \qquad (7\text{-}11)$$

Hence the entropy generation rate for the intercooler is expressed as

$$S_{gen} = I_{intercooler} = \dot{m}_2 T_0 (S_3 - S_2) \qquad (7\text{-}12)$$

The work input to the compressors will be least when the pressure ratio in each compression stage is the same i.e. $p_4/p_3 = p_2/p_1$ and when the air after the first stage is cooled in the intercooler back to the initial temperature before the first stage i.e. $T_3 = T_1$.

7.3.4 Combustor

Using the simple gas turbine of Figure 7-2, the mass balance of the combustor is given by

$$\dot{m}_2 + \dot{m}_{fuel} = \dot{m}_3 \qquad (7\text{-}13)$$

The energy balance equation for the combustor is expressed as

$$\dot{m}_2 h_2 + \dot{Q}_{comb} - \dot{m}_3 h_3 - \dot{Q}_{loss} \qquad (7\text{-}14)$$

Where

$$\dot{Q}_{comb} = m_{fuel} LHV \qquad (7\text{-}15)$$

$$\dot{Q}_{loss} = \eta_{comb} m_{fuel} LHV \qquad (7\text{-}16)$$

The entropy balance equation for the combustor can be written as

$$\dot{m}_2 T_0 S_2 + (\dot{m}S)_{fuel,comb} + \frac{\dot{Q}_{comb}}{T_{comb}} - \dot{m}_3 T_0 S_3 - \frac{\dot{Q}_{loss}}{T_0} + S_{gen} \qquad (7\text{-}17)$$

Thus the entropy generation within is combustor is given as

$$S_{gen} = T_0(\dot{m}_3 S_3 - \dot{m}_2 S_2) - (\dot{m}S)_{fuel,comb} - \frac{\dot{Q}_{comb}}{T_{comb}} + \frac{\dot{Q}_{loss}}{T_0} \qquad (7\text{-}18)$$

Where T_{comb} is the mean combustion temperature

Gas turbine

The work required for the compressor is provided by the gas turbine, taking into consideration the transmission losses, the gas turbine work is given by

$$W_{gt} = \frac{W_c}{\eta_t} \tag{7-19}$$

The outlet temperature from the turbine can be determined for Figure 7-1 when the turbine inlet temperature (TIT) is known, by using the turbine isentropic efficiency definition

$$\eta_{gt} = \frac{h_3 - h_4}{h_3 - h_{4s}} \tag{7-20}$$

The ideal temperature downstream from the turbine can then be evaluated after obtaining the exit pressure from the gas turbine with the isentropic relationship

$$\frac{p_4}{p_3} = \left(\frac{T_{4s}}{T_3}\right)^{\gamma/\gamma-1} \tag{7-21}$$

The entropy balance equation is thus expressed as

$$\dot{m}_3 T_0 S_3 - \dot{m}_4 T_0 S_4 + S_{gen} \tag{7-22}$$

Hence, the entropy generation rate is given by

$$S_{gen} = I_{gt} = \dot{m}_3 T_0 (S_3 - S_4) \tag{7-23}$$

7.4 Comparative performance of practical GT cycles

Performance curves are presented in this section to highlight the importance of key parameters. The curves use the air compression ratio r_p as the x-axis. The cycle efficiency and net-work output were evaluated from equations presented in section 7-3. The main operating parameters of the practical gas turbine plant are tabulated in Table 7-1

Table 7-1: Operating parameters for the practical gas turbine plant

isentropic efficiency of compressor $(\boldsymbol{\eta_c})$	0.85
Isentropic efficiency of turbine $(\boldsymbol{\eta_t})$	0.87
Mechanical transmission efficiency $(\boldsymbol{\eta_m})$	0.99
Combustion efficiency $(\boldsymbol{\eta_b})$	0.98
Recuperator effectiveness $(\boldsymbol{\eta_R})$	0.8
Pressure losses	
Combustor $(\Delta \boldsymbol{p_b})$	2%
Recuperator air side $(\Delta \boldsymbol{p_{Ra}})$	3%
Recuperator gas side $(\Delta \boldsymbol{p_{Rg}})$	4%
Ambient conditions	
Temperature $(\boldsymbol{T_1})$ $(\boldsymbol{K})$	288
Pressure $(\boldsymbol{p_1})$ $(\boldsymbol{atm})$	1
Source: Ref [119, 215]	

The gas turbine cycle efficiency is defined as the net work done by the turbine (specific work output) divided by the heat input to the combustor, which is the actual fuel-air ratio and calorific value of the fuel.

$$\eta_c = \frac{W_N}{f_R Q_{net}} \tag{7-24}$$

Where f_R is the actual fuel air ratio and Q_{net} is the fuel calorific value. If we assume that the fuel is completely burnt in the combustor, the combustion efficiency is defined as

$$\eta_b = \frac{theorectical\ f_R\ for\ given\ \Delta T}{actual\ f_R\ for\ given\ \Delta T} \tag{7-25}$$

7.4.1 Simple gas turbine cycle

The efficiency versus pressure ratio and specific work output against pressure ratio curves for a simple gas turbine cycle are presented in Figure 7-4. The figure shows that the cycle efficiency and the specific work output are dependent upon the Turbine inlet temperature (TIT) as well as the pressure ratio(r_p). Furthermore, the Figures show that for each value of TIT, the cycle efficiency has a peak value at a particular r_p

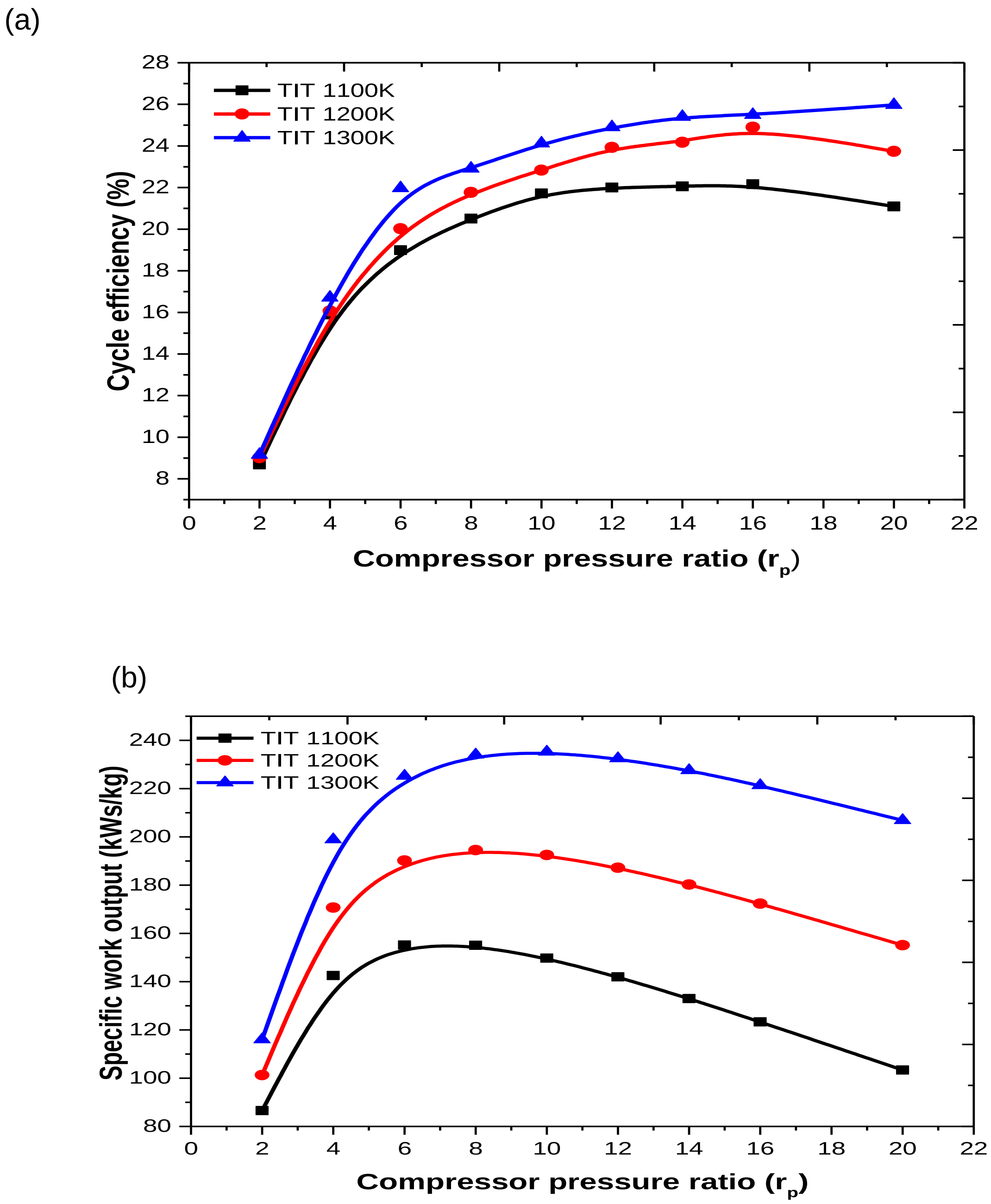

Figure 7-4: Performance of simple gas turbine cycle (a) efficiency (b) specific work

A slight reduction in the cycle efficiencies is noticed at higher pressure ratios, this is because of the reduction in fuel supply needed in maintaining the TIT. When the pressure ratio is high, the compressor exit temperature increases, thereby reducing the heat needed from the combustor to maintain the TIT. It is also noticed that the optimum r_p which gives the maximum efficiency is different from that for the maximum specific work output, using TIT at 1200K, r_p for maximum efficiency is 16 while that for the maximum specific work is 8, since the curves are quite flat near the peak, any r_p value between both can be used without any significant loss in efficiency.

The advantage of a high TIT is evident from the curves. The efficiency increases with increasing TIT; this is due to the improved positive turbine work compared to the negative compressor work. A close look at Figure 7-4a indicates that the efficiency gain is marginal when the TIT is increased from 1200K to 1300K, the same cannot be said for the specific work in Figure 7-4b where no such marginal increment is observed when the TIT is increased to 1300K.

7.4.2 Recuperated gas turbine cycle.

The performance curves for the recuperated gas turbine cycle is presented in Figure 7-5, In this case, the addition of a heat recovery steam generator (HRSG) only causes a slight reduction in the specific work output when compared to the simple gas turbine cycle of Figure 7-4b, this reduction is due to the pressure losses in the air and gas sides of the recuperator. However, as shown in Figure 7-5a, the efficiency curves are quite different. Recuperation substantially increases the cycle efficiency and reduces the optimum pressure ratio.

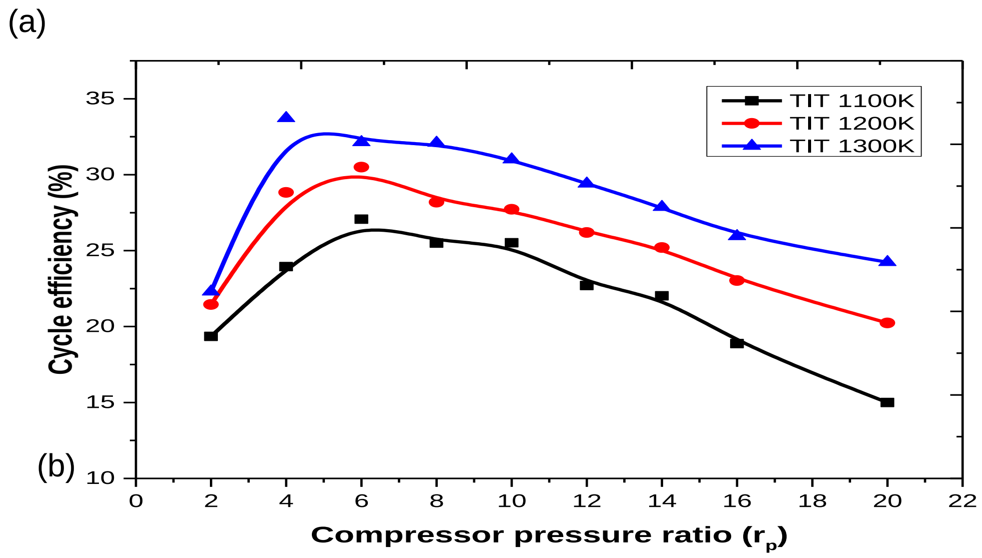

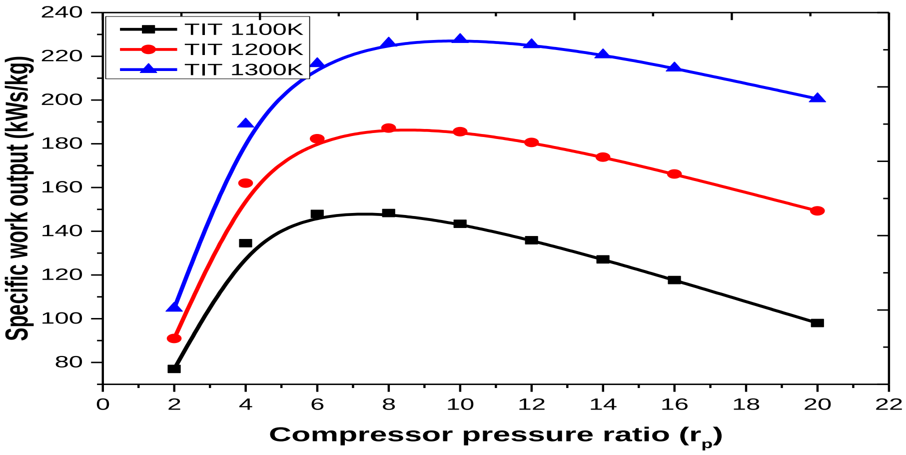

Figure 7-5: Performance of the recuperated gas turbine cycle (a) efficiency (b) specific work

Comparing the case for TIT 1200K, the maximum efficiency for the simple GT case was 24.9% at a r_p of 14, while for the recuperated GT case, the maximum efficiency is 30.5% at a r_p of 6. More observations can be made from Table 7-2 regarding the recuperated case at 1200K

Table 7-2: Results for 1200K turbine inlet temperature

r_p	$P_t - P_c (kWs/kg)$	$T_{c,exit}$ (K)	$T_{R,exit}$ (K)
2	90.94	362.4	573.5
4	161.99	452.9	593.99
6	182.28	514.78	614.82
8	187.18	563.23	634.12
10	185.51	603.66	651.53
12	180.58	638.65	667.55
14	173.87	669.7	682.35
16	166.16	697.72	696.36
20	149.28	747	721.27

First, in order to obtain a compressor delivery temperature of up to 1073K (for the cathode inlet for the SOFC-hybrid system) from compressor heating alone, the compression ratios have to be much greater than 20 ($r_p \geq 20$), at such pressure ratios, the net power from the turbine and cycle efficiencies will be significantly low, second, the table shows that for a recuperated cycle, heat exchanging between the turbine exhaust gases and inlet air to the combustor is only possible up to a r_p of 14, beyond this, the turbine exhaust gases will not have enough heat to increase the air temperature to the combustor.

Figure 7-6 compares the performance of a recuperated GT cycle with and without intercooling when the TIT is set at 1200K. For the recuperated case, the addition of an intercooler improves both the cycle efficiency and the specific work output considerably; this is because intercooling will reduce the overall compression power thereby increasing the turbine specific work output. The curves of Figure 7-6 are based on the assumption that the inlet air to the second compressor (AC2) is cooled to the inlet temperature of the first compressor (AC1) and that the pressure ratios for both compressors are equal.

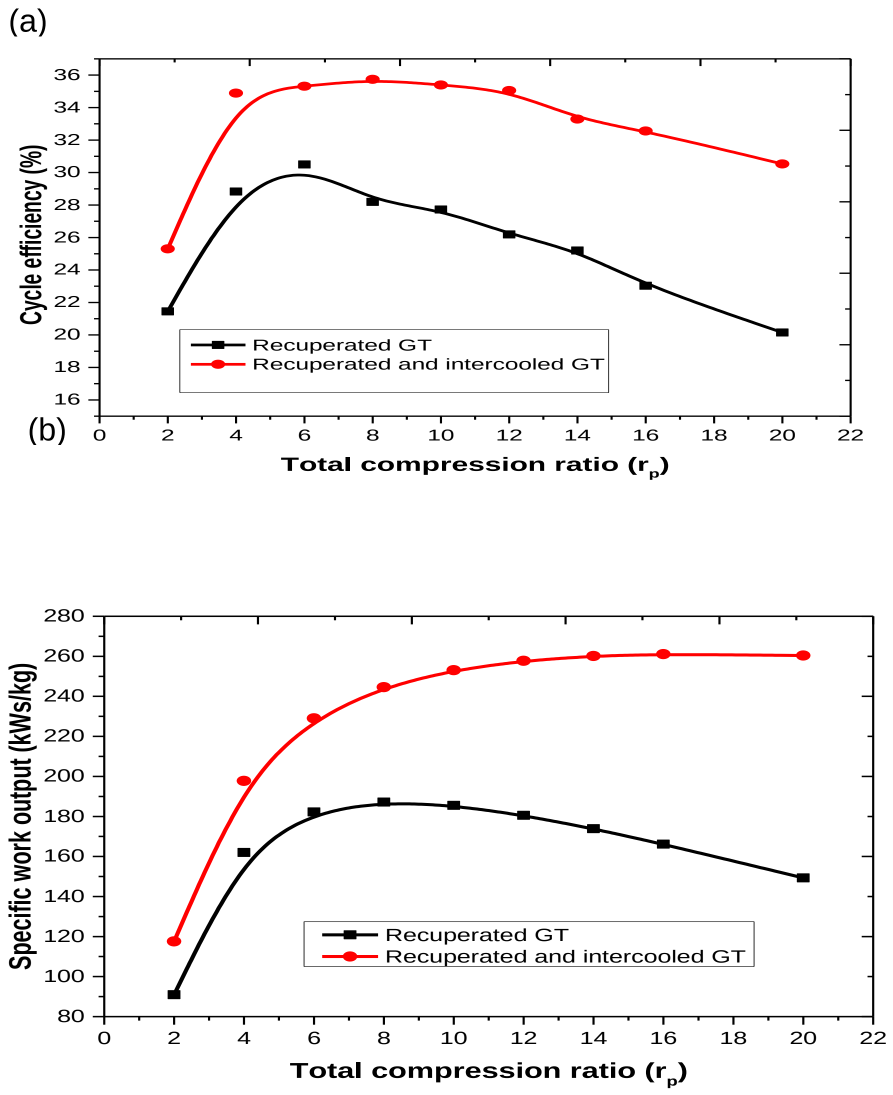

Figure 7-6: Comparison of recuperated GT cycle with and without intercooling (a) efficiency (b) specific work

Generally, the recuperated GT is preferred; the complexity in terms of cost and compactness can be quite significant when intercoolers are incorporated, as they are quite expensive and bulky.

7.5 Hybrid SOFC/GT system.

The hybrid system combines the SOFC with a GT plant, this system is identified as a superior power generation technology compared to other options[222], since the SOFC will produce a fraction of the total power, thereby increasing the efficiency of the cycle.

The simulation and performance analysis of the SOFC/GT hybrid system is carried out. Two basic SOFC/GT configurations for reheating the air into the cathode were studied (combustor exhaust recycle (CER) and recuperator heat exchanger (RHE)) and their performance compared

7.5.1 Combustor exhaust recycle (CER)

A portion of the exhaust flue gas after the combustor is recycled and mixed with the air going into the cathode in order to preheat the cathode inlet; the recirculated mass flow is adjusted to maintain the cathode inlet temperature at 1073K.

Simplified process flow sheet of the SOFC/GT hybrid system with the CER cycle is shown in Figure 7-7. The air (1) is compressed in the compressor AC (2) and preheated in the recuperator R1 (3) by the exhaust gases (11) from the gas turbine. Afterwards, the temperature of the preheated air (3) is increased by mixing in M1 with the recycled exhaust gases (10) from the combustor before going into the cathode (4) side of the SOFC. The air inlet temperature (4) of the cathode is controlled by adjusting the mass flow of the recycled portion (10) from the combustor exhaust. A high temperature booster (BS1) is used in recycling the flow. For the fuel stream, the methane gas (15) is compressed in the fuel compressor FC (16), after which it is preheated in the low temperature recuperator RE2 (17), it is then mixed with water from the heat recovery steam generator (HRSG) (25) in M3, here, the exhaust heat from R2 (13) is used in heating the water from the pump (25). The fuel stream (18) is then further mixed with some recirculated portion of the steam from the anode exit (21) in the pre-reformer PR, which pre- reforms the methane stream up to 30% before been completely reformed in the anode of the SOFC. The air steam (4) and the fuel stream (19) in the SOFC stack drive the electrochemical reactions occurring in the reaction layers of both electrodes. The DC current produced by the SOFC through an external circuit is converted to AC current by using a converter. The highly exothermic electrochemical reaction produces enough heat for the steam reforming reaction and also to heat up the cathode and anode streams. The unutilized fuel stream gas (20) are further heated in the combustor (C) located downstream from the SOFC. The outlet flow (8) temperature from the combustor has enough thermal energy to power the gas turbine (GT) and produce useful work.

The primary advantage of the CER configuration is to reduce cost as the need for one more recuperator is eliminated and also to reduce the air compressor work through a significant decrease in the compressor inlet flow.

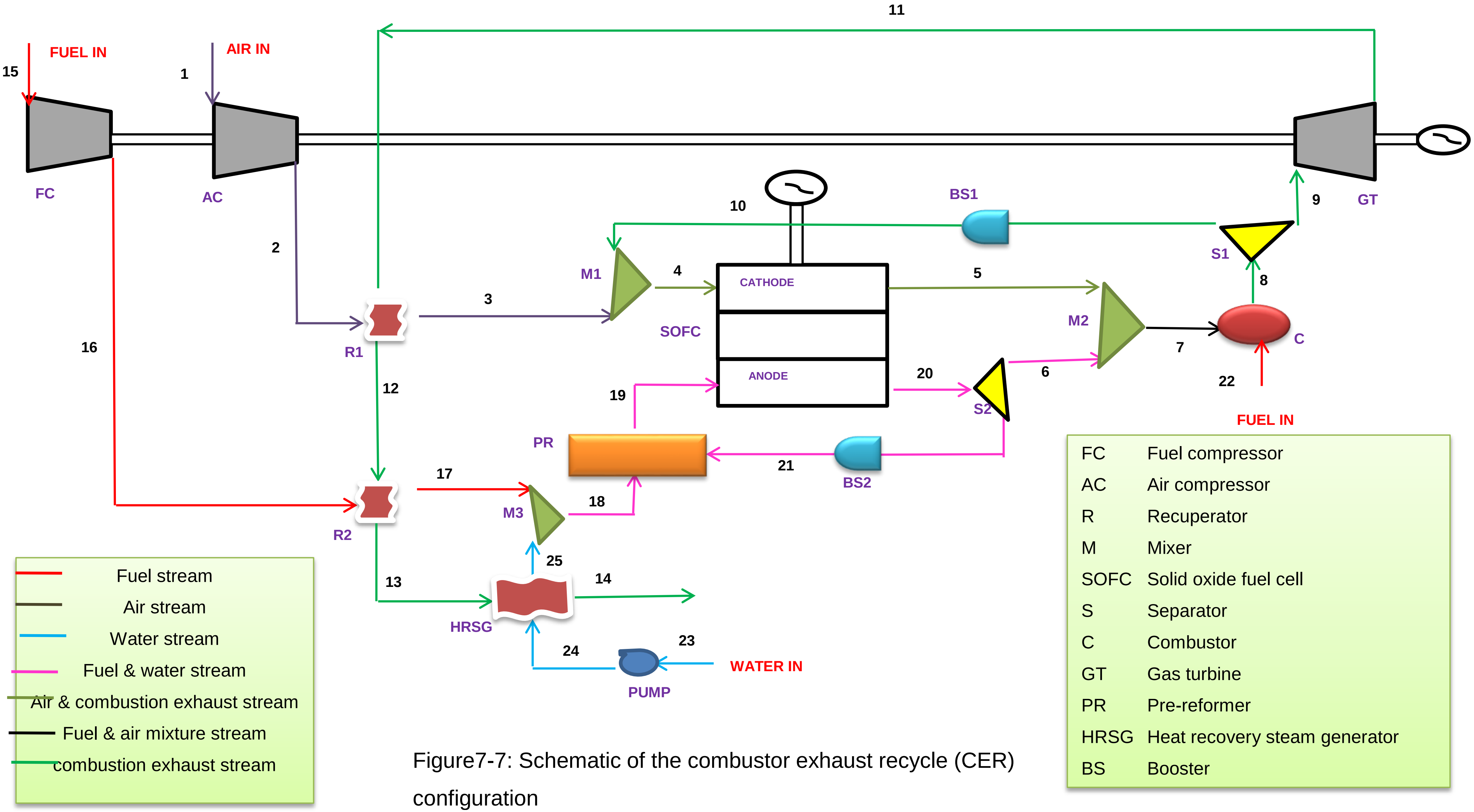

FC	Fuel compressor
AC	Air compressor
R	Recuperator
M	Mixer
SOFC	Solid oxide fuel cell
S	Separator
C	Combustor
GT	Gas turbine
PR	Pre-reformer
HRSG	Heat recovery steam generator
BS	Booster

Figure7-7: Schematic of the combustor exhaust recycle (CER) configuration

7.5.2 Recuperator heat exchanger (RHE)

The schematic of the process flow diagram for the recuperated case is shown in Figure 7-8, here the inlet air (1) from the air compressor (2) is preheated by the exhaust flow (14) from the gas turbine in the recuperator R1, after which it is re-heated (3) by a portion of the exhaust from the combustor (9) in the high temperature recuperator R3. The exit temperature of the air in R3 (4) is controlled by the mass flow of the stream (8) from the separator S2, it is also regulated by adding supplementary fuel (24) to the combustor, this elevates the turbine inlet temperature, thereby increasing the heat in the combustor exit ensuring that recuperation in R3 is sufficient to preheat the cathode inlet air flow (4) to the set temperature of 1073K. The fuel flow process is the same as described in the CER configuration.

Its primary advantage over other configurations is the potential for high energy efficiency at low pressure ratios.

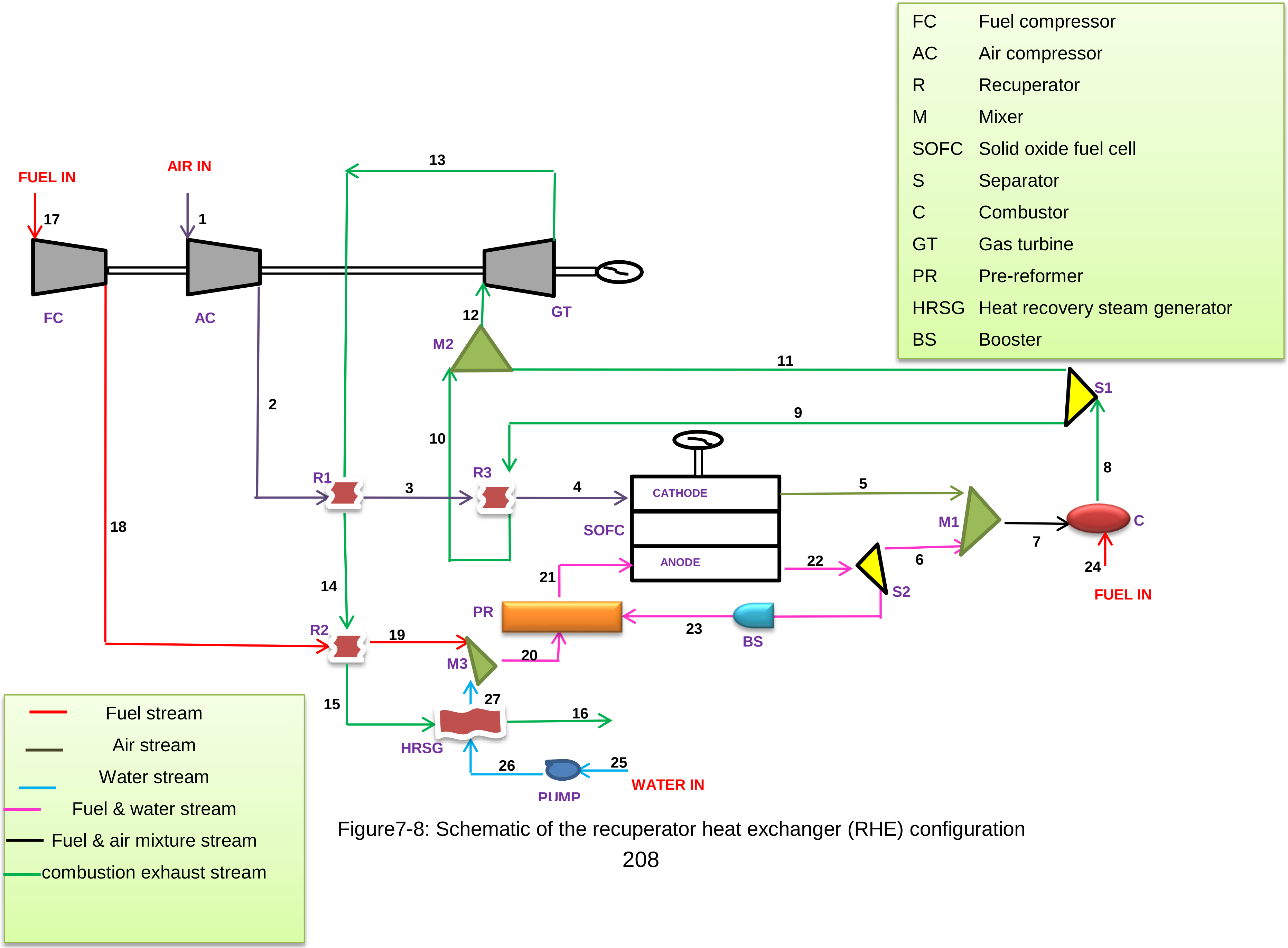

Figure7-8: Schematic of the recuperator heat exchanger (RHE) configuration

7.5.3 Further thermodynamic analysis of SOFC/GT hybrid plant

In addition to the thermodynamics analysis carried out for the practical gas turbine cycle in section 7-3, more analysis are carried out in this section on the recuperators, mixers, separators, SOFC and combustor.

Recuperators

There are two recuperators in the CER cycle (R1 and R2), while there are three in the RHE cycle (R1, R2 and R3). The recuperator effectiveness has already been defined in Equation 7-6.

The energy balance equations for the recuperators in the RHE cycle are expressed as:

$$m_2(h_3 - h_2) = m_{13}(h_{13} - h_{14})\ for\ R1 \tag{7-26}$$

$$m_{18}(h_{19} - h_{18}) = m_{14}(h_{14} - h_{15})\ for\ R2 \tag{7-27}$$

$$m_4(h_4 - h_3) = m_9(h_9 - h_{10})\ for\ R3 \tag{7-28}$$

The entropy balance equations for the recuperators in the RHE cycle are:

$$\dot{m}_2 T_0(S_3 - S_2) + \dot{m}_{13} T_0(S_{13} - S_{14}) = S_{gen}\ for\ R1 \tag{7-29}$$

$$\dot{m}_{18} T_0(S_{20} - S_{19}) + \dot{m}_{14} T_0(S_{14} - S_{15}) = S_{gen}\ for\ R2 \tag{7-30}$$

$$\dot{m}_3 T_0(S_4 - S_3) + \dot{m}_9 T_0(S_9 - S_{10}) = S_{gen}\ for\ R3 \tag{7-31}$$

Mixers

There are three mixers in both the CER and RHE cycles (M1, M2 and M3). The energy balance equations for the RHE mixers are expressed as:

$$m_5 h_5 + m_6 h_6 = m_7 h_7\ \ for\ M1 \tag{7-32}$$

$$m_{11} m_{11} + m_{10} h_{10} = m_{12} h_{12}\ \ for\ M2 \tag{7-33}$$

$$m_{19} h_{19} + m_{27} h_{27} = m_{20} h_{20}\ \ for\ M3 \tag{7-34}$$

While the entropy balance equation for the same RHE mixers are:

$$T_0[(m_7 S_7 - m_5 S_5) + (m_7 S_7 - m_6 S_6)] = S_{gen}\ for\ M1 \tag{7-35}$$

$$T_0[(m_{12}S_{12} - m_{11}S_{11}) + (m_{12}S_{12} - m_{10}S_{10})] = S_{gen}\, for\ M2 \tag{7-36}$$

$$T_0[(m_{20}S_{20} - m_{19}S_{19}) + (m_{20}S_{20} - m_{27}S_{27})] = S_{gen}\, for\ M3 \tag{7-37}$$

Separators

There is one separator in both the CER and RHE cycles (S1). The energy balance equation for the RHE separators is expressed as:

$$M_8h_8 = M_9h_9 + M_{11}h_{11} \tag{7-38}$$

While the entropy balance equation for the same RHE seperator is:

$$T_0[(m_8S_8 - m_9S_9) - (m_8S_8 - m_{11}S_{11})] = S_{gen} \tag{7-39}$$

SOFC

The modelling equations and solution to the non-isothermal SOFC model has already been carried out in Chapter 6. The Direct current (DC) electric power produced by the fuel cell is expressed as:

$$W_{sofc,DC} = V_{cell}i_{cell} \tag{7-40}$$

Where V_{cell} is the cell voltage and i_{cell} is the average current density.

A schematic of the SOFC from the RHE hybrid system is extracted and shown in Figure 7-9

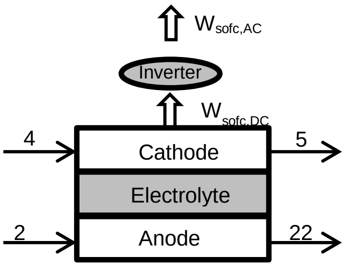

Figure 7-9: Schematic of SOFC in the RHE cycle

The mass balance for this SOFC system is given as:

$$\sum_{in} Mass\ flow = \sum_{out} Mass\ flow \tag{7-41}$$

Thus

$$m_4 + m_{21} = m_5 + m_{22}U_f + m_{22}(1 - U_f) \tag{7-42}$$

Where U_f is the fuel utilisation factor.

Applying the energy balance equation for the SOFC gives:

$$m_4h_4 + m_{21}(U_f)LHV + m_{21}(1 - U_f) = m_5h_5 + m_{22}U_fh_{22} + m_{22}(1 - U_f)h_{22} + W_{sofc,DC} \tag{7-43}$$

Where LHV is the lower heating value of the fuel.

The entropy balance equation of the SOFC is written as follows:

$$T_0[(m_5S_5 - m_4S_4) + (m_{22}U_fS_{22} - m_{21}S_{21}) - m_{22}(1 - U_f)T_0S_{22}] = S_{gen} \tag{7-44}$$

Combustor

The exhausts from the SOFC are further heated in the combustor as shown in Figure 7-10 for the RHE cycle. The non-reacted fuel from the SOFC is considered burnt up in the combustor with additional fuel supplied by bye-passing the SOFC.

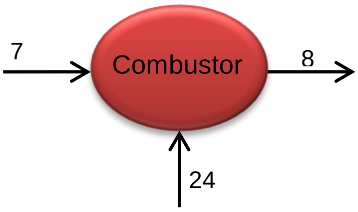

Figure 7-10: Schematic of Combustor in the RHE cycle

The mass balance for the combustor is given as:

$$m_7 + m_{24} = m_8 \tag{7-45}$$

While the energy balance equation can be expressed as:

$$m_7 U_f h_7 + Q_{comb} = m_8 h_8 - Q_{loss} \quad (7\text{-}46)$$

Where

$$Q_{comb} = \left[m_7\left(1 - U_f\right) + m_{24}\right] LHV \quad (7\text{-}47)$$

$$Q_{loss} = \left[m_7\left(1 - U_f\right) + m_{24}\right]\left(1 - \eta_{comb}\right) LHV \quad (7\text{-}48)$$

Where η_{comb} represents the combustor efficiency. The entropy balance equation for the combustor is given by:

$$m_7 T_0 S_7 + m_{24} T_0 S_{24} + \frac{Q_{comb}}{T_{comb}} + S_{gen} - m_8 T_0 S_8 - \frac{Q_{loss}}{T_0} \quad (7\text{-}49)$$

Where T_{comb} is the adiabatic flame temperature of the combustor.

7.5.4 Overall balance equation for hybrid cycle.

The entire SOFC-GT hybrid power plant in Figure 7-8 for the RHE cycle can by analysed as a lumped volume without considering the mass generation and consumption in the SOFC as shown in Figure 7-11. The figure shows the inlet and outlet flows at the control volume boundaries.

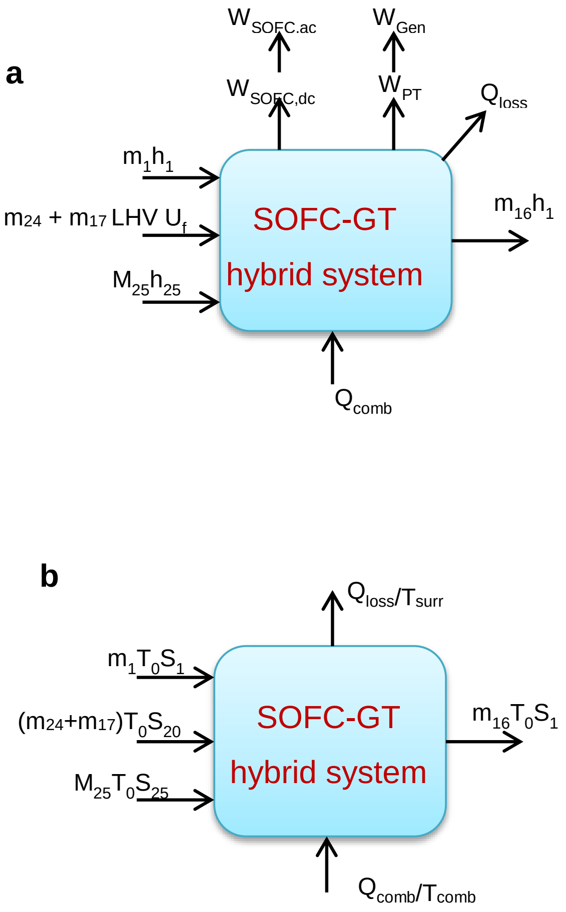

Figure 7-11: Lumped SOFC-GT hybrid model (a) energy balance (b) entropy balance

Mass balance

The overall mass balance for the system is written as:

$$m_1 + m_{17} + m_{24} + m_{25} = m_{16} \tag{7-50}$$

Where

$$m_1 = m_2 = m_3 = m_4 \tag{7-51}$$

$$m_{17} = m_{18} = m_{19} \tag{7-52}$$

$$m_{25} = m_{26} = m_{27} \tag{7-53}$$

$$m_{12} = m_{13} = m_{14} = m_{15} = m_{16} \tag{7-54}$$

Energy balance

The overall energy balance of the system is given as:

$$m_1 h_1 + m_{17} U_f LHV + Q_{comb} = m_{16} h_{16} + Q_{loss} + W_{sofc} + W_{GT} - W_{comp} \quad (7\text{-}55)$$

The total thermal efficiency of the SOFC-GT system is defined as the ratio of the network output to the total energy input to the system, i.e.,

$$\eta^{cyc} = \frac{\dot{W}_{net}}{Q_{tot}} \quad (7\text{-}56)$$

Where

$$\dot{W}_{net} = \dot{W}_{sofc,ac} + \dot{W}_{Gen} \quad (7\text{-}57)$$

$$\dot{W}_{sofc,ac} = \eta_{invert} n V_{sofc} I_{sofc} \quad (7\text{-}58)$$

$$\dot{W}_{Gen} = \eta_{Gen} \left(\dot{W}_{GT} - \dot{W}_{cp}{}^{air} - \dot{W}_{cp}{}^{fuel} - \dot{W}_{pump} \right) \quad (7\text{-}59)$$

$$Q_{tot} = m_f U_f LHV + Q_{comb} \quad (7\text{-}60)$$

where	
$\boldsymbol{\eta_{invert}}$	Is the DC-AC inverter efficiency
$\boldsymbol{\eta_{Gen}}$	Is the generator efficiency
$\boldsymbol{m_f}$	Is the mass flow of the fuel
$\boldsymbol{n}$	Is the number of cells in the sofc stack
$\boldsymbol{V_{sofc}}$	Is the cell voltage
$\boldsymbol{I_{sofc}}$	Is the current density
$\boldsymbol{\dot{W}_{GT}}$	is the work done by the gas turbine
$\boldsymbol{\dot{W}_{cp}{}^{air}}$	Is the workdone by the air compressor
$\boldsymbol{\dot{W}_{cp}{}^{fuel}}$	Is the work done by the fuel compressor
$\boldsymbol{\dot{W}_{pump}}$	Is the work done by the pump
$\boldsymbol{U_f}$	Is the fuel utilisation factor in the SOFC
LHV	Is the lower heating value of the fuel
$\boldsymbol{Q_{comb}}$	Is the heat generated in the combustor

Entropy balance

The overall entropy generation rate with the system is given as:

$$S_{gen}^{cyc} = \sum_{i} S_{gen,i} \qquad (7\text{-}61)$$

Where i is the compressor(s), recuperator(s), SOFC, combustor, gas turbine(s).

This can be expressed as

$$S_{gen}^{cyc} = m_{16}T_0S_{16} - m_1T_0S_1 \text{ - } m_{25}T_0S_{25} - m_{17}T_0S_{17} - \frac{Q_{comb}}{T_{comb}} + \frac{Q_{loss}}{T_{surr}} \qquad (7\text{-}62)$$

7.5.5 Simulation assumptions

The entire SOFC/GT hybrid cycle is analysed based on the following assumptions:

1. The flow is steady state and one dimensional.
2. Thermodynamic equilibrium exists in the system.
3. Kinetic and gravitational terms are neglected
4. The combustion process in the combustor is assumed complete.
5. Negligible heat loss to the environment.
6. Gas mixtures are considered ideal.
7. Pressure losses within the plant are neglected

7.5.6 Steady state simulation of the hybrid plant

The steady state simulation of the hybrid plant model was carried out partly in the Aspen Hysys V84 and partly in the COMSOL Multiphysics V4.3a modeller environment. The SOFC simulations was carried out in COMSOL while the gas turbine simulations was in Hysys, the models were integrated by defining the SOFC inlet conditions (1073K) and using the SOFC outlet conditions as the inlet conditions into the combustor, with all the other flow properties been synchronised.

Typical operating conditions for the design point simulations of the plant were adopted from Haseli et al[215] and Zhang et al[222] and tabulated in Table 7-3

Table 7-3: Parameters used at design conditions

Gas turbine cycle	
Compressor isentropic efficiency η_{comp}	85%
Pressure ratio r_p	6
Turbine isentropic efficiency η_{GT}	85%
Expansion ratio r_e	5.41
Heat exchanger effectiveness ϵ_R	0.85
Combustor efficiency η_{comb}	100
AC generator efficiency η_{gen}	0.95
SOFC	
Fuel utilisation factor U_f	0.85
Air utilisation factor U_a	0.25
Steam-methane ratio (SMR)	2.5
Inlet temperature $(T)(K)$	1073
Operating cell voltage(V)	0.7
DC-AC inverter efficiency η_{invert}	0.89
Number of cells in stack (n)	60
Ambient conditions	
Temperature (K)	298
Pressure (atm)	1
Inlet flow composition	
Air inlet	21% O_2, 79%N_2
Fuel inlet	100% CH_4

Table 7-4 lists the states along the flow stream for the CER cycle scheme at the design conditions, as seen, the specific heat capacity varies with the gas composition and the state temperature, a reduction in the mass flow rate through the cathode is noticed due to the consumption of species in the electrochemical reactions, the reverse is noticed in the flow through the anode where generation of species occur.

Table 7-4: Energy states for SOFC/GT system with the CER cycle

	$C_p\left(^{kJ}/_{kgK}\right)$	$\dot{m}(kg/s)$	$R\left(^{J}/_{kgK}\right)$	$T\,(K)$	$p(bar)$	$h\left(^{kJ}/_{kg}\right)$
1	1.012	1.138	288.2	298	1.0	301.58
2	1.062	1.138	288.2	525.8	6.0	558.40
3	1.127	1.138	288.2	881.4	6.0	993.34
4	1.219	1.959	294.6	1073	6.0	1307.99
5	1.261	1.914	298.2	1143	6.0	1441.32
6	2.106	0.1745	401.8	1163	6.0	2449.28
7	1.331	2.089	306.9	1145.6	6.0	1524.79
8	1.364	2.092	305.1	1300	6.0	1773.20
9	1.364	1.271	305.1	1300	6.0	1773.20
10	1.364	0.8205	305.1	1300	6.0	1773.20
11	1.289	1.271	305.1	944.1	1.1	1216.94
12	1.219	1.271	305.1	666.1	1.1	811.98
13	1.216	1.271	305.1	657.5	1.1	799.52
14	1.189	1.271	305.1	558	1.0	663.46
15	2.248	0.022	518.33	298	1.0	669.90
16	2.752	0.022	518.33	459.8	6.0	1265.37
17	3.398	0.022	518.33	635.2	6.0	2158.41
18	2.449	0.072	478.92	616	6.0	1508.58
19	2.512	0.195	457.2	1073	6.0	2695.38
20	2.106	0.348	401.84	1163	6.0	2449.28
21	2.106	0.1745	401.84	1163	6.0	2449.28
22	2.279	0.003	518.33	298	6.0	679.14
23	4.313	0.05	461.38	298	1.0	1285.27
24	4.313	0.05	461.38	298.03	6.0	1285.40
25	2.06	0.05	461.38	603.6	6.0	1243.42

From states 20 and 21, we see that about 51% of the flow from the anode exit is recirculated to the pre-reformer (PR). Also from state 10, the amount of exhaust gas recirculated from the separator S1 is about 72% of the fresh inlet air at state 1, this significantly increases the mass flow through the cathode; a fact responsible for the much smaller temperature difference through the SOFC in the CER cycle compared to the RHE cycle.

Table 7-5: Energy states for SOFC/GT system with the RHE cycle

	$C_p\left({}^{kJ}/_{kgK}\right)$	$\dot{m}(kg/s)$	$R\left({}^{J}/_{kgK}\right)$	$T\,(K)$	$p(bar)$	$h\left({}^{kJ}/_{kg}\right)$
1	1.012	1.67	288.2	298	1.0	301.58
2	1.062	1.67	288.2	525.8	6.0	558.40
3	1.3	1.67	288.2	893.8	6.0	1161.94
4	1.158	1.67	288.2	1073	6.0	1242.53
5	1.175	1.62	290.6	1158	6.0	1407.74
6	2.12	0.1745	400.29	1193	6.0	2436.43
7	1.259	1.78	402.23	1163	6.0	1499.18
8	1.324	1.789	305.44	1462	6.0	1905.83
9	1.324	0.542	305.44	1462	6.0	1905.83
10	1.227	0.542	305.44	914.1	6.0	1172.86
11	1.324	1.247	305.44	1462	6.0	1905.83
12	1.289	1.789	305.44	1300	6.0	1683.50
13	1.289	1.789	305.44	939.6	1.1	1173.56
14	1.162	1.789	305.44	638.5	1.1	740.64
15	1.160	1.789	305.44	633.6	1.1	735.59
16	1.143	1.789	305.44	560.7	1.0	640.19
17	2.248	0.022	518.33	298	1.0	669.90
18	2.753	0.022	518.33	459.6	6.0	1265.28
19	3.311	0.022	518.33	611.5	6.0	1938.14
20	2.415	0.0722	478.92	594.1	6.0	1399.82
21	2.512	0.195	457.2	1073	6.0	2695.38
22	2.12	0.319	400.29	1193	6.0	2436.43
23	2.12	0.1594	400.29	1193	6.0	2436.43
24	2.279	0.0081	518.33	298	6.0	679.14
25	4.313	0.05	461.38	298	1.0	1285.27
26	4.313	0.05	461.38	298.03	6.0	1285.40
27	2.049	0.05	461.38	583.3	6.0	1178.74

Table 7-5 shows the states for the RHE cycle scheme. We can see that about 30% of the combustor exhaust gases are recycled in the separated in S1 to heat the cathode inlet air to the required temperature according to the states 8 and 9.

Figures 7-12 and 7-13 show the gas outlet flow compositions from the cathode and anode for both cycle schemes. While the anode exit composition are quite similar, large differences can be found in the cathode exhaust in which the main compositions are N_2, H_2O and O_2 for the CER scheme whereas for the RHE scheme the exit gases are only O_2 and N_2. The partial pressure of steam in the anode outlet is quite high (0.748

for RHE and 0.69 for CER) due to the internal reforming reaction in which a mole of H_2O is produced for every mole of H_2 reacted. The low amount of CO produced by the internal reforming and the unreacted H_2 in the anode are burnt up in the combustor, thereby raising its outlet temperature.

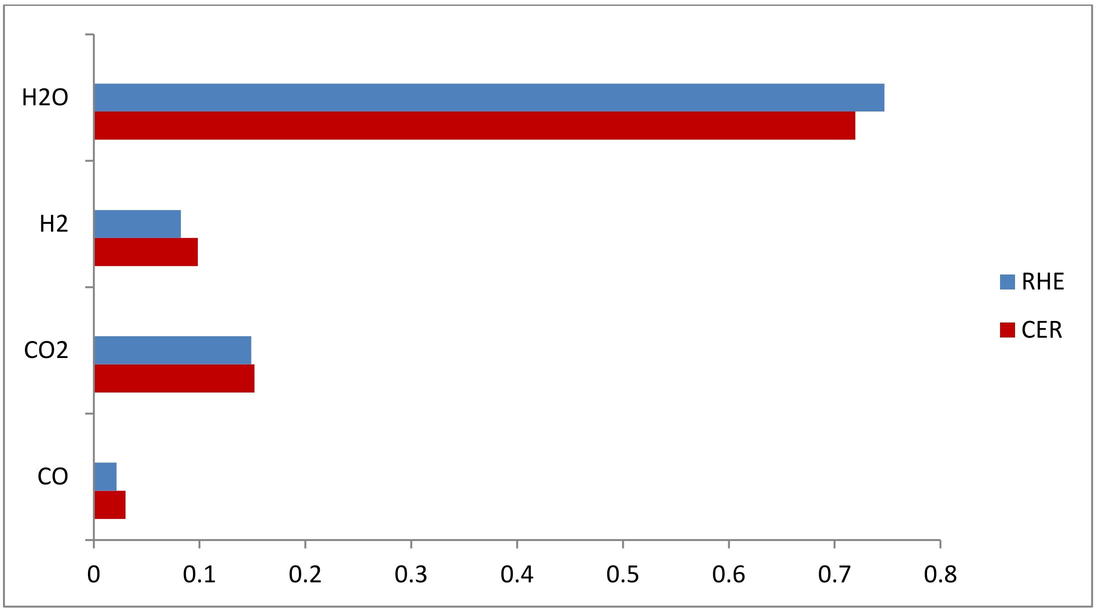

Figure 7-12: Anode outlet composition for CER and RHE cycles

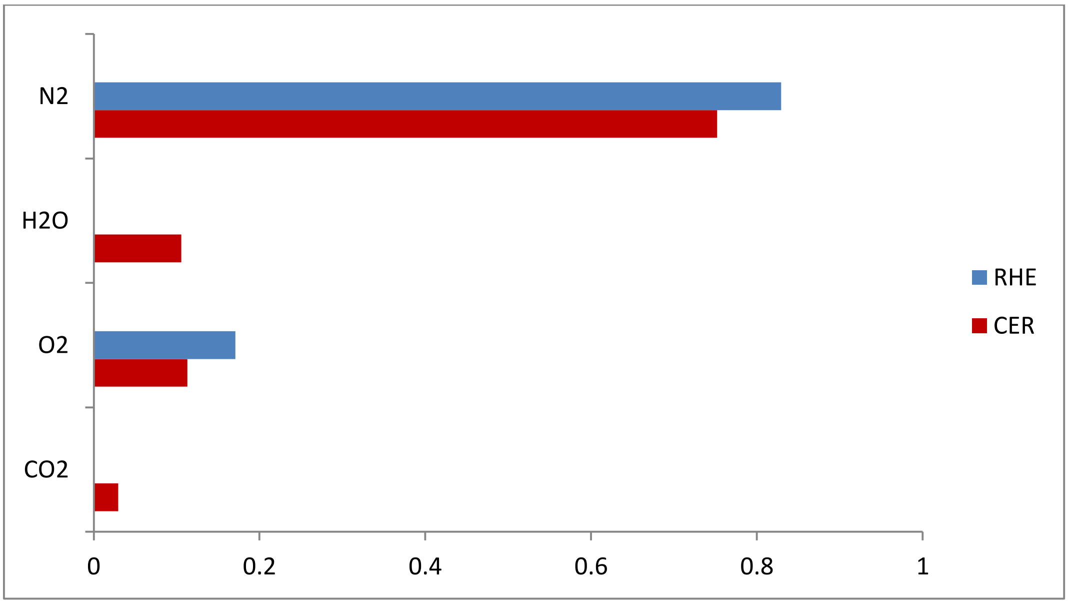

Figure 7-13: Cathode outlet composition for CER and RHE cycles

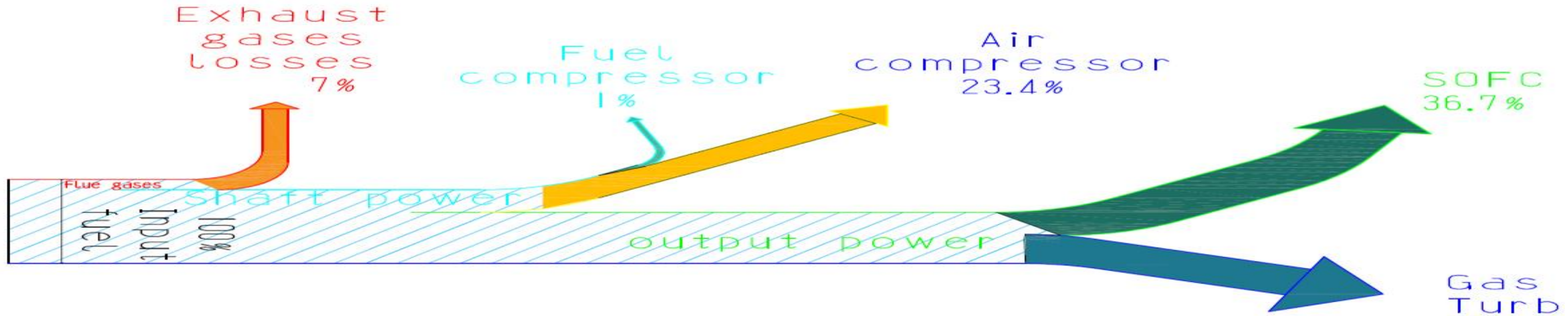

CATHODE EXHAUST RECYCLE (CER)

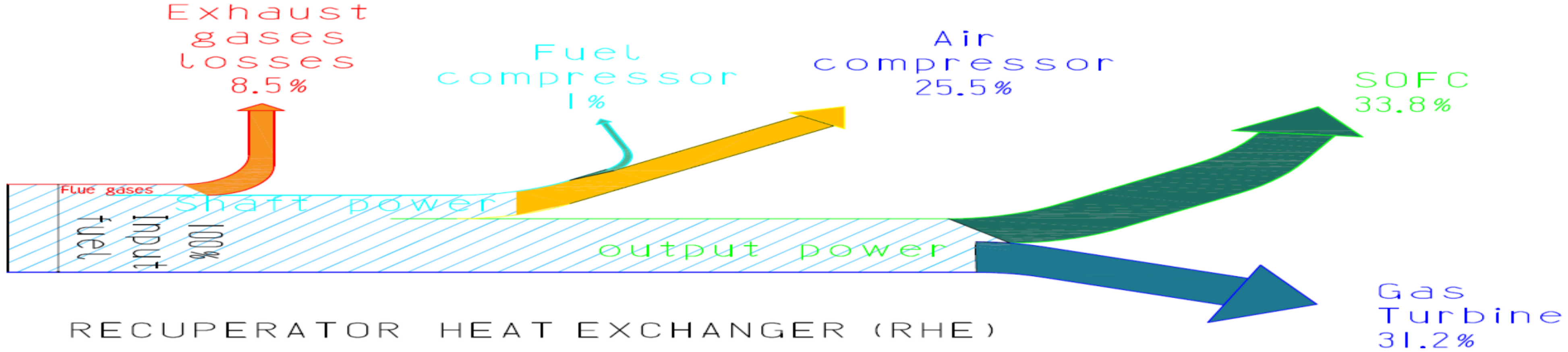

RECUPERATOR HEAT EXCHANGER (RHE)

Figure 7-14: Sankey diagrams for the energy flow in the hybrid system for the CER and RHE cycles

Figure 7-14 shows a Sankey diagram representation of the energy efficiency the hybrid plant. Component values are given as percentages of the fuel input

7.6 Hybrid system simulation results

The results obtained from the simulations studying the effect of operating conditions and design parameters on the hybrid system performance are presented and discussed in this section.

The main performance indicators of any thermodynamic cycle are the specific work output and the energy efficiency. A high specific work output is attractive because it requires reduced airflow through the compressor, which translates to smaller equipment thus reducing cost. A high efficiency is also attractive because it requires lower fuel consumption. However, a compromise between these performance indicators may have to be reached as both of them may not be maximised for the same hybrid system cycle.

7.6.1 Effect of system pressure on hybrid cycle performance

The hybrid cycle performance is studied by varying the system pressure between 2 and 14bar. Performance curves are presented in Figure 7-15 in terms of the compressors work, turbine work, SOFC work, total cycle work and its efficiency. As can be seen, increasing the system pressure increases the specific work output of both the SOFC and the GT.

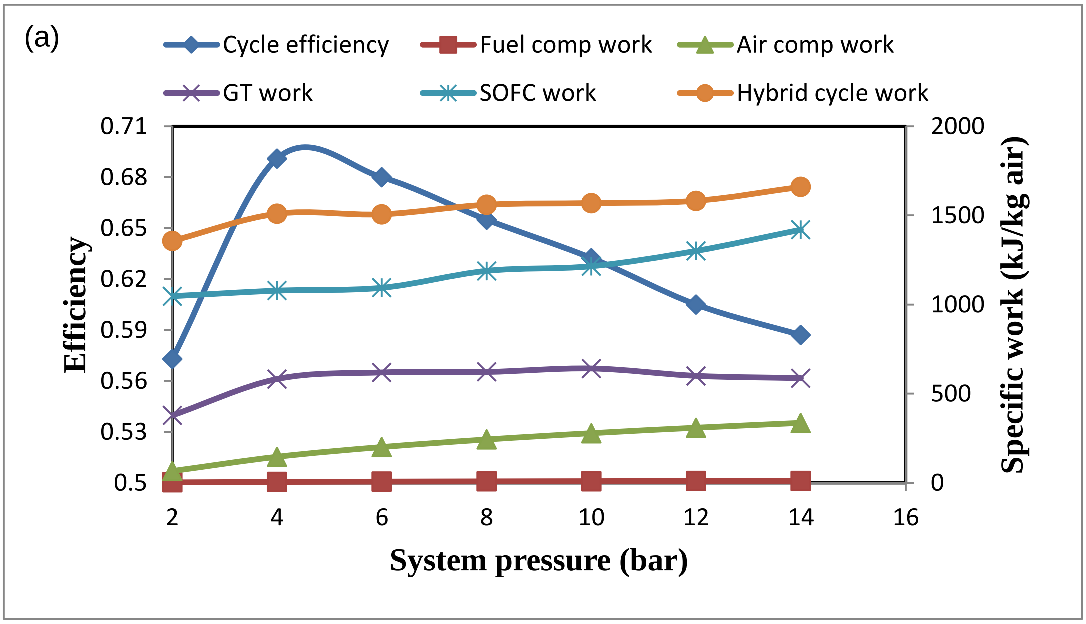

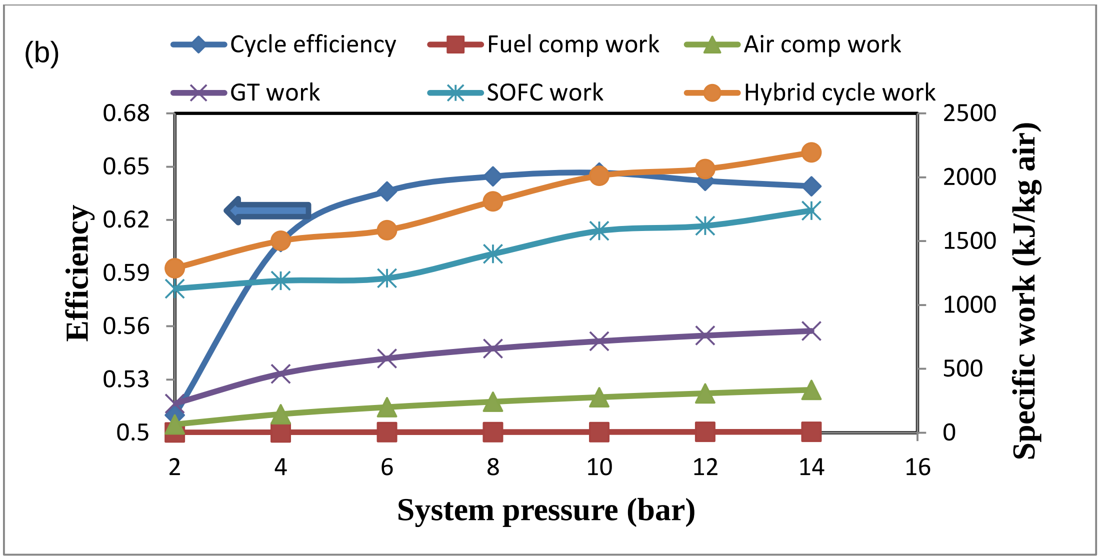

Figure 7-15: Effect of system pressure on hybrid performance (a) CER (b) RHE

Increasing pressure leads to an initial increase of the cycle efficiency until it reaches its peak pressure after which the efficiency starts to decrease. The peak pressure for the CER cycle is about 4bar, while that for the RHE cycle is about 10bar. At their peak pressures, the efficiency of the CER cycle is higher than that of the RHE, but the specific work is lower.

In the CER cycle, a fraction of the combustor exhaust is recirculated back into the stream before the inlet to the cathode, this adds energy to the cathode inlet steam thereby raising its temperature to the required inlet conditions, this in turn reduces the mass flow requirement through the air compressor, thus reducing the air compressor work thereby increasing the GT work output and efficiency. At high system pressures, a larger fraction of the combustor exhaust is required to be recirculated back to the stream to maintain the cathode inlet temperature, thus less mass flow is available for exon in the turbine; this is the reason for the significant drop in efficiency at higher pressures and why the SOFC and hybrid cycle work are more in the CER cycle than in the RHE cycle.

7.6.2 Effect of turbine inlet temperature (TIT) on hybrid cycle performance

The effect of varying the TIT on cycle performance at a constant system pressure is shown in Figure 7-16. The air-fuel ratio into the combustor is adjusted until the desired TIT is achieved. To increase the TIT afterwards, additional fuel is added directly into the combustor. As seen, a higher TIT improves the specific work output to the SOFC and hybrid system increases, but reduces the cycle efficiency.

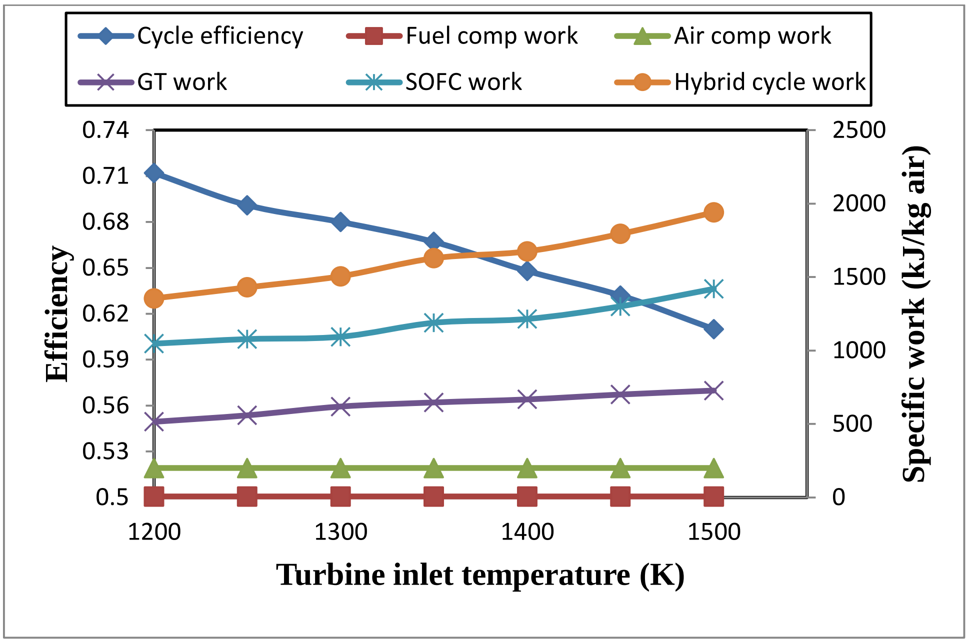

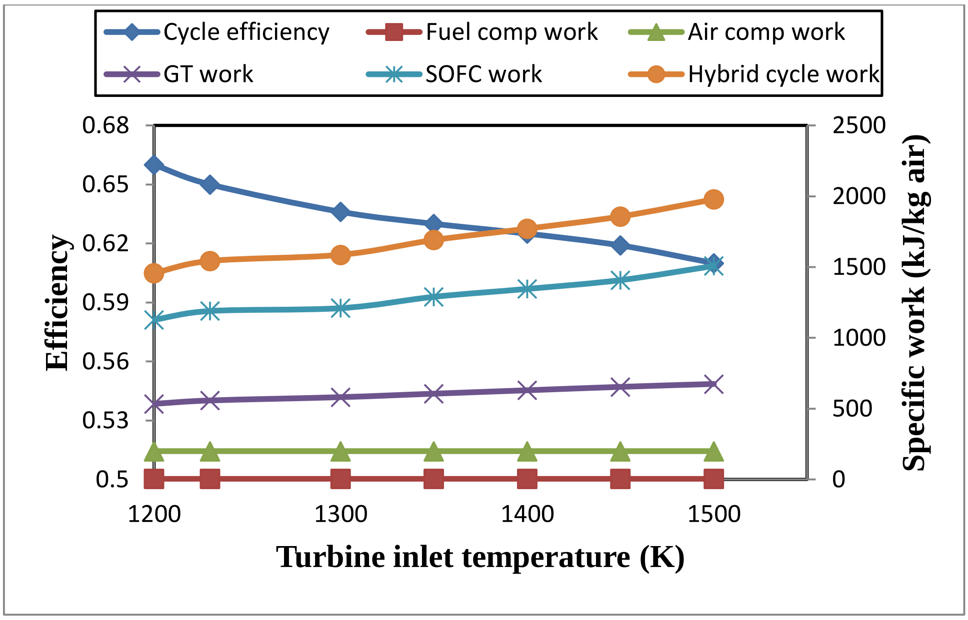

Figure 7-16: Effect of TIT on hybrid performance (a) CER (b) RHE

When the TIT increases, the GT output work increases while those of the other components including the SOFC remains constant. But since the SOFC is more efficient that the GT and additional fuel was added in the combustor, an overall lower cycle efficiency is noticed. This shows that further heating of the working fluid is not always an effective option. However, the primary reason for afterburning is to burn up the un-reacted gases from the SOFC [119, 215, 224].

7.6.3 Effect of fuel utilisation factor on hybrid cycle performance

The fuel utilisation factor is one of the most important parameters for SOFC operations as it has significant effect on the SOFC and the entire hybrid system efficiencies. The effect of varying the fuel utilisation at constant oxygen utilisation on the hybrid cycle performance is studied and presented in Figure 7-17. The mass flow rate of the fuel is set as an adjustable parameter to control the utilisation factor from 0.7 to 0.9. As the utilisation factor is increased, the current density decreases due to the increased depletion rate of the fuel thereby increasing the anode concentration polarisation in the SOFC, leading to a reduction in the SOFC efficiency.

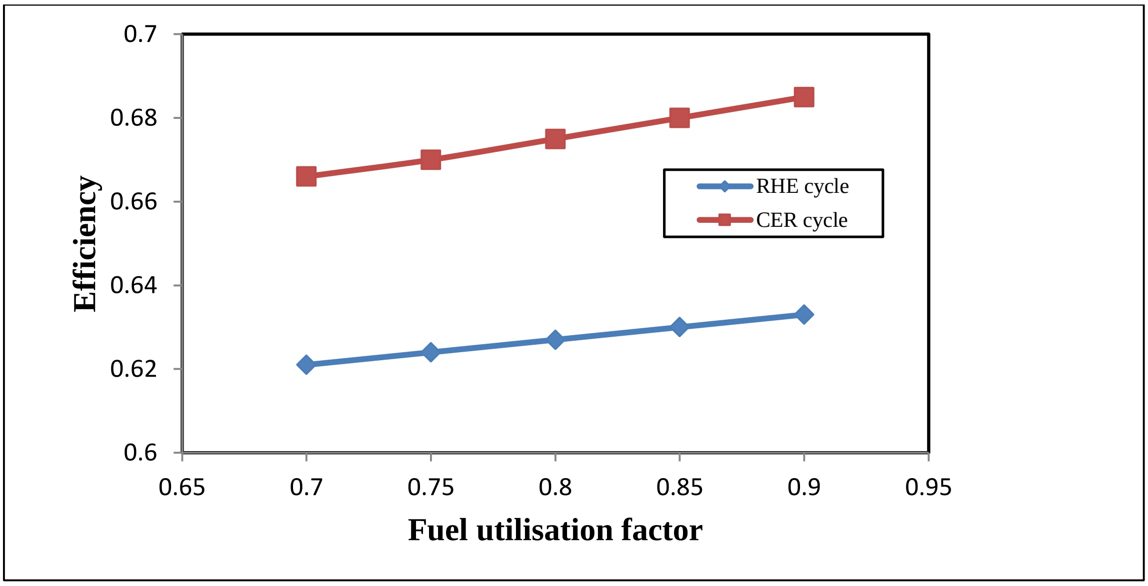

Figure 7-17: Effect of fuel utilisation factor on hybrid performance

However, at high utilisation factor, more of the hydrogen produced in the reforming reactions will be consumed during the electrochemical reaction, causing an increased rate of the electrochemical reaction which increases its exhaust temperature and its specific work output. With the higher SOFC exhaust temperatures, the requirement for additional fuel to the combustor is now reduced, leading to increased cycle efficiencies at high fuel utilisation factors for both the CER and RHE cycles.

7.6.4 Effect of component efficiencies on hybrid cycle performance

The effect of the some of the component efficiencies such as the air compressor, fuel compressor, turbine and recuperators on the overall hybrid efficiency are studied and presented in Table 7-6. The cycle efficiency at the base conditions using parameters tabulated in Table 7-3 is given tabulated in Table 7-6. The efficiencies of each component is then raised in turn by 5%, the resulting efficiencies are presented in the remaining columns of Table 7-6

Table 7-6: Effect of hybrid component efficiencies on cycle efficiency

	Base	$\boldsymbol{\eta_{F,comp}}(+5\%)$	$\boldsymbol{\eta_{A,comp}}(+5\%)$	$\boldsymbol{\eta_{GT}}(+5\%)$	$\boldsymbol{\epsilon_{R}}(+5\%)$
$\boldsymbol{\eta_{cyc}}(\%)\boldsymbol{CER}$	68.00	+0.03	+1.0	-0.21	+2.78
$\boldsymbol{\eta_{cyc}}(\%)\boldsymbol{RHE}$	63.61	+0.02	+1.16	+2.36	-0.02

From the table, we can see that the CER hybrid system is most sensitive to the heat exchanger effectiveness; a high effectiveness translates to a higher temperature of the stream going into the mixer M1, thus less fraction of the mass flow from the combustor will be needed to heat up the stream going to the cathode; this will ensure a higher mass flow into the turbine thereby increasing the cycle efficiency, the reverse is noticed when the isentropic efficiency of the turbine is increased, in which a low temperature stream goes into the mixer thus requiring a high fraction from the combustor. For the RHE case, the hybrid system is most sensitive to the gas turbine isentropic efficiency; a high isentropic efficiency produces a high specific work output, although the quality of the heat output to the recuperator is reduced, this is compensated by increasing the mass flow of fuel to the combustor in other to maintain the cathode inlet temperature.

7.6.5 Comparing the hybrid cycle to a conventional gas turbine cycle.

Figure 7-18 compares the performance of both GT/hybrid cycles against a conventional gas turbine cycle (has no SOFC). It can be seen that the hybrid cycles offer much more superior performance compared to the conventional cycle, this is mainly due to the presence of the SOFC as it acts as a pre-heater of the working fluid before entering the combustor, in addition to its considerable specific work output. Both factors are responsible for the higher energy efficiencies of the hybrid cycles compared to the conventional cycle.

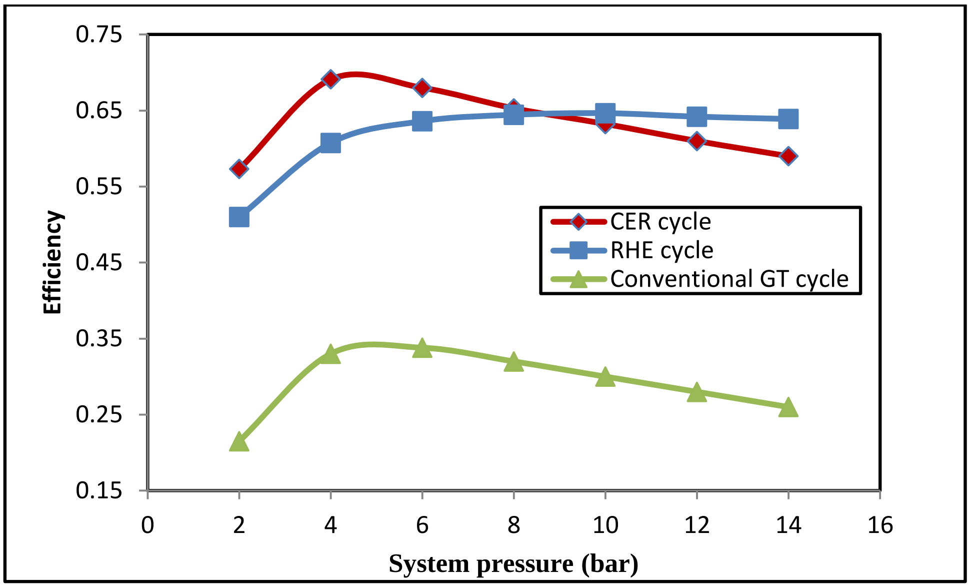

Figure 7-18: Comparison of cycle efficiency at various pressure ratios between the CER, RHE cycles and a conventional plant (no SOFC)

7.6.6 Exergy analysis of the SOFC/GT hybrid cycle

The scheme used in computing the exergy rates of the gas streams at the various state points for the CER cycle is presented in Table 7-7 while that for the RHE is presented in Table 7-8.

Table 7-7: Exergy states for SOFC/GT system with the CER

		$\dot{m}(kmol/s)$	$T(k)$	$p(bar)$	$[\Delta T]_0^x$	$[\Delta h]_0^x$	$[\Delta s]_y^x$	$T[\Delta s]_y^x$	$\widetilde{ex}_{ch}$	$\sum \widetilde{ex}$	$\dot{m}\sum \widetilde{ex}$	$\Delta \widetilde{ex}$	I
	1	0.0395	298	1	0	0		0			0		
AC	2	0.0395	525.8	6	227.8	6742.9	1.910337	569.2803		7312.18	288.8311		288.83
	2	0.0395	525.8	6	227.8	6742.9					288.83		
	3	0.0395	881.4	6	583.4	17840	15.79701	4707.51		13701.8	541.22	252.39	
	11	0.047	944.1	1.1	646.1	21957				22668.74	1065.43		364.46
R1	12	0.047	666.1	1.1	368.1	12224.6	11.383	3392.134		9544.21	448.6	616.85	
	3	0.0395	881.4	6	583.4	17840				13701.8	541.22		
	4	0.0696	1073	6	775	24993.5	6.641649	1979.212		18993	750.2235	209.0035	
	10	0.0301	1300	6	1002	34052	6.479699	1930.95		26120.55	786.2286		418.54
M1	4	0.0696	1073	6	775	24993.5				18993	571.6893	214.539	
	4	0.0696	1073	6	775					18993	1321.913		
	5	0.0687	1143	6	845	26383.77	2.101331	626.1966		19757.07	1357.31	35.4	
	19	0.013	1073	6	775	29706.93	35.843	10681.21	192934.2	233322.3	3033.19		1766.83
SOFC	20	0.0169	1163	6	865	33350.16	36.284	10812.63	32864.4	77027.19	1301.76	1731.43	
	5	0.0687	1143	6	845	26383.77				19757.07	1357.31		
	7	0.077	1145.6	6	847.6	26631.6	0.076457	22.78426		20027.68	1375.9	18.59	
	6	0.0084	1163	6	865	33350.16	0.529864	157.8994		33795	283.878		134.24
M2	7	0.077	1145.6	6	847.6	26631.6				20027.68	168.233	115.65	
	7	0.077	1145.6	6	847.6	26631.6				20027.68	1542.13		
	22	0.00021	298	6	0	0	0	0	836510	836510	175.6671	1717.83	
C	8	0.0768	1300	6	1002	34052	34.07	10152.86	1687.47	35773.54	2747.408	2747.408	1380.98
	8	0.0768	1300	6	1002	34052				35773.54	2747.408		
	10	0.0301	1300	6	1002	34053	0	0		35773.54	1076.8	1670.99	
	8	0.0768	1300	6	1002	35053				35773.54	2747.408		134.9
S1	9	0.047	1300	6	1002	34052	0	0		35773.54	1211.36	1536.1	
	9	0.047	1300	6	1002	34052	0	0		35773.54	1681.36		
GT	11	0.047	944.1	1.1	646.1	21957	3.388728	1009.841		22668.74	1065.43		615.93
	15	0.00139	298	1	0	0							
FC	16	0.00139	459.8	6	161.8	6447.7	2.277041	678.5582		7126.25	9.9		9.9

		$\dot{m}(kmol/s)$	$T(k)$	$p(bar)$	$[\Delta T]_0^x$	$[\Delta h]_0^x$	$[\Delta s]_y^x$	$T[\Delta s]_y^x$	$\widetilde{ex}_{ch}$	$\sum \widetilde{ex}$	$\dot{m} \sum \widetilde{ex}$	$\Delta \widetilde{ex}$	I
	12	0.047	666.1	1.1	368.1	12224.6				9444.21	448.6		
	13	0.047	657.5	1.1	359.5	11917.4	0.41389	123.34		9014.01	423.65	24.9	
	16	0.00139	459.8	6	161.8	6447.7				840.358	1.168098		5.1
R2	17	0.00139	635.2	6	337.2	15106.56	12.95825	3861.558		13398.7	18.641	19.801	
	23	0.0028	298	1	0	0							
Pump	24	0.0028	298.03	6	0.03	1.038	14.89	4437.22		4438.258	12.42712		12.42422
	13	0.047	657.5	1.1	359.5	11917.4				9014.01	423.65		
	14	0.047	558	1	260	8528	4.19576	1250.34		4374.38	205.6	218.05	
	24	0.0028	298.03	6	0.03	1.038				4437.22	12.42422		208.8
HRSG	25	0.0028	603.6	6	305.6	10573.76	24.40371	7272.307		7736.9	21.66332	9.239104	
	25	0.0028	603.6	6	305.6	10573.76				7736.9	21.66332		
	18	0.0042	616	6	318	12018.1	0.618191	184.221		10598.3	29.67524	8.01192	
	17	0.00139	635.2	6	337.2	15106.56	0.933066	278.0535		13398.7	56.27454		49.56872
M2	18	0.0042	616	6	318	12018.1				10588.3	14.71774	41.5568	
	18	0.0042	616	6	318	12018.1				10588.3	14.71774		
PR	19	0.013	1073	6	775	29706.93	35.843	10681.21	192934.2	233322.3	3033.19		1417.6
	21	0.0084	1163	6	865	33350.13	29.66		170578.9	33379.79	1600.86		

Table 7-8: Exergy states for SOFC/GT system with the RHE cycle

		$\dot{m}(kmol/s)$	$T(k)$	$p(bar)$	$[\Delta T]_0^x$	$[\Delta h]_0^x$	$[\Delta s]_y^x$	$T_0[\Delta s]_y^x$	$\widetilde{ex}_{ch}$	$\sum \widetilde{ex}$	$\dot{m}\sum \widetilde{ex}$	$\Delta \widetilde{ex}$	I
AC	1	0.0578	298	1	0	0		0			0		
	2	0.0578	525.8	6	227.8	6742.9	1.910337	569.2803		7312.18	422.64		422.64
R1	2	0.0578	525.8	6	227.8	6742.9					422.64		
	3	0.0578	893.8	6	595.8	19071	17.2	5126		14514	838.932	416.3	
	13	0.0645	939.6	1.1	641.6	21077				14404	929.07		451.55
	14	0.0645	638.5	1.1	340.5	11237	12.1	3615		949.39	61.24	867.83	
R3	3	0.0578	893.8	6	595.8	19071				14514	838.932		
	4	0.0578	1073	6	775	25660	5.98	1781		19322	1116.84	277.9	
	9	0.0195	1462	6	1164	39557				41362	806.57		184.75
	10	0.0195	914.1	6	616.1	20085	14.4	4253		17636	343.911	462.66	
SOFC	4	0.0696	1073	6	775					19322	1344.84		
	5	0.0687	1158	6	860	28857	2.5	745.2		21774	1495.86	151.01	
	21	0.013	1073	6	775	29707	35.8	10681.21	192934.2	233322.3	3033.19		1980.49
	22	0.0154	1193	6	895	34270	37.1	11029	32864	78163	1203.72	1829.47	
M1	5	0.0687	1158	6	860	28857				21773	1495.81		
	7	0.0643	1163	6	865	30540	0.14	43.2		23413	1608.48	112.68	
	6	0.0077	1193	6	895	34270	0.9	266.8		28512	219.54		151.93
	7	0.0643	1163	6	865	28905				23414	180.284	39.26	
C	7	0.0643	1163	6	865	28905				23414	1505.49		
	24	0.0006	298	6	0	0	0	0	836510	836510	501.91	1505.49	
	8	0.0645	1462	6	1164	39557	52.9	15749	1870.8	41480	2675.48	3177.38	1671.894
S1	8	0.0645	1462	6	1164	39557				41480	2667.87		
	9	0.0195	1462	6	1164	39557	0	0		41480	806.6		
	11	0.0195	1462	6	1164	39557	0	0		41480	1961.17		154.57
	10	0.0195	941.1	6	616.1	20085				17636	343.9		
	12	0.0645	1300	1.1	1002	33687				30156	588.04	244.13	

M2	11	0.0195	1462	6	1164	39557	17.9	5334		41362	1961.17		
	12	0.0645	1300	1.1	1002	33687				30156	1945.1	16.12	260.25
GT	12	0.0645	1300	6	1002	33687				30156	1945.05		
	13	0.0645	639.6	1.1	641.6	21077	10.5	3141		14404	929.07		1015.99
Pump	25	0.0028	298	1.1							0		
	26	0.0028	298.03	6	0.03	1.038	14.9	4437		4438.3	12.43		12.43
FC	17	0.0014	298	1	0	0					0		
	18	0.0014	459.6	6	161.6	14482	28.6	8508		23018	32.23		32.23
R2	14	0.0645	638.5	1.1	340.5	11237				949	61.21		
	15	0.0645	633.6	1.1	335.6	10907	0.23	69.14		550.36	35.499	25.7	
	18	0.0014	459.6	6	161.6	11482				23018	32.22		
	19	0.0014	611.5	6	313.5	10001	9.08	2706		15831	221.638	189.413	215.13
HRSG	15	0.0645	633.6	1.1	335.6	10907				550.36	35.49		
	16	0.0645	560.7	1	262.7	8669.1	1.65	491.7		-2179.2	-140.56	-176.06	
	26	0.0028	298.03	6	0.03	1.038				4438.3	286.33		89.65
	27	0.0028	583.3	6	285.3	9808.6	23.2	6902		7344.1	20.56	265.7	
M3	19	0.0014	611.5	6	313.5	10001				15831	221.64		
	20	0.0042	518.3	6	220.3	6962.4	5.24	1562		11232	47.17	174.5	
	27	0.0028	583.3	6	285.3	9808.6				7344.1	20.56		201.07
	20	0.0042	518.3	6	220.3					11232	47.17	26.61	
PR	20	0.0042	518.33	6	220.3					11232	47.1724		
	21	0.013	1073	6	775	29707	35.843	10681.21	192934.2	233322.3	3033.19		1250.78
	23	0.0077	1193	6	895	34270	37.11	11029	180058	225357	1735.25		

First, the exergy value of the inlet fluids (fuel and air) are calculated in the entry states into the plant (1, 15, 22 and 23 for the CER) and (1, 17, 24 and 25 for the RHE), the exergy values of the products from the reactions in the SOFC, combustor and pre-reformer were also calculated. These values were computed using equations in chapter 3. The computed values were then used in calculating the exergy of other states of the particular working fluid by evaluating the difference in enthalpy and entropy between the known state and the state under consideration. The difference between the exergy values gives the destroyed exergy rate or irreversibility in the component.

As an illustration, the formula for calculating the exergy rates of the air compressor (AC) is given as:

$$\breve{\boldsymbol{ex}}_1 + [\Delta \boldsymbol{h}]_{\boldsymbol{0}}^{\boldsymbol{2}} - [\Delta \boldsymbol{h}]_{\boldsymbol{0}}^{\boldsymbol{1}} - \boldsymbol{T_0}[\Delta \boldsymbol{s}]_{\boldsymbol{1}}^{\boldsymbol{2}} = \breve{\boldsymbol{ex}}_2 \tag{7-63}$$

$$I_{2-1} = \breve{\boldsymbol{ex}}_2 - \breve{\boldsymbol{ex}}_1 = destroyed\ exergy\ rate. \tag{7-64}$$

Figure 7-19 and 7-20 illustrates the contribution of each plant component to the total plant irreversibility for the CER and RHE schemes respectively. The Sankey diagram representation of the irreversibility's due to the exergy destruction in both the CER and RHE cycles are presented in Figure 7-21

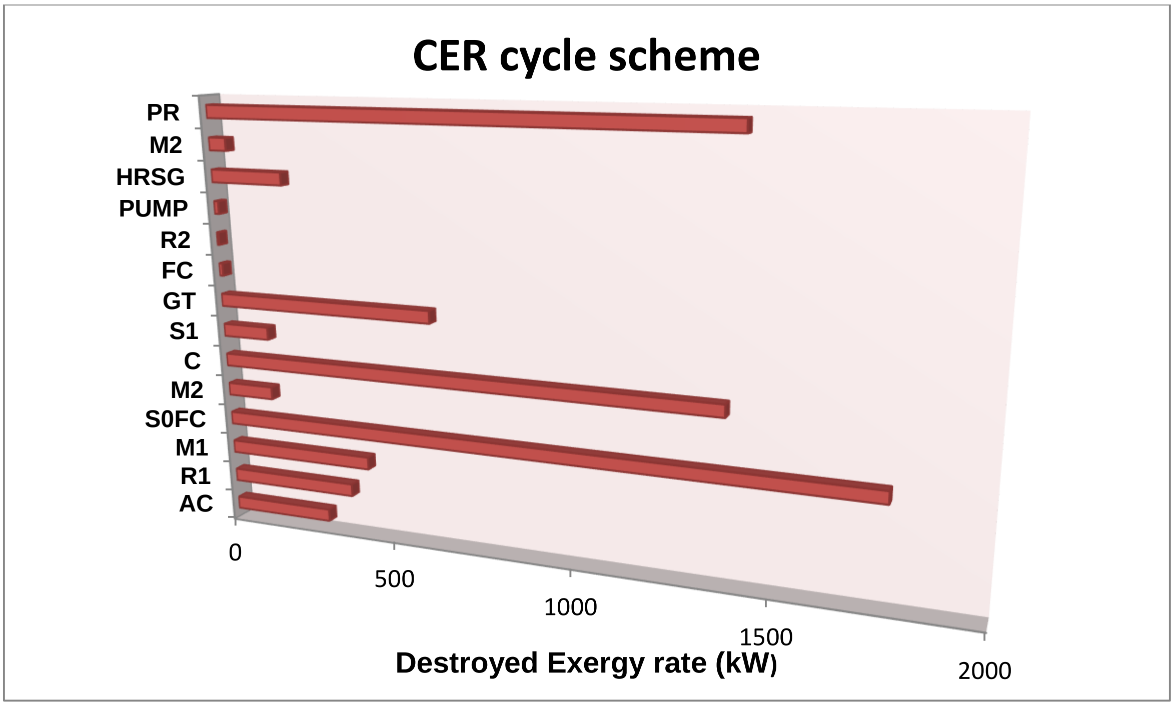

Figure 7-19: Destroyed exergy rate (irreversibility's) in each plant component for the CER

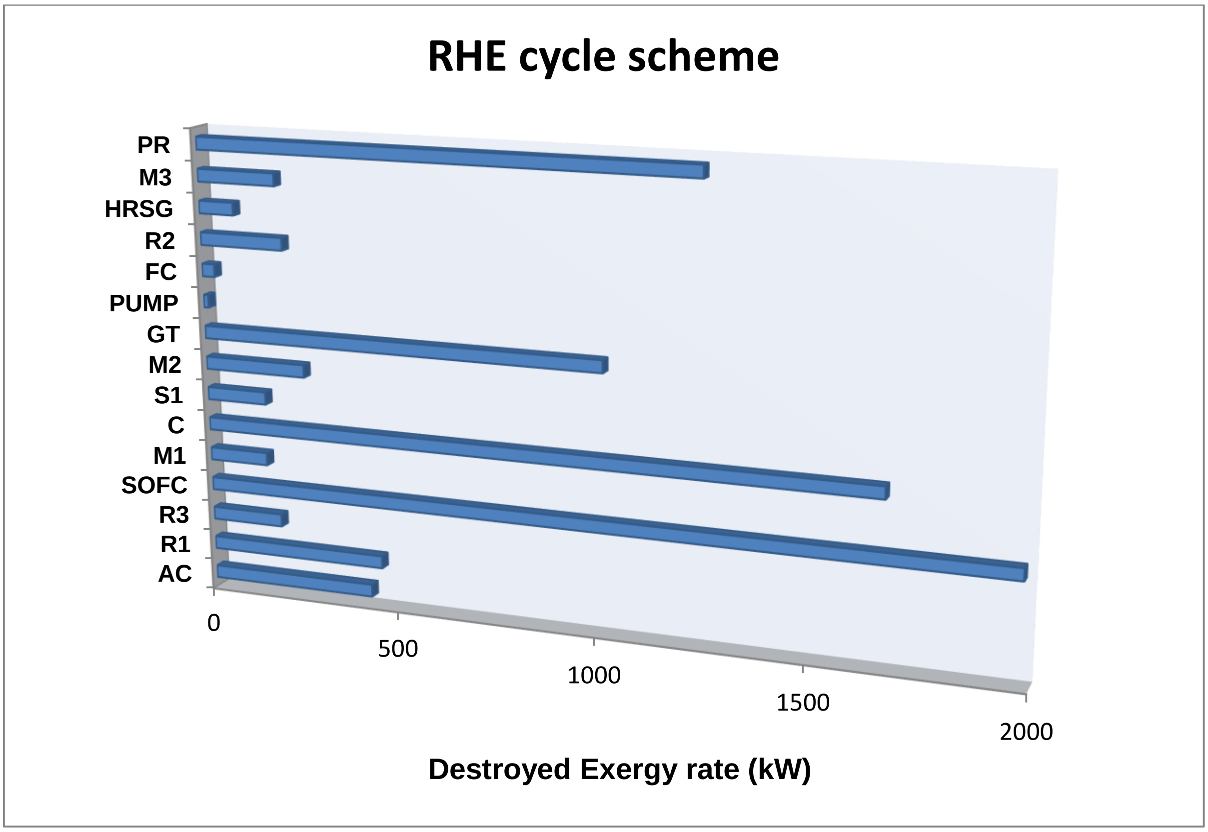

Figure 7-20: Destroyed exergy rate (irreversibility's) in each plant component for the RHE

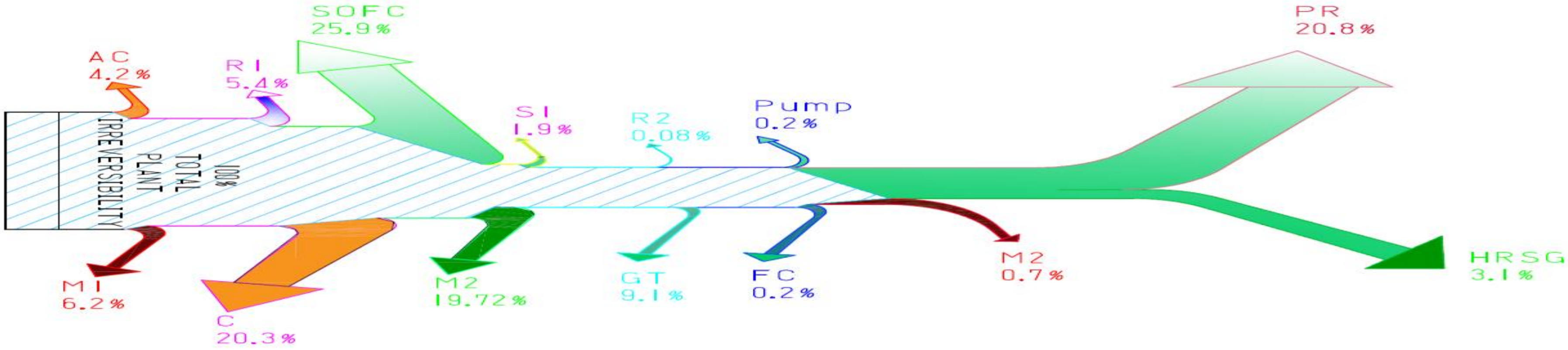

EXERGY DESTRUCTION (IRREVERSIBILITY) FOR CER SYSTEM

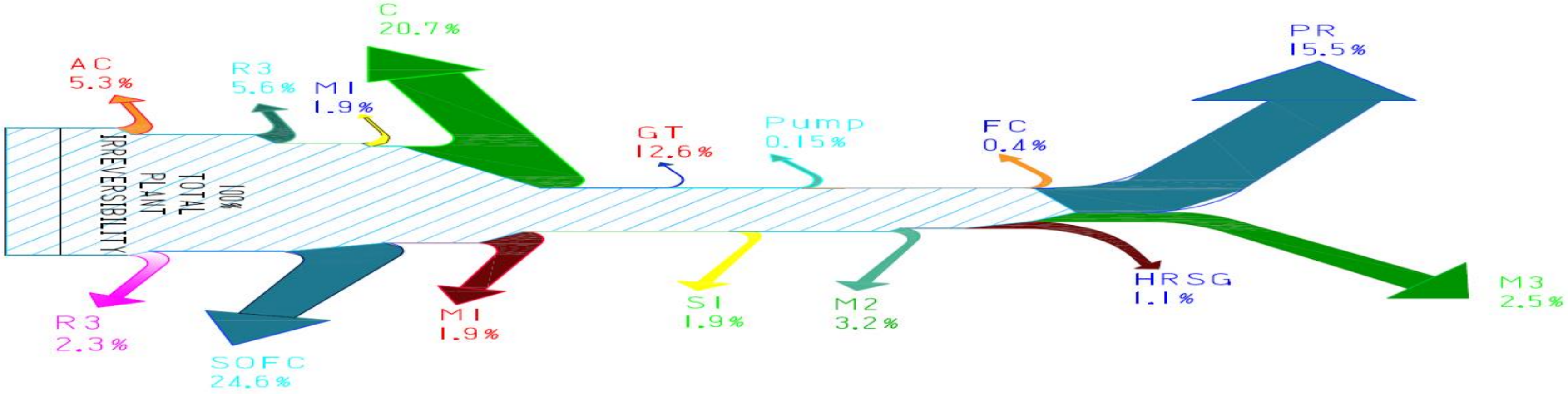

EXERGY DESTRUCTION (IRREVERSIBILITY) FOR RHE SYSTEM

Figure 7-21: Sankey diagram for the destroyed exergy (Irreversibility's) in each component for the CER and RHE cycles.

The figures show that components where chemical (combustor) or electrochemical (SOFC, PR) reactions occur have very high irreversibility's, with the maximum irreversibility occurring in the SOFC. However, other factors that affect the irreversibility's include temperature and pressure drop across the component; as seen in the turbine (GT) component.

From Figure 7.19, the most irreversible component in the CER scheme is first the SOFC, then the pre-reformer, combustor and GT in that order contributing 28.7%, 23.04%, 22.44% and 10% in that order while from Figure 7-20, in the RHE scheme the most irreversible components are the SOFC, combustor, pre-reformer and GT contributing 24.4%, 20.7%, 15.5% and 12.6% in that order.

A further illustration of the irreversibility's of the plant for both the CER and RHE schemes is shown in Figure 7-22 where the effect of system pressure on exergy destruction rate is presented.

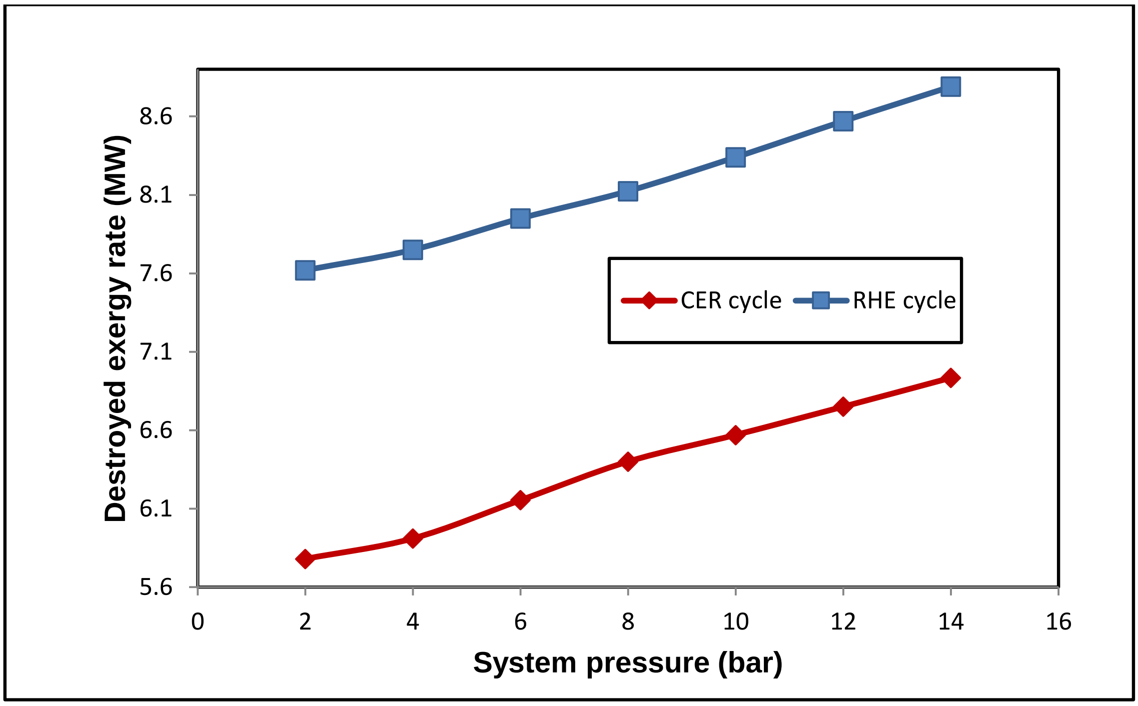

Figure 7-22: Effect of system pressures on the destroyed exergy rate (irreversibility's)

The effect of system pressure on exergy rate is studied between 2 bar and 14 bar, while all the other parameters are kept constant. As seen, the higher the system pressure, the higher the rate of exergy destroyed within both cycle schemes, predominantly in the compressors, gas turbine and combustor. A higher system pressure would entail more compressor work input, leading to increased irreversibility's in the compressor. Since the compressor is work is supplied by the turbine, its irreversibility's also increases. Also, when the system pressure is increased, SOFC outlet temperature will decrease; this will lead to an increase in the combustor irreversibility since more fuel will now need to be added to maintain the turbine inlet temperature requirements. On the other hand, the reduced SOFC outlet temperature lowers SOFC irreversibility's. However, the increased irreversibility's from some plant components is greater that the lowered irreversibility's of the other ones; ensuring an overall increased irreversibility rate of the entire plant for both schemes.

Figure 7-23 shows how the turbine inlet temperature (TIT) affects the exergy destruction rate. The turbine inlet temperature is varied between 1200K and 1500K while all the other cycle parameters are kept constant. Increasing the TIT would translate to an increased rate of heat transfer from the combustor; this can be achieved by increasing the mass flow of fuel either into the plant through the fuel compressor or directly into the combustor. This leads to an increased mass flow within the plant and increased operating temperatures after the combustor due to the higher rates of chemical reactions, both factors contribute the a higher rate of irreversibility's in the combustor, gas turbine and all other components upstream of the gas turbine thereby increasing the total irreversibility's of the plant.

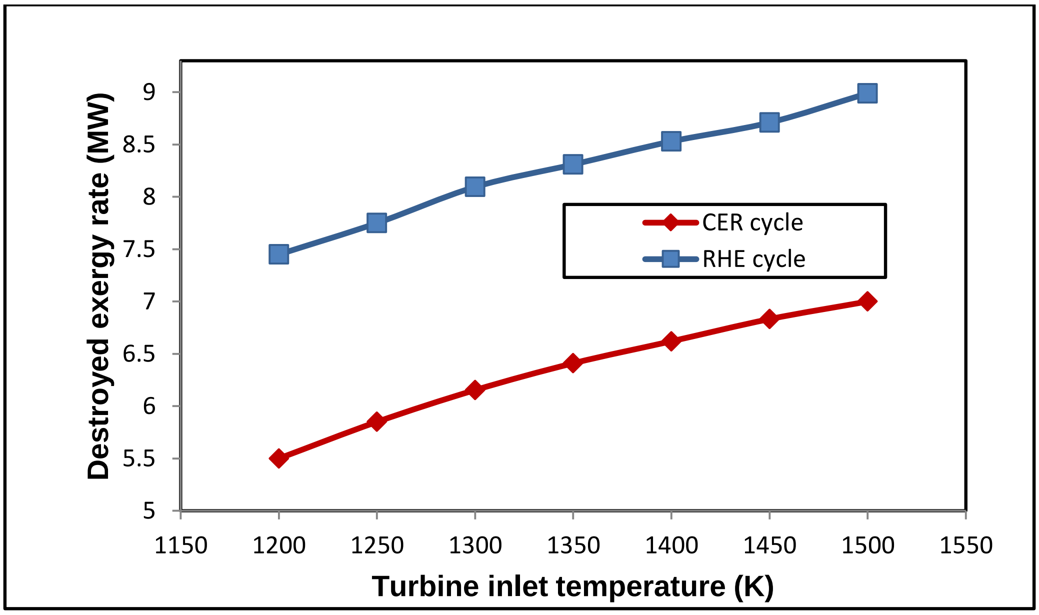

Figure 7-31: Effect of TIT on the destroyed exergy rate (irreversibility's)

7.7 Conclusion

The solutions obtained from the thermodynamic model of the hybrid GT/SOFC cycle are presented. The model was developed by applying the first and second laws of thermodynamics for each of the components in the system and also for the entire cycle when treated as a lumped volume.

Different configurations of the convention gas turbine cycles are first presented and first law thermodynamic analysis were carried out on them. The effect of compression ratio on cycle efficiency and the specific work output is studied. Findings revealed that a compromise between cycle efficiency and specific work output has to be maintained for an ideal cycle and that an optimum pressure ratio exits for a cycle after which its performance begins to decline

Two cycle schemes based on the cathode inlet air re-heating method for the hybrid GT/SOFC cycle is proposed and simulated. The combustor exhaust recirculated (CER) cycle is found to have a higher system efficiency at low pressure ratios than the recuperator heat exchanger (RHE) cycle. However, as the pressure ratio increases, the RHE cycle gave better system efficiencies. The effects of pressure ratio on the specific work output of various components in the hybrid system for both cycles were also investigated.

The effect of fuel utilisation factor, turbine inlet temperature and the efficiencies of some plant components on the cycle energy efficiency were investigated and discussed. High fuel utilisation factors results in improved cycle efficiency while increasing turbine inlet temperature results in a drop in cycle efficiency for both cycles. The assessment of individual component efficiency indicate that the CER cycle efficiency is most sensitive to the heat exchanger recuperator effectiveness, while the RHE is most sensitive to the isentropic efficiency of the turbine.

Exergy analysis were also carried out on both cycles to determine the amount of exergy destroyed in each component and in the entire cycle, this gives an indication of the irreversibility in the system. It is observed that the SOFC, combustor, pre-reformer and the gas turbine contribute significantly to the total irreversibility of the entire system, contributing as much as 84% of the total irreversibility in the CER scheme and 73% in the RHE scheme. Studies also show that the irreversibility’s increases as the system pressure and the turbine inlet temperatures increases.

CHAPTER8 : Conclusions and Future work

8.1 Conclusions

This thesis contributes to a better understanding of the physical, chemical and electrochemical processes in a SOFC and its integration with other energy systems. This developed model is expected to be useful in analysing the transport, chemical reaction, electrochemical reaction and integration processes involved in the operations of the fuel cell, with the primary aim of predicting its performance.

A mechanistic mathematical model of SOFC’s has been developed in this thesis. The model computes the various interlinked physical and chemical processes occurring simultaneously by prescribing algebraic and differential equations. Four important characteristics are outlined namely.

1) The treatment of the electrodes; in which the electrochemical reactions are assumed to occur in a separate reaction layer (finite volume) consisting of void spaces, ionic and electronic conducting particles; in this layer, the micro modelling approach was used, however, the other part of the electrode was assumed to consist of electronic conducting particles and the void spaces; as such equations of charge, energy, transport and chemical reactions are considered in the region where electrochemical reaction occurs
2) Based on the finite volume and micro-modelling consideration, the micro-structural properties of the cell e.g. porosity, specific area per unit volume, pore diameter, permeability, particle diameter are algebraically linked and calculated
3) The models flexibility in choice of fuel, in addition to hydrogen, any hydrocarbon composed of multi-component mixture can be used and reformed within the cell.
4) A good number of the parameters used are functions of temperature, pressure, porosity and particle diameter. As such, the model is capable of performing several parametric studies at a variety of design and operating conditions; this analysis would normally be quite difficult to obtain by experiments.

The developed isothermal SOFC model is validated with experimental and numerical data published in literature. The model predicts the performance of the different self-supported structures. The anode supported SOFC, in which the anode layer was the thickest component was found to exhibit the best electrical performance amongst all three support structures, and the most suitable for intermediate temperature operations due to its thin electrolyte layer, whereas the electrolyte supported SOFC are suitable only for high temperature operations. In anode supported SOFCs, the cathode overpotentials are quite significant especially its activation and ohmic components. Parametric studies were also carried to investigate the effect of key operating and design conditions, results obtained reveal that significant drop in performance is noticed when the temperature is reduced from 1073K to 873K, whereas, the performance improves when the operating pressure is increased, however constraints of material selection and mechanical rigidity would greatly limit the use of pressured SOFCs

The model of the along the channel micro-scale non-isothermal model is presented. The model was validated with experimental data published in literature. The cell performance was compared using isothermal conditions, the difference was measured in terms of the potential gain due to temperature rising. The contribution of Joule heating, reversible heat sources and irreversible heat sources were evenly distributed. Velocity and pressure profiles inside the electrodes were also studied. Both the velocity and pressure profiles increased in the anode side due to the expansion of gases (as a result of the increasing temperatures) and generation of water from the oxidation reactions, while the profile on the cathode sides remained constant as the increased due to temperature rising was cancelled out by the decreased due to the consumption of oxygen in the reduction reaction

A reformate mixture (30% reformed natural gas) was then introduced as fuel, the model was then used to predict the performance when reforming and water-gas shift reactions were considered in the anode electrodes, initial investigation to reveal the effect of the chemical reactions on cell performance showed significant improvement when the reactions are considered in the model. the chemical reactions aid in reducing the concentration overpotentials in the cell and that there is negligible temperature difference along the thickness of both diffusion and reaction layers

Parametric studies on the micro-structural properties of the reaction layer were also carried out. Smaller particle diameter leadS to better cell performance due to the increased reaction area. This result is consistent at low current densities, at high current densities and for very low particle sizes, increased concentration polarisation is noticed due to the Knudsen diffusion process been inhibited. The effect of porosity, volume fraction and tortuosity on cell performance was also investigated.

The developed SOFC model is integrated in a gas turbine hybrid system. Both first and second law thermodynamics analysis was carried out for each component and for the entire cycle. Two cycle schemes based on cathode inlet-air reheating method for the hybrid system was proposed and simulated. The combustor exhaust recycle system (CER) was found to have higher efficiencies at low pressure ratios than that of the recuperator heat exchanger system (RHE). Effect of fuel utilisation factor, turbine inlet temperature and plant individual efficiencies were also investigated. tHE efficiency decreases with increasing turbine inlet temperatures but the specific work increases, also efficiency increases with increasing fuel utilisation factor. The difference in efficiency when the SOFC is integrated and when it wasn't were compared and found to very significant. Exergy which measures the irreversibility's in the system was also investigated. The SOFC, combustor, pre-reformers and gas turbine unit were the most significant contributors to the total system irreversibility's contributing over 73% of the total. The effect of system pressure and turbine inlet temperatures on exergy loss was also studied.

8.2 Recommendations for future works

From the results obtained from the research and in order to improve the reliability of the model, some aspects for future research are suggested:

- The computation domain included in the present study considered only the contact of the interconnect with the diffusion layer (accounting for the flow channels), In order to account for all the heat transfers and losses in the cell, the computational domain should include the interconnects

- Steady state models for the isothermal, non-isothermal and hybrid models should be extended to dynamic simulations, which will be capable of predicting time-dependent behaviour of the cells such as degradation, start up, shut down and control processes.

- The non-isothermal model should be extended to include heat losses which were not considered in this present model

- The non-isothermal aspect of the model should be extended to include internal stress studies in other to determine the stress distribution within the cell.

- The current two dimensional models can be extended to three dimensional models as they give better approximation of actual cell operations

- The present single cell model can be extended to stack SOFC modelling

- The present model only considered along the channel flow, future studies can be extended to include across the channel flow and their performances compare

References

1. Das, D. and T.N. Veziroğlu, *Hydrogen production by biological processes: a survey of literature.* International Journal of Hydrogen Energy, 2001. **26**(1): p. 13-28.

2. Edwards, P.P., et al., *Hydrogen and fuel cells: Towards a sustainable energy future.* Energy Policy, 2008. **36**(12): p. 4356-4362.

3. Dincer, I., *Renewable energy and sustainable development: a crucial review.* Renewable and Sustainable Energy Reviews, 2000. **4**(2): p. 157-175.

4. IEA, *World Energy Outlook*, in *Renewable Energy Outlook*. 2013.

5. OECD/IEA, *World Energy Outlook*. 2004.

6. Penner, S.S., *Steps toward the hydrogen economy.* Energy, 2006. **31**(1): p. 33-43.

7. Marbán, G. and T. Valdés-Solís, *Towards the hydrogen economy?* International Journal of Hydrogen Energy, 2007. **32**(12): p. 1625-1637.

8. Wee, J.-H., *Applications of proton exchange membrane fuel cell systems.* Renewable and Sustainable Energy Reviews, 2007. **11**(8): p. 1720-1738.

9. Lund, H. and P.A. Østergaard, *Electric grid and heat planning scenarios with centralised and distributed sources of conventional, CHP and wind generation.* Energy, 2000. **25**(4): p. 299-312.

10. Wells, S.A., et al., *Hydrogen Economy*, in *Encyclopedia of Inorganic Chemistry*. 2006, John Wiley & Sons, Ltd.

11. Dunn, S., *Hydrogen futures: toward a sustainable energy system.* International Journal of Hydrogen Energy, 2002. **27**(3): p. 235-264.

12. Frano, B., *PEM fuel cells : theory and practice*. 2nd ed. 2013, London: Academic. xvii, 518 p.

13. Grove, W.R., *On voltaic series and the combination of gases by platinum.* London and Edinburge philosophical magazine and journal of science, 1839. **14**: p. 127-130.

14. Larminie, J. and A. Dicks, *Fuel cell systems explained*. 2nd ed. 2003, Chichester, West Sussex: J. Wiley. xxii, 406 p.

15. Vielstich, W., A. Lamm, and H.A. Gasteiger, *Handbook of Fuel Cells: Fundamentals, Technology, and Applications*. 2003: Wiley.

16. Hajimolana, S.A. and M. Soroush, *Dynamics and Control of a Tubular Solid-Oxide Fuel Cell.* Industrial & Engineering Chemistry Research, 2009. **48**(13): p. 6112-6125.

17. Milewski, J., *Advanced methods of solid oxide fuel cell modeling*, in *Green energy and technology*. 2011, Springer,: London ; New York. p. 1 online resource (xiv, 217 p.).

18. Viswanathan, B. and M.A. Scibioh, *Fuel cells : principles and applications*. 2007, Hyderabad Boca Raton, FL: Universities Press ; Distributed by CRC Press. x, 494 p.

19. Singhal, S.C., *Solid oxide fuel cells for stationary, mobile, and military applications.* Solid State Ionics, 2002. **152–153**(0): p. 405-410.

20. Bove, R. and S. Ubertini, *Modeling Solid Oxide Fuel Cells Methods, Procedures and Techniques*, in *Fuel Cells and Hydrogen Energy*. 2008, Springer,: Dordrecht. p. 1 online resource (404 p.).

21. Singhal, S.C. and K. Kendall, *High-temperature solid oxide fuel cells : fundamentals, design, and applications*. 2003, New York: Elsevier Advanced Technology. xvi, 405 p.

22. Sammes, N.M., *Fuel cell technology : reaching towards commercialization*. Engineering materials and processes. 2006, London: Springer. xiv, 298 p.

23. Ralph, J.M., A.C. Schoeler, and M. Krumpelt, *Materials for lower temperature solid oxide fuel cells.* Journal of Materials Science, 2001. **36**(5): p. 1161-1172.

24. Janardhanan, V.M. and O. Deutschmann, *Review paper: Modeling of Solid - Oxide Fuel Cells.* Journal of Physical Chemistry., 2007. **221**: p. 443-478.

25. Weber, A. and E. Ivers-Tiffée, *Materials and concepts for solid oxide fuel cells (SOFCs) in stationary and mobile applications.* Journal of Power Sources, 2004. **127**(1–2): p. 273-283.

26. Yamamoto, O., *Solid oxide fuel cells: fundamental aspects and prospects.* Electrochimica Acta, 2000. **45**(15–16): p. 2423-2435.

27. Badwal, S.P.S., *Stability of solid oxide fuel cell components.* Solid State Ionics, 2001. **143**(1): p. 39-46.

28. Ishihara, T., H. Matsuda, and Y. Takita, *Effects of rare earth cations doped for La site on the oxide ionic conductivity of LaGaO3-based perovskite type oxide.* Solid State Ionics, 1995. **79**(0): p. 147-151.

29. Basu, R.N., et al., *Simplified processing of anode-supported thin film planar solid oxide fuel cells.* Journal of the European Ceramic Society, 2005. **25**(4): p. 463-471.

30. Nakagawa, N., H. Sagara, and K. Kato, *Catalytic activity of Ni–YSZ–CeO2 anode for the steam reforming of methane in a direct internal-reforming solid oxide fuel cell.* Journal of Power Sources, 2001. **92**(1–2): p. 88-94.

31. Murray, E.P., T. Tsai, and S.A. Barnett, *A direct-methane fuel cell with a ceria-based anode.* Nature, 1999. **400**(6745): p. 649-651.

32. Brett, D.J.L., et al., *Intermediate temperature solid oxide fuel cells.* Chemical Society Reviews, 2008. **37**(8): p. 1568-1578.

33. Fergus, J.W., *Metallic interconnects for solid oxide fuel cells.* Materials Science and Engineering: A, 2005. **397**(1–2): p. 271-283.

34. Steele, B.C.H., *Material science and engineering: The enabling technology for the commercialisation of fuel cell systems.* Journal of Materials Science, 2001. **36**(5): p. 1053-1068.

35. Hussain, M.M., X. Li, and I. Dincer, *Mathematical modeling of planar solid oxide fuel cells.* Journal of Power Sources, 2006. **161**(2): p. 1012-1022.

36. Minh, N.Q., *Solid oxide fuel cell technology—features and applications.* Solid State Ionics, 2004. **174**(1–4): p. 271-277.

37. Dokmaingam, P., et al., *Modeling of IT-SOFC with indirect internal reforming operation fueled by methane: Effect of oxygen adding as autothermal reforming.* International Journal of Hydrogen Energy, 2010. **35**(24): p. 13271-13279.

38. Chan, S.H., H.K. Ho, and Y. Tian, *Modelling of simple hybrid solid oxide fuel cell and gas turbine power plant.* Journal of Power Sources, 2002. **109**(1): p. 111-120.

39. Chinda, P. and P. Brault, *The hybrid solid oxide fuel cell (SOFC) and gas turbine (GT) systems steady state modeling.* International Journal of Hydrogen Energy, 2012. **37**(11): p. 9237-9248.

40. Bhattacharyya, D. and R. Rengaswamy, *A Review of Solid Oxide Fuel Cell (SOFC) Dynamic Models.* Industrial & Engineering Chemistry Research, 2009. **48**(13): p. 6068-6086.

41. Palsson, J., A. Selimovic, and L. Sjunnesson, *Combined solid oxide fuel cell and gas turbine systems for efficient power and heat generation.* Journal of Power Sources, 2000. **86**(1): p. 442-448.

42. Jiang, S. and S. Chan, *A review of anode materials development in solid oxide fuel cells.* Journal of Materials Science, 2004. **39**(14): p. 4405-4439.

43. Secanell, M., J. Wishart, and P. Dobson, *Computational design and optimization of fuel cells and fuel cell systems: A review.* Journal of Power Sources, 2011. **196**(8): p. 3690-3704.

44. Hajimolana, S.A., et al., *Mathematical modeling of solid oxide fuel cells: A review.* Renewable and Sustainable Energy Reviews, 2011. **15**(4): p. 1893-1917.

45. Wang, K., et al., *A Review on solid oxide fuel cell models.* International Journal of Hydrogen Energy, 2011. **36**(12): p. 7212-7228.

46. Damm, D.L. and A.G. Fedorov, *Radiation heat transfer in SOFC materials and components.* Journal of Power Sources, 2005. **143**(1-2): p. 158-165.

47. Aguiar, P., C.S. Adjiman, and N.P. Brandon, *Anode-supported intermediate-temperature direct internal reforming solid oxide fuel cell: II. Model-based dynamic performance and control.* Journal of Power Sources, 2005. **147**(1-2): p. 136-147.

48. Leah, R.T., N.P. Brandon, and P. Aguiar, *Modelling of cells, stacks and systems based around metal-supported planar IT-SOFC cells with CGO electrolytes operating at 500-600°C.* Journal of Power Sources, 2005. **145**(2): p. 336-352.

49. Murshed, A.M., B. Huang, and K. Nandakumar, *Control relevant modeling of planer solid oxide fuel cell system.* Journal of Power Sources, 2007. **163**(2): p. 830-845.

50. Kakaç, S., A. Pramuanjaroenkij, and X.Y. Zhou, *A review of numerical modeling of solid oxide fuel cells.* International Journal of Hydrogen Energy, 2007. **32**(7): p. 761-786.

51. Vandersteen, J., et al. *Mathematical modelling of the transport phenomena and the chemical/electrochemical reactions in solid oxide fuel cells; A review*. in *Hydrogen and Fuel cells 2004*. 2004. Toronto, Canada.

52. Chinda, P., et al., *Mathematical modelling of a solid oxide fuel cell with nearly spherical shaped electrode particles.* Journal of sustainable energy and environment, 2010. **1**(4): p. 181-184.

53. Shixue, L., W. Kong, and Z. Lin, *A microscale modeling tool for the design and optimisation of solid oxide fuel cells.* Energies, 2009. **2**: p. 427-444.

54. Tanner, C.W., K.Z. Fung, and A.V. Virkar, *The Effect of Porous Composite Electrode Structure on Solid Oxide Fuel Cell Performance: I. Theoretical Analysis.* Journal of The Electrochemical Society, 1997. **144**(1): p. 21-30.

55. Sunde, S., *Calculation of Conductivity and Polarization Resistance of Composite SOFC Electrodes from Random Resistor Networks.* Journal of The Electrochemical Society, 1995. **142**(4): p. L50-L52.

56. Sunde, S., *Monte Carlo Simulations of Polarization Resistance of Composite Electrodes for Solid Oxide Fuel Cells.* Journal of The Electrochemical Society, 1996. **143**(6): p. 1930-1939.

57. Sunde, S., *Monte Carlo Simulations of Conductivity of Composite Electrodes for Solid Oxide Fuel Cells.* Journal of The Electrochemical Society, 1996. **143**(3): p. 1123-1132.

58. Wang, L., H. Zhang, and S. Weng, *Modeling and simulation of solid oxide fuel cell based on the volume–resistance characteristic modeling technique.* Journal of Power Sources, 2008. **177**(2): p. 579-589.

59. Costamagna, P., P. Costa, and V. Antonucci, *Micro-modelling of solid oxide fuel cell electrodes.* Electrochimica Acta, 1998. **43**(3–4): p. 375-394.

60. Chan, S.H. and Z.T. Xia, *Anode Micro Model of Solid Oxide Fuel Cell.* Journal of The Electrochemical Society, 2001. **148**(4): p. A388-A394.

61. Chinda, P., *The Performance Improvement of a Thick Electrode Solid Oxide Fuel Cell.* Energy Procedia, 2013. **34**(0): p. 243-261.

62. Bouvard, D. and F.F. Lange, *Relation between percolation and particle coordination in binary powder mixtures.* Acta Metallurgica et Materialia, 1991. **39**(12): p. 3083-3090.

63. Xia, Z.T., S.H. Chan, and K.A. Khor, *An Improved Anode Micro Model of SOFC.* Electrochemical and Solid-State Letters, 2004. **7**(3): p. A63-A65.

64. Ni, M., M.K.H. Leung, and D.Y.C. Leung, *Micro-Scale Modeling of a Functionally Graded Ni-YSZ Anode.* Chemical Engineering & Technology, 2007. **30**(5): p. 587-592.

65. Chan, S.H., X.J. Chen, and K.A. Khor, *Cathode Micromodel of Solid Oxide Fuel Cell.* Journal of The Electrochemical Society, 2004. **151**(1): p. A164-A172.

66. Chen, X.J., S.H. Chan, and K.A. Khor, *Simulation of a composite cathode in solid oxide fuel cells.* Electrochimica Acta, 2004. **49**(11): p. 1851-1861.

67. Deseure, J., et al., *Modelling the porous cathode of a SOFC: oxygen reduction mechanism effect.* Journal of Applied Electrochemistry, 2007. **37**(1): p. 129-136.

68. Lehnert, W., J. Meusinger, and F. Thom, *Modelling of gas transport phenomena in SOFC anodes.* Journal of Power Sources, 2000. **87**(1–2): p. 57-63.

69. Yakabe, H., et al., *Evaluation and modeling of performance of anode-supported solid oxide fuel cell.* Journal of Power Sources, 2000. **86**(1–2): p. 423-431.

70. Suwanwarangkul, R., et al., *Performance comparison of Fick's, dusty-gas and Stefan–Maxwell models to predict the concentration overpotential of a SOFC anode.* Journal of Power Sources, 2003. **122**(1): p. 9-18.

71. Tseronis, K., I.K. Kookos, and C. Theodoropoulos, *Modelling mass transport in solid oxide fuel cell anodes: a case for a multidimensional dusty gas-based model.* Chemical Engineering Science, 2008. **63**(23): p. 5626-5638.

72. Grigoruk, D.G. and E.V. Kasilova, *Two-component mass transport in the anode of solid-oxide fuel cells.* Power Technology and Engineering, 2012. **46**(2): p. 138-142.

73. Damm, D.L. and A.G. Fedorov, *Local thermal non-equilibrium effects in porous electrodes of the hydrogen-fueled SOFC.* Journal of Power Sources, 2006. **159**(2): p. 1153-1157.

74. Yuan, J., et al., *Analysis of parameter effects on chemical reaction coupled transport phenomena in SOFC anodes.* Heat and Mass Transfer, 2009. **45**(4): p. 471-484.

75. Nam, J.H. and D.H. Jeon, *A comprehensive micro-scale model for transport and reaction in intermediate temperature solid oxide fuel cells.* Electrochimica Acta, 2006. **51**(17): p. 3446-3460.

76. Andersson, M., J. Yuan, and B. Sundén, *SOFC modeling considering electrochemical reactions at the active three phase boundaries.* International Journal of Heat and Mass Transfer, 2012. **55**(4): p. 773-788.

77. Hussain, M.M., X. Li, and I. Dincer, *A numerical investigation of modeling an SOFC electrode as two finite layers.* International Journal of Hydrogen Energy, 2009. **34**(7): p. 3134-3144.

78. Sunde, S., *Simulations of Composite Electrodes in Fuel Cells.* Journal of Electroceramics, 2000. **5**(2): p. 153-182.

79. Ho, T.X., et al., *Numerical analysis of a planar anode-supported SOFC with composite electrodes.* International Journal of Hydrogen Energy, 2009. **34**(8): p. 3488-3499.

80. Hussain, M.M., X. Li, and I. Dincer, *Multi-component mathematical model of solid oxide fuel cell anode.* International Journal of Energy Research, 2005. **29**(12): p. 1083-1101.

81. Farhad, S. and F. Hamdullahpur, *Micro-modeling of porous composite anodes for solid oxide fuel cells.* Aiche Journal, 2012. **58**(6): p. 1893-1906.

82. Ubertini, S. and R. Bove, *Mathematical Models: A General Overview*, in *Modeling Solid Oxide Fuel cELLS*, R. Bove and S. Ubertini, Editors. 2008, Springer Science +Business Media, B.V. p. 51-93.

83. Jeon, D.H., *A comprehensive CFD model of anode-supported solid oxide fuel cells.* Electrochimica Acta, 2009. **54**(10): p. 2727-2736.

84. Ferguson, J.R., J.M. Fiard, and R. Herbin, *Three-dimensional numerical simulation for various geometries of solid oxide fuel cells.* Journal of Power Sources, 1996. **58**(2): p. 109-122.

85. Kim, J.W., et al., *Polarization Effects in Intermediate Temperature, Anode-Supported Solid Oxide Fuel Cells.* Journal of The Electrochemical Society, 1999. **146**(1): p. 69-78.

86. Iwai, H., et al., *Numerical simulation of intermediate-temperature direct-internal-reforming planar solid oxide fuel cell.* Energy, 2011. **36**(4): p. 2225-2234.

87. Chinda, P., et al., *A planar anode-supported Solid Oxide Fuel Cell model with internal reforming of natural gas.* The European Physical Journal - Applied Physics, 2011. **54**(02): p. null-null.

88. Costamagna, P. and K. Honegger, *Modeling of Solid Oxide Heat Exchanger Integrated Stacks and Simulation at High Fuel Utilization.* Journal of The Electrochemical Society, 1998. **145**(11): p. 3995-4007.

89. Ota, T., et al., *Object-based modeling of SOFC system: dynamic behavior of micro-tube SOFC.* Journal of Power Sources, 2003. **118**(1–2): p. 430-439.

90. Aguiar, P., C.S. Adjiman, and N.P. Brandon, *Anode-supported intermediate temperature direct internal reforming solid oxide fuel cell. I: model-based steady-state performance.* Journal of Power Sources, 2004. **138**(1–2): p. 120-136.

91. Xue, X., et al., *Dynamic modeling of single tubular SOFC combining heat/mass transfer and electrochemical reaction effects.* Journal of Power Sources, 2005. **142**(1–2): p. 211-222.

92. Daun, K.J., et al., *Radiation heat transfer in planar SOFC electrolytes.* Journal of Power Sources, 2006. **157**(1): p. 302-310.

93. Sánchez, D., A. Muñoz, and T. Sánchez, *An assessment on convective and radiative heat transfer modelling in tubular solid oxide fuel cells.* Journal of Power Sources, 2007. **169**(1): p. 25-34.

94. Kee, R.J., B.L. Kee, and J.L. Martin, *Radiative and convective heat transport within tubular solid-oxide fuel-cell stacks.* Journal of Power Sources, 2010. **195**(19): p. 6688-6698.

95. Virkar, A.V., et al., *The role of electrode microstructure on activation and concentration polarizations in solid oxide fuel cells.* Solid State Ionics, 2000. **131**(1–2): p. 189-198.

96. Burt, A.C., et al., *A numerical study of cell-to-cell variations in a SOFC stack.* Journal of Power Sources, 2004. **126**(1–2): p. 76-87.

97. Recknagle, K.P., et al., *Three-dimensional thermo-fluid electrochemical modeling of planar SOFC stacks.* Journal of Power Sources, 2003. **113**(1): p. 109-114.

98. Yakabe, H., et al., *3-D model calculation for planar SOFC.* Journal of Power Sources, 2001. **102**(1–2): p. 144-154.

99. Liu, H.-C., et al., *Performance simulation for an anode-supported SOFC using Star-CD code.* Journal of Power Sources, 2007. **167**(2): p. 406-412.

100. Ackmann, T., et al., *Modeling of Mass and Heat Transport in Planar Substrate Type SOFCs.* Journal of The Electrochemical Society, 2003. **150**(6): p. A783-A789.

101. Autissier, N., et al., *CFD simulation tool for solid oxide fuel cells.* Journal of Power Sources, 2004. **131**(1–2): p. 313-319.

102. Danilov, V.A. and M.O. Tade, *A CFD-based model of a planar SOFC for anode flow field design.* International Journal of Hydrogen Energy, 2009. **34**(21): p. 8998-9006.

103. Beale, S.B., et al., *Computer methods for performance prediction in fuel cells.* Journal of Power Sources, 2003. **118**(1–2): p. 79-85.

104. Lin, C.-K., et al., *Thermal stress analysis of a planar SOFC stack.* Journal of Power Sources, 2007. **164**(1): p. 238-251.

105. Selimovic, A., et al., *Steady state and transient thermal stress analysis in planar solid oxide fuel cells.* Journal of Power Sources, 2005. **145**(2): p. 463-469.

106. Campanari, S. and P. Iora, *Definition and sensitivity analysis of a finite volume SOFC model for a tubular cell geometry.* Journal of Power Sources, 2004. **132**(1–2): p. 113-126.

107. Patcharavorachot, Y., A. Arpornwichanop, and A. Chuachuensuk, *Electrochemical study of a planar solid oxide fuel cell: Role of support structures.* Journal of Power Sources, 2008. **177**(2): p. 254-261.

108. Jeon, D.H., J.H. Nam, and C.-J. Kim, *Microstructural Optimization of Anode-Supported Solid Oxide Fuel Cells by a Comprehensive Microscale Model.* Journal of The Electrochemical Society, 2006. **153**(2): p. A406-A417.

109. Janardhanan, V.M. and O. Deutschmann, *CFD analysis of a solid oxide fuel cell with internal reforming: Coupled interactions of transport, heterogeneous catalysis and electrochemical processes.* Journal of Power Sources, 2006. **162**(2): p. 1192-1202.

110. Stiller, C., et al., *Finite-volume modeling and hybrid-cycle performance of planar and tubular solid oxide fuel cells.* Journal of Power Sources, 2005. **141**(2): p. 227-240.

111. Zhang, X., et al., *Numerical study on electric characteristics of solid oxide fuel cells.* Energy Conversion and Management, 2007. **48**(3): p. 977-989.

112. Dollard, W.J., *Solid oxide fuel cell developments at Westinghouse.* Journal of Power Sources, 1992. **37**(1–2): p. 133-139.

113. Ho, T.X., et al., *Numerical modeling of solid oxide fuel cells.* Chemical Engineering Science, 2008. **63**(21): p. 5356-5365.

114. Chan, S.H., K.A. Khor, and Z.T. Xia, *A complete polarization model of a solid oxide fuel cell and its sensitivity to the change of cell component thickness.* Journal of Power Sources, 2001. **93**(1–2): p. 130-140.

115. Yuan, J. and B. Sundén, *Analysis of Intermediate Temperature Solid Oxide Fuel Cell Transport Processes and Performance.* Journal of Heat Transfer, 2005. **127**(12): p. 1380-1390.

116. Shi, Y., N. Cai, and C. Li, *Numerical modeling of an anode-supported SOFC button cell considering anodic surface diffusion.* Journal of Power Sources, 2007. **164**(2): p. 639-648.

117. Paradis, H., et al., *CFD Modeling: Different Kinetic Approaches for Internal Reforming Reactions in an Anode-Supported SOFC.* Journal of Fuel Cell Science and Technology, 2011. **8**(3): p. 031014-031014.

118. Zhu, H., et al., *Modeling Elementary Heterogeneous Chemistry and Electrochemistry in Solid-Oxide Fuel Cells.* Journal of The Electrochemical Society, 2005. **152**(12): p. A2427-A2440.

119. Calise, F., et al., *Simulation and exergy analysis of a hybrid Solid Oxide Fuel Cell (SOFC)–Gas Turbine System.* Energy, 2006. **31**(15): p. 3278-3299.

120. Zabihian, F. and A. Fung, *A review on modelling of hybrid solid oxide fuel cell systems.* International journal of engineering, 2009. **3**(2): p. 85-119.

121. Harvey, S. and H. Richter, *Improved gas turbine power plant efficiency by use of recycled exhaust gases and fuel cell technology.* American Society of Mechanical Engineers, Advanced Energy Systems Division (AES), 1993. **30**: p. 199-207.

122. Harvey, S. and H. Richter, *Gas turbine cycles with solid oxide fuel cells. Part I: Improved gas turbine power plant efficiency by use of recycled exhaust gases and fuel cell technology.* Journal of Energy Resources Technology, 1994. **116**: p. 305-311.

123. Harvey, S. and H. Richter, *Gas turbine cycles with solid oxide fuel cells. Partr II: A detailed study of a gas turbine cycle with integrated internal reforming solid oxide fuel cell.* Journal of Energy Resources Technology, 1994. **116**: p. 312-318.

124. Gogoi, T.K., P. Sarmah, and D. Deb Nath, *Energy and exergy based performance analyses of a solid oxide fuel cell integrated combined cycle power plant.* Energy Conversion and Management, 2014. **86**: p. 507-519.

125. Chan, S.H., H.K. Ho, and Y. Tian, *Multi-level modeling of SOFC–gas turbine hybrid system.* International Journal of Hydrogen Energy, 2003. **28**(8): p. 889-900.

126. Palsson, J., A. Selimovic, and L. Sjunnesson, *Combined solid oxide fuel cell and gas turbine systems for efficient power and heat generation.* Journal of Power Sources, 2000. **86**(1–2): p. 442-448.

127. Chaisantikulwat, A., C. Diaz-Goano, and E.S. Meadows, *Dynamic modelling and control of planar anode-supported solid oxide fuel cell.* Computers & Chemical Engineering, 2008. **32**(10): p. 2365-2381.

128. Sánchez, D., et al., *On the effect of methane internal reforming modelling in solid oxide fuel cells.* International Journal of Hydrogen Energy, 2008. **33**(7): p. 1834-1844.

129. Iwata, M., et al., *Performance analysis of planar-type unit SOFC considering current and temperature distributions.* Solid State Ionics, 2000. **132**(3–4): p. 297-308.

130. Jin, X. and X. Xue, *Mathematical modeling analysis of regenerative solid oxide fuel cells in switching mode conditions.* Journal of Power Sources, 2010. **195**(19): p. 6652-6658.

131. Veldsink, J.W., et al., *The use of the dusty-gas model for the description of mass transport with chemical reaction in porous media.* The Chemical Engineering Journal and the Biochemical Engineering Journal, 1995. **57**(2): p. 115-125.

132. Izzo Jr, J.R., A.A. Peracchio, and W.K.S. Chiu, *Modeling of gas transport through a tubular solid oxide fuel cell and the porous anode layer.* Journal of Power Sources, 2008. **176**(1): p. 200-206.

133. Cayan, F.N., et al., *On modeling multi-component diffusion inside the porous anode of solid oxide fuel cells using Fick's model.* Journal of Power Sources, 2009. **192**(2): p. 467-474.

134. Khaleel, M.A., et al., *A finite element analysis modeling tool for solid oxide fuel cell development: coupled electrochemistry, thermal and flow analysis in MARC®.* Journal of Power Sources, 2004. **130**(1–2): p. 136-148.

135. Xie, Y. and X. Xue, *Transient modeling of anode-supported solid oxide fuel cells.* International Journal of Hydrogen Energy, 2009. **34**(16): p. 6882-6891.

136. Morel, B., et al., *Anode-Supported SOFC Model Centered on the Direct Internal Reforming.* Journal of The Electrochemical Society, 2005. **152**(7): p. A1382-A1389.

137. Suwanwarangkul, R., et al., *Modelling of a cathode-supported tubular solid oxide fuel cell operating with biomass-derived synthesis gas.* Journal of Power Sources, 2007. **166**(2): p. 386-399.

138. Ni, M., *2D thermal-fluid modeling and parametric analysis of a planar solid oxide fuel cell.* Energy Conversion and Management, 2010. **51**(4): p. 714-721.

139. Bhattacharyya, D., R. Rengaswamy, and C. Finnerty, *Isothermal models for anode-supported tubular solid oxide fuel cells.* Chemical Engineering Science, 2007. **62**(16): p. 4250-4267.

140. Monder, D.S., K. Nandakumar, and K.T. Chuang, *Model development for a SOFC button cell using H2S as fuel.* Journal of Power Sources, 2006. **162**(1): p. 400-414.

141. Pramuanjaroenkij, A., S. Kakaç, and X. Yang Zhou, *Mathematical analysis of planar solid oxide fuel cells.* International Journal of Hydrogen Energy, 2008. **33**(10): p. 2547-2565.

142. Andersson, M., et al. *LTNE approach and simulation for anode-supported SOFCs*. in *ASME 2009 7th International Conference on Fuel Cell Science, Engineering and Technology*. 2009. American Society of Mechanical Engineers.

143. Zhu, H. and R.J. Kee, *A general mathematical model for analyzing the performance of fuel-cell membrane-electrode assemblies.* Journal of Power Sources, 2003. **117**(1-2): p. 61-74.

144. Brown, M., S. Primdahl, and M. Mogensen, *Structure/Performance Relations for Ni/Yttria-Stabilized Zirconia Anodes for Solid Oxide Fuel Cells.* Journal of The Electrochemical Society, 2000. **147**(2): p. 475-485.

145. Qi, Y., B. Huang, and J. Luo, *Dynamic modeling of a finite volume of solid oxide fuel cell: The effect of transport dynamics.* Chemical Engineering Science, 2006. **61**(18): p. 6057-6076.

146. Achenbach, E., *Three-dimensional and time-dependent simulation of a planar solid oxide fuel cell stack.* Journal of Power Sources, 1994. **49**(1–3): p. 333-348.

147. Andersson, M., J. Yuan, and B. Sundén, *SOFC modeling considering hydrogen and carbon monoxide as electrochemical reactants.* Journal of Power Sources, 2013. **232**(0): p. 42-54.

148. Aloui, T. and K. Halouani, *Analytical modeling of polarizations in a solid oxide fuel cell using biomass syngas product as fuel.* Applied Thermal Engineering, 2007. **27**(4): p. 731-737.

149. Ho, T.X., et al., *Transport, chemical and electrochemical processes in a planar solid oxide fuel cell: Detailed three-dimensional modeling.* Journal of Power Sources, 2010. **195**(19): p. 6764-6773.

150. Haberman, B.A. and J.B. Young, *Three-dimensional simulation of chemically reacting gas flows in the porous support structure of an integrated-planar solid oxide fuel cell.* International Journal of Heat and Mass Transfer, 2004. **47**(17–18): p. 3617-3629.

151. Klein, J.M., S. Georges, and Y. Bultel, *Modeling of a SOFC Fueled by Methane:Anode Barrier to Allow Gradual Internal Reforming Without Coking.* Journal of The Electrochemical Society, 2008. **155**(4): p. B333-B339.

152. Achenbach, E. and E. Riensche, *Methane/steam reforming kinetics for solid oxide fuel cells.* Journal of Power Sources, 1994. **52**(2): p. 283-288.

153. Aguiar, P., D. Chadwick, and L. Kershenbaum, *Modelling of an indirect internal reforming solid oxide fuel cell.* Chemical Engineering Science, 2002. **57**(10): p. 1665-1677.

154. Dokamaingam, P., et al., *Modeling of SOFC with indirect internal reforming operation: Comparison of conventional packed-bed and catalytic coated-wall internal reformer.* International Journal of Hydrogen Energy, 2009. **34**(1): p. 410-421.

155. Andersson, M., J. Yuan, and B. Sundén, *Review on modeling development for multiscale chemical reactions coupled transport phenomena in solid oxide fuel cells.* Applied Energy, 2010. **87**(5): p. 1461-1476.

156. Wang, G., et al., *3-D model of thermo-fluid and electrochemical for planar SOFC.* Journal of Power Sources, 2007. **167**(2): p. 398-405.

157. Andersson, M., et al., *Three dimensional modeling of an solid oxide fuel cell coupling charge transfer phenomena with transport processes and heat generation.* Electrochimica Acta, 2013. **109**(0): p. 881-893.

158. Colpan, C.O., I. Dincer, and F. Hamdullahpur, *A review on macro-level modeling of planar solid oxide fuel cells.* International Journal of Energy Research, 2008. **32**(4): p. 336-355.

159. Oniciu, L., *Fuel Cells*. 1976, Tunbridge Wells, Kent: Abacus press.

160. Winkler, W., *Thermodynamics*, in *High temperature solid oxide fuel cells: Fundamentals, Design and Applications*
S.C. Singhal and K. Kendall, Editors. 2004, Elsevier p. 53-82.

161. Costamagna, P., et al., *Electrochemical model of the integrated planar solid oxide fuel cell (IP-SOFC).* Chemical Engineering Journal, 2004. **102**(1): p. 61-69.

162. Barbir, F., *PEM fuel cells : theory and practice*. 2nd ed. 2013, London: Academic. xvii, 518 p.

163. Suther, T., et al., *Effects of operating and design parameters on the performance of a solid oxide fuel cell–gas turbine system.* International Journal of Energy Research, 2011. **35**(7): p. 616-632.

164. Kotas, T.J., *Chapter 2 - Basic exergy concepts*, in *The Exergy Method of Thermal Plant Analysis*, T.J. Kotas, Editor. 1985, Butterworth-Heinemann. p. 29-56.

165. Bedringås, K.W., et al., *Exergy analysis of solid-oxide fuel-cell (SOFC) systems.* Energy, 1997. **22**(4): p. 403-412.

166. Barbir, F., *PEM fuel cells : theory and practice*. Sustainable world series. 2005, Oxford: Academic. xv, 433 p.

167. Zhao, F. and A.V. Virkar, *Dependence of polarization in anode-supported solid oxide fuel cells on various cell parameters.* Journal of Power Sources, 2005. **141**(1): p. 79-95.

168. Bird, R.B., W.E. Stewart, and E.N. Lightfoot, *Transport Phenomena*. 2007: Wiley.

169. Ni, M., D.Y.C. Leung, and M.K.H. Leung, *Electrochemical modeling and parametric study of methane fed solid oxide fuel cells.* Energy Conversion and Management, 2009. **50**(2): p. 268-278.

170. Karcz, M., *From 0D to 1D modeling of tubular solid oxide fuel cell.* Energy Conversion and Management, 2009. **50**(9): p. 2307-2315.

171. Hussain, M.M., X. Li, and I. Dincer, *A general electrolyte–electrode-assembly model for the performance characteristics of planar anode-supported solid oxide fuel cells.* Journal of Power Sources, 2009. **189**(2): p. 916-928.

172. Krishna, R. and J.A. Wesselingh, *The Maxwell-Stefan approach to mass transfer.* Chemical Engineering Science, 1997. **52**(6): p. 861-911.

173. Cussler, E.L., *Diffusion: Mass Transfer in Fluid Systems*. 1997: Cambridge University Press.

174. Fairbanks, D.F. and C.R. Wilke, *Diffusion Coefficients in Multicomponent Gas Mixtures.* Industrial & Engineering Chemistry, 1950. **42**(3): p. 471-475.

175. Curtiss, C.F. and R.B. Bird, *Multicomponent Diffusion.* Industrial & Engineering Chemistry Research, 1999. **38**(7): p. 2515-2522.

176. Ngo, N.D. and K.K. Tamma, *Microscale permeability predictions of porous fibrous media.* International Journal of Heat and Mass Transfer, 2001. **44**(16): p. 3135-3145.

177. Litster, S. and N. Djilali, *Two-phase transport in porous gas diffusion electrode*, in *Transport phenomena in fuel cells*, B. Sunden and M. Faghri, Editors. 2005, WIT press: Southampton. p. 175-213.

178. Todd, B. and J.B. Young, *Thermodynamic and transport properties of gases for use in solid oxide fuel cell modelling.* Journal of Power Sources, 2002. **110**(1): p. 186-200.

179. Welty, J.R., C.E. Wicks, and R.E. Wilson, *Fundamentals of momentum, heat, and mass transfer*. 1976: Wiley.

180. Taylor, R. and R. Krishna, *Multicomponent Mass Transfer*. 1993: Wiley.

181. Farhad, S. and F. Hamdullahpur, *Optimization of the microstructure of porous composite cathodes in solid oxide fuel cells.* AIChE Journal, 2012. **58**(4): p. 1248-1261.

182. Kenney, B., et al., *Computation of TPB length, surface area and pore size from numerical reconstruction of composite solid oxide fuel cell electrodes.* Journal of Power Sources, 2009. **189**(2): p. 1051-1059.

183. Kenjo, T., S. Osawa, and K. Fujikawa, *High Temperature Air Cathodes Containing Ion Conductive Oxides.* Journal of The Electrochemical Society, 1991. **138**(2): p. 349-355.

184. Kenjo, T. and M. Nishiya, *LaMnO3 air cathodes containing ZrO2 electrolyte for high temperature solid oxide fuel cells.* Solid State Ionics, 1992. **57**(3–4): p. 295-302.

185. Jeon, D.H., J.H. Nam, and C.-J. Kim, *A random resistor network analysis on anodic performance enhancement of solid oxide fuel cells by penetrating electrolyte structures.* Journal of Power Sources, 2005. **139**(1–2): p. 21-29.

186. Abel, J., A.A. Kornyshev, and W. Lehnert, *Correlated Resistor Network Study of Porous Solid Oxide Fuel Cell Anodes.* Journal of The Electrochemical Society, 1997. **144**(12): p. 4253-4259.

187. Costamagna, P., P. Costa, and E. Arato, *Some more considerations on the optimization of cermet solid oxide fuel cell electrodes.* Electrochimica Acta, 1998. **43**(8): p. 967-972.

188. Yang, Y., et al., *Comparison of heat and mass transfer between planar and MOLB-type SOFCs.* Journal of Power Sources, 2008. **177**(2): p. 426-433.

189. Dyer, C.K., *Replacing the battery in portable electronics.* Scientific American, 1999. **281**(1): p. 88-93.

190. Staniforth, J. and R.M. Ormerod, *Implications for Using Biogas as a Fuel Source for Solid Oxide Fuel Cells: Internal Dry Reforming in a Small Tubular Solid Oxide Fuel Cell.* Catalysis Letters, 2002. **81**(1-2): p. 19-23.

191. Ormerod, R.C., *Solid oxide fuel cells.* Chemical Society Reviews, 2003. **32**: p. 17-28.

192. Yuan, J., M. Rokni, and B. Sunden, *Three dimensional computational analysis of gas and heat transport phenomena in ducts relevant for anode supported solid oxide fuel cells.* International Journal of Heat and Mass Transfer, 2003. **46**(5): p. 809-821.

193. Steele, B.C.H. and A. Heinzel, *Materials for fuel-cell technologies.* Nature, 2001. **414**(6861): p. 345-352.

194. Huang, K., J.-H. Wan, and J.B. Goodenough, *Increasing Power Density of LSGM-Based Solid Oxide Fuel Cells Using New Anode Materials.* Journal of The Electrochemical Society, 2001. **148**(7): p. A788-A794.

195. P, H.J.P., V.B.F.P. F, and G.M. Christie, *Intermediate temperature SOFC - a promise for the 21st century.* Journal of Power Sources, 1998. **71**: p. 107-110.

196. Sun, C. and U. Stimming, *Recent anode advances in solid oxide fuel cells.* Journal of Power Sources, 2007. **171**(2): p. 247-260.

197. McIntosh, S. and R.J. Gorte, *Direct Hydrocarbon Solid Oxide Fuel Cells.* Chemical Reviews, 2004. **104**(10): p. 4845-4866.

198. Peters, C., A. Weber, and E. Ivers-Tiffée, *Nanoscaled (La0.5Sr0.5) CoO3 − δ Thin Film Cathodes for SOFC Application at 500 ° C < T < 700 ° C.* Journal of The Electrochemical Society, 2008. **155**(7): p. B730-B737.

199. Takagi, Y., et al., *Low temperature thin film solid oxide fuel cells with nanoporous ruthenium anodes for direct methane operation.* Energy & Environmental Science, 2011. **4**(9): p. 3473-3478.

200. Kwon, C.-W., et al., *High-Performance Micro-Solid Oxide Fuel Cells Fabricated on Nanoporous Anodic Aluminum Oxide Templates.* Advanced Functional Materials, 2011. **21**(6): p. 1154-1159.

201. Ko, C., K. Kerman, and S. Ramanathan, *Ultra-thin film Solid oxide fuel cells utilising undoped nanostructured zirconia electrolytes.* Journal of Power Sources, 2012. **213**: p. 343-349.

202. Chen, X., et al., *Thin-film heterostructure solid oxide fuel cells.* Applied Physics Letters, 2004. **84**(14): p. 2700-2702.

203. Lin, Z., J.W. Stevenson, and M.A. Khaleel, *The effect of interconnect rib size on the fuel cell concentration polarization in planar SOFCs.* Journal of Power Sources, 2003. **117**(1–2): p. 92-97.

204. Liu, S., C. Song, and Z. Lin, *The effects of the interconnect rib contact resistance on the performance of planar solid oxide fuel cell stack and the rib design optimization.* Journal of Power Sources, 2008. **183**(1): p. 214-225.

205. Golbert, J., C.S. Adjiman, and N.P. Brandon, *Microstructural Modeling of Solid Oxide Fuel Cell Anodes.* Industrial & Engineering Chemistry Research, 2008. **47**(20): p. 7693-7699.

206. Liu, S., W. Kong, and Z. Lin, *A microscale modeling tool for the design and optimisation of solid oxide fuel cells.* Energies, 2009. **2**: p. 427-444.

207. Kenney, B. and K. Karan, *Engineering of microstructure and design of a planar porous composite SOFC cathode: A numerical analysis.* Solid State Ionics, 2007. **178**(3–4): p. 297-306.

208. Jung, H.Y., et al., *Effect of cathode current-collecting layer on unit-cell performance of anode-supported solid oxide fuel cells.* Journal of Power Sources, 2006. **155**(2): p. 145-151.

209. Liu, M., et al., *High-performance cathode-supported SOFCs prepared by a single-step co-firing process.* Journal of Power Sources, 2008. **182**(2): p. 585-588.

210. Yamahara, K., et al., *Catalyst-infiltrated supporting cathode for thin-film SOFCs.* Solid State Ionics, 2005. **176**(5-6): p. 451-456.

211. Nagel, F.P., et al., *Charge, mass and heat transfer interactions in solid oxide fuel cells operated with different fuel gases—A sensitivity analysis.* Journal of Power Sources, 2008. **184**(1): p. 129-142.

212. Damm, D.L. and A.G. Fedorov, *Reduced-order transient thermal modeling for SOFC heating and cooling.* Journal of Power Sources, 2006. **159**(2): p. 956-967.

213. Kang, Y., et al., *One-dimensional Dynamic Modeling and Simulation of a Planar Direct Internal Reforming Solid Oxide Fuel Cell.* Chinese Journal of Chemical Engineering, 2009. **17**(2): p. 304-317.

214. Zitouni, B., et al., *Two-dimensional numerical study of temperature field in an anode supported planar SOFC: Effect of the chemical reaction.* International Journal of Hydrogen Energy, 2011. **36**(6): p. 4228-4235.

215. Haseli, Y., I. Dincer, and G.F. Naterer, *Thermodynamic modeling of a gas turbine cycle combined with a solid oxide fuel cell.* International Journal of Hydrogen Energy, 2008. **33**(20): p. 5811-5822.

216. Zabihian, F. and F. Alan, *A review on modeling of hybrid solid oxide fuel cell systems.* International journal of engineering, 2009. **3**(2): p. 85-219.

217. Massardo, A.F. and F. Lubelli, *Internal Reforming Solid Oxide Fuel Cell-Gas Turbine Combined Cycles (IRSOFC-GT): Part A—Cell Model and Cycle Thermodynamic Analysis.* Journal of Engineering for Gas Turbines and Power, 1999. **122**(1): p. 27-35.

218. Ameri, M. and R. Mohammadi, *Simulation of an atmospheric SOFC and gas turbine hybrid system using Aspen Plus software.* International Journal of Energy Research, 2013. **37**(5): p. 412-425.

219. Burbank Jr, W., D.D. Witmer, and F. Holcomb, *Model of a novel pressurized solid oxide fuel cell gas turbine hybrid engine.* Journal of Power Sources, 2009. **193**(2): p. 656-664.

220. Yang, W.J., et al., *Design performance analysis of pressurized solid oxide fuel cell/gas turbine hybrid systems considering temperature constraints.* Journal of Power Sources, 2006. **160**(1): p. 462-473.

221. Tucker, D., et al., *Evaluation of Methods for Thermal Management in a Coal-Based SOFC Turbine Hybrid Through Numerical Simulation.* Journal of Fuel Cell Science and Technology, 2012. **9**(4): p. 041004-041004.

222. Zhang, X., et al., *Cycle analysis of an integrated solid oxide fuel cell and recuperative gas turbine with an air reheating system.* Journal of Power Sources, 2007. **164**(2): p. 752-760.

223. Granovskii, M., I. Dincer, and M.A. Rosen, *Performance comparison of two combined SOFC–gas turbine systems.* Journal of Power Sources, 2007. **165**(1): p. 307-314.

224. Calise, F., A. Palombo, and L. Vanoli, *Design and partial load exergy analysis of hybrid SOFC–GT power plant.* Journal of Power Sources, 2006. **158**(1): p. 225-244.